DESIGN AND SYNTHESIS OF STRUCTURALLY ORDERED IONIC POLYMERS VIA DYNAMIC BORATE CHEMISTRY

by

Lacey J. Wayment

B.S., The College of Idaho, 2016

A thesis submitted to the
Faculty of the Graduate School of the
University of Colorado in partial fulfillment
of the requirement for the degree of
Doctor of Philosophy
Department of Chemistry
2024

Committee members
Wei Zhang
Jihye Park
Sandeep Sharma
David Walba
Yinghua Jin

Thesis Abstract

Wayment, Lacey J.

Design and Synthesis of Structurally Ordered Ionic Polymers Via Dynamic Borate Chemistry

Thesis directed by Professor Wei Zhang

Crystalline polymers with well-defined structures have garnered considerable interest across multiple disciplines. Dynamic covalent chemistry (DCvC) is often employed in constructing crystalline polymers due to the light elements, covalent bonds, and error correction that facilitates the formation of ordered structures. Despite advancements, there remains a significant knowledge gap concerning the energetics of various polymeric phases and the impact of non-covalent interactions on the thermodynamics of the system. Recent progress in tuning the equilibrium has enabled the synthesis of high-quality crystalline samples for characterization with atomic resolution. Much of this progress has been centered on imine chemistry, leaving other DCvC linkages relatively unexplored. Charged borates present an avenue for creating intriguing and functionally relevant polymers. This thesis explores how dynamic borate chemistry can be utilized in crafting crystalline polymers. Additionally, this work explores the synergistic relationship between DCvC and supramolecular chemistry.

Chapter 1 will introduce Dynamic Covalent Chemistry and discuss state of the art for the synthesis of crystalline polymers. First, the fundamental principles of DCvC will be presented. Subsequently, recent progress in developing DCvC linkages and techniques for tuning their equilibrium will be discussed. Lastly, the design of topologies, polymetric phases, and the synergistic interplay between DCvC and supramolecular chemistry will be examined.

In Chapter 2, the discovery of a 3D COF as a metastable intermediate to the formation of a 1D helical covalent polymer (HCP) will be presented. The experimental evidence and theoretical calculation demonstrate that the 3D COF is a kinetically trapped state while the HCP topology is more thermodynamically favorable. This demonstrates that a series of hydrogen bonding interactions can be more favorable than a fully covalently bonded framework.

Chapter 3 will discuss new HCP structures developed by tuning the supramolecular interactions between the helical chains. The first portion will discuss the effect of counter-ion on the topology, which utilized single crystal XRD to unveil a novel entwinement mode. Then, ion exchange studies demonstrate that the hydrogen-bonded HCP can be converted into a metal-coordinated topology. In Chapter 4, I will present a novel borate linkage. By removing the chelating effect of the spiroborate, a novel tetra-substituted borate chemistry can be formed. This chapter will discuss frameworks synthesized by tetraborate and flexible linkages to form dia networks. Then, the utility of these materials will be demonstrated by their use in solid-state electrolytes for metal-ion batteries. Finally, Chapter 5 will review the previous chapters and suggest future works.

DEDICATION

To my family

ACKNOWLEDGEMENTS

I am profoundly grateful to everyone who has contributed to the completion of this thesis. Their support, guidance, and encouragement have been invaluable throughout this journey. First and foremost, I would like to express my deepest gratitude to my supervisor, Prof. Wei Zhang, for his support, expert guidance, and insightful feedback. His mentorship has been instrumental in shaping this thesis and in my growth as a researcher. I am also thankful to the members of my thesis committee, Prof. Jihye Park, Prof. Sandeep Sharma, Prof. David Walba, and Dr. Yinghua Alice Jin. I appreciate the staff and faculty of the University of Colorado Boulder, whose resources and facilities have allowed me to conduct experiments.

To my friends and colleagues, thank you for your encouragement, camaraderie, and understanding during moments of stress and success. Your friendship has made this endeavor all the more rewarding. I would like to express my gratitude to all the participants and individuals who shared their time and insights into this research. Their contributions are invaluable and have enriched the findings of this thesis. Some of my lab mates who are co-authors of this work include Dr. Yiming Hu, Dr. Zepeng Lei, Shaofeng Huang, Hongxuan Chen, and Matthew McCoy. I would also like to thank Ashley Ley, Joy Liu, and Matthew McCoy for allowing me to mentor them in some capacity. They have all kept me on my toes and I believe they will do great things.

I would also like to thank many of the professors from my undergraduate school for encouraging me to apply to graduate school. Prof. Scott Truksa first showed me how interesting organic chemistry can be. Prof. Chris Saunders was my academic advisor and was so kind throughout. Prof. Ken Cornell was a collaborator that turned in to a second research advisor while I was a research technician. Finally, Prof. John Thurston was my first research advisor, and I always enjoyed our chats about life.

I am deeply indebted to my family for their unwavering love, support, and understanding throughout this academic journey. I am forever grateful for their sacrifices and encouragement. My partner, Dr. James B. Franek, has been particularly supportive and always encouraged me to do my best.

I am sincerely thankful to everyone who has played a part, however small, in the completion of this thesis. Your support and encouragement have been instrumental, and I am deeply appreciative of your contributions.

Table of Contents

List of Figures

List of Tables

Chapter 1: Introduction to Crystalline Polymers Built via DCvC

Nature frequently serves as a wellspring of inspiration for scientists, owing to the remarkable properties exhibited by many natural polymers. Collagen, for instance, is a common protein found in bone, hair, skin, and joints.[1,2] On the molecular level, collagen consists of 1D peptide chains intertwined through hydrogen bonding interactions to form a triple helix.[1,2] The remarkable strength and elasticity are attributed to its structure.[1,2] For decades, chemists studied methods for precisely controlling the assembly of molecular components in a bottom-up approach to mimic the sophisticated motifs in nature. Supramolecular chemistry was an early approach that utilized non-covalent bonds to form extended structures such as hydrogen bonds, metal-coordination, or host-guest interaction.[3, 4] The weak interactions are dynamic due to the low energy barrier for breaking and reforming the interactions. This allows error correction, so molecules self-assemble to form a structure representing a thermodynamic minimum as the major species. However, it also limits the stability of the resulting material due to the low energy barrier for breaking the non-covalent bonds. Dynamic covalent chemistry (DCvC) has been developed to overcome this limitation. DCvC uses the principle of thermodynamic control, like supramolecular chemistry, while relying on more durable covalent bonds.[5-7] Many molecular architectures, such as macrocycles, covalent organic polyhedron/organic molecular cages (COP/OMC), and covalent organic frameworks (COF), have been developed using DCvC.

Despite great stives, it is still challenging to synthesize single-crystal polymeric samples suitable for atomic resolution. It has been demonstrated that the degree of structural order will affect the properties.[8- 10] Thus, it is crucial to understand the factors that can facilitate the synthesis of high-quality samples to unlock novel functionality. This chapter will discuss the guiding principles in designing crystalline polymers with DCvC. First, the general principles of DCvC will be introduced. Then common DCvC linkages in crystalline polymers will be discussed followed by methods to tune the equilibrium from the reaction conditions. Finally, the topology of ordered polymers will be discussed.

1.1 Introduction to DCvC Principles

A simple reaction that involves a dynamic bond will include a mixture of species, such as starting materials, semi-stable intermediates, and products (Figure 1a). [3, 5, 6, 11] The kinetic product will form initially in a higher concentration since the activation energy barrier is lower than the thermodynamic pathway. The concentrations will shift until equilibrium is reached, where the product distribution will reflect the relative difference in Gibbs' free energy of the products. If the monomer can make two DCvC linkages such as in a cyclooligomerization then the initial species will include a mixture of liner and cyclic oligomers. As the system reaches equilibrium, the product distribution will be simplified to those representing the system's thermodynamic minimums at equilibrium (Figure 1.1b).[11]

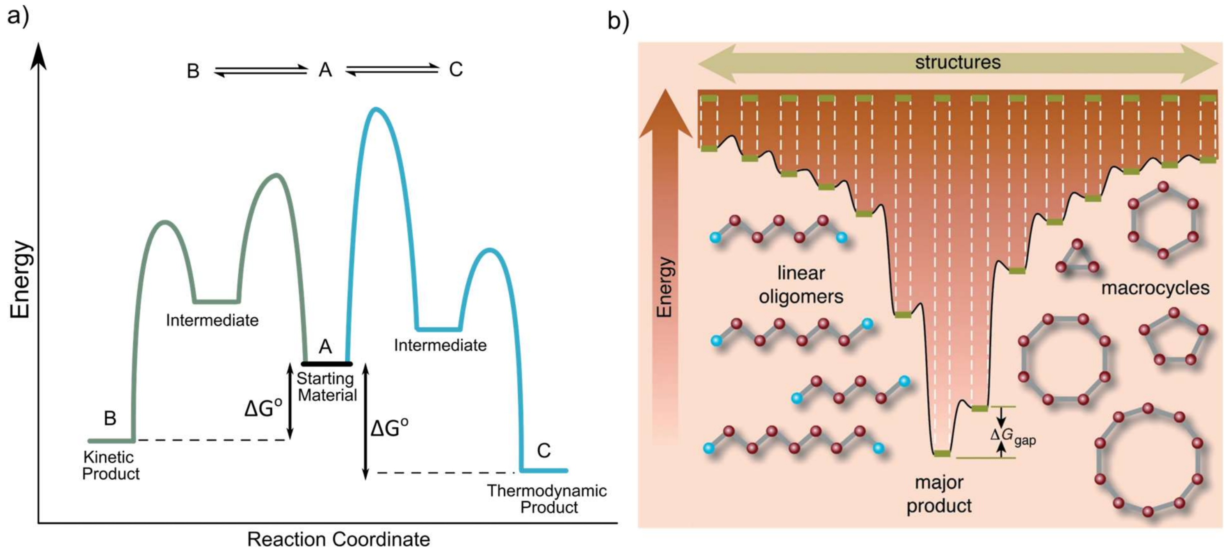

Figure 1.1. (a) A general reaction diagram of a simple dynamic reaction. (b) Energy landscape of cyclooligomerization. Partially reproduced from Ref. 11 with permission. Copyright Wiley-VCH, 2006. (Ref. 11b)

The structures that are thermodynamic minimums will be dependent on entropy and enthalpy. Entropy generally dictates that many small molecules will be favorable compared to fewer larger molecules. On the other hand, enthalpy favors structures with no strain such as bond angle or steric strain. Thus, DCvC can be used to make specific structures by meticulous selection of monomers. There are some kinetic and thermodynamic controls that can be introduced to tune the equilibrium to favor specific products if there are multiple species with similar energetics.

Closed structures like macrocycles or COPs/OMCs generally have solubilizing chains to ensure that all intermediates stay in solution to participate in the exchange of molecular components (thermodynamic control). Kinetic controls must also be considered to ensure a high conversion. Removing a product or byproduct from the reaction system is an effective method to tune the equilibrium via Le Chatelier's principle. For example, full conversion in alkyne metathesis requires the removal of the byproduct. Figure 1.2 illustrates a simple alkyne metathesis reaction, where exchange mechanisms operate through two pathways. The first pathway involves a non-productive pathway where the molecular components are exchanged without generating new species (Figure 1.2). The productive pathway leads to the formation of two new species (Figure 1.2). To ensure a high conversion, one of the species is designated as a byproduct that can be removed though the use of vacuum, molecular sieves, or by precipitate it out.[12] Alternatively, the reaction system can be designed to selectively precipitate out one of the products as a kinetically

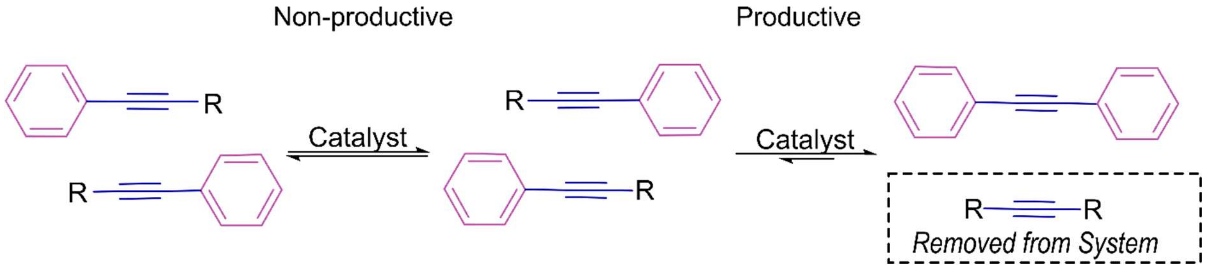

Figure 1.2. Model alkyne metathesis reaction.

trapped state (kinetic control).[13] Most crystalline polymers are synthesized under solvothermal conditions. The polymers typically precipitate out of solution over the course of the reaction.

Precipitation likely acts as a kinetic driving force towards polymerization, but it is unclear how large crystalline domains are formed. Thus far, there are two proposed mechanisms for crystalline polymers (Figure 1.3).[14] Small crystalline nuclei could form first and then continue to grow or elongate. Alternatively, a cross linked amorphous polymer could form first. Then crystalline domains form after the longs undergo error correct. There is evidence that a 2D COF with boronate ester linkages will go through the first mechanism while imine linked 2D COFs will undergo the second mechanism.[14] However, there is evidence that 3D imine COFs could occur though the top mechanism (Figure 1.3). Wang et al. recently demonstrated that they could track the growth of single crystals and the rate of growth was dependent on the reaction condition.[15] Additionally, Kawano and Murakami reported crystals of a kinetically trapped phase will dissolve and reform the thermodynamically favored topology in 3D imine linked COFs.[16] There is still much unknown about the crystallization mechanism and its dependence on reaction conditions, the type of dynamic bonds, 1D or 3D topologies, or polymers that exhibit different polymetric phases.

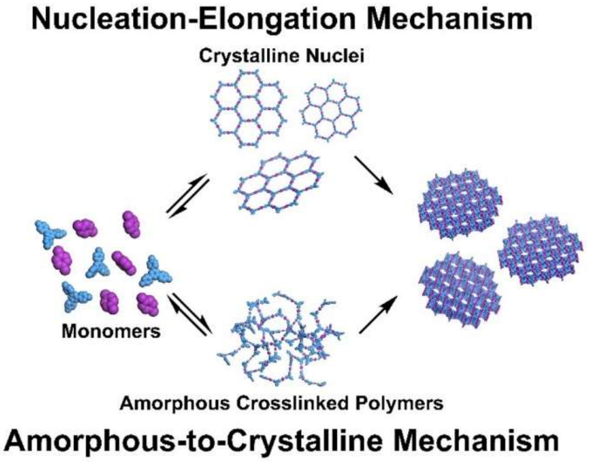

Figure 1.3. Proposed mechanism for 2D polymerization in solution. Copyright 2022 American Chemical Society. Ref. 14.

1.2 Dynamic linkages in Crystaline polymers

This section will explore the utilization of dynamic bonds in the development of crystalline polymers. It will emphasize boronic acid and imine derivatives since most of the materials being developed rely on these dynamic bonds. Additionally, the relationship between structure, stability, and exchange rate will be discussed.

1.2.1 Boronic Acid Derivatives

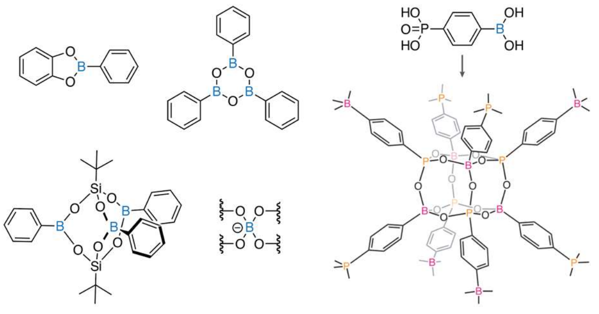

Figure 1.4. Scheme of boronic acid derivatives developed for crystalline polymers.

The Yaghi group are pioneers in the formation of 2D COFs. In 2005, they first demonstrated the formation of COFs using the boronate ester and boroxine (Figure 1.4).[17] In this seminal study, COF-1 was synthesized directly from the condensation of 1,4-benzenediboronic acid (BDBA). Similarly, boronate ester linkages were employed to produce COF-5 through the condensation of 2,3,6,7,10,11-hexahydroxytriphenylene (HHTP) and phenylboronic acid. The versatility of these linkages has been demonstrated through the development of numerous COFs with various monomers, topologies, and synthetic conditions.[18-20] However, their practical applications are limited due to the instability resulting from the Lewis acid nature of the boron in these linkages.

To overcome these limitations and broaden structural diversity, several derivatives have been developed. The dynamic spiroborate bond was designed to enhance the stability of materials in nucleophilic solvents.[21] Unlike previous boronic acid derivatives, the spiroborate bond is sp^3 hybridized, eliminating the empty p-orbital that rendered them unstable (Figure 1.4). Recently, more interest in this bond has been garnered since it exhibits configurational flexibility and a highly dynamic nature.[22-24] Thus far, researchers have utilized variations in monomer geometry and counter-ions to create 1D polymers and 3D frameworks.[22-26] In these structures the dihedral angle of the spiroborate can be varied from 66° to 90°. Likewise, boronic acids can be condensed with silicates[27] and phosphates[28] to create diverse topologies from relatively simple building blocks (Figure 1.4). Or condensed together and form a mixture of neutral and charged boron in a 1D polymer.[29]

1.2.2 Imine Derivatives

The imine linkage was first reported in 2009 and has become the most widely used linkage used in the development of new crystalline polymers (Figure 1.5).[30] The imine linkage is compatible with many monomer combinations, will quantitatively link monomers, and it is directional for precise ordering of monomers in a lattice. Moreover, the imine bond is highly dynamic like boronate esters and boroxine bond while improving the stability of the material. The greatest disadvantage of this chemistry is the imine linkages can still be vulnerable to hydrolysis, and it often doesn't contribute to the material properties. Much research effort has been focused on developing this chemistry further by

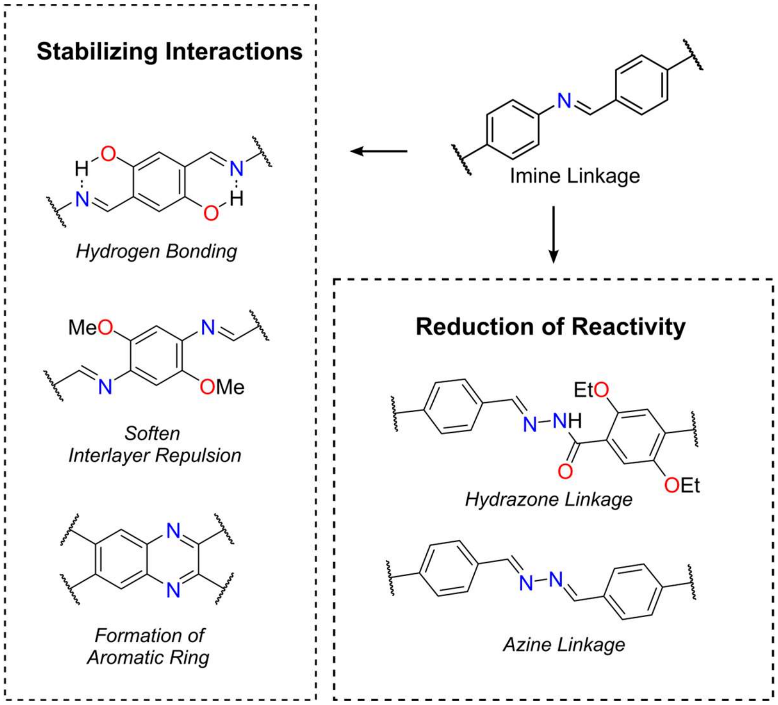

Figure 1.5. Methods for derivatizing the imine linkage.

modifying the structure of the linkages to improve crystallinity, stability, and functionality.

Employing dynamic covalent bonds with low disassociation energy, such as the azodioxide linkage, can result in highly crystalline framework, similar to supramolecular polymerizations. [31] If bonds break too readily then the resulting material could have instability issues. Hence, achieving a balance between stability and reactivity is essential to leverage the benefits of exchanging dynamic covalent bonds while simultaneously enhancing the material's stability. Thus far, it has been demonstrated that intermolecular and intramolecular hydrogen bonding can improve a material's stability (Figure 1.5).[32,33] Similarly, it has been reported that interlayer repulsion can by reduced by introducing methoxy groups while neighboring methyl groups decrease the imines linkage from hyperconjugation.[34] The linkage itself can also be derivatized to develop novel linkages in crystalline polymers. The hydrazone[35] and azide[36] bond will are analogous to imine linkages, but electronic effects reduce the reactivity.

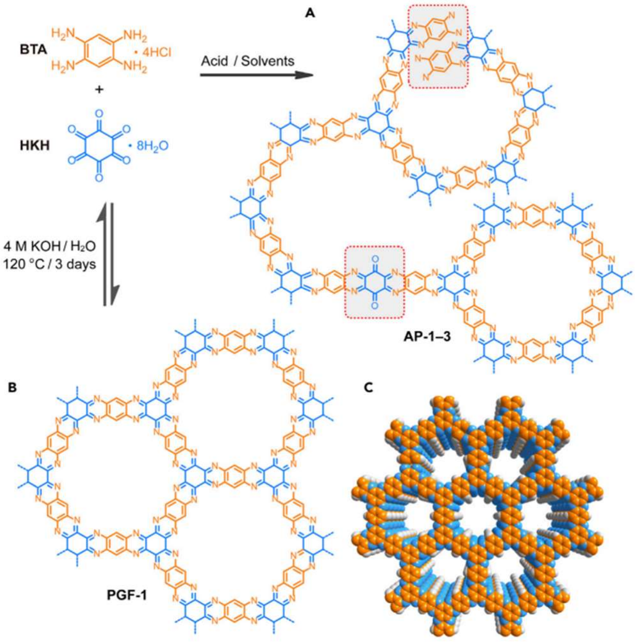

Figure 1.6. Schematic of phenazine-linked frameworks under acidic and basic conditions. Reprinted with permission from 2020 Elsevier Ref. 46

The phenazine linkage is an aromatic ring formed from a 1,2-substituted amine condensed with a diketone monomer. This linkage is considered an ultra-stable linkage, and there were only a few examples of crystalline materials with this linkage. [37-41] Previously it was proposed that the initial condensation would be reversible while the second condensation that resulted in the aromatic ring was irreversible. Zhang and Lui recently demonstrated that the dynamic nature of the phenazine can be unlocked (Figure 1.6).[42] Scrambling experiments between hexamethyl substituted hexaazatrinaphthalene (HATN-Me) and 1,2-phenylenediamine (PDA) only showed exchange when they used aqueous potassium hydroxide as a catalyst. NMR and MALDI-MS showed a mixture of species under the basic conditions while acid or neutral conditions showed no evidence of exchange. The authors demonstrated that basic conditions resulted in greater crystallinity in the polymer. Strategically inducing the exchange of dynamic covalent bonds is a potent method for synthesizing stable crystalline materials.

An alternative approach to enhance material properties involves utilizing DCvC bonds to construct ordered frameworks, followed by converting the linkage into a novel functional group in an irreversible manner. The crystalline polymers with the dynamic imine linkage have been transformed into functional groups such as amine, thiazole, benzoxazole, and many more (Figure 1.7).[43, 44] This conversion can be achieved through post-synthetic modification, in-situ reaction, or as part of a multi-component synthesis process. The thiazole linkages have been demonstrated to be installed

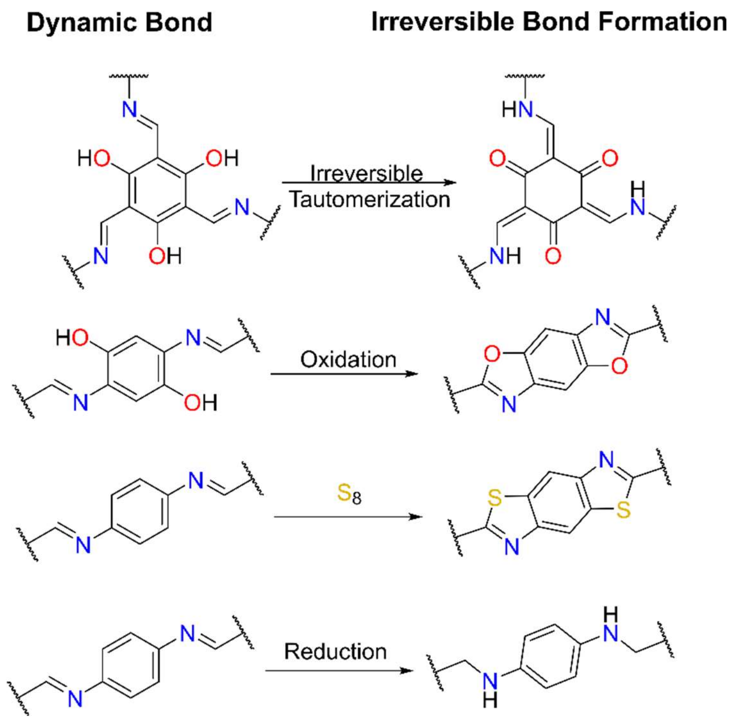

Figure 1.7. Irreversible linkages in COFs built on dynamic imine bond.

three ways where two are though a two-step process and one is in situ. The first procedure treated an imine COF with sulfur at high temperatures.[45] Alternatively, the thiazole functional groups can be introduced by subjecting an imine COF to a monomers exchange with subsequent oxidation.[46] The most recent example used an in situ conversion by adding sulfur, acetic acid, and DMSO as an oxidative agent.[47] Similarly, the amine-based[48] and benzoxazole[49] COFs can be produced step-wise or in situ as part of a cascade reaction. The β-ketoenamine[43] is a very common linkage used in materials due to its high stability and it introduces redox-active groups that could be used to add functionality to the material. Generally, this linkage will undergo an enol-to-keto tautomerization after forming an ordered framework due to the reversibility of the imine linkage. Recently, Tang, Yu, and Zhang et al. demonstrated that the reversibility of the linkages can be unlocked by using a secondary amine.[50] The secondary amine is proposed to remove the hydrogen bonding interactions to reduce the stability of the linkage.

DCvC and these strategies have significantly expanded the utility and potential of crystalline polymers by enhancing their robustness. It is essential to carefully balance the thermodynamics and kinetics of the reaction system to obtain highly crystalline material. The imine linkages are primarily responsible for the orderliness of the structure, and the irreversible step needs to occur rapidly enough to ensure a complete conversion of the imine linkage. If the irreversible step(s) are too quick then ordered frameworks may not form. Similarly, post-synthetic methods require thorough assessment of the conversion process while preserving the framework's crystalline structure. Model compounds can assist in studying changes in chemical composition, but it may not accurately reflect efficiency due to differences in solubility of a small molecule compared to insoluble polymer species. Another difficulty is some structures are susceptible to solvent inducing order. In 2019, Medina, Bein, and co-workers demonstrated that solvent or solvent vapors could disturb the layered arrangement of 2D imine COFs.[51] They also determined this disarray can be counteracted by activating some materials with supercritical CO_2.

In summary, the inherent organic nature of these connections enables remarkable flexibility in structure to tune the DCvC properties. A wide array of materials can be crafted to understand the underlying dynamics of these linkages based on electronic or steric effects. The irreversible functionalization of dynamic linkages can enrich the structural diversity of materials. Other types of dynamic bonds have not been applied to these strategies; their adoption could pave the way for fascinating new avenues in chemistry.

1.3 Effect of Reaction Conditions on Crystalline Polymers

Balancing the thermodynamic and kinetic driving forces is crucial for synthesizing ordered structures. The polymer will most likely be amorphous if only kinetic controls are in place because little error correction will occur. Conversely, the polymerization degree can suffer if only thermodynamic driving forces exist. Reaction conditions such as solvent, catalyst, time, monomer design, and temperature are all screened to achieve crystalline polymers. This section will demonstrate some methods for tuning the kinetic and thermodynamic driving forces for

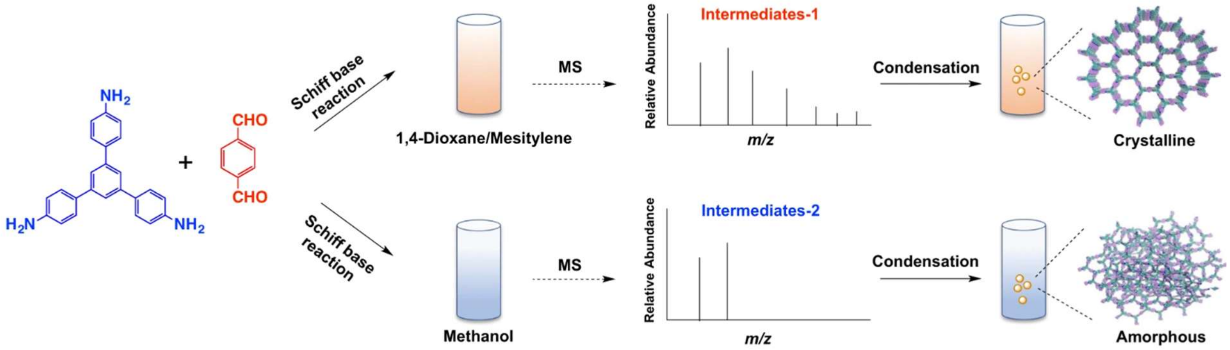

Figure 1.8. The effect of solvent on monomers in solution as detected with mass spectrometry. TPBA aggregates were observed in dioxane/mesitylene solution during the synthesis of crystalline COF. When the solvent is changed to methanol then no packing is observed, and the resulting polymer is amorphous. This figure is reproduced with permission from ref 52. Copyright 2020 Springer Nature.

synthesizing crystalline polymers.

Crystaline polymers are generally synthesized using a polar solvent and an aromatic solvent. The solvents are typically screened with little insight into why some solvent combinations work while others result in amorphous polymers. Recently, Zhao and coworkers have demonstrated that the solvent choice can affect how the monomer organizes in solution before any polymerization.[52] They used a 2D COF made from 1,3,5-tris(4-aminophenyl)benzene/ terephthalaldehyde (TAPB/TA) for their model system. The COF made with methanol as the solvent was amorphous, while a solvent system of dioxane and mesitylene resulted in a highly crystalline sample. They observed TAPB aggregates in the dioxane/mesitylene system prior to any precipitation forming, while the methanol system showed no evidence of preorganization. This indicates that the initial arrangement of monomers, possibly through pre-aggregation, influences the nucleation and growth of crystalline domains within the COF structure. This observation underscores the critical role of solvent choice in synthesizing crystalline polymers.

Alternatively, a catalyst can be introduced to lower the energy barrier exchange or affect the mechanism in which molecular components are exchanged. Many imine linked polymers use BrØnsted acids or Lewis acids to facilitate bond exchange by making the imine linkage more susceptible to nucleophilic attack. For other reactions, catalysts can be the key to facilitate bond exchange and unlock high crystallinity. Recently, Feng and co-workers reported the synthesis of vinylene-linked 2D COFs from Knoevenagel polycondensation reactions[53] and the exchange of molecular components from dynamic Michael-addition-elimination reactions (Figure 1.9). They used a model reaction to demonstrate the exchange using aqueous cesium carbonate as a catalyst, and double bond formation from the Knoevenagel reaction is not reversible. Calculations revealed

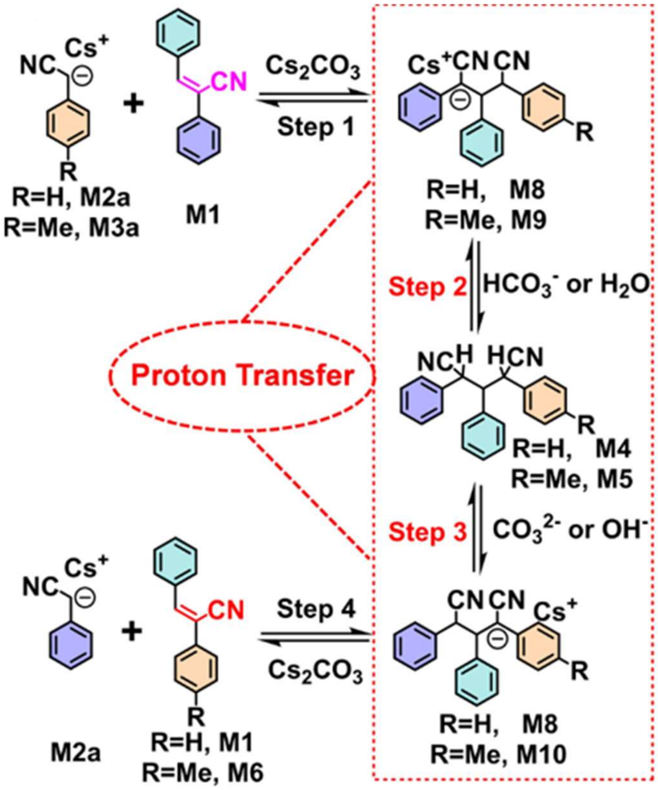

Figure 1.9. Dynamic Michael-addition-elimination reaction for COF synthesis. Copyright Wiley-VCH 2022. Ref. 53.

that water lowers the activation energy for the rate-limiting step and facilitates the exchange reaction more than using non-aqueous cesium carbonate as a base. This was also reflected in the crystallinity of the COF materials synthesized using analogous conditions.

Probably the most influential discovery of synthesizing crystalline polymers has been the use of modulators. A modulator is a small molecule that can compete with the monomers to slow the equilibrium. It is proposed that this will limit the number of nucleation sites so they can grow to larger sizes. In 2018, Wang, Sun, and Yaghi demonstrated the synthesis of imine based 3D COFs that could be resolved with SCXRD (Figure 1.10a).[54] In this work they used aniline as the modulator to react with the aldehyde monomer and acetic acid to catalyst the exchange. The growth of these crystals

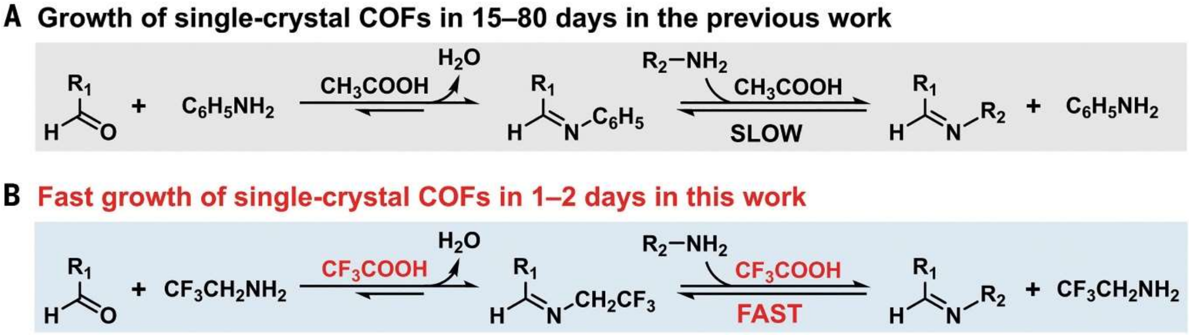

Figure 1.10. Methods to grow single crystal imine linked COFs from 2018 (a) and 2024 (b). Copyright AAAS 2024. Ref. 15

was relatively slow and small. Recently, Wang demonstrated that changing the catalyst and modulator can result in larger single crystals in only a few days (Figure 1.10b). [15] They swapped acetic acid with 2,2,2-trifluoroacetic acid (TFA) to increase the imine exchange. They found that aniline wasn't sufficient for suppressing the initial nucleation. By screening different bases, they found 2,2,2-trifluoroethylamine resulting in much larger crystals. The TFA/2,2,2-trifluoroethylamine was tested across 16 different structures and all resulting large single crystals that could be formed in a couple of days. Many of the imine COFs have adopted aniline as the modulator to result in single crystals that can be resolved by electron or x-ray diffraction so TFA/2,2,2-trifluoroethylamine will undoubtedly be broadly adopted as well. There are only a few examples of other dynamic linkages that have adopted the modulator strategy.[55-57] Thus this is an area that could be explored further to advance the adoption of novel dynamic linkages.

When designing the synthetic conditions of crystalline polymers, various factors must be carefully considered, such as solvent choice, catalyst selection, monomer design, reaction time, and temperature. By exploring the intricacies of the chemistry principles underlying these processes, we can gain valuable insights into the thermodynamics of the system. This understanding facilitates the production of high-quality samples with potential for revealing novel functionalities.

1.4 Introduction to the principles of reticulation

Tessellation, when combined with reticulation, serves as a fundamental principle for creating ordered crystalline polymers. Tessellation involves shapes fit together seamlessly without gaps or overlaps.[58] This process is crucial for constructing ordered polymer structures. DCvC aids in error correction during the polymerization so periodic structures form. A successful design approach involves selecting monomers with innate functionalities, which are further enhanced when precisely arranged within the polymer through covalent bonds. This section will explore the general principles of designing crystalline polymers using DCvC and how topology affects their properties. Since the emergence of COFs in 2005[59], numerous monomers have been developed for various applications like metal-ion batteries, gas storage/separation, and photocatalysts. The selection of monomers, DCvC linkage, and overall topology provides significant tuneability in tailoring materials for specific applications. There are still many unknown factors that go into forming strain-free structures. Some of these include introducing supramolecular interactions and flexible monomers that may affect the observed topology or interpenetration. This section will describe the fundamentals of designing crystalline polymer with DCvC.

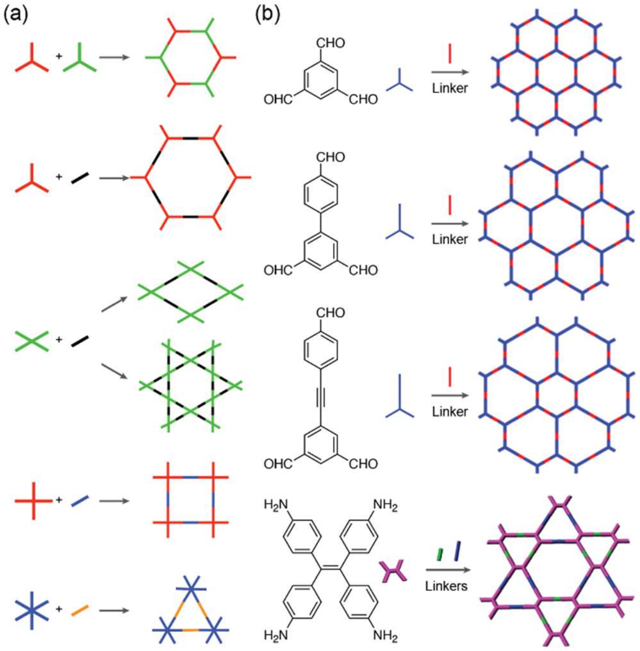

Figure 1.11. Common 2D topologies. (a) Overview of the different monomer geometry combination and resulting topologies. (b) Plausible heterosporous structures from lowering the symmetry of a monomer. Panel b is reproduced with permission from ref 60 and 61. Copyright 2015 American Chemical Society.

Many of the COFs produced are 2D COFs with uniporous designs to form organized 1D channels. Common pore structures are shown in Figure 1.11a with the corresponding vertex geometry. The vertex can either be the monomer, the DCvC linkage, or a combination of both. When the monomer's symmetry is reduced then the complexity of the pore structure can be increased. 5-(4-formylphenyl)isophthalaldehyde and 5-((4-

formylphenyl)ethylene)isophthalaldehyde were designed to elongate one of the arms of the monomer to have C_{2v} symmetry. These were then polymerized with a linear hydrazine linker to form 2D COFs (Figure 1.11b).[60] The simulated PXRD patterns were similar so analyzing the pore size distribution was the key to matching the experimental data to theoretical isomers. Another method to reduce the symmetry of the monomer is to change the angle between reactive sites. 4,4′,4″,4‴-(ethene-1,1,2,2-tetrayl)-tetraanilinethene (ETTA), is a monomer with two distinct angles (60° and 120°) with D_{2h} symmetry (Figure 1.11b).[62] This monomer can adopt either a uniporous pore structure or a heterogenous porous structure. When this monomer was subjected to imine condensation, it was found to prefer the heterosporous topology. Similarly, a monomer designed to undergo a boronate condensation was found to adopt the same topology.[63]

Another method to increase the complexity of the pore structure is to use a mixed component approach. This involves using multiple vertex or linear monomers with different lengths in a one pot synthesis. It is noteworthy that, under thermodynamic conditions, the distribution of the linkers can gradually attain order, ultimately leading to the formation of crystalline structures. Zhao et al. synthesized SIOC-COF-1 by blending a tetraamine vertex with a 1:1 molar ratio of two dialdehydes of various sizes.[61] This creates a crystalline framework with a triple pore structure. The same group has also demonstrated the synthesis of SIOC-COF-6,[61] consisting of irregular hexagons and rhombuses pores, and the transformation of heterosporous COFs monomer exchange.[64]

Alternatively, precise ordering of heterogeneous pores can be accomplished with a macrocycle-to-framework or cage-to-framework approach. Triangular shaped macrocycles have been incorporated primarily into 2D boronate COF, where the length of the linear linker can regulate the pores.[65, 66] The McGrier group has also demonstrated the utility of these building blocks by doping in nickel to utilize the dual pore material as a heterogeneous catalyst.[67, 68] The structure is not limited to these types of macrocycles. It was recently demonstrated that a square macrocycle can form a 2D network through imine condensation.[69] Additionally, Cooper et al. first reported the synthesis of 3D-CageCOF-1,[70] forming a 3D framework with *acs-c* topology and two-fold interpenetration. Furthermore, as more complex macrocycles or cages are incorporated into frameworks, more opportunities for imparting additional functionality, such as host-guest interactions, are opened.

The formation of 3D architectures can also be accomplished by using monomers that have valances of 3 or more. Figure 1.12 shows some examples of 3D topologies that have been reported.[71] Elements like interpenetration and the use of flexible monomers can lead to an unexpected topology. Often, the two phases can be separated, as DCvC allows for thermodynamic minimums to form, and many recent works have explored the equilibrium between phases.

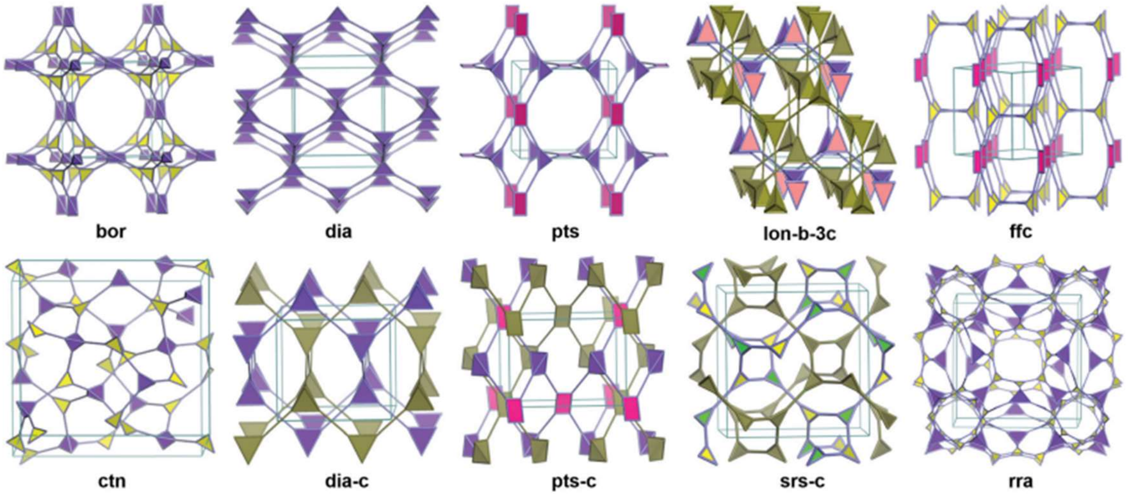

Figure 1.12. Common 3d topologies of COFs. This figure is reproduced with permission from ref 71. Copyright 2020 Royal Society of Chemistry.

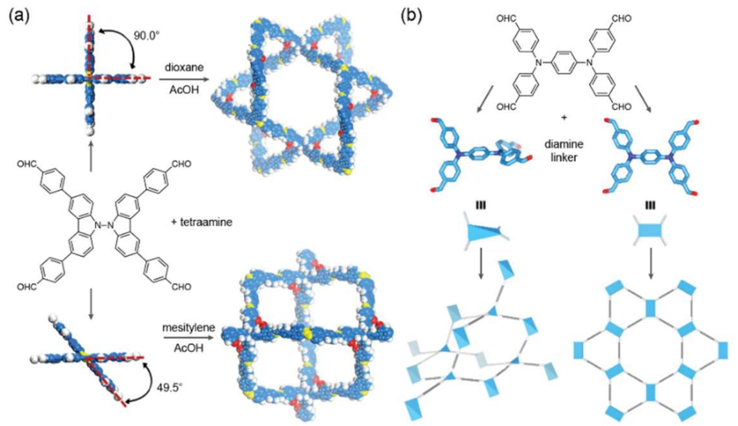

Figure 1.13. DCvC enables the same combination of monomers to result in different topologies. The dihedral angle of the monomer will dictate what vertices are formed to produce topology (a) or dimension isomerization (b). Panel a is reproduced with permission from 72. Copyright 2023 American Chemical Society. Panel b is reproduced with permission from 73. Copyright 2023 American Chemical Society.

Unlocking different topologies from the same combination of building blocks not only gives important insights into the formation of 3D structures using DCvC bonds, but also enables the structure-function property relationship to be studied from the same set of building blocks. Feng and coworkers revealed that COFs with the dia and *qzt* topology could be achieved using a 9,9′-bicarbazole (BC) derivative as a tetrahedral monomer (Figure 1.13a). Theoretical calculations indicated that BC has a low activation energy for the different confirmation of its dihedral angle compared to other tetrahedral building blocks. They selectively made the *dia* topology, JUC-620,[72] by utilizing mesitylene and acetic acid, whereas the *qzt* topology, JUC-621, was unlocked with dioxane and acetic acid. They probed the effect of topology on porous properties by studying the material's uptake of crystal violate and iodine capture. JUC-621 showed more dye and iodine uptake due to the higher porosity. Under a similar design approach, Weng et al. used 4,4′,4,″4‴-(1,4-phenylenebis(azanetriyl)) tetra benzaldehyde (PATB) as a monomer which can have both a planar and tetrahedral geometry showcase dimensional isomerization (Figure 1.13b).[73] 2D-PATB-COF was found to be a heterosporous COF with AA stacking, while 3D- PATB-COF exhibited a dia topology with interpenetration that was 6 x 2-fold interpenetrated. The solid-state absorption was similar for both materials, but only 3D-PATB-COF showed a good photoluminescence quantum yield (PLQY) of 3.6%. This is due to non-radiative decay pathways from the π-π stacking between the PATB monomers in the 2D structure.

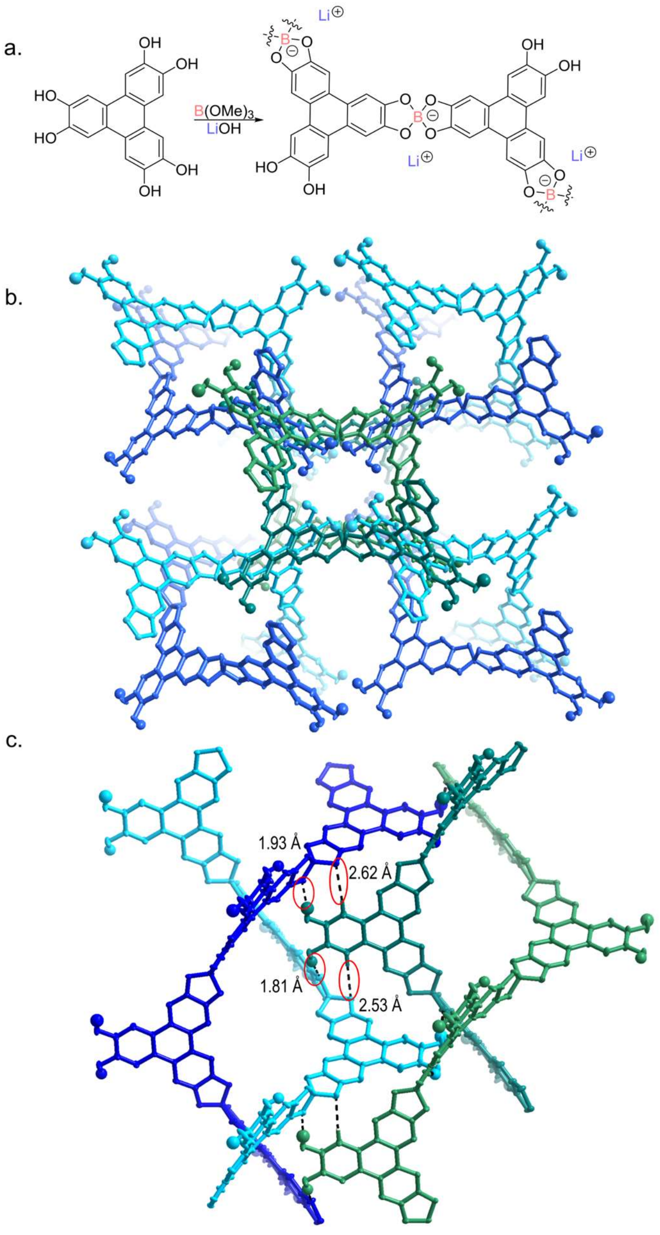

Figure 1.14. (a) Synthesis of HCP-Li. (b) Top view of HCP-Li packing. (c) Side view of the interactions between the polymer chains.

Finally, supramolecular chemistry can be used in conjugation with DCvC to create novel structures. Thus far, metal coordination, hydrogen bonding, and π-π bonding have been used to form expected and unexpected topologies.[74-77] Generally, these systems are comprised of 1D polymer strands with covalent bonds that are organized in the 3D space with the weaker bonds. Previously we reported the synthesis a helical covalent polymer (HCP-Li) which utilized the dynamic spiroborate to link HHTP molecules together (Figure 1.14a). SCXRD revealed an unexpected topology that stems from only two of the three diols of the monomer reacting to form 1D chains. The polymer chains form mechanically entwined double helices (Figure 1.14b) that are assembled through hydrogen bonding interactions. The unreacted diol will form a strong (O–B–O…H–O) and a weak (Ar–

H…O–B–O) hydrogen bonding interaction with the adjacent helices (Figure 1.14c). Another interesting aspect of this work is the helices have the same handedness in a single crystalline domain where the bulk sample is racemic. Further understanding of these complex systems will facilitate the development of sophisticated chiral polymeric structures with novel functionality.

1.4 Conclusions and outlook

In conclusion, there has been much success in developing methods to control the equilibrium of polymerizations with DCvC, with primary focus on imine and boronate ester linkages. By understanding the fundamental chemical properties of the linkages and monomer designs we can structurally modify the stabilizing of the linkage to affect the dynamic capacity.

The reaction conditions can be screened by controlling the thermodynamic and kinetic controls that ensures both structural order and a high polymerization. A modulator introduces a novel parameter for adjusting the polymerization rate and facilitating a self-correction pathway, leading to the formation of highly ordered frameworks. Though, the incorporation of modulators in other DCvC reactions remains relatively underexplored. This area will likely continue to be explored.

The scientific community will likely continue to explore methods of increasing structural diversity to induce more functionality. As other bonds are further developed we will likely see more orthogonal DCvC or polymers from multiple DCvC linkages. By combining multiple DCvC linkages we can use simple building blocks to design complex topologies. In a similar vein, the synergistic relationship of DCvC and supramolecular chemistry will continue to be explored.

1.5 References

(1) Shoulders, M. D.; Raines, R. T. Collagen Structure and Stability. *Annu. Rev. Biochem.* **2009**, *78* (1), 929-958. DOI: 10.1146/annurev.biochem.77.032207.120833.

(2) Coudrillier, B.; Pijanka, J.; Jefferys, J.; Sorensen, T.; Quigley, H. A.; Boote, C.; Nguyen, T. D. Collagen structure and mechanical properties of the human sclera: analysis for the effects of age. *J. Biomech. Eng.* **2015**, *137* (4), 041006.

(3) Lehn, J.-M. From supramolecular chemistry towards constitutional dynamic chemistry and adaptive chemistry. *Chem. Soc. Rev.* **2007**, *36* (2), 151-160, DOI: 10.1039/B616752G.

(4) Moulin, E.; Cormos, G.; Giuseppone, N. Dynamic combinatorial chemistry as a tool for the design of functional materials and devices. *Chem. Soc. Rev.* **2012**, *41* (3), 1031-1049, DOI: 10.1039/C1CS15185A.

(5) Rowan, S. J.; Cantrill, S. J.; Cousins, G. R. L.; Sanders, J. K. M.; Stoddart, J. F. Dynamic Covalent Chemistry. *Angew. Chem. Int. Ed.* **2002**, *41* (6), 898-952 DOI: 10.1002/1521-3773(20020315)41:6.

(6) Jin, Y.; Yu, C.; Denman, R. J.; Zhang, W. Recent advances in dynamic covalent chemistry. *Chem. Soc. Rev.* **2013**, *42* (16), 6634-6654, DOI: 10.1039/C3CS60044K.

(7) Wayment, L. J.; Lei, Z.; Jin, Y.; Zhang, W. Recent Progress in Constructing Structurally Ordered Polymeric Architectures via Dynamic Covalent Chemistry. *CCS Chem.* **2023**, *5* (10), 2194-2206. DOI: doi:10.31635/ccschem.023.202303004.

(8) Natraj, A.; Ji, W.; Xin, J.; Castano, I.; Burke, D. W.; Evans, A. M.; Strauss, M. J.; Ateia, M.; Hamachi, L. S.; Gianneschi, N. C.; ALOthman, Z. A.; Sun, J.; Yusuf, K.; Dichtel, W. R. Single-Crystalline Imine-Linked Two-Dimensional Covalent Organic Frameworks Separate Benzene and Cyclohexane Efficiently. *J. Am. Chem. Soc.* **2022**, *144* (43), 19813-19824. DOI: 10.1021/jacs.2c07166.

(9) Day, R. W.; Bediako, D. K.; Rezaee, M.; Parent, L. R.; Skorupskii, G.; Arguilla, M. Q.; Hendon, C. H.; Stassen, I.; Gianneschi, N. C.; Kim, P.; Dincă, M. Single Crystals of Electrically Conductive Two-Dimensional Metal–Organic Frameworks: Structural and Electrical Transport Properties. *ACS Cent. Sci.* **2019**, *5* (12), 1959-1964. DOI: 10.1021/acscentsci.9b01006.

(10) Zhang, J.; Zhou, G.; Un, H.-I.; Zheng, F.; Jastrzembski, K.; Wang, M.; Guo, Q.; Mücke, D.; Qi, H.; Lu, Y.; Wang, Z.; Liang, Y.; Löffler, Kaiser, U.; Franeheim, T.; Mateo-Alonso, A.; Huang, Z.; Sirringhaus, H.; Feng, X.; Dong, R. Wavy Two-Dimensional Conjugated Metal–Organic Framework with Metallic Charge Transport. *J. Am. Chem. Soc.* **2023**, *145* (43), 23630-23638. DOI: 10.1021/jacs.3c07682.

(11) a. Jin, Y.; Wang, Q.; Taynton, P.; Zhang, W. Dynamic Covalent Chemistry Approaches Toward Macrocycles, Molecular Cages, and Polymers. *Acc. Chem. Res.* **2014**, *47* (5), 1575-1586. DOI: 10.1021/ar500037v. b. Zhang, W.; Moore, J. S. "Shape-Persistent Macrocycles: Structures and Synthetic Approaches from Arylene and Ethynylene Building Blocks" (review) *Angew. Chem. Int. Ed.* **2006**, 45, 4416-4439.

(12) Huang, S.; Lei, Z.; Jin, Y.; Zhang, W. By-design molecular architectures via alkyne metathesis. *Chem. Sci.* **2021**, *12* (28), 9591-9606, DOI: 10.1039/D1SC01881G.

(13) Lee, S.; Yang, A.; Moneypenny, T. P., II; Moore, J. S. Kinetically Trapped Tetrahedral Cages via Alkyne Metathesis. *J. Am. Chem. Soc.* **2016**, *138* (7), 2182-2185. DOI: 10.1021/jacs.6b00468.

(14) Evans, A. M.; Strauss, M. J.; Corcos, A. R.; Hirani, Z.; Ji, W.; Hamachi, L. S.; Aguilar-Enriquez, X.; Chavez, A. D.; Smith, B. J.; Dichtel, W. R. Two-Dimensional Polymers and Polymerizations. *Chem. Rev.* **2022**, *122* (1), 442-564. DOI: 10.1021/acs.chemrev.0c01184.

(15) Han, J.; Feng, J.; Kang, J.; Chen, J.-M.; Du, X.-Y.; Ding, S.-Y.; Liang, L.; Wang, W. Fast growth of single-crystal covalent organic frameworks for laboratory x-ray diffraction. *Science* **2024**, *383* (6686), 1014-1019. DOI: 10.1126/science.adk8680 .

(16) Wang, X.; Wada, Y.; Shimada, T.; Kosaka, A.; Adachi, K.; Hashizume, D.; Yazawa, K.; Uekusa, H.; Shoji, Y.; Fukushima, T.; et al. Triple Isomerism in 3D Covalent Organic Frameworks. *J. Am. Chem. Soc.* **2024**. DOI: 10.1021/jacs.3c13863.

(17) Côté Adrien, P.; Benin Annabelle, I.; Ockwig Nathan, W.; O'Keeffe, M.; Matzger Adam, J.; Yaghi Omar, M. Porous, Crystalline, Covalent Organic Frameworks. *Science* **2005**, *310* (5751), 1166-1170. DOI: 10.1126/science.1120411.

(18) El-Kaderi, H. M.; Hunt, J. R.; Mendoza-Cortés, J. L.; Côté, A. P.; Taylor, R. E.; O'Keeffe, M.; Yaghi, O. M. Designed Synthesis of 3D Covalent Organic Frameworks. *Science* **2007**, *316* (5822), 268-272. DOI: doi:10.1126/science.1139915.

(19) Martínez-Abadía, M.; Stoppiello, C. T.; Strutynski, K.; Lerma-Berlanga, B.; Martí-Gastaldo, C.; Saeki, A.; Melle-Franco, M.; Khlobystov, A. N.; Mateo-Alonso, A. A Wavy Two-Dimensional Covalent Organic Framework from Core-Twisted Polycyclic Aromatic Hydrocarbons. *J. Am. Chem. Soc.* **2019**, *141* (36), 14403-14410. DOI: 10.1021/jacs.9b07383.

(20) Evans, A. M.; Parent, L. R.; Flanders, N. C.; Bisbey, R. P.; Vitaku, E.; Kirschner, M. S.; Schaller, R. D.; Chen, L. X.; Gianneschi, N. C.; Dichtel, W. R. Seeded growth of single-crystal two-dimensional covalent organic frameworks. *Science* **2018**, *361* (6397), 52-57. DOI: 10.1126/science.aar7883.

(21) Du, Y.; Yang, H.; Whiteley, J. M.; Wan, S.; Jin, Y.; Lee, S.-H.; Zhang, W. Ionic Covalent Organic Frameworks with Spiroborate Linkage. *Angew. Chem. Int. Ed.* **2016**, *55* (5), 1737-1741, DOI: 10.1002/anie.201509014.

(22) Hu, Y.; Teat, S. J.; Gong, W.; Zhou, Z.; Jin, Y.; Chen, H.; Wu, J.; Cui, Y.; Jiang, T.; Cheng, X.; Zhang, W. Single crystals of mechanically entwined helical covalent polymers. *Nat. Chem.* **2021**, *13* (7), 660-665. DOI: 10.1038/s41557-021-00686-2.

(23) Wang, X.; Bahri, M.; Fu, Z.; Little, M. A.; Liu, L.; Niu, H.; Browning, N. D.; Chong, S. Y.; Chen, L.; Ward, J. W.; Cooper, A. I. A Cubic 3D Covalent Organic Framework with nbo Topology. *J. Am. Chem. Soc.* **2021**, *143* (37), 15011-15016, DOI: 10.1021/jacs.1c08351.

(24) Xu, Q.; Wang, X.; Huang, S.; Hu, Y.; Teat, S. J.; Settineri, N. S.; Chen, H.; Wayment, L. J.; Jin, Y.; Sharma, S.; Zhang, W. Dynamic Covalent Self-sorting in Molecular and Polymeric Architectures Enabled by Spiroborate Bond Exchange. *Angew. Chem. Int. Ed.* **2023**, *62* (27), e202304279. DOI: 10.1002/anie.202304279.

(25) Wayment, L. J.; Wang, X.; Huang, S.; McCoy, M. S.; Chen, H.; Hu, Y.; Jin, Y.; Sharma, S.; Zhang, W. 3D Covalent Organic Framework as a Metastable Intermediate in the Formation of a Double-Stranded Helical Covalent Polymer. *J. Am. Chem. Soc.* **2023**, *145* (28), 15547-15552. DOI: 10.1021/jacs.3c04734.

(26) Wayment, L. J.; Teat, S. J.; Huang, S.; Chen, H.; Zhang, W. Dynamic Entwined Topology in Helical Covalent Polymers Dictated by Competing Supramolecular Interactions. *Angew. Chem. Int. Ed.*, e202403599. DOI: 10.1002/anie.202403599.

(27) Hunt, J. R.; Doonan, C. J.; LeVangie, J. D.; Côté, A. P.; Yaghi, O. M. Reticular Synthesis of Covalent Organic Borosilicate Frameworks. *J. Am. Chem. Soc.* **2008**, *130* (36), 11872-11873. DOI: 10.1021/ja805064f.

(28) Gropp, C.; Ma, T.; Hanikel, N.; Yaghi Omar, M. Design of higher valency in covalent organic frameworks. *Science* **2020**, *370* (6515), eabd6406. DOI: 10.1126/science.abd6406.

(29) Liu, B.-T.; Gong, S.-H.; Jiang, X.-T.; Zhang, Y.; Wang, R.; Chen, Z.; Zhang, S.; Kirlikovali, K. O.; Liu, T.-F.; Farha, O. K.; Cao, R. A solution processible single-crystal porous organic polymer. *Nat. Synth.* **2023**, *2* (9), 873-879. DOI: 10.1038/s44160-023-00316-4.

(30) Uribe-Romo, F. J.; Hunt, J. R.; Furukawa, H.; Klöck, C.; O'Keeffe, M.; Yaghi, O. M. A Crystalline Imine-Linked 3-D Porous Covalent Organic Framework. *J. Am. Chem. Soc.* **2009**, *131* (13), 4570-4571. DOI: 10.1021/ja8096256.

(31) Beaudoin, D.; Maris, T.; Wuest, J. D. Constructing monocrystalline covalent organic networks by polymerization. *Nat. Chem.* **2013**, *5* (10), 830-834. DOI: 10.1038/nchem.1730.

(32) Alahakoon, S. B.; Tan, K.; Pandey, H.; Diwakara, S. D.; McCandless, G. T.; Grinffiel, D. I.; Durand-Silva, A.; Thonhauser, T.; Smaldone, R. A. 2D-Covalent Organic Frameworks with Interlayer Hydrogen Bonding Oriented through Designed Nonplanarity. *J. Am. Chem. Soc.* **2020**, *142* (30), 12987-12994. DOI: 10.1021/jacs.0c03409.

(33) Kandambeth, S.; Shinde, D. B.; Panda, M. K.; Lukose, B.; Heine, T.; Banerjee, R. Enhancement of Chemical Stability and Crystallinity in Porphyrin-Containing Covalent Organic Frameworks by Intramolecular Hydrogen Bonds. *Angew. Chem. Int. Ed.* **2013**, *52* (49), 13052-13056. DOI: 10.1002/anie.201306775.

(34) Xu, H.; Gao, J.; Jiang, D. Stable, crystalline, porous, covalent organic frameworks as a platform for chiral organocatalysts. *Nat. Chem.* **2015**, *7* (11), 905-912. DOI: 10.1038/nchem.2352.

(35) Uribe-Romo, F. J.; Doonan, C. J.; Furukawa, H.; Oisaki, K.; Yaghi, O. M. Crystalline Covalent Organic Frameworks with Hydrazone Linkages. *J. Am. Chem. Soc.* **2011**, *133* (30), 11478-11481. DOI: 10.1021/ja204728y.

(36) Dalapati, S.; Jin, S.; Gao, J.; Xu, Y.; Nagai, A.; Jiang, D. An Azine-Linked Covalent Organic Framework. *J. Am. Chem. Soc.* **2013**, *135* (46), 17310-17313. DOI: 10.1021/ja4103293.

(37) Guo, J.; Xu, Y.; Jin, S.; Chen, L.; Kaji, T.; Honsho, Y.; Addicoat, M. A.; Kim, J.; Saeki, A.; Ihee, H.; Seki, S.; Irle, S.; Hiramoto, M.; Gao, J.; Jiang, D. Conjugated organic framework with three-dimensionally ordered stable structure and delocalized π clouds. *Nat. Commun.* **2013**, *4* (1), 2736. DOI: 10.1038/ncomms3736.

(38) Mahmood, J.; Lee, E. K.; Jung, M.; Shin, D.; Jeon, I.-Y.; Jung, S.-M.; Choi, H.-J.; Seo, J.-M.; Bae, S.-Y.; Sohn, S.-D.; et al. Nitrogenated holey two-dimensional structures. *Nat. Commun.* **2015**, *6* (1), 6486. DOI: 10.1038/ncomms7486.

(39) Meng, Z.; Aykanat, A.; Mirica, K. A. Proton Conduction in 2D Aza-Fused Covalent Organic Frameworks. *Chem. Mater.* **2019**, *31* (3), 819-825. DOI: 10.1021/acs.chemmater.8b03897.

(40) Wang, M.; Ballabio, M.; Wang, M.; Lin, H.-H.; Biswal, B. P.; Han, X.; Paasch, S.; Brunner, E.; Liu, P.; Chen, M.; et al. Unveiling Electronic Properties in Metal–Phthalocyanine-Based Pyrazine-Linked Conjugated Two-Dimensional Covalent Organic Frameworks. *J. Am. Chem. Soc.* **2019**, *141* (42), 16810-16816. DOI: 10.1021/jacs.9b07644.

(41) Meng, Z.; Stolz, R. M.; Mirica, K. A. Two-Dimensional Chemiresistive Covalent Organic Framework with High Intrinsic Conductivity. *J. Am. Chem. Soc.* **2019**, *141* (30), 11929-11937. DOI: 10.1021/jacs.9b03441.

(42) Li, X.; Wang, H.; Chen, H.; Zheng, Q.; Zhang, Q.; Mao, H.; Liu, Y.; Cai, S.; Sun, B.; Dun, C.; Gordan, M. P.; Zheng, H.; Reimer, J. A.; Urban, J. J.; Ciston, J.; Tan, T.; Chan, E. M.; Zhang, J.; Liu, Y. Dynamic Covalent Synthesis of Crystalline Porous Graphitic Frameworks. *Chem* **2020**, *6* (4), 933-944. DOI: 10.1016/j.chempr.2020.01.011.

(43) Kandambeth, S.; Mallick, A.; Lukose, B.; Mane, M. V.; Heine, T.; Banerjee, R. Construction of Crystalline 2D Covalent Organic Frameworks with Remarkable Chemical (Acid/Base)

Stability via a Combined Reversible and Irreversible Route. *J. Am. Chem. Soc.* **2012**, *134* (48), 19524-19527. DOI: 10.1021/ja308278w.

(44) Banerjee, S.; Tripathy, R.; Cozzens, D.; Nagy, T.; Keki, S.; Zsuga, M.; Faust, R. Photoinduced Smart, Self-Healing Polymer Sealant for Photovoltaics. *ACS Appl. Mater. Interfaces* **2015**, *7* (3), 2064-2072. DOI: 10.1021/am508096c.

(45) Haase, F.; Troschke, E.; Savasci, G.; Banerjee, T.; Duppel, V.; Dörfler, S.; Grundei, M. M. J.; Burow, A. M.; Ochsenfeld, C.; Kaskel, S.; et al. Topochemical conversion of an imine- into a thiazole-linked covalent organic framework enabling real structure analysis. *Nat. Commun.* **2018**, *9* (1), 2600. DOI: 10.1038/s41467-018-04979-y.

(46) Waller, P. J.; AlFaraj, Y. S.; Diercks, C. S.; Jarenwattananon, N. N.; Yaghi, O. M. Conversion of Imine to Oxazole and Thiazole Linkages in Covalent Organic Frameworks. *J. Am. Chem. Soc.* **2018**, *140* (29), 9099-9103. DOI: 10.1021/jacs.8b05830.

(47) Wang, K.; Jia, Z.; Bai, Y.; Wang, X.; Hodgkiss, S. E.; Chen, L.; Chong, S. Y.; Wang, X.; Yang, H.; Xu, Y.; Feng, F., Ward, J. W.; Cooper, A. I. Synthesis of Stable Thiazole-Linked Covalent Organic Frameworks via a Multicomponent Reaction. *J. Am. Chem. Soc.* **2020**, *142* (25), 11131-11138. DOI: 10.1021/jacs.0c03418.

(48) Grunenberg, L.; Savasci, G.; Terban, M. W.; Duppel, V.; Moudrakovski, I.; Etter, M.; Dinnebier, R. E.; Ochsenfeld, C.; Lotsch, B. V. Amine-Linked Covalent Organic Frameworks as a Platform for Postsynthetic Structure Interconversion and Pore-Wall Modification. *J. Am. Chem. Soc.* **2021**, *143* (9), 3430-3438. DOI: 10.1021/jacs.0c12249.

(49) Wei, P.-F.; Qi, M.-Z.; Wang, Z.-P.; Ding, S.-Y.; Yu, W.; Liu, Q.; Wang, L.-K.; Wang, H.-Z.; An, W.-K.; Wang, W. Benzoxazole-Linked Ultrastable Covalent Organic Frameworks for Photocatalysis. *J. Am. Chem. Soc.* **2018**, *140* (13), 4623-4631. DOI: 10.1021/jacs.8b00571.

(50) Hu, Z.; Hu, F.; Deng, L.; Yang, Y.; Xie, Q.; Gao, Z.; Pan, C.; Jin, Y.; Tang, J.; Yu, G.; Zhang, W. Reprocessible Triketoenamine-Based Vitrimers with Closed-Loop Recyclability. *Angew. Chem. Int. Ed.* **2023**, *62* (34), e202306039. DOI: 10.1002/anie.202306039.

(51) Sick, T.; Rotter, J. M.; Reuter, S.; Kandambeth, S.; Bach, N. N.; Döblinger, M.; Merz, J.; Clark, T.; Marder, T. B.; Bein, T.; Medina, D. D. Switching on and off Interlayer Correlations and Porosity in 2D Covalent Organic Frameworks. *J. Am. Chem. Soc.* **2019**, *141* (32), 12570-12581. DOI: 10.1021/jacs.9b02800.

(52) Kang, C.; Yang, K.; Zhang, Z.; Usadi, A. K.; Calabro, D. C.; Baugh, L. S.; Wang, Y.; Jiang, J.; Zou, X.; Huang, Z.; Zhao, D. Growing single crystals of two-dimensional covalent organic frameworks enabled by intermediate tracing study. *Nat. Commun.* **2022**, *13* (1), 1370. DOI: 10.1038/s41467-022-29086-x.

(53) Xu, S.; Liao, Z.; Dianat, A.; Park, S.-W.; Addicoat, M. A.; Fu, Y.; Pastoetter, D. L.; Fabozzi, F. G.; Liu, Y.; Cuniberti, G.; Richter, M.; Hecht, S.; Feng, X. Combination of Knoevenagel Polycondensation and Water-Assisted Dynamic Michael-Addition-Elimination for the Synthesis of Vinylene-Linked 2D Covalent Organic Frameworks. *Angew. Chem. Int. Ed.* **2022**, *61* (21), e202202492. DOI: 10.1002/anie.202202492.

(54) Ma, T.; Kapustin, E. A.; Yin, S. X.; Liang, L.; Zhou, Z.; Niu, J.; Li, L.-H.; Wang, Y.; Su, J.; Li, J.; Wang, X.; Wang, W. D.; Wang, W.; Sun, J.; Yaghi, O. M. Single-crystal x-ray diffraction structures of covalent organic frameworks. *Science* **2018**, *361* (6397), 48-52. DOI: 10.1126/science.aat7679.

(55) Hu, Y.; Wu, C.; Pan, Q.; Jin, Y.; Lyu, R.; Martinez, V.; Huang, S.; Wu, J.; Wayment, L. J.; Clark, N. A.; Raschke, M. B.; Zhao, Y.; Zhang, W. Synthesis of γ-graphyne using dynamic covalent chemistry. *Nat. Synth.* **2022**, *1* (6), 449-454. DOI: 10.1038/s44160-022-00068-7.

(56) Calik, M.; Sick, T.; Dogru, M.; Döblinger, M.; Datz, S.; Budde, H.; Hartschuh, A.; Auras, F.; Bein, T. From Highly Crystalline to Outer Surface-Functionalized Covalent Organic Frameworks—A Modulation Approach. *J. Am. Chem. Soc.* **2016**, *138* (4), 1234-1239. DOI: 10.1021/jacs.5b10708.

(57) Castano, I.; Evans, A. M.; Li, H.; Vitaku, E.; Strauss, M. J.; Brédas, J.-L.; Gianneschi, N. C.; Dichtel, W. R. Chemical Control over Nucleation and Anisotropic Growth of Two-Dimensional Covalent Organic Frameworks. *ACS Cent. Sci.* **2019**, *5* (11), 1892-1899. DOI: 10.1021/acscentsci.9b00944.

(58) Jin, Y.; Hu, Y.; Zhang, W. Tessellated multiporous two-dimensional covalent organic frameworks. *Nat. Rev. Chem.* **2017**, *1* (7), 0056. DOI: 10.1038/s41570-017-0056.

(59) Côté, A. P.; Benin, A. I.; Ockwig, N. W.; O'Keeffe, M.; Matzger, A. J.; Yaghi, O. M. Porous, Crystalline, Covalent Organic Frameworks. *Science* **2005**, *310* (5751), 1166-1170. DOI: 10.1126/science.1120411.

(60) Zhu, Y.; Wan, S.; Jin, Y.; Zhang, W. Desymmetrized Vertex Design for the Synthesis of Covalent Organic Frameworks with Periodically Heterogeneous Pore Structures. *J. Am. Chem. Soc.* **2015**, *137* (43), 13772-13775. DOI: 10.1021/jacs.5b09487.

(61) Pang, Z.-F.; Xu, S.-Q.; Zhou, T.-Y.; Liang, R.-R.; Zhan, T.-G.; Zhao, X. Construction of Covalent Organic Frameworks Bearing Three Different Kinds of Pores through the Heterostructural Mixed Linker Strategy. *J. Am. Chem. Soc.* **2016**, *138* (14), 4710-4713. DOI: 10.1021/jacs.6b01244.

(62) Zhou, T.-Y.; Xu, S.-Q.; Wen, Q.; Pang, Z.-F.; Zhao, X. One-Step Construction of Two Different Kinds of Pores in a 2D Covalent Organic Framework. *J. Am. Chem. Soc.* **2014**, *136* (45), 15885-15888. DOI: 10.1021/ja5092936.

(63) Dalapati, S.; Jin, E.; Addicoat, M.; Heine, T.; Jiang, D. Highly Emissive Covalent Organic Frameworks. *J. Am. Chem. Soc.* **2016**, *138* (18), 5797-5800. DOI: 10.1021/jacs.6b02700.

(64) Qian, C.; Qi, Q.-Y.; Jiang, G.-F.; Cui, F.-Z.; Tian, Y.; Zhao, X. Toward Covalent Organic Frameworks Bearing Three Different Kinds of Pores: The Strategy for Construction and COF-to-COF Transformation via Heterogeneous Linker Exchange. *J. Am. Chem. Soc.* **2017**, *139* (19), 6736-6743. DOI: 10.1021/jacs.7b02303.

(65) Feng, X.; Dong, Y.; Jiang, D. Star-shaped two-dimensional covalent organic frameworks. *CrystEngComm* **2013**, *15* (8), 1508-1511, DOI: 10.1039/C2CE26371H.

(66) Yang, H.; Du, Y.; Wan, S.; Trahan, G. D.; Jin, Y.; Zhang, W. Mesoporous 2D covalent organic frameworks based on shape-persistent arylene-ethynylene macrocycles. *Chem. Sci.* **2015**, *6* (7), 4049-4053, DOI: 10.1039/C5SC00894H.

(67) Haug, W. K.; Wolfson, E. R.; Morman, B. T.; Thomas, C. M.; McGrier, P. L. A Nickel-Doped Dehydrobenzoannulene-Based Two-Dimensional Covalent Organic Framework for the Reductive Cleavage of Inert Aryl C–S Bonds. *J. Am. Chem. Soc.* **2020**, *142* (12), 5521-5525. DOI: 10.1021/jacs.0c01026.

(68) Baldwin, L. A.; Crowe, J. W.; Pyles, D. A.; McGrier, P. L. Metalation of a Mesoporous Three-Dimensional Covalent Organic Framework. *J. Am. Chem. Soc.* **2016**, *138* (46), 15134-15137. DOI: 10.1021/jacs.6b10316.

(69) Huang, S.; Choi, J. Y.; Xu, Q.; Jin, Y.; Park, J.; Zhang, W. Carbazolylene-Ethynylene Macrocycle based Conductive Covalent Organic Frameworks. *Angew. Chem. Int. Ed.* **2023**, *62* (22), e202303538. DOI: 10.1002/anie.202303538.

(70) Zhu, Q.; Wang, X.; Clowes, R.; Cui, P.; Chen, L.; Little, M. A.; Cooper, A. I. 3D Cage COFs: A Dynamic Three-Dimensional Covalent Organic Framework with High-Connectivity

Organic Cage Nodes. *J. Am. Chem. Soc.* **2020**, *142* (39), 16842-16848. DOI: 10.1021/jacs.0c07732.

(71) Guan, X.; Chen, F.; Fang, Q.; Qiu, S. Design and applications of three dimensional covalent organic frameworks. *Chem. Soc. Rev.* **2020**, *49* (5), 1357-1384. DOI: 10.1039/C9CS00911F.

(72) Liu, Y.; Li, J.; Lv, J.; Wang, Z.; Suo, J.; Ren, J.; Liu, J.; Liu, D.; Wang, Y.; Valtchev, V.; Qiu, S.; Zhang, D.; Fang, Q. Topological Isomerism in Three-Dimensional Covalent Organic Frameworks. *J. Am. Chem. Soc.* **2023**, *145* (17), 9679-9685. DOI: 10.1021/jacs.3c01070.

(73) Gui, B.; Xin, J.; Cheng, Y.; Zhang, Y.; Lin, G.; Chen, P.; Ma, J.-X.; Zhou, X.; Sun, J.; Wang, C. Crystallization of Dimensional Isomers in Covalent Organic Frameworks. *J. Am. Chem. Soc.* **2023**, *145* (20), 11276-11281. DOI: 10.1021/jacs.3c01729.

(74) Xu, H.-S.; Luo, Y.; Li, X.; See, P. Z.; Chen, Z.; Ma, T.; Liang, L.; Leng, K.; Abdelwahab, I.; Wang, L.; Li, R.; Shi, X.; Zhou, Y.; Lu, X. F.; Zhao, X.; Liu, C.; Sun, J.; Loh, K. P. Single crystal of a one-dimensional metallo-covalent organic framework. *Nat. Commun.* **2020**, *11* (1), 1434. DOI: 10.1038/s41467-020-15281-1.

(75) De Bolòs, E.; Martínez-Abadía, M.; Hernández-Culebras, F.; Haymaker, A.; Swain, K.; Strutyński, K.; Weare, B. L.; Castells-Gil, J.; Padial, N. M.; Martí-Gastaldo, C.; Khlobstov, A. N.; Saeki, A.; Melle-Franco, M.; Nannenga, B. L.; Mateo-Alonso, A. A Crystalline 1D Dynamic Covalent Polymer. *J. Am. Chem. Soc.* **2022**, *144* (34), 15443-15450. DOI: 10.1021/jacs.2c06446.

(76) Yang, Y.; Lin, E.; Wang, S.; Wang, T.; Wang, Z.; Zhang, Z. Single-Crystal One-Dimensional Porous Ladder Covalent Polymers. *J. Am. Chem. Soc.* **2024**, *146* (1), 782-790. DOI: 10.1021/jacs.3c10812.

(77) Liu, Y.; Ma, Y.; Zhao, Y.; Sun, X.; Gándara, F.; Furukawa, H.; Liu, Z.; Zhu, H.; Zhu, C.; Suenaga, K.; Oleynikov, P.; Alshammari, A. S.; Zhang, X.; Terasaki, O.; Yaghi, O. M. Weaving of organic threads into a crystalline covalent organic framework. *Science* **2016**, *351* (6271), 365-369. DOI: 10.1126/science.aad4011.

Chapter 2: 3D Covalent Organic Framework as a Metastable Intermediate in the Formation of a Double-stranded Helical Covalent Polymer

(This chapter was originally published as: Wayment, L.J.; Wang, X.; Huang, S.; McCoy, M. S.; Chen, H.; Hu, Y.; Jin, Y.; Sharma, S.; Zhang, W. "3D Covalent Organic Framework as a Metastable Intermediate in the Formation of a Double-stranded Helical Covalent Polymer" J. Am. Chem. Soc. 2023, 145, 28, 15547–15552)

2.1 Abstract

The design and development of intricate artificial architectures have been pursued for decades. Helical covalent polymer (HCP) was recently reported as an unexpected topology that consists of chiral 1D polymers assembled through weak hydrogen bonds from achiral building blocks. However, many questions remained about the formation, driving force, and the single-handedness observed in each crystal. In this work, we reveal a metastable, racemic, fully covalently cross-linked, 3D covalent organic framework (COF) as an intermediate in the early stage of polymerization, which slowly converts into single-handed HCP double helices through partial fragmentation and self-sorting with the aid of a series of hydrogen bonding. Our work provides an intriguing example where weak noncovalent bonds serve as the determining factor of the overall product structure and facilitate the formation of a sophisticated polymeric architecture.

2.2 Introduction

Helices are an intriguing class of structural motifs that have been studied for decades, from the initial discovery of the double helices of DNA[1] to the development of novel helical foldamers (oligomers)[2,3], small molecule assembly[4], and large polymers.[5,6] Recently, we reported a single-crystal structure of 1D helical covalent polymer (HCP), which forms an extended network of mechanically entwined double helices held together by hydrogen bonding interactions. HCP was formed from 2,3,6,7,10,11-hexahydroxyltriphenylene (HHTP) with three pairs of reactive diols utilizing the dynamic spiroborate linkage.[7] Interestingly, only two pairs of diols of each HHTP reacted to form helical strands, leaving one unreacted diol group. The HCP has several unique features such as a high degree of polymerization, aligned lithium-ions in the channels of the double helices that allow for excellent directional lithium-ion conduction, and each single crystal domain has a single chirality, where the bulk sample is racemic.[7,8] However, some fundamental questions remain to be answered: 1) What is the driving force for the helical structure formation through the conversion of only two pairs of diols to spiroborates and one unreacted? 2) Can we convert all three diols into spiroborates and obtain an open framework using a similar synthetic approach? 3) Is HCP a kinetically trapped state or the most thermodynamically favorable topology? 4) How does the chirality evolve?

Herein, we report a detailed study on the reaction progress of the HCP formation and reveal the intricate equilibrium between the HCP topology and a 3D covalent organic framework with srs topology (srs-COF) (Figure 2.1). We found either srs-COF or the 1D HCP polymer can be obtained as the major species by a meticulous selection of reaction conditions, yet the HCP topology is more thermodynamically favored. We also reveal the possible mechanism of the chirality evolution in the HCP, which involves pre-organization of racemic helical structures in srs-COF and further self-sorting to form the single handed HCP structure.[9,10,11,12] Our study sheds light on how weak supramolecular interactions compete with covalent bond formation and exert a control on eventual reaction pathway. We anticipate that many intriguing synthetic polymers with remarkable structural features resembling sophisticated biological macromolecules can be formed through deliberate incorporation of weak supramolecular interactions into dynamic covalent polymerization process.

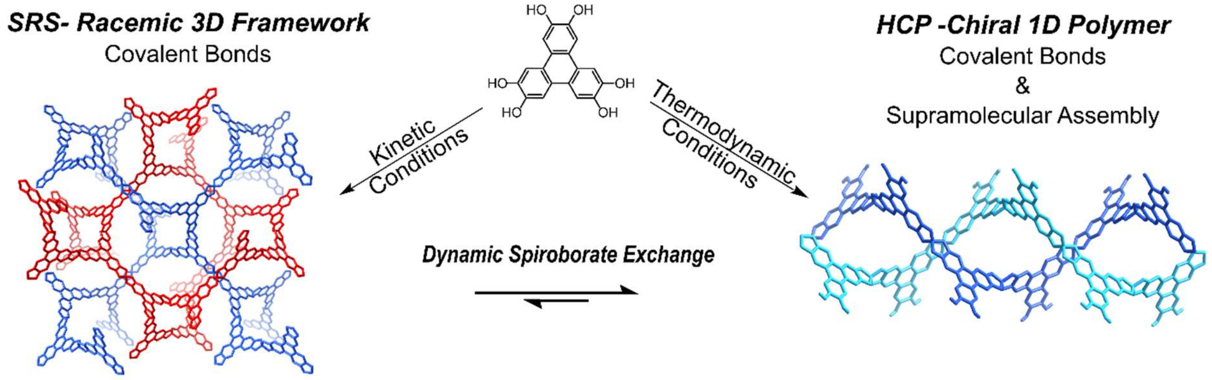

Figure 2.1. Illustration of srs-COF and HCP formation utilizing the dynamic spiroborate linkage. Kinetic conditions favor the formation of srs-COF while thermodynamic conditions favor HCP formation. srs-COF is a racemic framework connected with purely covalent bonds, whereas HCP is composed of 1D helical polymer chains with single-handedness (in each crystalline domain) that are assembled through hydrogen bonding interactions. The red and blue/light blue indicates opposite handedness and guest molecules are omitted from the structures for clarity.

2.3 Results and Discussion

2.3.1 Equilibrium Studies

The progress of the polymerization was monitored by PXRD to investigate the mechanism of the HCP formation through the condensation reaction of HHTP with trimethyl borate ($B(OMe)_3$) in the presence of lithium hydroxide (LiOH). At different time intervals, the reaction was quenched and washed with methanol and acetone to analyze the polymeric reaction mixture. After 12 hours at 120 °C, there was a mixture of two phases, HCP phase and a new unknown phase. However, by 24 hours HCP became the major species and after approximately 3 days the new phase was no longer present (Figure 2.2a). These results indicate that the new phase is a metastable intermediate and only present at the early stage of the polymerization. We hypothesized that the new phase is likely an open framework structure where all three pairs of diols are fully reacted. To determine

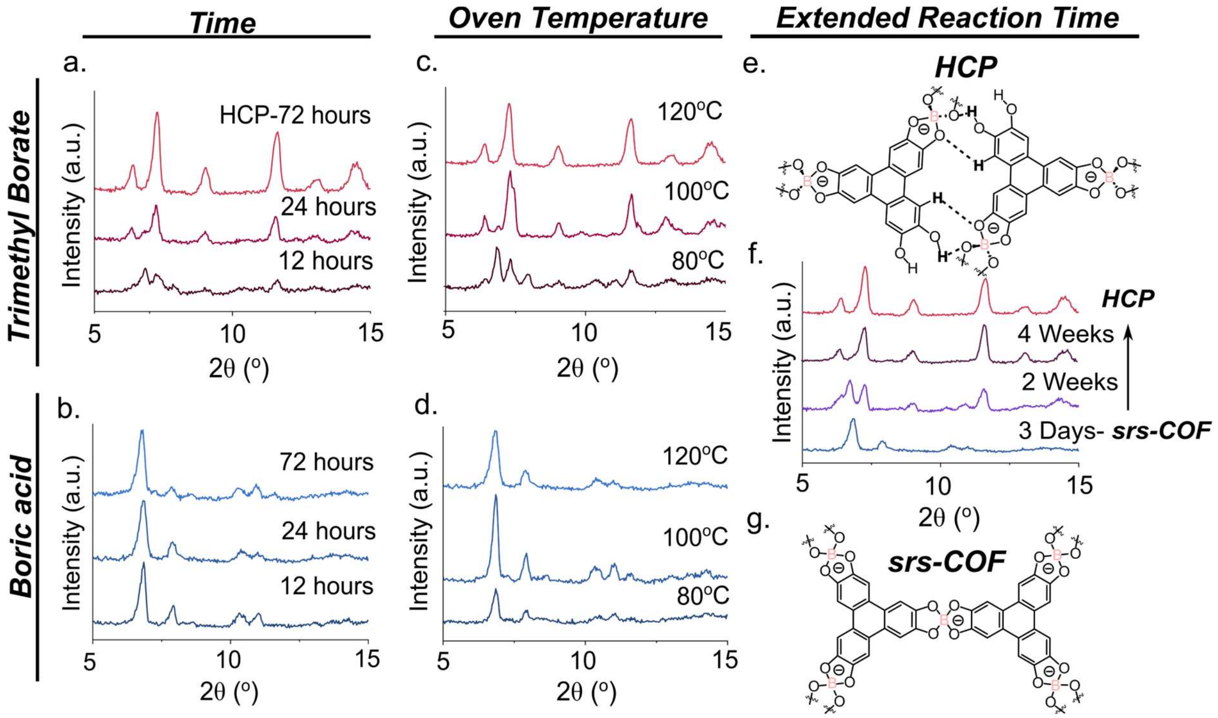

Figure 2.2. Experimental diffraction patterns of the polymers obtained when reaction times and oven temperatures were varied during spiroborate polymerization, using either trimethyl borate (a, c) or boric acid (b, d) as the boron reagent, respectively. Extending the reaction time of the spiroborate polymerization with boric acid resulted in the shift from srs-COF (g) to HCP (e) as the major phase after four weeks (f). The polymeric backbone of the structures is shown where the srs-COF backbone is built on purely covalent bonds (g) while HCP (e) is built on covalent and hydrogen bonds.

the structure of this new phase, we probed the reaction conditions, such as solvation of LiOH, boron reagent, water concentration, temperature, and time, in the hope of forming the new phase predominantly.

Previously, the spiroborate polymerization was carried out by pre-stirring the reaction mixture at a lower temperature to dissolve the LiOH, which acts as a base and deprotonates the diols, and then heating the mixture in an oven without stirring to promote the growth and crystallization of the HCP. Using this synthetic approach, we observed that modulating the rate at which LiOH dissolves into solution is a key parameter for controlling the formation of the HCP crystals. To allow for better solvation of LiOH and facilitate the reaction of diols with the boron reagent, initially we attempted to incorporate more water in the reaction solution. However, although we observed the increase of the formation of the new phase with a higher content of water, the polymerization of HHTP with $B(OMe)_3$ consistently provided the HCP as the major species (Figure 2.5).

Interestingly, when we used boric acid ($B(OH)_3$) instead of $B(OMe)_3$ as the boron source, the new phase became much more evident with new visible peaks at 6.72°, 7.81°, 10.22°, and 10.90° (Figure 2.5). Additional water enhanced the formation of the new phase, but the phases became mixed, and the overall crystallinity diminished with excess water. We found it is challenging to get an unequivocal new phase due to slight shifts in the concentration of water that significantly affect the phase distribution when heating at 120 °C for 3 days.

Therefore, we next explored changing the temperatures and reaction time to better control the distribution of the phases. The effect of temperature on the phase distribution was studied in two ways: 1) the initial stir temperature was varied; 2) the oven temperature was varied. When the initial stir temperature was varied from 80 °C to 100 °C and 120 °C, we did not observe obvious change in the final phase distribution, indicating the initial nuclei that form during the stirring step, do not have a significant effect on the product distribution (Figure 2.6). When the initial stir temperature was kept the same (80 °C) and the oven reaction temperature was lowered to 80 °C, the reaction of HHTP with $B(OH)_3$ produced the new phase as the major phase (Figure 2.2d). Whereas the reaction of HHTP with $B(OMe)_3$ still produced a mixture of phases at 80 °C, and HCP as the major phase at 100 °C (Figure 2.2c). Lowering the oven temperature during the polymerization process limits the reaction kinetics and the topological rearrangement, resulting in the formation of srs-COF as a kinetically trapped intermediate. The fact that the oven temperature, which influences the exchange, hydrolysis, and growth of the polymer phases, dictates the final phase distribution more significantly than the initial nucleation of the phases further suggest HCP is more thermodynamically favored and the new phase is only a metastable intermediate.

To intercept the polymerization at the COF stage, we quenched the reaction prematurely. As expected, the new phase was the only phase formed at shorter times (12 or 24 hours) when using boric acid ($B(OH)_3$) (Figure 2.2b). When the polymerization time with $B(OH)_3$ was extended past three days, the new srs-COF began to be converted to the HCP phase. After reacting for 2 weeks, a mixture of phases was present, and by 4 weeks HCP was the only phase observed (Figure 2.2f). Although the HHTP polymerization kinetics and equilibrium heavily depend on the boron reagent, we observed that srs-COF will be gradually transformed to HCP with extended times and elevated temperatures. These results are consistent with our previous observation and further confirm HCP is the thermodynamic topology.

2.3.2 Characterization of srs-COF

We isolated srs-COF by reacting HHTP, $B(OH)_3$, and LiOH under solvothermal conditions at 100 $^{\circ}$C for 3 days and characterized it with FT-IR, NMR, PXRD, HR-TEM and SEM to elucidate the structure. FT-IR spectrum supports the notion that the new phase is a spiroborate polymer, which shows a strong B-O stretch absorption at 1053 cm^{-1} (Figure 2.7).[7,13,14] The fingerprint region of the FT-IR spectrum shows only slight differences when compared to that of HCP and the OH stretch is attenuated as compared with HHTP (Figure 2.7). Solid-state ^{13}C NMR spectrum suggests all three sides of HHTP are fully reacted as indicated by three symmetrical carbon signals. However, the broadening of the peaks implies that the polymerization in srs-COF is incomplete likely due to the difficulty of suppressing the HCP formation (Figure 2.8). Similarly, the solid-state ^{11}B NMR (Figure 2.9) showed the presence of several boron species, which can be attributed to the relatively low polymerization degree and lower stability of srs-COF. However, the observed signals of boron species are consistent with those found in other recently reported materials. [7,13,14] Meanwhile, the ^{7}Li NMR spectrum (Figure 2.10) exhibited a dominant Li^+ species that is in agreement with previous reports.[7,14]

The SEM and HR-TEM analysis revealed a rod like morphology of the srs-COF phase, which is notably different from the HCP single crystal morphology (Figure 2.11 and 2.12). In addition, the HR-TEM analysis also showed a lattice fringe with a d spacing of 1.3 nm that matches well with the $d_{(112)}$ and the electron diffraction pattern obtained from an orthorhombic crystal lattice (Figure 2.12). The PXRD demonstrates a clear structural difference between the phases (Figure 2.2f). We also compared the PXRD pattern to the starting materials (HHTP, LiOH, $B(OH)_3$) and confirmed that no major peaks are attributed to the starting materials (Figure 2.13). Based on the chemical characterization it was evident that this new phase is a spiroborate polymer with a unique structure compared to HCP.

The spiroborate linkage contains a boron vertex that preferentially adopts a tetrahedral geometry.[13,15] However, the HCP single crystal structure demonstrates that the B-O bonds of the spiroborate are flexible and can adopt a strained dihedral angle of 66°.[7] Thus, the new phase was anticipated to be a 3D COF with srs topology when considering the geometry of the HHTP and spiroborate.[16,17,18,19] Additionally, the spiroborate COF has the potential to display chirality since the extended structure consist of helices that can have either left or right handedness. So, models of the COF with srs topology with either mixed or a single handedness were created and up to four-fold interpenetration was explored (Figure 2.3a).[20,21,22] The simulations of these models show the PXRD patterns of the new species match well with those of a racemic srs framework with the 2-fold interpenetration (Figure 2.3b). The major peaks at 6.72°, 7.81°, 8.55°, 10.22°, and 10.90° correspond to the (112), (202), (321), (130) and (004) planes, respectively. We determined the unit cell dimensions to be nearly cubic with a=32.4043 Å, b=32.3597 Å, and c=31.8323 Å and a symmetry group of PCA21 through Pawley refinement (RWP = 5.04% and RP = 3.12%) (Figure 2.3c).

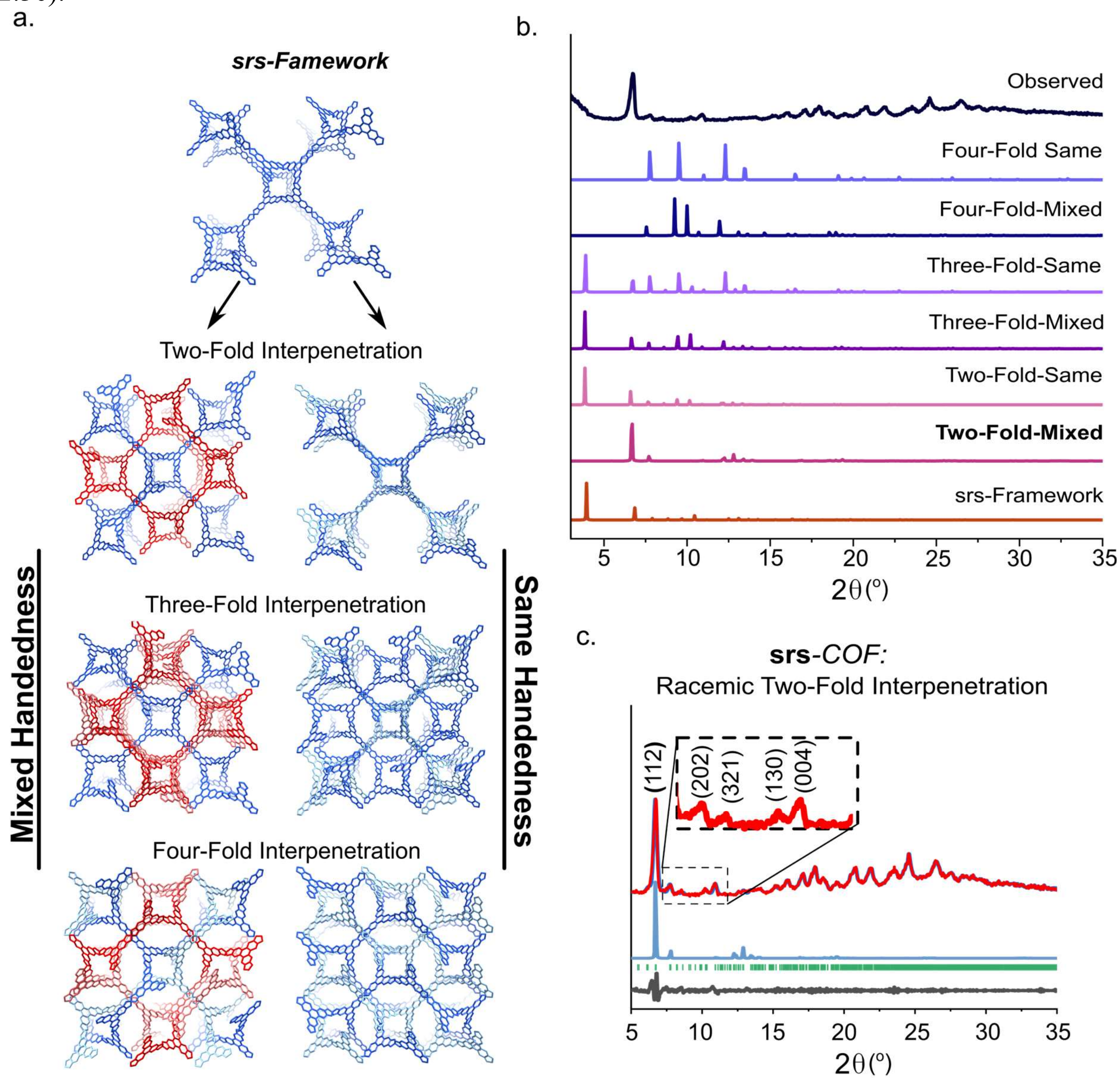

Figure 2.3. Simulated models of the srs-COF, with increasing interpenetration, where the handedness can be added to form frameworks with either all the same or mixed handedness. The red/pink and blue/light blue represents opposite handedness (a). The resulting diffraction patterns for the models show that only the two-fold interpenetration with mixed handedness matches the experimental pattern (b). Pawley refinement (dark blue) of the experimental data (red) with the simulation of the racemic two-fold interpenetrated (light blue), the difference between the simulation and experimental data (black), and the Bragg reflections are noted with green lines (c).

2.3.3 Rearrangement of srs-COF to HCP

Although HCP crystals display a single handedness in each crystalline domain, the intermediate in the polymerization is racemic srs-COF with a two-fold interpenetrated structure, as has been observed in other COF systems.[20,21] srs-COF and HCP are distinctly related because both contain helical components that have either right handedness or left handedness (Figure 2.4). In our previous work, we proposed that helical oligomers would initially form and subsequently become entwined as the hydrogen bonding interactions drove the formation of the HCP.[7] However, in this work we observed that the racemic srs-COF structure is present in the early stage of the polymerization and slowly converts to the HCP.

Therefore, we propose that srs-COF is an intermediate species and contributes to the formation of the HCP in two ways: 1) pre-organize the helices and 2) supply helical oligomers that will self-sort as the HCP crystals grow. The transformation requires the oligomers to undergo a partial hydrolysis (slice) then self-sort into the correct orientation for the hydrogen bonding stabilization when condensing into the HCP structure. The thermodynamic favorability of HCP and srs-COF cannot be directly compared due to the difference in their compositions. However, the stoichiometric relationship between HHTP, HCP, and srs-COF can be used to find the effective energy difference for the spiroborate linkage within the two polymeric structures. First, we calculated the electronic energy of a known HHTP crystal structure, the HCP crystal structure, and the srs-COF crystal structure while optimizing the geometry using self-consistent charge density functional tight-binding (DFTB) theory. Then, the effective reaction energy per spiroborate unit was calculated for HCP and srs-COF by accounting for the number of HHTP monomers and spiroborate bonds within the respective unit cells. This calculation shows the energy of spiroborate formation in the HCP structure is 36.8 kJ/mol lower than that of the srs-COF and supports the

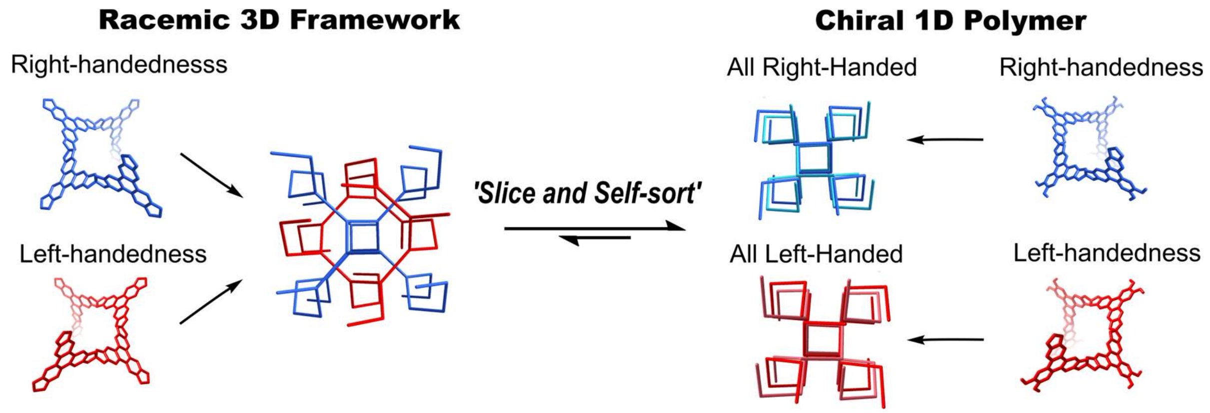

Figure 2.4. srs-COF and HCP architectures are built with helical components that have either left handedness or right handedness. However, the srs-COF structure is a racemic framework whereas HCP consists of 1D polymer chains where each crystalline domain has single handedness. We propose that the srs-COF will pre-organize the helices and provide helical oligomers that undergo a slice and self-sort transformation in order to be incorporated in the HCP topology.

notion that the HCP is thermodynamically more favorable compared to srs-COF. The experimental and calculation results indicate that the hydrogen bonding interactions provide higher stabilization force compared to covalent spiroborate formation.

2.4 Conclusions

In summary, to understand the formation of the unexpectedly chiral HCP topology that consists of covalent and non-covalent bonds in the spiroborate polymerization, we investigated the mechanism by exploring the parameters such as time, water content, and temperature. We found the racemic srs-COF is formed as a metastable intermediate in the early stage of the polymerization but is transformed to the thermodynamically favored HCP. srs-COF is proposed to pre-organize the helical structures and supplies helical oligomers that will self-sort to grow the HCP structure. Although an individual hydrogen bond is much weaker than a typical covalent bond, the combined effect of a series of hydrogen bonding interactions is nearly additive and could be a determining factor of a product's structure. The strategy of incorporating weak secondary interactions into the synthetic design of polymetric architectures will undoubtably lead to novel structures and functions.

2.5 Experimental section

2.5.1. Materials and Methods

All chemicals were purchased from either Aldrich Chemical Company or TCL and used without further purification. The 2,3,6,7,10,11-hexahydroxytriphenylene (HHTP) used in this study was synthesized according to the reported procedure.[23] All reactions were conducted under inert atmosphere (nitrogen) unless noted otherwise.

The Fourier-transform infrared (FT-IR) spectra were obtained from an Agilent Technologies Cary 630 FT-IR spectrometer. Scanning Electron Microscopy images (SEM) were recorded using a JSM-6480LV (LVSEM) at 30 kV. NMR spectra were taken on Bruker 300, Inova 400, or Inova 500 spectrometers. DMSO (2.50 ppm) and $CHCl_3$ (7.26 ppm) were used as internal references in ^1H NMR. ^1H NMR data is reported in the following order: chemical shift, multiplicity (s, singlet; br s, broad singlet; d, doublet; triplet, t), number of protons, and proton assignment.

Solid-state cross polarization magic angle spinning (CP/MAS) NMR spectra were recorded on an Inova 400 NMR spectrometer. ^{11}B MAS NMR was referred to Boron trifluoride etherate and ^7Li MAS NMR was referred to Lithium Chloride (1 M solution in water). Deuterated solvents were purchased from Cambridge Isotope Laboratories (Andover, MA) and used as received.

The Powder XRD data was collected on a Bruker D8 Advance A25 system with a monochromated Cu Kα radiation source. The sample was measured under ambient conditions and the X-ray source was operated at 40 kV and 40 mA.

Nitrogen isotherm was evaluated using the Quantachrome Autosorb AsiQ automated gas sorption analyzer. The sample was activated by soxhlet extraction with acetone for 12h and then dried under vacuum for activation. Ultra-high purity grade (99.999 % purity) N_2 were used for all free space corrections and measurements. For the gas adsorption measurement, the temperatures were controlled by using a refrigerated bath of liquid N_2 (77 K). Thermogravimetric analysis (TGA) was performed using a thermogravimetric/differential thermal analyzer.

2.5.2. Experimental Procedures

2.5.2.1 Synthesis of HHTP

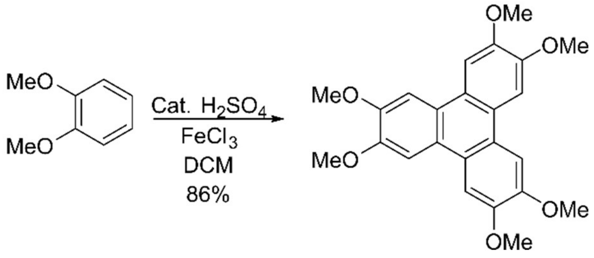

Anhydrous $FeCl_3$ (25.5 g, 15.7 mmol, 0.3 eq) was added to 150 mL of DCM in dry 3-neck round bottom flask followed by a catalytic amount of concentrated sulfuric acid (0.35 mL, 1.95 mmol, 0.04 eq). The reaction was chilled on ice before a solution of 1,2-dimethoxybenzene (6.4 mL, 50.0 mmol, 1 eq) in DCM (70 mL) was added dropwise. The resulting suspension was stirred at room temperature for 3 hours. After the reaction period, the reaction was returned to an ice bath and slowly quenched with 200 mL of methanol. During the quenching, the reaction turned from a dark blue to a white suspension. The reaction was allowed to stir for an additional 30 minutes, before the product was isolated as a white principate by vacuum filtration. The product was washed with methanol, before being dried under vacuum. Characterization matched what has previously been reported.[23] (Yield 5.8561 g, 86%). ^{1}H NMR (300 MHz, $CDCl_3$): δ 7.83 (s, 6H, Ar-H), 4.14 (s, 18H, OMe).

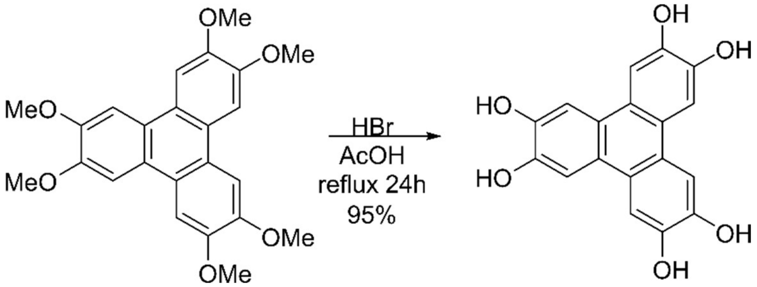

The starting material (2.3063 g, 5.65 mmol, 1 eq) was added to a dry 3-neck round bottom flask under nitrogen atmosphere. It was then suspended in 1:1 solution of HBr (48% in water) and acetic acid (125 mL total). The suspension was refluxed for 24 hours. Then it was cooled, and the product was filtered off as a grey solid that was washed with a copious amount of water and dried under vacuum. (Yield 1.739g, 95%) ^{1}H NMR (300 MHz, DMSO-d_6): δ 9.28 (br S, 6H, OH), 7.60 (s, 6H, Ar-H).[23]

2.5.2.2 Synthesis of srs-COF

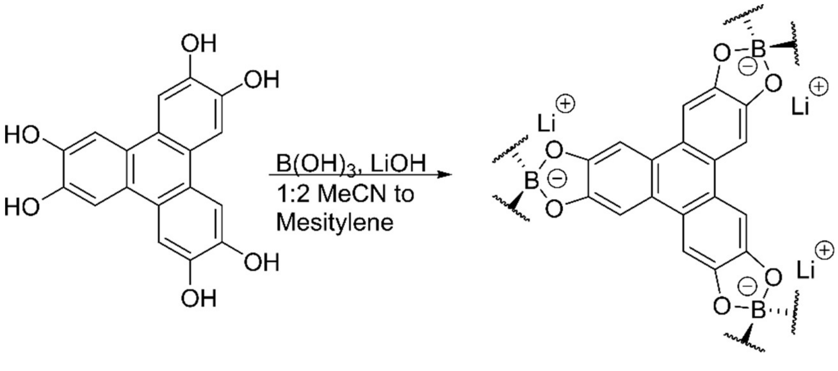

The typical procedure was to add HHTP (32.4 mg, 0.1 mmol), LiOH (3.6 mg, 0.15 mmol), and boric acid (9.3 mg, 0.15 mmol) to an ampule. Then 1.8 mL of 1:2 MeCN to mesitylene with 4.05 μL of water was added to the ampule that was premixed in a vial. Acetonitrile was dried over molecular sieves and incremental percentages of water were added to determine the optimal amount. The resulting suspension was sonicated for 20 mins before a stir bar was added. The reaction was cooled in liquid nitrogen and sealed under vacuum. The reaction was stirred at 80 °C for 12 hours before being transferred to a 100 °C oven for 3 days. After the reaction period, the polymer was isolated by vacuum filtration and washed with acetone and methanol. Then it was dried under high vacuum to give a light purple solid (25.9 mg, Yield 77%).

2.5.3. Equilibrium Studies

The equilibrium studies were carried out analogously to the procedure for synthesizing srs-COF. The conditions in Table 2.1 list the different conditions tested.

Table 2.1. Summary of conditions tested in evaluating the relationship between HCP and srs-COF. The solvent lists the ratio of acetonitrile to mesitylene where the total solvent is 1.8 mL.

Trial	Boron Reagent	Solvent	Water (volume%)	Stir temp. (time)	Oven Temp. (time)	Results
1	$B(OMe)_3$	1:2	0.07%	80 °C (12 h)	120 °C (3 d)	Low crystallinity
2	$B(OMe)_3$	1:2	0.23%	80 °C (12 h)	120 °C (3 d)	HCP
3	$B(OMe)_3$	1:2	0.3%	80 °C (12 h)	120 °C (3 d)	HCP with small amount of srs
4	$B(OH)_3$	1:2	0.07%	80 °C (12 h)	120 °C (3 d)	Mixture
5	$B(OH)_3$	1:2	0.23%	80 °C (12 h)	120 °C (3 d)	srs
6	$B(OH)_3$	1:2	0.07%	80 °C (12 h)	120 °C (3 d)	Mixture
7	$B(OMe)_3$	1:2	0.23%	80 °C (12 h)	80 °C (3 d)	Mixture
8	$B(OMe)_3$	1:2	0.23%	80 °C (12 h)	100 °C (3 d)	HCP with small amount of srs
9	$B(OH)_3$	1:2	0.23%	80 °C (12 h)	80 °C (3 d)	srs
10	$B(OH)_3$	1:2	0.23%	80 °C (12 h)	100 °C (3 d)	srs
11	$B(OH)_3$	1:2	0.15%	100 °C (12 h)	120 °C (3 d)	Mixture
12	$B(OH)_3$	1:2	0.23%	100 °C (12h)	120 °C (3 d)	Mixture
13	$B(OH)_3$	1:2	0.30%	100 °C (12 h)	120 °C (3 d)	srs
14	$B(OH)_3$	1:2	0.38%	100 °C (12 h)	120 °C (3 d)	HCP with small amount of srs

15	$B(OH)_3$	1:2	0.15%	120 °C (12 h)	120 °C (3 d)	Mixture
16	$B(OH)_3$	1:2	0.23%	120 °C (12 h)	120 °C (3 d)	Mixture
17	$B(OH)_3$	1:2	0.30%	120 °C (12 h)	120 °C (3 d)	srs
18	$B(OH)_3$	1:2	0.38%	120 °C (12 h)	120 °C (3 d)	Mixture
19	$B(OMe)_3$	1:2	0.23%	80 °C (12 h)	---	No crystallinity
20	$B(OMe)_3$	1:2	0.23%	80 °C (12 h)	120 °C (12 h)	Mixture
21	$B(OMe)_3$	1:2	0.23%	80 °C (12 h)	120 °C (1 d)	HCP with small amount of srs
22	$B(OH)_3$	1:2	0.23%	80 °C (12 h)	---	No crystallinity
23	$B(OH)_3$	1:2	0.23%	80 °C (12 h)	120 °C (12 h)	srs
24	$B(OH)_3$	1:2	0.23%	80 °C (12 h)	120 °C (1 d)	srs
25	$B(OH)_3$	1:2	0.23%	80 °C (12 h)	120 °C (14 d)	Mixture
26	$B(OH)_3$	1:2	0.23%	80 °C (12 h)	120 °C (30 d)	HCP

2.5.3.1 Effect of Water Content

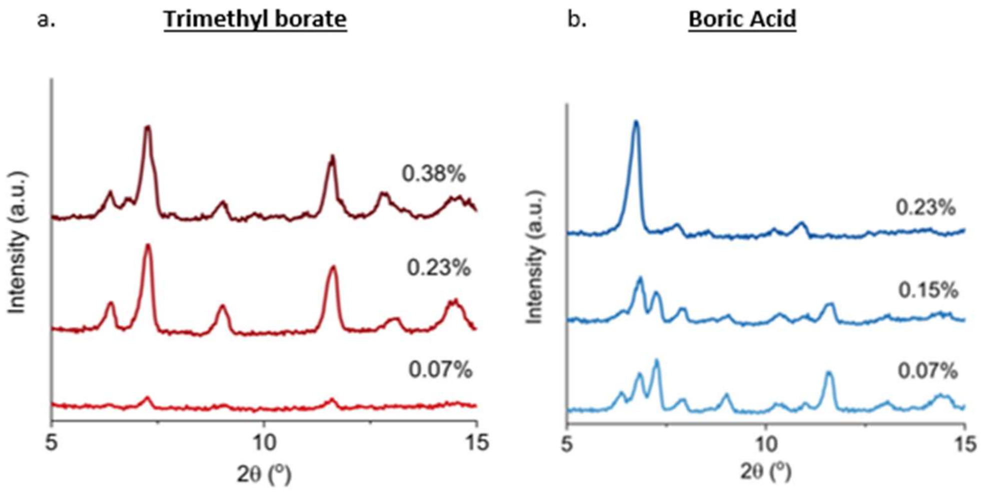

Figure 2.5. The effect of water content in the reaction solution on the experimental diffraction pattern measured when monitoring the polymeric phase of the spiroborate formation using trimethyl borate (a) and boric acid (b) using 1:2 acetonitrile to mesitylene with difference water content based on the volume%.

2.5.3.2 Effect of Stir Temperature

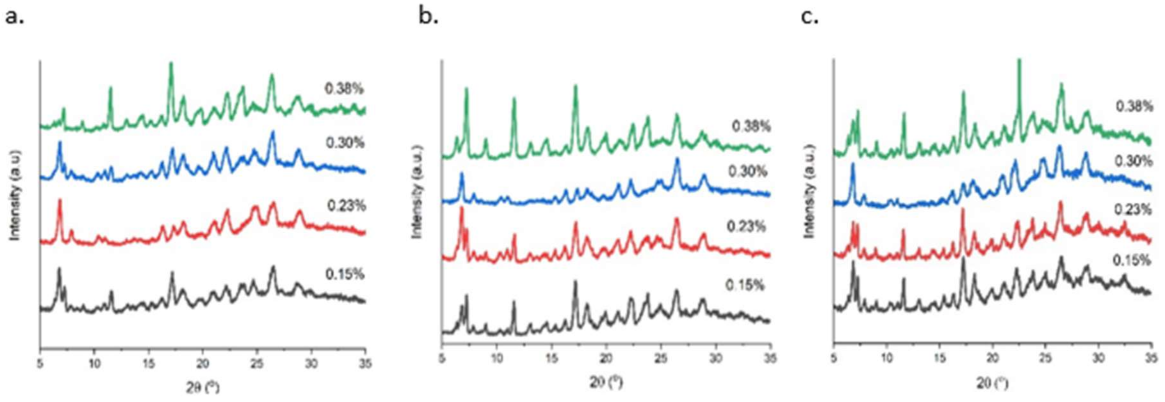

Figure 2.6. The evolution of the PXRD spectrum when the water content is varied at stir temperatures of 80 °C (a), 100 °C (b), and 120 °C (c). The reactions were all set up using 1:2 acetonitrile to mesitylene (1.8 mL) with different percentages of water. Then, they were heated at the respective stir temperatures for 12 hours before being moved to a 120 °C oven for 3 days. The volume% of water is indicated for each PXRD spectrum.

2.5.4. Fourier-transform infrared spectroscopy

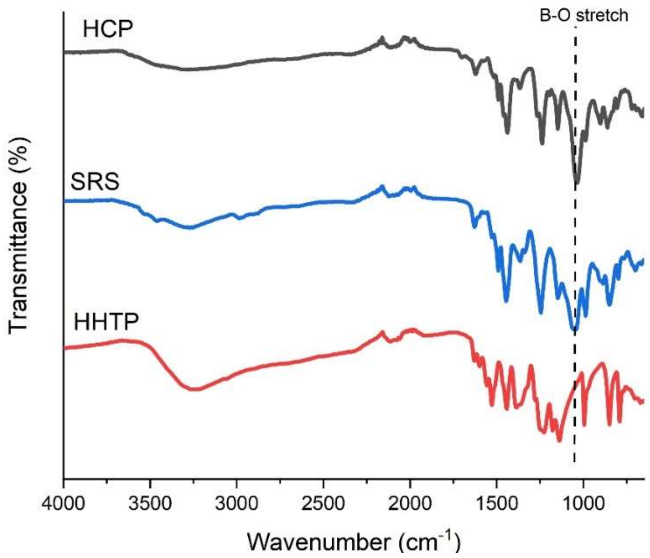

Figure 2.7. FT-IR comparison of HHTP, srs-COF, and HCP**.**

2.5.5. Solid-State NMR Spectra

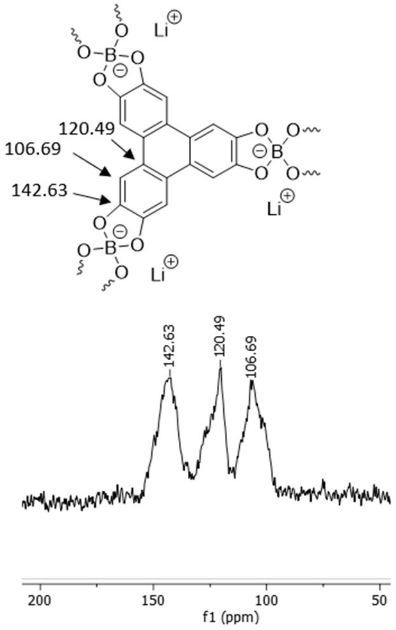

Figure 2.8. Solid-state ^{13}C NMR spectrum of srs-COF.

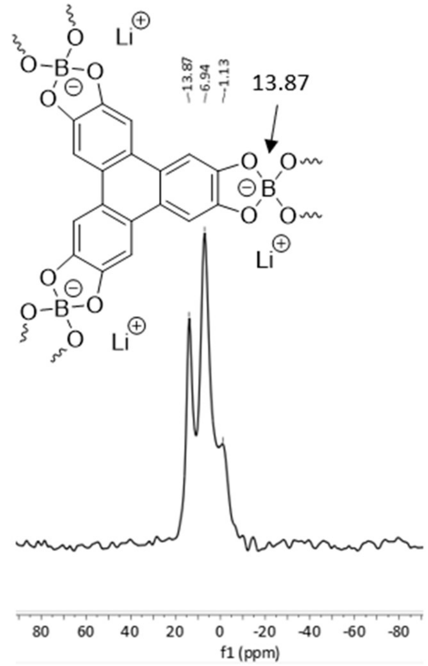

Figure 2.9. Solid-state ^{11}B NMR spectrum of **srs-**COF

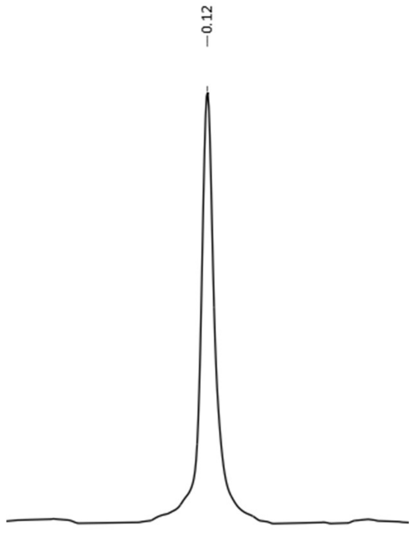

Figure 2.10. Solid-state ^{7}Li NMR spectrum of **srs**-COF

2.5.6. Scanning Electron Microscope and Transmission Electron Microscopy

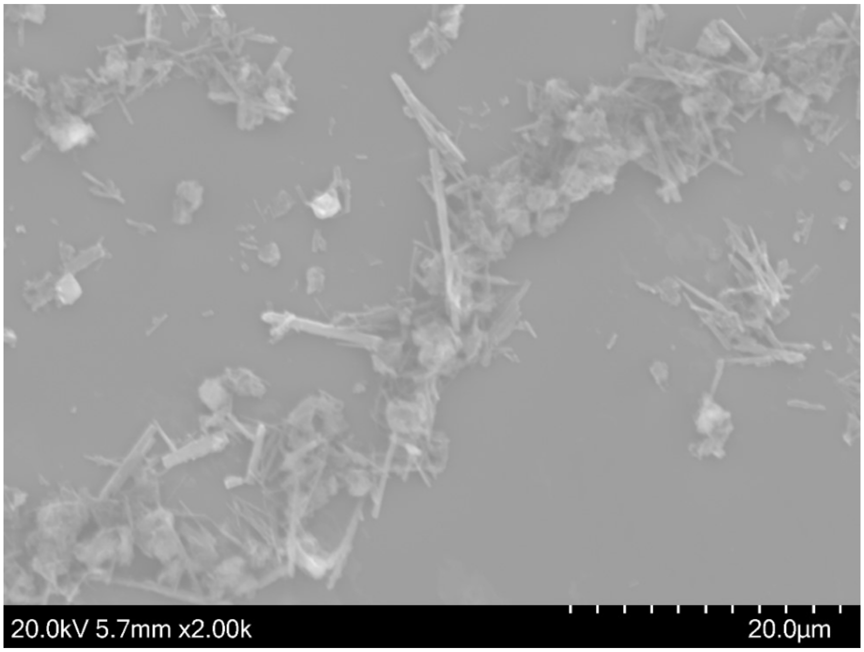

Figure 2.11. SEM image of isolated **srs**-COF

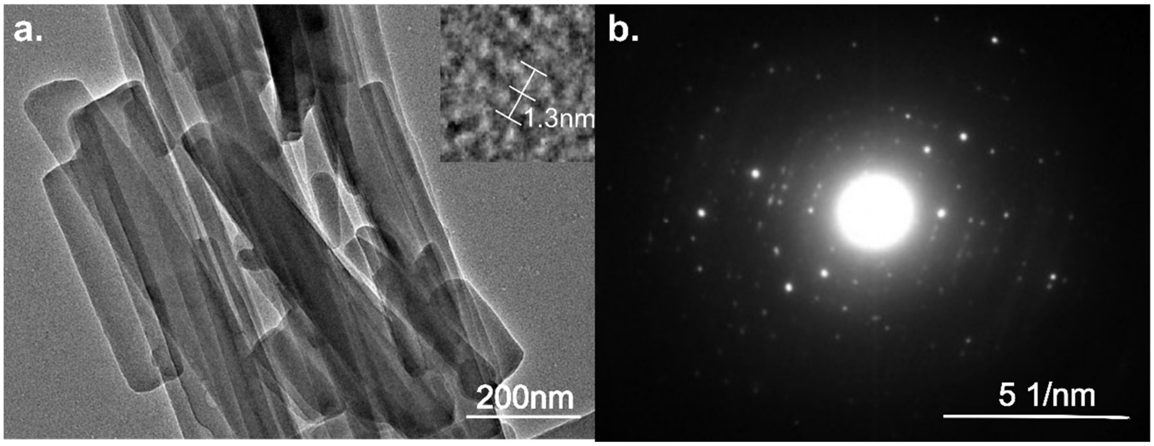

Figure 2.12. (a)HR-TEM of **srs**-COF with an insert of the lattice fringe that matches $d_{(112)}$=1.3 nm. (b)The SAED pattern of **srs**-COF.

2.5.7. PXRD spectra of srs-COF compared to the starting materials

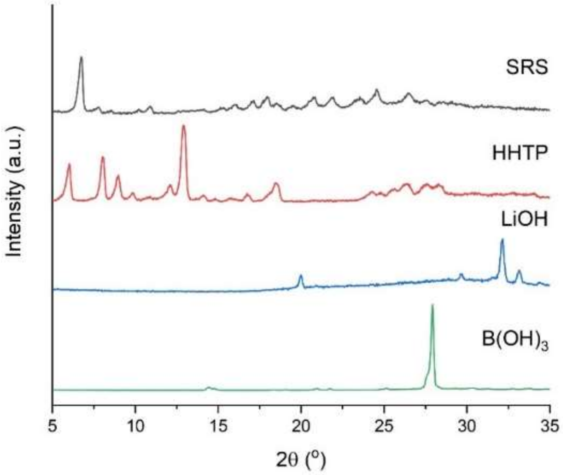

Figure 2.13. PXRD comparison of **srs-**COF to HHTP, lithium hydroxide (LiOH), and boric acid ($B(OH)_3$).

2.5.8. Calculated X-ray diffraction of SRS framework models

The **srs** models were built in Material Studio based on the information found on reticular chemistry structure resource database[24], other reported **srs** frameworks[25], and in part with the **HCP** crystal structure[26]. The ideal space group for the racemic two-fold interpenetrated framework is IA3D. However, the lithium counterions cause some dissymmetry in the framework. So, a lower symmetry space group of PAC21 was found to better match the experimental spectrum. This section includes tables with the fractional atomic coordinates for each model.

Table 2.2. Fractional coordinates of the srs-non interpenetrated structure

srs-non interpenetrated			
Space group- I4132 a=b=c= 31.6563 Å			
Atom	X	Y	Z
C	0.59321	0.40871	0.80054
H	0.56955	0.39468	0.78311
C	0.61028	0.44407	0.78575
O	0.59919	0.4633	0.75046
C	0.60712	0.39274	0.83759
B	0.625	0.5	0.75

Table 2.3. Fractional coordinates of the srs-two-fold interpenetration-same chirality

srs-two-fold- same chirality			
Space group- P4222 a=b= 22.9561 Å c= 16.4645 Å			
Atom	X	Y	Z
O	0.4047	0.59666	-0.82349
C	0.42915	0.64416	-0.86145
C	0.4341	0.7483	-0.854
C	0.46558	0.74934	-0.92741
C	0.58208	0.69483	-1.17811
C	0.53765	0.64283	-1.06813
C	0.51759	0.69585	-1.03509
O	0.61197	0.68636	-1.24958
O	0.03767	0.53675	-1.55243
C	0.09308	0.51991	-1.53071
C	0.14411	0.46089	-1.43268
C	0.19758	0.48103	-1.46315
H	0.42243	0.79085	-0.82222
H	0.52653	0.59988	-1.03703
H	0.14325	0.42949	-1.37905
B	0.62253	1.37747	-0.75
B	0.5	1	-1

Table 2.4. Fractional coordinates of the srs-three-fold interpenetration-same chirality

srs-Three-Fold Interpenetration-Same Chirality			
Space group- I4132 a=b=c= 32.1886 Å			
Atom	X	Y	Z
O	0.00077	0.71512	0.14942
C	0.03358	0.69533	0.14091
C	0.09049	0.70093	0.09067
C	0.10674	0.66334	0.10636
O	0.00079	0.28488	-0.14957
C	0.0336	0.30466	-0.14103
C	0.09049	0.29906	-0.09076
C	0.10673	0.33666	-0.10641
O	-0.00078	0.71512	-0.1495

C	-0.03358	0.69534	-0.14097
C	-0.09048	0.70096	-0.09072
C	-0.10672	0.66337	-0.10639
H	0.10676	0.71744	0.06389
H	0.10675	0.28253	0.93601
H	0.89325	0.71748	0.93605
B	0.125	0.5	-0.25
B	-0.12492	0.5	-0.25

Table 2.5. Fractional coordinates of the srs-four-fold interpenetration-same chirality

srs-Four-Fold Interpenetration- Same Chirality			
Space group- P4232 a=b=c= 16.0943 Å			
Atom	X	Y	Z
O	0.49783	0.07239	0.80088
C	0.4296	0.11038	0.78112
C	0.31835	0.10268	0.68234
C	0.28513	0.17745	0.71432
H	0.28673	0.07034	0.62783
B	0.75	0.5	0

Table 2.6. Fractional coordinates of the srs-two-fold interpenetration-mixed chirality

srs-Two-Fold Interpenetration- Mixed Chirality			
Space group- PAC21 a=32.4043 Å b=32.3597 Å c=31.8323 Å			
Atom	X	Y	Z
C	1.33686	0.14105	0.76133
O	1.24592	0.20958	0.76769
C	1.35604	0.10701	0.78047
O	1.3483	0.03658	0.87005
C	1.39157	0.08901	0.76251
O	1.40185	0.00074	0.83463
C	0.94491	0.40668	0.52483
C	0.95996	0.38946	0.56039

C	0.90396	0.34303	0.56497
C	0.9394	0.35991	0.58057
C	0.78124	0.30803	0.47588
C	0.79709	0.34339	0.45892
C	0.84247	0.64551	0.25785
O	0.75833	0.71698	0.26504
C	0.86004	0.61019	0.27627
O	0.84906	0.5385	0.36449
C	0.89462	0.59082	0.25787
O	0.90075	0.50079	0.32835
C	1.44874	-0.09371	0.0294
C	1.46423	-0.11116	0.06465
C	1.40975	-0.15954	0.06813
C	1.44465	-0.14187	0.08413
C	1.28824	-0.19642	0.97826
C	1.30399	-0.16069	0.9615
C	1.35917	-0.16318	0.01193
O	1.2885	-0.25285	0.01904
C	1.39343	-0.14446	0.03081
O	1.46388	-0.15333	0.11977
C	1.41174	-0.10887	0.01266
O	1.49956	-0.09955	0.0842
C	1.09169	0.44737	0.77408
C	1.10953	0.46292	0.80914
C	1.15529	0.40616	0.81347
C	1.13909	0.44224	0.82895
C	1.18869	0.28148	0.72556
C	1.15362	0.2977	0.70859
C	0.85353	0.33935	0.50869
O	0.78246	0.25431	0.51565
C	0.88815	0.35769	0.52724
O	0.95829	0.34861	0.61644
C	0.90735	0.39242	0.50848
O	0.99573	0.40025	0.57959
C	1.59301	-0.05184	0.27943
C	1.61017	-0.03609	0.31473
C	1.6586	-0.09063	0.31793
C	1.64074	-0.05568	0.33412
C	1.69787	-0.21173	0.22753
C	1.66184	-0.19704	0.21117
C	1.65906	0.14429	0.47698

O	1.74725	0.21575	0.46649
C	1.64069	0.10935	0.45903
O	1.64803	0.03686	0.37334
C	1.60661	0.09014	0.47812
O	1.59879	-0.00099	0.40879
C	1.0489	0.40605	0.70766
C	1.03265	0.38876	0.67263
C	1.08694	0.34032	0.66791
C	1.05184	0.35815	0.65264
C	1.20923	0.30131	0.75525
C	1.19475	0.33744	0.77228
C	1.16496	0.64136	0.97372
O	1.25131	0.71041	0.96694
C	1.14567	0.60705	0.95511
O	1.1522	0.53615	0.8657
C	1.11062	0.58884	0.97378
O	1.09974	0.50009	0.90239
C	1.55204	-0.09392	0.21234
C	1.53651	-0.11135	0.17706
C	1.59289	-0.15719	0.17148
C	1.55697	-0.14076	0.15658
C	1.71762	-0.19132	0.25737
C	1.70124	-0.15645	0.27523
C	1.6446	-0.16002	0.22656
O	1.7181	-0.24682	0.2154
C	1.6093	-0.14226	0.20881
O	1.53777	-0.1521	0.12091
C	1.59001	-0.10783	0.22803
O	1.5005	-0.10067	0.15821
C	0.90479	0.44855	0.45733
C	0.88826	0.46427	0.42175
C	0.84035	0.40936	0.41736
C	0.85829	0.44451	0.40164
C	0.8017	0.28665	0.50662
C	0.83721	0.30154	0.52355
C	1.1382	0.33584	0.72329
O	1.2079	0.24544	0.71433
C	1.1039	0.35504	0.70507
O	1.03215	0.34701	0.61719
C	1.08618	0.39067	0.72367
O	0.99707	0.4006	0.65363

C	1.40721	-0.05175	0.96257
C	1.39014	-0.03543	0.92743
C	1.34446	-0.09195	0.91938
C	1.36117	-0.05539	0.90589
C	1.30779	-0.21673	0.00835
C	1.34276	-0.20104	0.02619
B	1.3756	0.00023	0.8715
B	0.87447	0.50074	0.36521
B	1.50041	-0.12643	0.12079
B	0.99579	0.37412	0.61673
B	1.24452	0.24633	0.74084
B	1.25193	-0.25323	-0.00761
H	0.96326	0.43005	0.51065
H	0.88941	0.31963	0.58302
H	0.77947	0.35819	0.43546
H	1.46635	-0.06946	0.01571
H	1.39607	-0.18395	0.08554
H	1.28678	-0.14631	0.93747
H	1.06828	0.46576	0.76018
H	1.17872	0.39159	0.83126
H	1.13919	0.27987	0.68504
H	1.56869	-0.03435	0.26594
H	1.68276	-0.1044	0.33539
H	1.64808	-0.21523	0.18748
H	1.03169	0.43038	0.72171
H	1.1003	0.31611	0.65
H	1.21314	0.35147	0.79561
H	1.5338	-0.07061	0.22678
H	1.60729	-0.18045	0.15315
H	1.71901	-0.14197	0.29875
H	0.92858	0.46629	0.47143
H	0.81667	0.39545	0.39936
H	0.85129	0.28327	0.547
H	1.43031	-0.03353	0.97722
H	1.32258	-0.1072	0.90013
H	1.35639	-0.21909	0.05006

Table 2.7. Fractional coordinates of the srs-three-fold interpenetration-mixed chirality

srs-Three-Fold Interpenetration- Mixed Chirality
Space group- I4122

a=b=c= 32.4800 Å			
Atom	X	Y	Z
O	0.15261	0.75023	-0.1614
C	0.14171	0.78593	-0.18098
C	0.09247	0.84086	-0.17771
C	0.10812	0.85719	-0.21437
C	0.19422	0.88923	-0.33848
C	0.19813	0.84045	-0.28397
C	0.16138	0.85657	-0.26735
O	0.21343	0.89964	-0.374
O	0.00065	0.5367	-0.52574
C	0.03651	0.55623	-0.51528
C	0.09144	0.5528	-0.46677
C	0.10806	0.58974	-0.48248
O	0.10036	0.78657	-0.126
C	0.11077	0.80578	-0.16152
C	0.15956	0.80187	-0.21603
C	0.14343	0.83862	-0.23265
O	0.0367	0.99935	-0.27574
C	0.08974	0.89194	-0.23248
C	0.05623	0.96349	-0.26528
C	0.0528	0.90856	-0.21677
O	0.24977	0.65261	-0.4114
C	0.21407	0.64171	-0.43098
C	0.15914	0.59247	-0.42771
C	0.14281	0.60812	-0.46437
B	-0.12638	1.25	-0.125
O	-0.4023	0.78714	-0.37595
C	-0.15857	0.5909	-0.67569
C	-0.19403	0.60925	-0.66027
C	-0.39272	0.85695	-0.28697
C	-0.39305	0.91197	-0.23228
O	-0.46285	1.00095	-0.2227
C	-0.6591	1.30068	-0.46643
C	-0.64075	1.28526	-0.43098
C	-0.33803	0.85728	-0.23195
O	-0.24906	0.8477	-0.16215
C	0.05068	1.09143	0.0341
C	0.03527	1.05597	0.01575
H	0.03339	0.10633	0.06076
H	0.31423	0.2834	0.51867

H	0.06527	0.85633	0.83819
H	0.21397	0.81325	0.73157
H	0.10691	0.53672	0.56032
H	0.18674	0.7854	0.76907
H	0.03672	0.89309	0.81032
H	0.14367	0.56527	0.58819
H	0.85633	0.56423	0.34159
B	0	1	-0.25
B	-0.5	1	-0.25
B	-0.25	0.875	-0.125

Table 2.8. Fractional coordinates of the srs-four-fold interpenetration-mixed chirality

<table>
<tr><th colspan="4">srs-Four-Fold Interpenetration- Mixed Chirality</th></tr>
<tr><td colspan="4">Space group- P42/NBC
a=b=23.3752 Å
c= 16.5875 Å</td></tr>
<tr><td>Atom</td><td>X</td><td>Y</td><td>Z</td></tr>
<tr><td>C</td><td>0.25088</td><td>0.46498</td><td>0.82192</td></tr>
<tr><td>O</td><td>0.18754</td><td>0.38593</td><td>0.99937</td></tr>
<tr><td>C</td><td>0.75048</td><td>0.43214</td><td>0.60164</td></tr>
<tr><td>C</td><td>0.80326</td><td>0.41573</td><td>0.57119</td></tr>
<tr><td>C</td><td>0.30271</td><td>-0.48105</td><td>0.7137</td></tr>
<tr><td>O</td><td>0.46298</td><td>-0.46354</td><td>0.69774</td></tr>
<tr><td>C</td><td>0.95995</td><td>-0.35861</td><td>1.1816</td></tr>
<tr><td>C</td><td>0.9268</td><td>-0.3557</td><td>1.11235</td></tr>
<tr><td>C</td><td>0.1955</td><td>-0.48227</td><td>0.71602</td></tr>
<tr><td>O</td><td>0.0986</td><td>-0.40187</td><td>0.57323</td></tr>
<tr><td>C</td><td>0.04004</td><td>0.14182</td><td>1.18215</td></tr>
<tr><td>C</td><td>0.02065</td><td>0.09195</td><td>1.21833</td></tr>
<tr><td>H</td><td>0.70962</td><td>0.42033</td><td>0.56801</td></tr>
<tr><td>H</td><td>0.07137</td><td>0.13945</td><td>0.12959</td></tr>
<tr><td>H</td><td>0.96938</td><td>0.59817</td><td>0.21053</td></tr>
<tr><td>B</td><td>0.5</td><td>-0.5</td><td>0.75</td></tr>
<tr><td>B</td><td>0.12458</td><td>-0.37542</td><td>0.5</td></tr>
</table>

2.5.9. Gas Sorption Isotherms

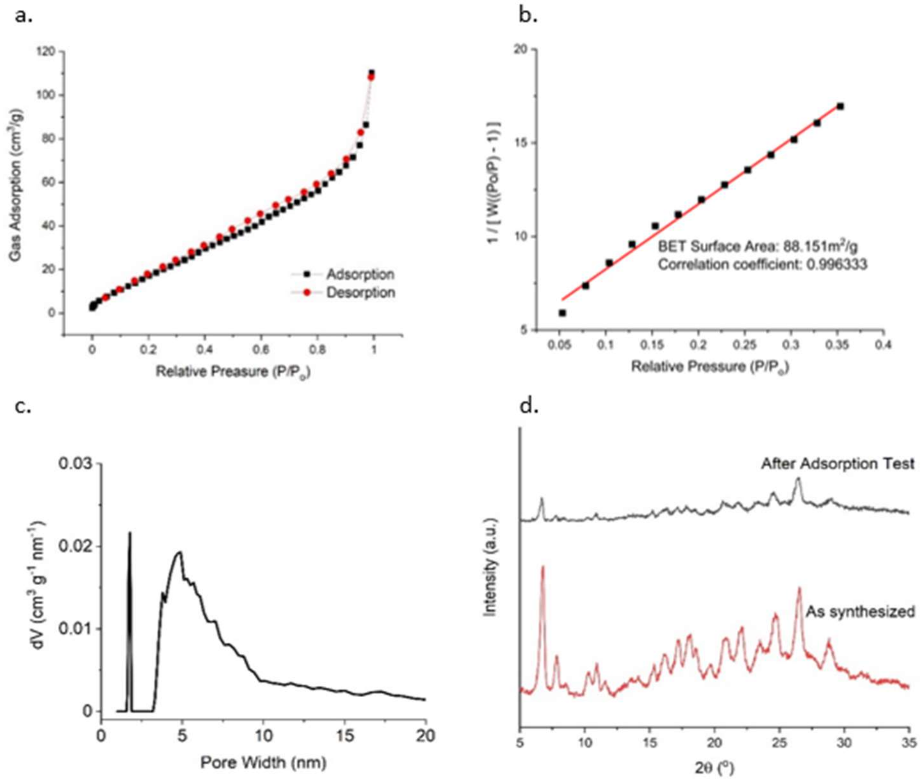

Figure 2.14. (a)Nitrogen isotherm for **srs-**COF. The calculated BET surface area (b) and pore size distribution where there is micropore at 1.7 nm (c). (d)The structure appears to collapse during the activation for the adsorption test as the crystallinity becomes greatly diminished.

2.5.10. Thermogravimetric Analysis

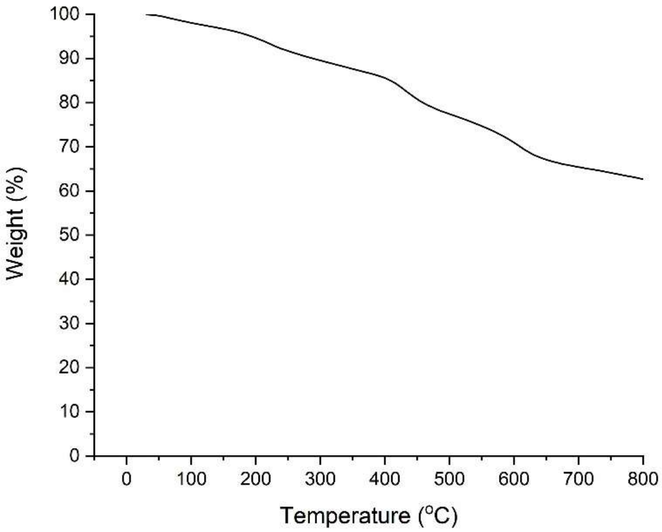

Figure 2.15. Thermal gravimetric analysis of **srs-**COF.

2.5.11. Chemical stability tests

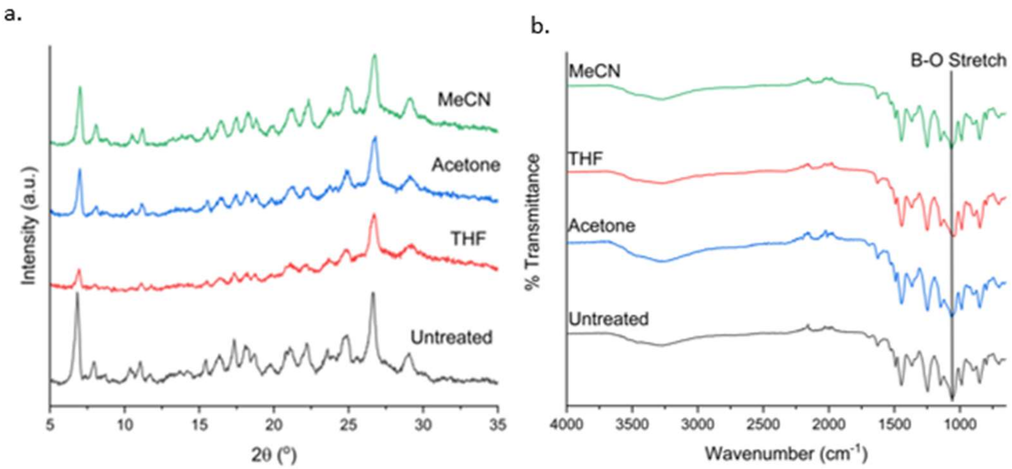

Figure 2.16. PXRD (a) and IR (b) of **srs-**COF after being soaked in different solvents overnight to determine the chemical stability.

2.5.12. DBFT method and calculations

The experimental evidence indicates the formation of **srs-**COF is favored under kinetic conditions and the **HCP** is more thermodynamically favorable. However, it is inadequate to directly compare the energies of the structures because the difference in composition. To overcome the difference in composition, we effectively calculated the difference in energy for the spiroborate formation in the two structures.

First, we determined the stoichiometric relationship between a known HHTP crystal structure, the **HCP** crystal structure, and our proposed **srs** framework in order to overcome the difference in composition and to determine the effective energy of formation per spiroborate in the polymers. The formula of HHTP is $C_{18}H_{12}O_6$ where each unit cell has 4 HHTP and the cell formula is $C_{72}H_{48}O_{24}$. Whereas the HCP cell formula is $C_{144}H_{64}O_{48}B_8Li_8$. The unit cell of the **srs** framework has a formula of $C_{288}H_{96}O_{96}B_{24}Li_{24}$. Each unit cell of the HCP structure contains 8 spiroborate linkages while each **srs-**COF structure has 24. We hereby present the balanced reactions for **HCP** and **srs-**COF:

<u>Balanced equation for HCP:</u>

$$8C_{18}H_{12}O_6 + 8B(OMe)_3 + 8LiOH = C_{144}H_{64}O_{48}B_8Li_8 + 24MeOH + 8H_2O$$

<u>Balanced equation for</u> <u>**srs-***COF:*</u>

$$16C_{18}H_{12}O_6 + 24B(OMe)_3 + 24LiOH = C_{288}H_{96}O_{96}B_{24}Li_{24} + 72MeOH + 24H_2O$$

In the actual calculation, we optimize the geometry and compute the electronic energy of these three solids, i.e., HHTP, **HCP** and **srs-**COF using self-consistent charge density functional tight-binding (DFTB) theory using DFTB+ package. In DFTB, a tight-binding Hamiltonian is being used to reduce the ab initio calculation of integrals, the tight-binding parameters are taken from a precalculated DFT calculation using PBE functional and has been proved to provide results of near PBE quality. A charged unit cell was utilized, because the lithium ions were disregarded since the exact position is unknown.

	Energy (Hartree)
HHTP	-221.41855
HCP	-442.21034
srs-COF	-883.45691

The reaction energy of the spiroborate reactions cannot be calculated directly since the energy of the solids does not contain any information about the methanol, water and lithium hydroxide that are initially in the reaction system. However, the effective reaction energy for per unit of spiroborate reaction can determined by using the stoichiometric relationship between HHTP and the respective polymers that is divided by the number of spiroborate linkages in the unit of the **HCP** and **srs-**COF.

$$E_{eff,HCP} = \frac{E_{HCP} - 2E_{HHTP}}{8} = 0.07834\ Hartree = 205.7\ kJ/mol$$

$$E_{eff,SRS} = \frac{E_{SRS} - 4E_{HHTP}}{24} = 0.09239 Hartree = 242.5\ kJ/mol$$

This effective reaction energies themselves are meaningless, but by taking the difference we can determine the relationship between the spiroborate formation in the two systems. The reaction energy of spiroborate reaction in **HCP** is 36.8 kJ/mol lower than that in the **srs** structure. This calculation demonstrates that the formation of the **HCP** structure is thermodynamically more favorable compared to **srs-**COF.

2.6 References

(1) Watson, J. D.; Crick, F. H. C. Molecular Structure of Nucleic Acids: A Structure for Deoxyribose Nucleic Acid. *Nature* **1953**, *171* (4356), 737-738. DOI: 10.1038/171737a0.

(2) Hill, D. J.; Mio, M. J.; Prince, R. B.; Hughes, T. S.; Moore, J. S. A Field Guide to Foldamers. *Chem. Rev.* **2001**, *101* (12), 3893-4012. DOI: 10.1021/cr990120t.

(3) Zhang, D.-W.; Zhao, X.; Hou, J.-L.; Li, Z.-T. Aromatic Amide Foldamers: Structures, Properties, and Functions. *Chem. Rev.* **2012**, *112* (10), 5271-5316. DOI: 10.1021/cr300116k.

(4) Yashima, E.; Ousaka, N.; Taura, D.; Shimomura, K.; Ikai, T.; Maeda, K. Supramolecular Helical Systems: Helical Assemblies of Small Molecules, Foldamers, and Polymers with Chiral Amplification and Their Functions. *Chem. Rev.* **2016**, *116* (22), 13752-13990. DOI: 10.1021/acs.chemrev.6b00354.

(5) Nakano, T.; Okamoto, Y. Synthetic Helical Polymers: Conformation and Function. *Chem. Rev.* **2001**, *101* (12), 4013-4038. DOI: 10.1021/cr0000978.

(6) Yashima, E.; Maeda, K.; Iida, H.; Furusho, Y.; Nagai, K. Helical Polymers: Synthesis, Structures, and Functions. *Chem. Rev.* **2009**, *109* (11), 6102-6211. DOI: 10.1021/cr900162q.

(7) Hu, Y.; Teat, S. J.; Gong, W.; Zhou, Z.; Jin, Y.; Chen, H.; Wu, J.; Cui, Y.; Jiang, T.; Cheng, X.; Zhang, W. Single crystals of mechanically entwined helical covalent polymers. *Nat. Chem.* **2021**, *13* (7), 660-665. DOI: 10.1038/s41557-021-00686-2.

(8) Hu, Y.; Dunlap, N.; Long, H.; Chen, H.; Wayment, L. J.; Ortiz, M.; Jin, Y.; Nijamudheen, A.; Mendoza-Cortes, J. L.; Lee, S.-h.; Zhang, W. Helical Covalent Polymers with Unidirectional Ion Channels as Single Lithium-Ion Conducting Electrolytes. *CCS Chem.* **2021**, *3* (12), 2762-2770. DOI: 10.31635/ccschem.021.202101257.

(9) Ji, Q.; Lirag, R. C.; Miljanić, O. Š. Kinetically controlled phenomena in dynamic combinatorial libraries. *Chem. Soc. Rev.* **2014**, *43* (6), 1873-1884. DOI: 10.1039/C3CS60356C.

(10) Safont-Sempere, M. M.; Fernández, G.; Würthner, F. Self-Sorting Phenomena in Complex Supramolecular Systems. *Chem. Rev.* **2011**, *111* (9), 5784-5814. DOI: 10.1021/cr100357h.

(11) Liu, M.; Zhang, L.; Wang, T. Supramolecular Chirality in Self-Assembled Systems. *Chem. Rev.* **2015**, *115* (15), 7304-7397. DOI: 10.1021/cr500671p.

(12) Hsu, C.-W.; Miljanić, O. Š. Self-sorting through Dynamic Covalent Chemistry. In *Dynamic Covalent Chemistry*, 2017; pp 253-286.

(13) Wang, X.; Bahri, M.; Fu, Z.; Little, M. A.; Liu, L.; Niu, H.; Browning, N. D.; Chong, S. Y.; Chen, L.; Ward, J. W.; Cooper, A. I. A Cubic 3D Covalent Organic Framework with nbo Topology. *J. Am. Chem. Soc.* **2021**, *143* (37), 15011-15016. DOI: 10.1021/jacs.1c08351.

(14) Du, Y.; Yang, H.; Whiteley, J. M.; Wan, S.; Jin, Y.; Lee, S.-H.; Zhang, W. Ionic Covalent Organic Frameworks with Spiroborate Linkage. *Angew. Chem. Int. Ed.* **2016**, *55* (5), 1737-1741. DOI: 10.1002/anie.201509014.

(15) Downard, A.; Nieuwenhuyzen, M.; Seddon, K. R.; van den Berg, J.-A.; Schmidt, M. A.; Vaughan, J. F. S.; Welz-Biermann, U. Structural Features of Lithium Organoborates. *Cryst. Growth Des.* **2002**, *2* (2), 111-119. DOI: 10.1021/cg010035q.

(16) O'Keeffe, M.; Peskov, M. A.; Ramsden, S. J.; Yaghi, O. M. The Reticular Chemistry Structure Resource (RCSR) Database of, and Symbols for, Crystal Nets. *Acc. Chem. Res.* **2008**, *41* (12), 1782-1789. DOI: 10.1021/ar800124u.

(17) Yaghi, O. M.; O'Keeffe, M.; Ockwig, N. W.; Chae, H. K.; Eddaoudi, M.; Kim, J. Reticular synthesis and the design of new materials. *Nature* **2003**, *423* (6941), 705-714. DOI: 10.1038/nature01650.

(18) Kalmutzki, M. J.; Hanikel, N.; Yaghi, O. M. Secondary building units as the turning point in the development of the reticular chemistry of MOFs. *Sci. Adv.* *4* (10), eaat9180. DOI: 10.1126/sciadv.aat9180.

(19) Park, J.; Hinckley, A. C.; Huang, Z.; Chen, G.; Yakovenko, A. A.; Zou, X.; Bao, Z. High Thermopower in a Zn-Based 3D Semiconductive Metal–Organic Framework. *J. Am. Chem. Soc.* **2020**, *142* (49), 20531-20535. DOI: 10.1021/jacs.0c09573.

(20) Liu, Y.; Ma, Y.; Zhao, Y.; Sun, X.; Gándara, F.; Furukawa, H.; Liu, Z.; Zhu, H.; Zhu, C.; Suenaga, K.; Oleynikov, P.; Alshammari, A. S.; Zhang, X.; Terasaki, O.; Yaghi, O. M. Weaving of organic threads into a crystalline covalent organic framework. *Science* **2016**, *351* (6271), 365-369. DOI: 10.1126/science.aad4011.

(21) Yahiaoui, O.; Fitch, A. N.; Hoffmann, F.; Fröba, M.; Thomas, A.; Roeser, J. 3D Anionic Silicate Covalent Organic Framework with srs Topology. *J. Am. Chem. Soc.* **2018**, *140* (16), 5330-5333. DOI: 10.1021/jacs.8b01774.

(22) Han, X.; Yuan, C.; Hou, B.; Liu, L.; Li, H.; Liu, Y.; Cui, Y. Chiral covalent organic frameworks: design, synthesis and property. *Chem. Soc. Rev.* **2020**, *49* (17), 6248-6272. DOI: 10.1039/D0CS00009D.

(23) Krebs, F. C.; Schiødt, N. C.; Batsberg, W.; Bechgaard, K. Purification of 2, 3, 6, 7, 10, 11-Hexamtheoxytriphenylene and Preparation of Hexakiscarbonylmethyl and Hexakiscyanomethyl Derivatives of 2, 3, 6, 7, 10, 11-Hexahydroxytriphenylene. *Synthesis* **1997**, 1285-1290.

(24) O'Keeffe, M.; Peskov, M. A.; Ramsden, S. J.; Yaghi, O. M. The Reticular Chemistry Structure Resource (RCSR) Database of, and Symbols for, Crystal Nets. *Acc. Chem. Res.* **2008**, *41* (12), 1782-1789. DOI: 10.1021/ar800124u.

(25) Park, J.; Hinckley, A. C.; Huang, Z.; Chen, G.; Yakovenko, A. A.; Zou, X.; Bao, Z. High Thermopower in a Zn-Based 3D Semiconductive Metal–Organic Framework. *J. Am. Chem. Soc.* **2020**, *142* (49), 20531-20535. DOI: 10.1021/jacs.0c09573.

(26) Hu, Y.; Teat, S. J.; Gong, W.; Zhou, Z.; Jin, Y.; Chen, H.; Wu, J.; Cui, Y.; Jiang, T.; Cheng, X.; Zhang, W. Single crystals of mechanically entwined helical covalent polymers. *Nat. Chem.* **2021**, *13* (7), 660-665. DOI: 10.1038/s41557-021-00686-2.

Chapter 3: Dynamic Entwined Topology in Helical Covalent Polymer Dictated by Competing Supramolecular Interactions

3.1 Abstract

Naturally occurring polymeric structures often consist of 1D polymer chains intricately folded and entwined through non-covalent bonds, adopting precise topologies crucial for their functionality. The exploration of crystalline 1D polymers through dynamic covalent chemistry (DCvC) and supramolecular interactions represents a novel approach for developing crystalline polymers. This study shows that sub-angstrom differences in the counter-ion size can lead to various helical covalent polymer (HCP) topologies, including a novel metal-coordination HCP (m-HCP) motif. Single crystal X-ray diffraction (SCXRD) analysis of HCP-Na revealed double helical pairs are formed by sodium-ions coordinating to spiroborate linkages to form rectangular pores. The double helices are interpenetrated by the unreacted diols coordinating sodium-ions. The reticulation of the m-HCP structure was demonstrated by the successful synthesis of HCP-K. Finally, ion-exchange studies were conducted to show the interconversion between HCP structures. This research illustrates how seemingly simple modifications, such as changes in counter-ion size, can significantly influence the polymer topology and determine which supramolecular interactions dominate the crystal lattice.

3.2 Introduction

Natural polymeric structures, such as those found in DNA or collagen, typically incorporate both covalent and non-covalent bonds. The covalent bonds serve as the polymer's backbone, providing stability, while hydrogen bonding intertwines the polymer strands, forming helical structures.[1,2] There have been great strides in developing small molecule, oligomer, and polymeric helical structures.[1-5] Yet, it is rare to obtain single crystals that enable detailed analysis of the structure to clearly elucidate the structure-function properties.[6-8] Dynamic covalent chemistry (DCvC) has been utilized to design and synthesize crystalline polymers in a bottom-up approach using the principles of reticulation.[9-16] The dynamic nature of the bonds enables error correction as a thermodynamic control to favor the formation of structures that represent thermodynamic minimums. There is great interest in further understanding the factors that lead to certain structures being more thermodynamically favorable and the equilibrium between polymetric phases.[17-22] Additionally, it has been demonstrated that minor changes to the structure, such as larger counter-ions or the introduction of steric interactions, can change the interpenetration, stacking between layers, and topology.[23-27] Elucidating the crystal structures of the polymers through single-crystal XRD (SCXRD) or electron diffraction techniques enabled the detailed analysis of polymeric structures at the atomic level.[8,18, 22, 28-36] This provides a deeper understanding of the synergistic interplay between DCvC and supramolecular chemistry. Synthesizing samples suitable for these techniques is rare, and only a few comprise 1D polymer chains.[8, 17, 33, 37-40]

The high conformational freedom of 1D polymers makes organizing the strands within 3D space challenging, so most 1D polymers are amorphous or semi-crystalline. Introducing weaker non-covalent interaction enables a thermodynamic driving force to further organize the polymer strands. The synergistic relationship between DCvC and supramolecular chemistry has yet to be broadly adopted due to the difficulty in predicting the structure. Thus far, metal-coordination, hydrogen bonding, and π- stacking have been used to construct both expected and unexpected architectures. However, little is known about the effect of multiple competing supramolecular interactions on the polymer topology. Previously, we reported the helical covalent polymer (HCP-Li) as a 1D polymer that adopts a double helical structure where the double helices are mechanically entwined by hydrogen bonding interactions of adjacent double helices.[8] The lithium counter-ions were observed inside the channels of the double helices without any coordinating interaction and were not part of the structure's backbone. Although this is an intriguing discovery, some important questions remain unanswered about the HCP polymers, such as will larger counter-ions adopt the same hydrogen bonding topology, participate in coordination with polymer strands, or demonstrate orthogonality with supramolecular chemistry? Additionally, small molecule double helices can exhibit a spring like motion when the counter-ion is exchanged.[41, 42] This begs the question, can the HCPs exhibit dynamic modes of entwinement based on counter-ion exchange?

Herein, novel metal-coordinated helical covalent polymers (m-HCP) are reported. SCXRD unambiguously confirms the structure of HCP-Na, which shows the counterions are incorporated into the polymer's backbone by physically entwining double helices. The polymer strands adopt novel rectangular pores because the spiroborate linkages coordinate to the sodium-ions, and the resulting helical structure forms two types of ion channels. Additionally, adjacent pairs are interpenetrated and held together through metal-coordination between the unreacted diols and the counter-ions. The crystal structure shows no strong hydrogen bonding interaction contributing to the organization of the 1D polymers. The reticulation of the m-HCP topology is established by demonstrating that HCP-K adopts the same topology. This also demonstrates a new mode of reticulation by incorporating the counter-ion into the backbone of the polymer. Furthermore, ion exchange experiments were used to investigate the dynamic nature of the different entwining modes and establish a novel pathway for synthesizing HCPs. The hydrogen bonded HCP structure can be converted to the m-HCPs. Interestingly, the m-HCPs cannot be converted back to the hydrogen bonded HCP under the same conditions.

3.3 Results and Discussion

HCP-Na synthesis involves reacting 2,3,6,7,10,11-hexahydroxytriphenylene (HHTP), trimethyl borate, and sodium hydroxide in 1.8 mL of a 1:1 aqueous acetonitrile/mesitylene mixture (Figure 3.1a). Single crystals of HCP-Na were obtained by stirring the reaction in a sealed ampule under vacuum at 80 °C for 12 hours. Subsequently, the reaction was heated at 120 °C for 30 days. The formation of HCP-Na follows an intermediate srs-phase, as previously reported (Figure 3.5).[20] Notably, the srs-phase persists more when using alternative solvent systems, such as 1:2 acetonitrile/mesitylene or boric acid as the boron source (Table 3.1). This persistence is attributed to the difference in the reaction kinetics and the availability of HHTP in solution. Previous work demonstrated that the spiroborate bond will not undergo metathesis with sodium as the counter-ion. So, HHTP or the unreacted diols likely trigger the bond exchange.[43] Adding additional water to facilitate the solvation of sodium hydroxide, increasing the ratio of non-polar solvents, or changing the initial boron species all affect the amount of HHTP present in the solution to participate in the exchange. The conditions screened for forming HCP-Na are summarized in Table 3.1.

The HCP-Na single crystals exhibit a rectangular bipyramid shape, as revealed by SEM and optical microscope analyses, with an average length ranging from 20 to 30 μm (Figure 3.1b). The largest crystals reach up to 50 μm (Figure 3.1b). The FT-IR spectrum of HCP-Na shows the presence of the B-O stretch at 1043 cm^{-1} and a reduction in the intensity of the hydroxyl peak (Figure 3.6). The solid-state carbon NMR spectrum displays signal splitting, attributed to the dissymmetry of the monomer due to the unreacted diols (Figure 3.1c). The solid-state boron NMR

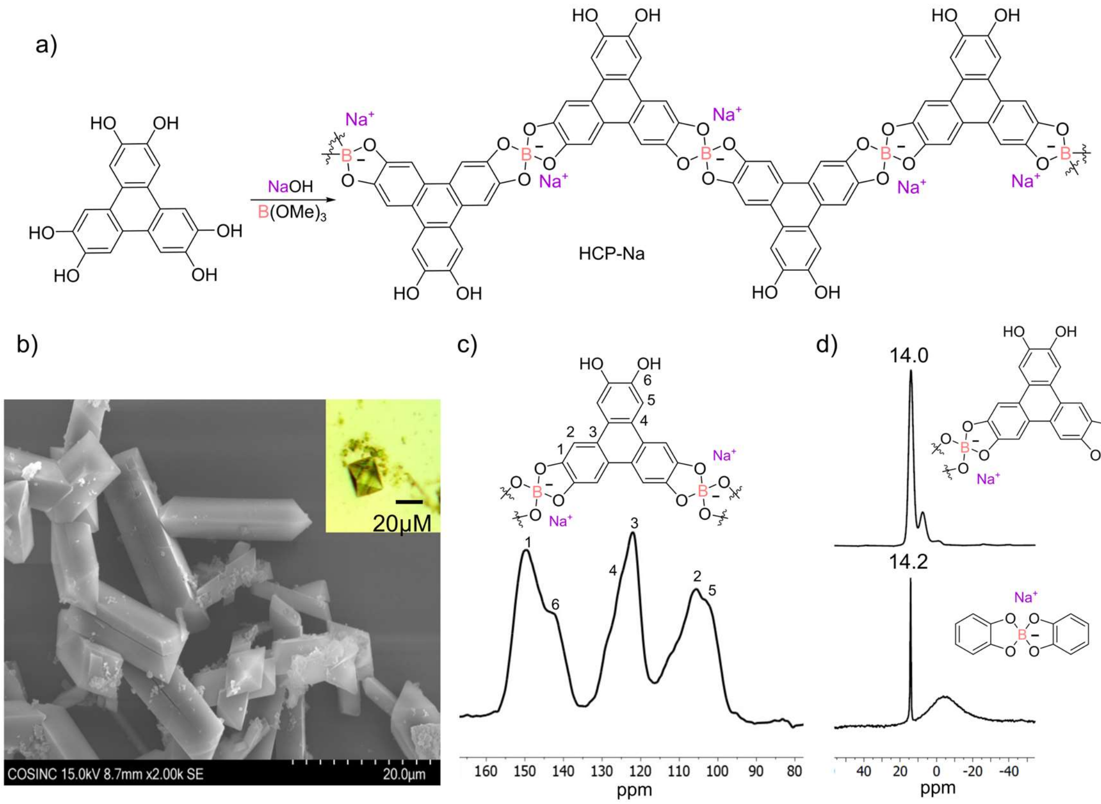

Figure 3.1. Synthesis and chemical characterization of HCP-Na. (a) Synthetic Scheme of HCP-Na. (b) SEM of average-sized single crystals from HCP-Na. Insert: Optical image of the largest single crystals that were observed. (c) Solid-state ^{13}C spectrum of HCP-Na. The non-equivalent aryl carbons are labeled 1-6. (d) The solid-state ^{11}B spectrum of HCP-Na and compound 1.

spectrum reveals a prominent signal at 14.0 ppm, aligning well with compound **1** (Figure 3.1d) and consistent with previous literature reports.[8, 44]

The structure of HCP-Na was elucidated by SCXRD using a synchrotron light source with a discrepancy factor R of 7.36 %, which enables a detailed evaluation of the structure. The unit cell of HCP-Na is orthorhombic with a space group of I222 and dimensions of a= 15.2478 Å, b= 17.8361 Å, and c= 17.8380 Å. The HHTP and spiroborate linkages form helical 1D polymers entwined by sodium-ions. Every other spiroborate along the 1D strands are linked through a sodium-ion and extends the helical pitch of the 1D polymer strands to 31.61 Å (Figure 3.2a). The

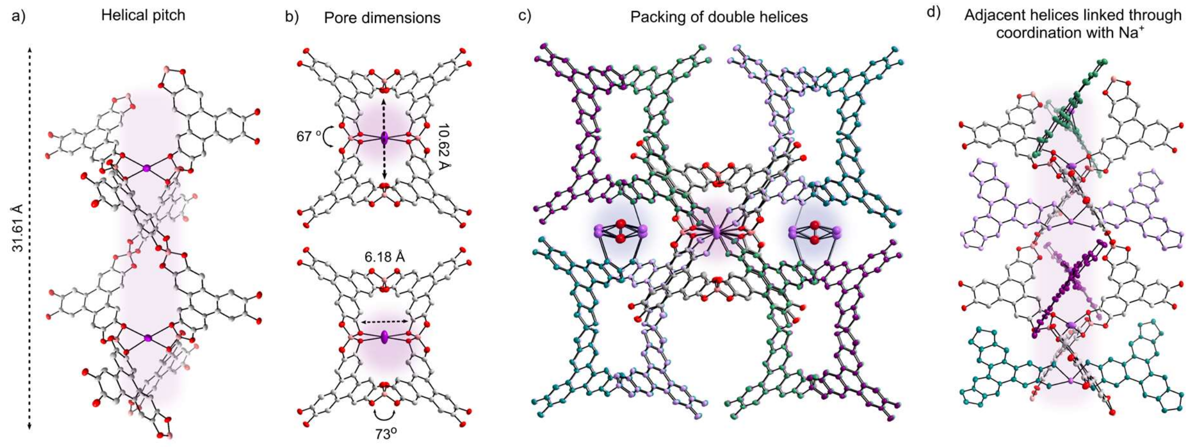

Figure 3.2. Single crystal structure of HCP-Na. The physical dimensions of HCP-Na helices are where the channels are highlighted in purple and blue to indicate if they are within the double helices or adjacent, respectively. (a) The helical pitch of entwined 1D polymer strands with coordinated sodium-ions. (b) Top-down view of the rectangular pores of the double helices where the pore dimension is 6.18 Å by 10.62 Å when measuring boron to boron. Top-down view (c) and side view (d) of the double helices packed together. A second sodium-ion channel exists between adjacent helices. There is some disorder in the position of the ion. (d) The adjacent double helices pairs are linked through the unreacted diols coordinating sodium-ions. Solvent molecules were removed for better clarity of the structure.

double helices adopt rectangular pores to accommodate the bridging sodium-ions inside the channels. The rectangular pore dimensions are 10.62 Å by 6.18 Å, and the spiroborate groups display alternating dihedral angles of 67° and 73° (Figure 3.2b).

Adjacent double helices are inserted into and held together by coordinating the sodium-ions (Figure 3.2c and d). The rectangular pores also enable the formation of two unique channels, highlighted as purple and blue in Figure 3.2c. The channel adjacent to the double helices (blue) shows coordination of sodium-ions and displays some disorder. In contrast, there is little disorder of the sodium-ion in the double helix channel (purple). Adjacent polymer strands are interpenetrated and held together through the coordination of the sodium-ion through unreacted diols (Figure 3.2d). The crystal structure contained no evidence of any strong hydrogen bonding interactions with the unreacted diols. There was uncertainty in the position of the hydrogen on the unreacted diol, which suggests that they don't strongly contribute to the overall structure as previously observed.[8] The minimal distance between the oxygen of the spiroborate and unreacted diol spans 2.94 Å. If the hydrogen bond angle was 180° then the hydrogen bonding interaction would be moderate to weak. This change is due to the distortion of the polymer strands to accommodate the coordination of the sodium-ions.

Theoretically, the ion channels of the hydrogen bonded HCP are large enough to accommodate the sodium and potassium-ions without metal coordination. Thus, the phase purity of the bulk HCP-Na was evaluated by comparing the bulk experimental PXRD pattern to the simulated diffraction pattern (Figure 3.3a). A simulation of the HCP-Na PXRD pattern was created from the single crystal data and matches well with the experimental pattern. There are some differences in the signal intensities that can be attributed to the difference in temperature during collection or some disorder of solvent molecules within the channels rather than mixed phases. Next, reticulation of this new mode of entwinement was evaluated by switching the counter-cations from sodium-ions to potassium-ions.

We posited that the alteration in the entwinement mode between the strands (HCP-Li vs. HCP-Na) was influenced by the larger counter-ion size. The m-HCP topology adds significance since it offers a secondary method of reticulation, distinct from merely modifying the organic building blocks, as the counter-ion is incorporated into the backbone of the structure. To assess the reticulation of this new entwinement mode, potassium-ions were employed. HCP-K can be synthesized by utilizing similar methods, such as directly or utilizing phenol as a modulator (Figure 3.3b). SEM analysis showed that the crystals are not a single domain as indicated by uneven surface (Figure 3.8). FT-IR also confirms the formation of the spiroborate linkage with the appearance of the B-O stretch at 1036 cm^{-1} and a reduction of the hydroxyl peak (Figure 3.7). The

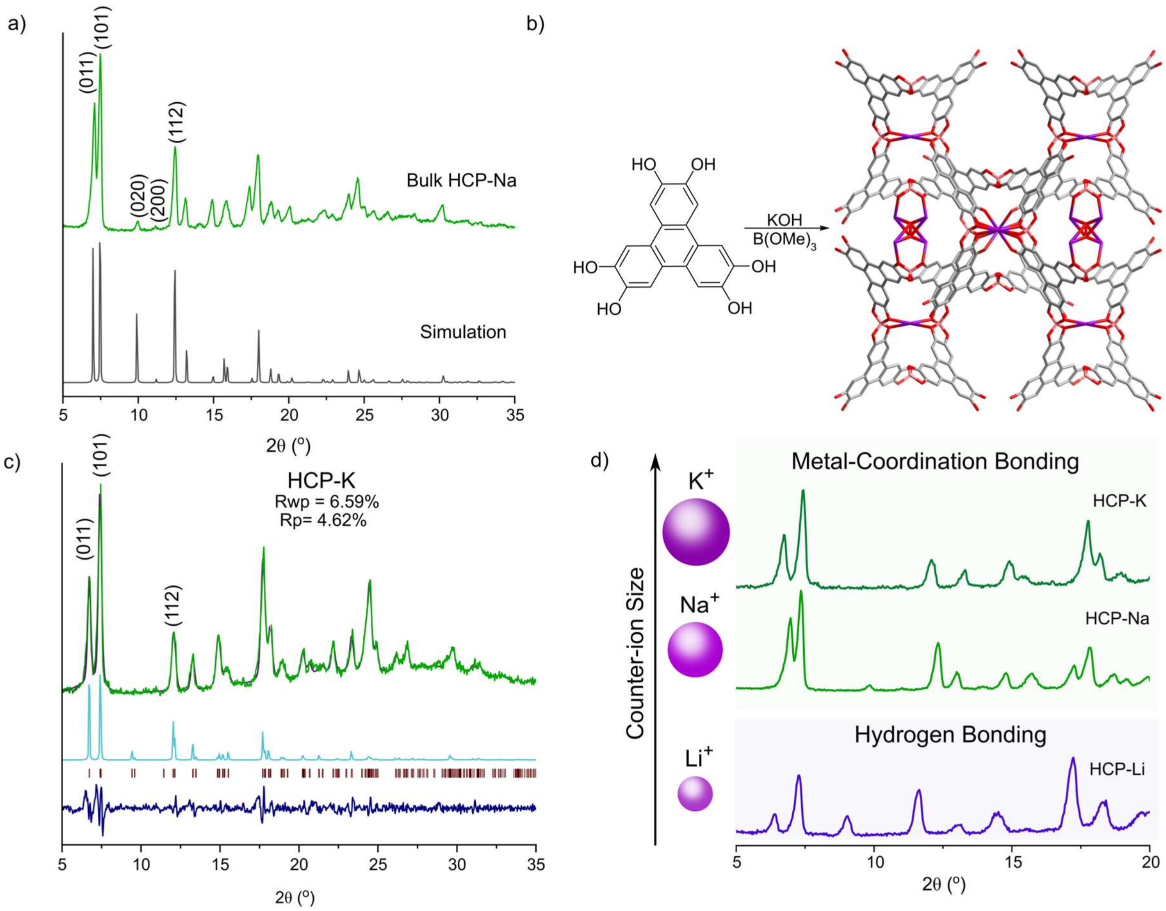

Figure 3.3. Bulk synthesis of HCP-Na and HCP-K. (a) Bulk HCP-Na compared to the simulation where the first five miller planes are identified. (b) the synthesis of HCP-K that forms the m-HCP topology. (c) Pawly refinement of HCP-K. Green is the experiment data; black is the refined pattern; light blue is the simulation; purple dashed represents the miller plane locations; and dark blue is the difference between the experimental and theoretical diffraction patterns. (d) A comparison of the diffraction patterns of HCP-Li, HCP-Na, and HCP-K. HCP-Li adopts hydrogen bonded HCP, while HCP-Na and HCP-K adopts the new m-HCP topology.

solid-state carbon NMR shows splitting of the aryl carbon signals due to the unreacted diols (Figure 3.10). Solid state boron NMR shows the spiroborate signal at 13.9 ppm and matches well with compound **2** (Figure 3.10).

The experimental diffraction pattern of HCP-K matches well with the new m-HCP topology. A model was built based on the HCP-Na crystal structure in Materials Studio. The solvent was removed to simplify the model, and the second ion channel was retained in the model. The unit cell dimensions were found to be a = 15.4737 Å, b = 18.4251 Å, and c = 18.7580 Å with a space group of I222 through Pawley refinement (RWP = 6.59 % and RP = 4.62 %) (Figure 3.3c). By comparing the crystal structures and the PXRD patterns, there is a contraction in the unit cell size when the m-HCP topology is adopted compared to the hydrogen bonding topology, particularly in the b and c dimensions of the unit cell. When the counter-ion is changed from sodium to potassium, then the unit cell is expanded in the b and c dimensions while there is a slight contraction in the a dimension. Sodium and potassium-ions generally require more coordinating groups. Likely, metal-coordination becomes more favorable when the counter-ion becomes larger due an increase in electrostatic attraction as the distance between larger counter-ions and spiroborate groups decreases.

This expansion and contraction of the crystal structure can be envisioned to mimic a spring structure. To evaluate the HCPs in this capacity, they were subjected to ion exchange studies to test crystal to crystal transformation (Figure 3.4). The flexibility of the spiroborate linkages and the demonstrated ion conductivity of HCP-Li[45] enables the transformation of HCP to the new m-HCPs. An isolated polycrystalline sample of HCP-Li was treated with 1 eq of sodium tert-butoxide in acetonitrile.

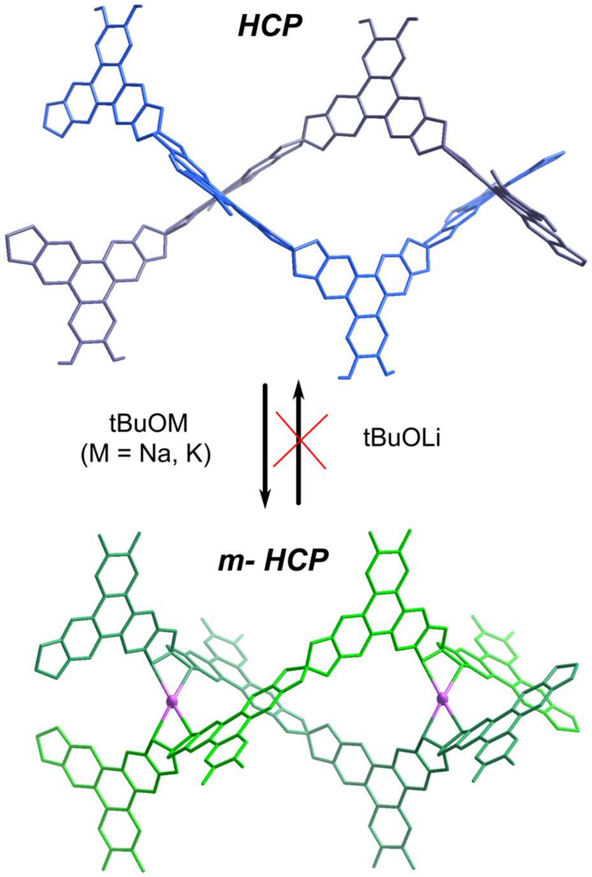

Figure 3.4. Scheme of ion exchange studies. HCP samples were suspended in tert-butoxide salts dissolved in acetonitrile and left to exchange at room temperature.

PXRD showed the conversion of HCP-Li to HCP-Na within 24 hours (Figure 3.11). When the sample was treated with 1 eq of lithium tert-butoxide in acetonitrile there was no conversion back to HCP-Li after 24h, and the sample showed a degradation in crystallinity after the second treatment (Figure 3.11). HCP-K can also be formed though ion exchange when HCP-Li is treated with potassium tert-butoxide (Figure 3.12). These ion exchange studies show that the HCP structures can be interconverted and considered an alternative method to synthesize new HCPs.

3.4 Conclusions

In conclusion, this work introduces a novel m-HCP topology that provides a unique approach to tuning HCP topologies through variations in counter-ion size and competing supramolecular interactions. A comprehensive single crystal analysis of HCP-Na offers a detailed insight into the m-HCP topology. The synthesis of HCP-K establishes the reticulation of m-HCP. This topology incorporates the counter-ion into the backbone of the polymeric structure. Thus, offering a novel alternative method to tune the dimensions of the crystal structure. Ion-exchange studies enable interconversion of HCP structures and unveil an alternative synthetic pathway for constructing HCP structures. This research significantly contributes to a deeper understanding of the interplay between DCvC and supramolecular chemistry, paving the way for the precise design of materials at the atomic level. As this field expands, polymers with more sophisticated structure motifs will become synthetically attenable for advanced functionality.

3.5 Experimental section

3.5.1. Materials and Methods

The chemicals used in this study were purchased and used without further purification from Aldrich Chemical Company, TCL, or Oakwood Chemicals. 2,3,6,7,10,11-hexahydroxytriphenylene (HHTP) was prepared according to the previously reported procedure.[46]

Nuclear Magnetic Resonance (NMR) spectra were acquired using Bruker 300, Inova 400, or Inova 500 spectrometers. For ^{1}H NMR, deuterated dimethyl sulfoxide (DMSO-d6) at 2.50 ppm and deuterated chloroform ($CDCl_3$) at 7.26 ppm served as internal references. The presentation of ^{1}H NMR data includes the chemical shift, multiplicity (s for singlet, br s for broad singlet, d for doublet, t for triplet), the number of protons, and proton assignments. Deuterated solvents were procured from Cambridge Isotope Laboratories (Andover, MA) and were utilized as received.

Solid-state Cross Polarization Magic Angle Spinning (CP/MAS) NMR spectra were recorded on an Inova 400 NMR spectrometer. ^{11}B MAS NMR was referenced to boron trifluoride etherate.

Agilent Technology Cary 630 FT-IR spectrometer was used to collect the Fourier-transformed infrared (FT-IR) spectra. A JSM-640LV (LVSEM) was utilized to collect scanning electron microscopy (SEM) images at 30 kV. The Powder XRD data was collected on a Bruker D8 Advance A25 system with a monochromated Cu Kα radiation source. The sample was measured under ambient conditions, and the X-ray source was operated at 40 kV and 40 mA. Thermogravimetric analysis (TGA) was performed using a thermogravimetric/differential thermal analyzer.

Single crystal XRD data was collected at the Advance Light Source (ALS) beamline 12.2.1 located at the Lawrence Berkely National Laboratory.

3.5.2 Experimental Procedures

3.5.2.1. General procedure for making model spiroborate compounds:

A round bottom flask was charged with boric acid (140.4 mg, 2.27 mmol, 1 eq), catechol (500.0 mg, 4.54 mmol, 1 eq), and the respective hydroxide salt (90.8 mg of NaOH or 127.4 mg of KOH, 2.27 mmol, 1 eq). Then 10 mL of DMF was added. The reaction was stirred at 80 °C for

16 hours. After cooling to room temperature, the solution was concentrated to approximately half of the original volume under vacuum. Then, the solution was slowly added to diethyl ether (100 mL) to precipitate the product. The product was then isolated by vacuum filtration and washed with ether. Residual DMF was removed by heating the solid in a 150 °C oven.

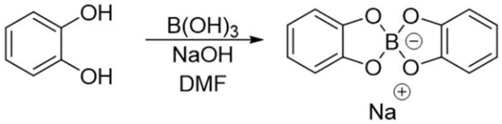

Compound **1.** Yield: 526.7 mg (93%); ^{1}H-NMR (300 MHz, DMSO-d_6): δ 6.47 (s, 8H, Ar-H); ^{13}C NMR (75 MHz, DMSO-d_6): δ 151.56, 117.29, 107.61; ^{11}B NMR (96 MHz, DMSO-d_6): δ 14.22; HRMS (ESI): Calcd for C12H8BO4 [DPSB]$^-$227.0518; Found, 227.0512.

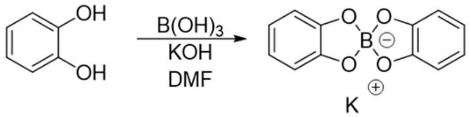

Compound **2.** Yield: 538.6 mg (89%); ^{1}H-NMR (300 MHz, DMSO-d_6): δ 6.47 (s, 8H, Ar-H); ^{13}C NMR (75 MHz, DMSO-d_6): δ 151.55, 117.30, 107.61; ^{11}B NMR (96 MHz, DMSO-d_6): δ 14.21; HRMS (ESI): Calcd for C12H8BO4 [DPSB]$^-$227.0518; Found, 227.0512.

3.5.2.2 Synthesis of Spiroborate Polymers

General procedure for the synthesis of spiroborate polymers:

HHTP (32.4 mg, 0.10 mmol, 1.0 eq), the boron reagent (17 µL of trimethyl borate or 9.3 mg of boric acid, 0.15 mmol, 1.5 eq), and the corresponding hydroxide salt (6.0 mg of NaOH or 8.4 mg of KOH, 0.15 mmol, 1.5 eq) were added to a 5 mL ampule. The hydroxide salts were freshly ground before use. The salts are hygroscopic, so the exact water percentage that gave the best crystallinity varied slightly, but typically 0.45 vol% gave the best result. Then, the solvent and a stir bar were added, and the resulting suspension was sonicated for 30 minutes. Next, the ampules were cooled in a liquid nitrogen bath and sealed under vacuum at 150 mTorr. The reaction was stirred at 80 °C for 12 h before being transferred to a 120 °C oven. Single crystals can be obtained after 30 days in the oven. Tables S1 and S2 summarize the conditions screened and the results for synthesizing the HCP-Na and HCP-K, respectively.

Table 3.1. The condition was screened for forming sodium-based spiroborate polymers.

Trial	Solvent	120 °C Oven time	Boron Source	Modulator	Result
1	1:1 Acetonitrile: Mesitylene	30 days	$B(OMe)_3$	--	HCP-Na Single Crystals
2	1:1 Acetonitrile: Mesitylene	30 days	$B(OH)_3$	--	srs phase
3	1:1 Acetonitrile: Mesitylene	30 days	$B(OH)_3$	50 mol% Phenol	HCP-Na
4	1:1 Acetonitrile: Mesitylene	7 days	$B(OMe)_3$	10 mol% Phenol	HCP-Na
5	1:1 Acetonitrile: Mesitylene	7 days	$B(OMe)_3$		HCP-Na Generally, lower-quality, or mixed phases
6	1:2 Acetonitrile: Mesitylene	7 days	$B(OMe)_3$		Generally, mixed phases

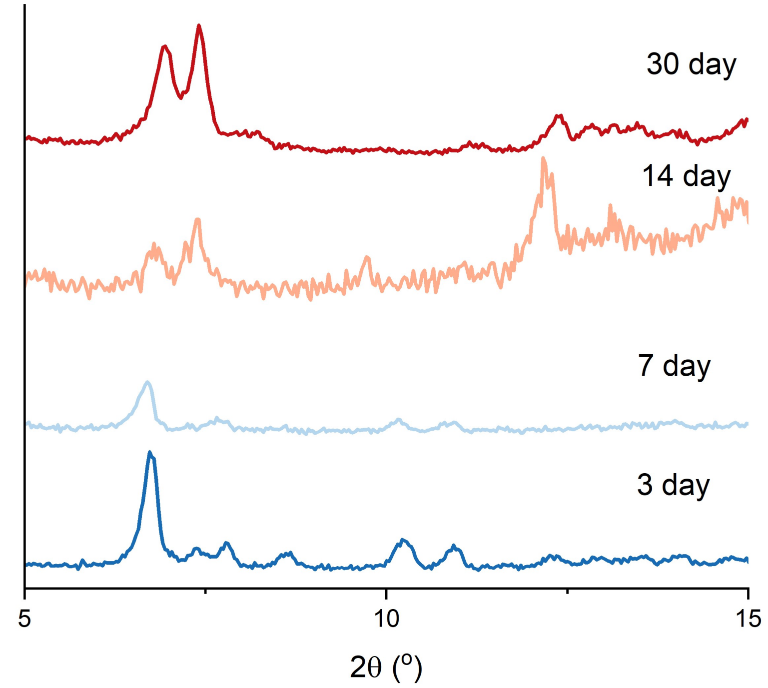

Figure 3.5. (a) Transformation of srs phase to HCP-Na phase over time using condition 1 in Table S1 at different time points. After 3 and 7 days in the 120 °C oven, srs is the major phase. Meanwhile, the HCP phase becomes apparent after 14 days. This equilibrium between the two phases will be shifted slightly when the % water included in the reaction is shifted.

Table 3.2. Best conditions for forming potassium-based spiroborate polymers.

Trial	Solvent	120 °C Oven time	Boron Source	Modulator	Result
1	1:1 Acetonitrile: Mesitylene	30 days	$B(OMe)_3$	--	HCP-K
2	1:1 Acetonitrile: Mesitylene	7 days	$B(OMe)_3$	10 mol% Phenol	HCP-K
3	1:1 Acetonitrile: Mesitylene	7 days	$B(OMe)_3$		Mixed phases

3.5.3. FT-IR of mHCPs

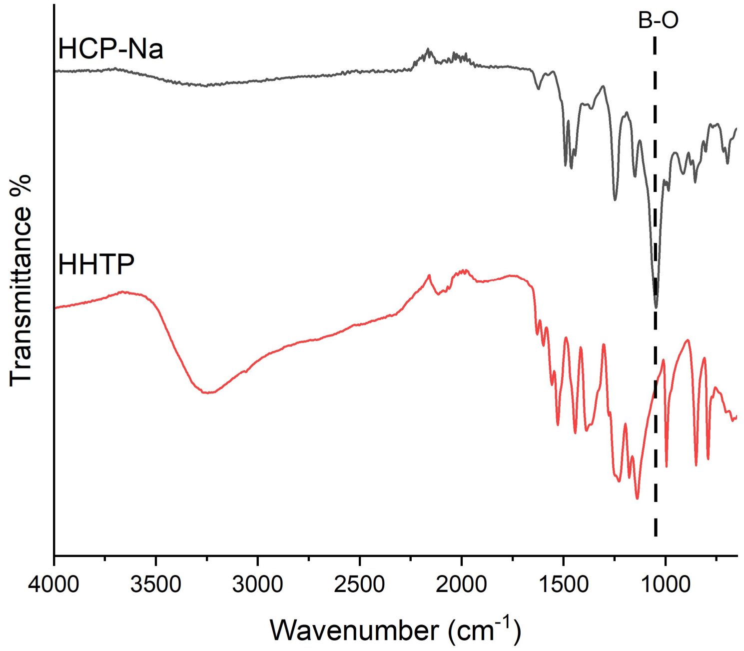

Figure 3.6. FT-IR of HCP-Na and HHTP.

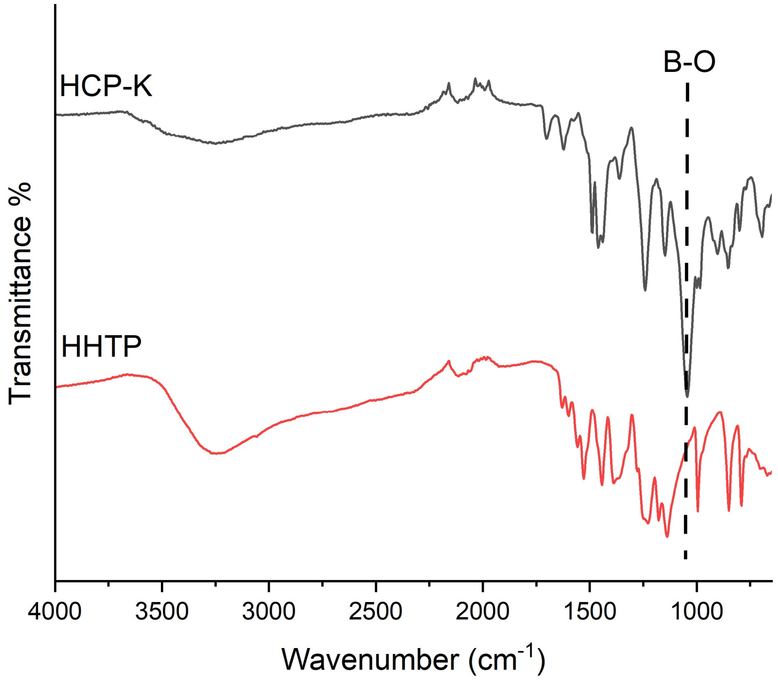

Figure S3.7. FT-IR of HCP-K and HHTP

3.5.4. Single-crystal XRD

Table 3.3. Summary of crystal data and structure refinement of HCP-Na.[47-52]

Identification Code	2328716 (CCDC)
Empirical Formula	$C_{81.60} H_{48.40} B_4 N_{4.80} Na_4 O_{27}$
Chemical Formula	1663.25
Temperature (K)	100
Wavelength (Å)	0.72880
Crystal System	Orthorhombic
Space Group	I222
Unit Cell Dimensions	a= 15.8037(14) Å, b= 17.8361(16) Å, c= 17.8380(16) Å α= 90 °, β= 90 °, γ= 90°
Volume (Å^3), Z	5028.1(8), 2
Density (mg/m^3)	1.099
Adsorption coefficient (mm^{-1})	0.101
(000)	1703
Crystal Size (mm)	0.05 x 0.04 x 0.03
Theta range for data collection	2.342 to 22.595 deg.
Limiting indices	$-16 \le h \le 16$, $-18 \le k \le 18$, $-18 \le l \le 18$
Reflections collected / unique	28852/ 3105
R_{int}	0.0600
Completeness to theta	22.595, 99.8%
Refinement method	Full-matrix least-squares on F^2
Data/restraints/parameters	3105/12/279
Goodness-of-fit on F^2	1.01
Final R indices [I>2sigma(I)]	R_1= 0.0736, wR_2= 0.1886
R indices (all data)	R_1= 0.0763, wR_2= 0.1923
Absolute structure parameter	-0.1(2)
Largest diff. peak and hole (e.A^{-3})	1.092 and -0.435

3.5.5. SEM of HCP-K

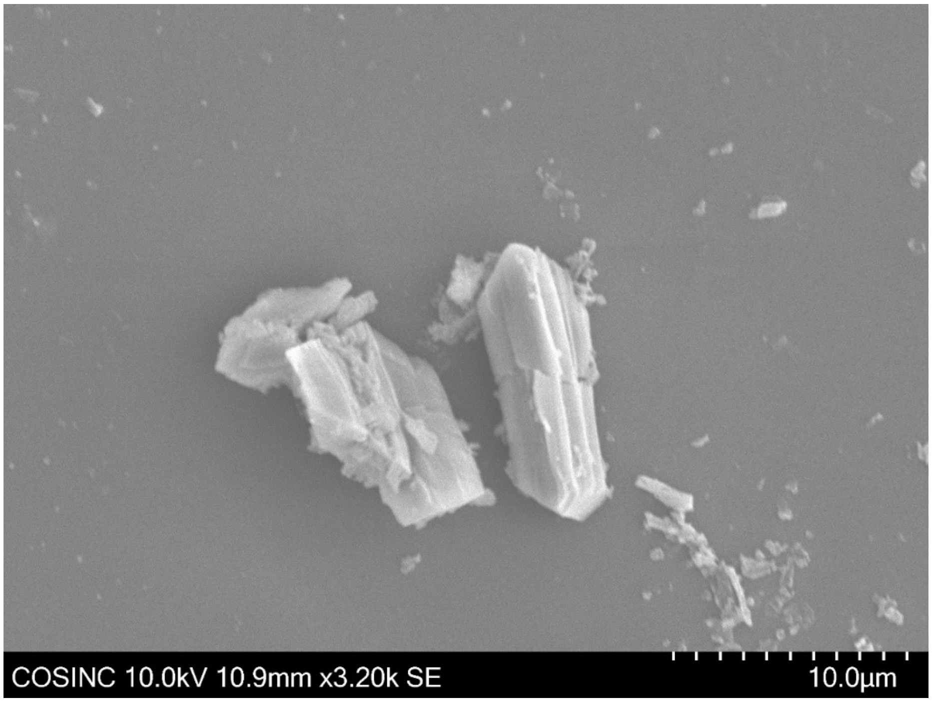

Figure 3.8. SEM image of crystals for HCP-K.

3.5.6. Solid-state NMR spectra of HCP-K

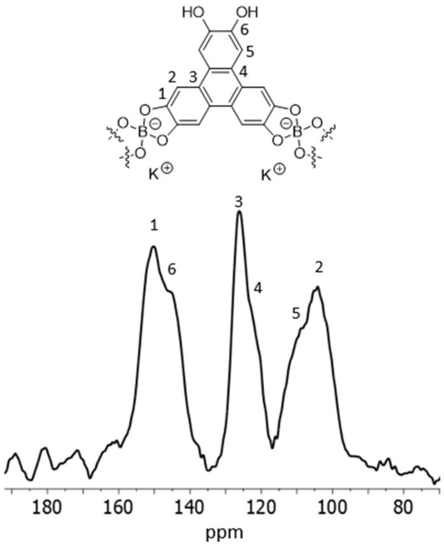

Figure 3.9. ^{13}C ssNMR of HCP-K.

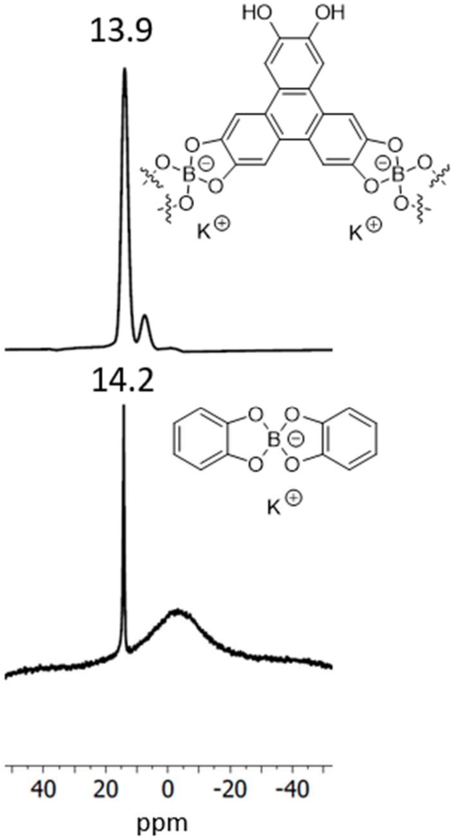

Figure 3.10. ^{11}B ssNMR of HCP-K (top) and ^{11}B solution NMR of **2** (bottom).

3.5.7. Atom Coordinates of HCP-K

Table 3.4. Atom Coordinates of HCP-K.

HCP-K

Space Group= I222
a = 15.4737 Å, b = 18.4251 Å, and c = 18.7580 Å
α= β=γ= 90 °

Atom	X	Y	Z
K	-0.0291	0.3864	0.0126
C	0.3457	0.124	0.1337
O	0.3865	0.0583	0.1115
C	0.27	0.14	0.0971
O	0.2398	0.0912	0.0448
C	0.2258	0.2048	0.1176
H	0.17412	0.2164	0.09291
C	0.2565	0.2541	0.1747
C	0.2108	0.3211	0.1968
C	0.1353	0.3414	0.1585
H	0.11442	0.31222	0.11806
C	0.0942	0.404	0.1818
O	0.0193	0.4339	0.1558
C	0.1247	0.4494	0.2392
O	0.0753	0.5103	0.2508
C	0.1989	0.4302	0.2762
H	0.22074	0.46196	0.31429
C	0.2411	0.3644	0.2573
C	0.3142	0.3395	0.3013
C	0.3329	0.3753	0.3686
H	0.30004	0.41646	0.38567
C	0.4	0.3493	0.4094
O	0.4262	0.3742	0.4797
C	0.451	0.2914	0.3841
O	0.5156	0.2781	0.4332
C	0.4315	0.2543	0.3191
H	0.46515	0.2132	0.303
C	0.3621	0.277	0.2768
C	0.3325	0.2333	0.2128
C	0.376	0.1699	0.1884
H	0.42896	0.15826	0.21081
K	0.3478	0	0
K	0.5	0.5	0.5
O	0	0.5	-0.0381
B	0	0.5	0.2022
B	0.5	0.3269	0.5

3.5.8. Ion Exchange Studies

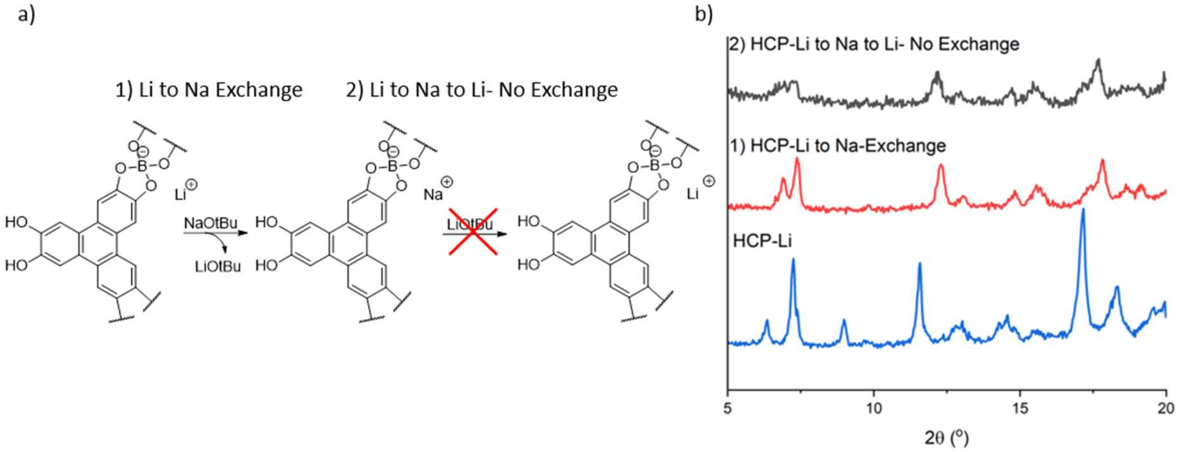

Figure 3.11. Sequence of ion exchange experiment. (a) First, HCP-Li (1 mmol) was transformed to HCP-Na by utilizing 1 eq of NaOtBu in 1 mL acetonitrile. The sample was isolated and washed with acetonitrile, methanol, and acetone. Then, the HCP-Li to Na- Exchange sample was subjected to 1 eq LiOtBu in 1 mL acetonitrile. (b) PXRD of the HCP-Li (blue), the crystallinity after being treated with NaOtBu (red), and the diffraction pattern after being treated with LiOtBu.

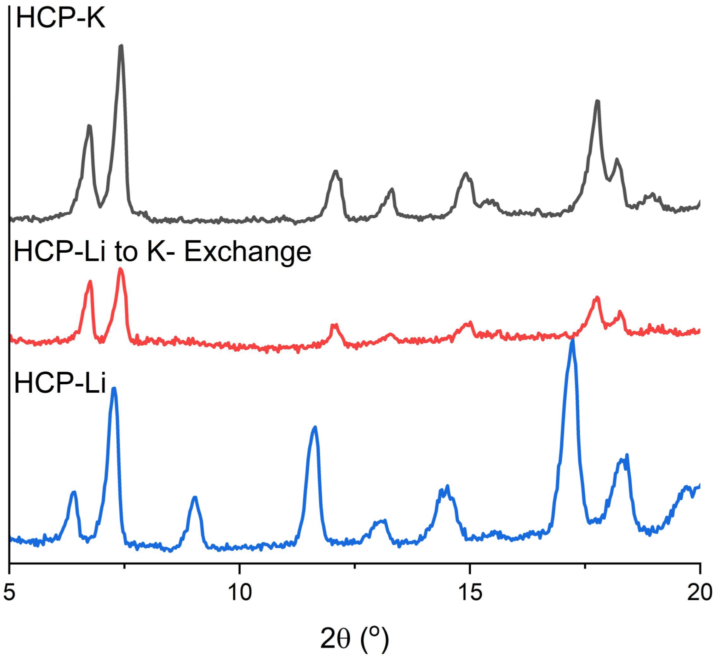

Figure 3.12. The ion exchange experiment of HCP-Li to HCP-K was conducted using 1 eq of KOtBu in 1 mL of acetonitrile. After 24 hours, the solid was isolated and washed with acetonitrile, methanol, and acetone.

3.5.9. Solvent Stability

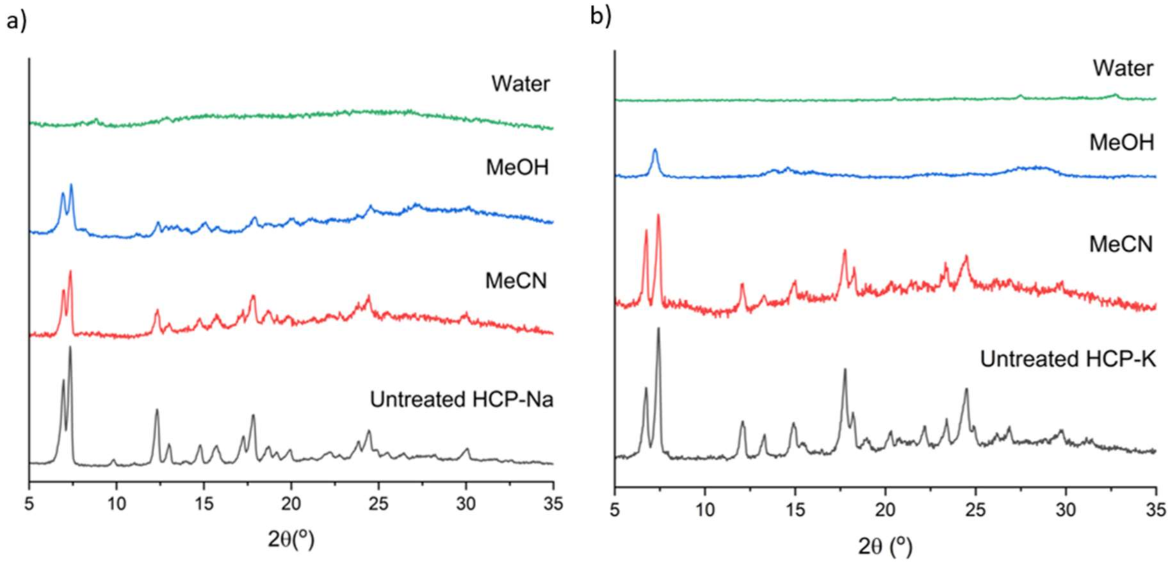

Figure 3.13. Stability of HCP-Na and HCP-K in acetonitrile (MeCN), methanol (MeOH), and water. These samples were soaked in the representative solvents for 24 hours, filtered, and dried under a high vacuum.

3.5.10. Thermogravimetric analysis of HCP-Na and HCP-K

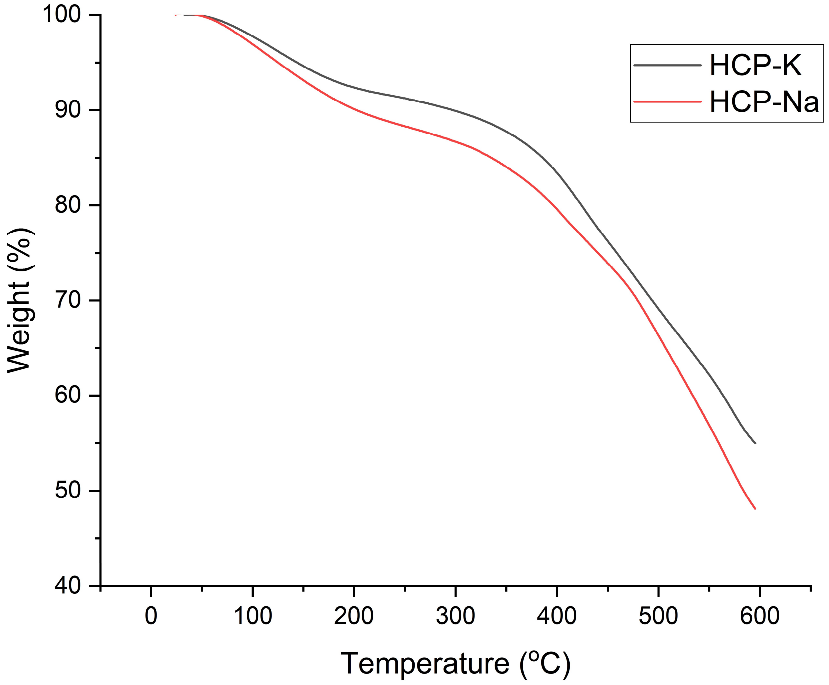

Figure 3.14. Thermogravimetric analysis of HCP-Na (red) and HCP-K (black).

3.5.11. NMR spectra of model compounds

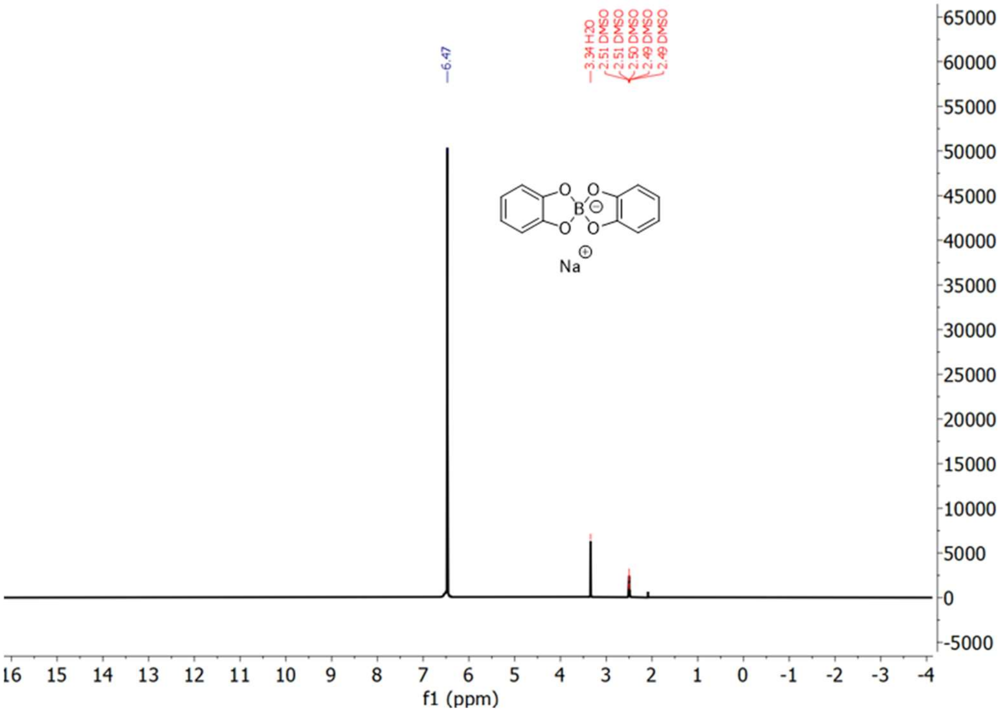

Figure 3.15. ^{1}H NMR of **1** in DMSO-d6.

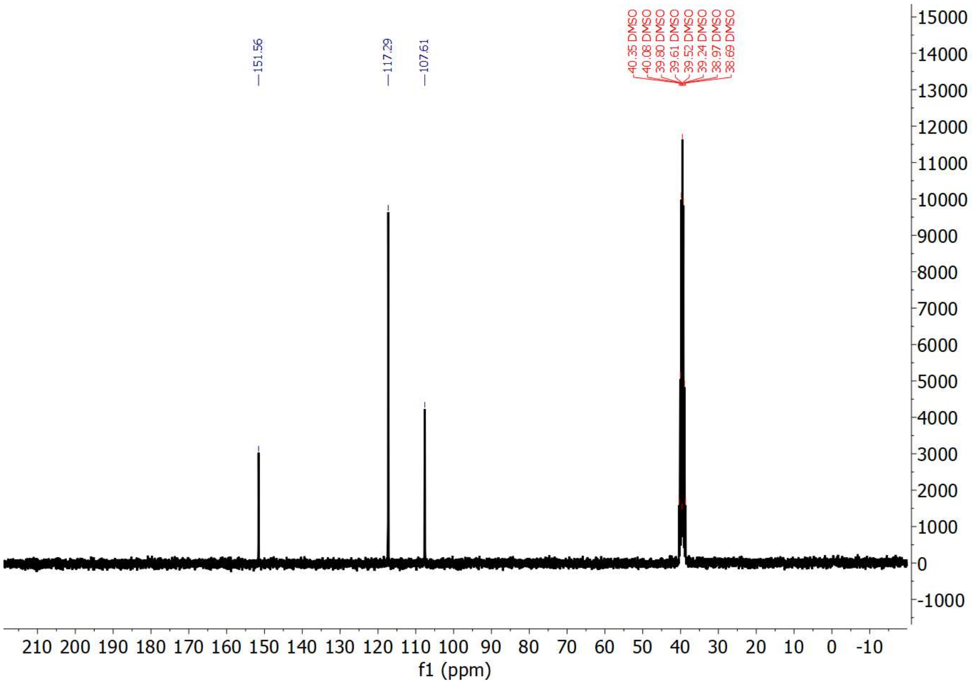

Figure 3.16. ^{13}C NMR of **1** in DMSO-d6.

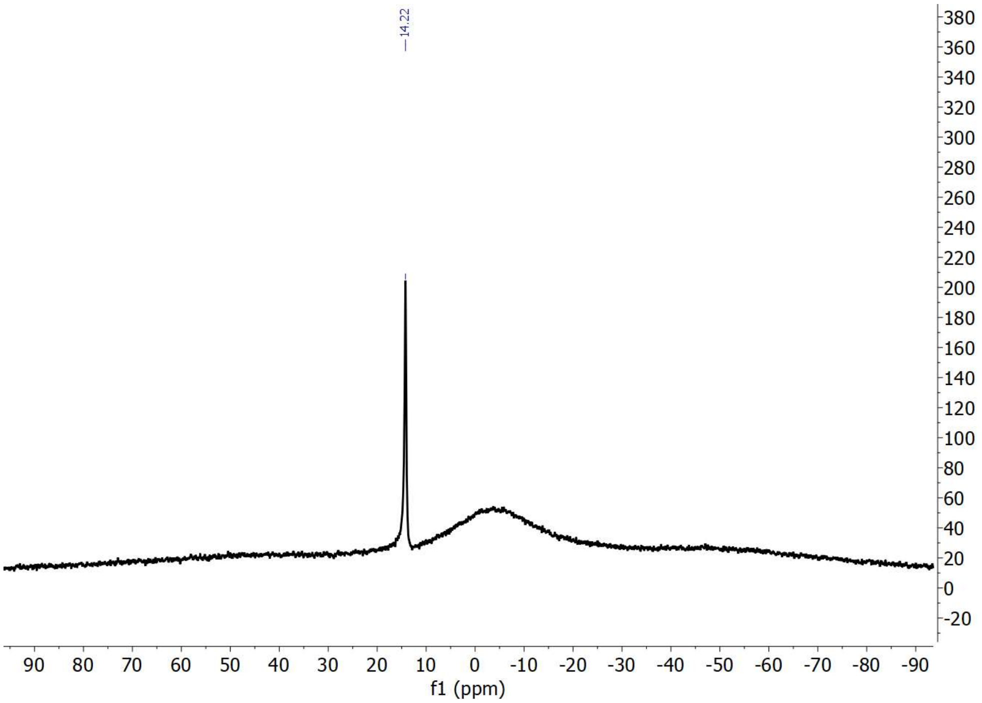

Figure 3.17. ^{11}B NMR of **1** in DMSO-d6.

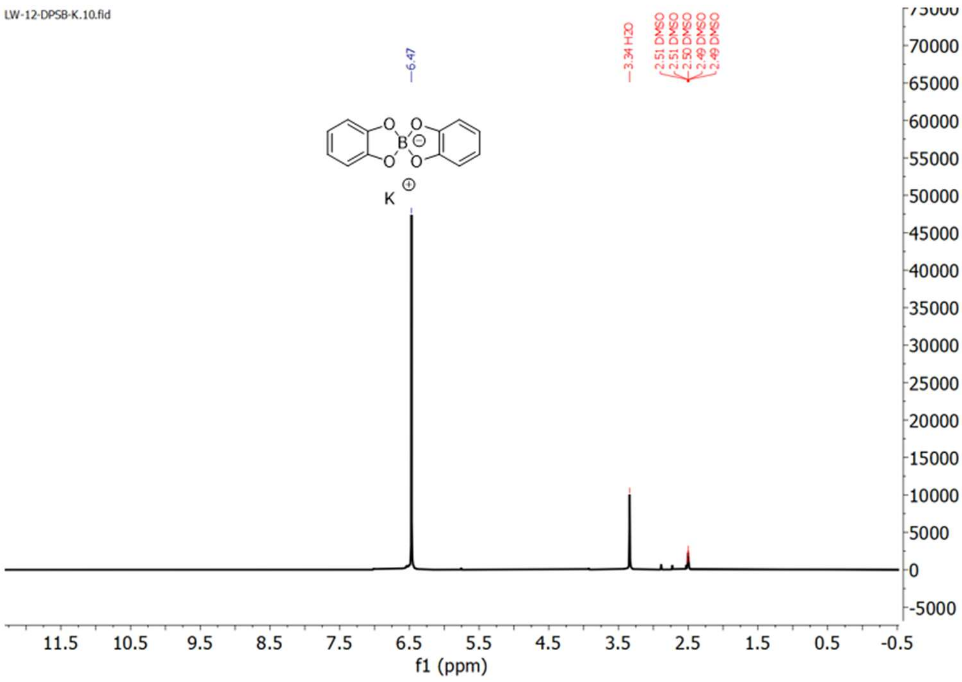

Figure 3.18. ^{1}H NMR of **2** in DMSO-d6.

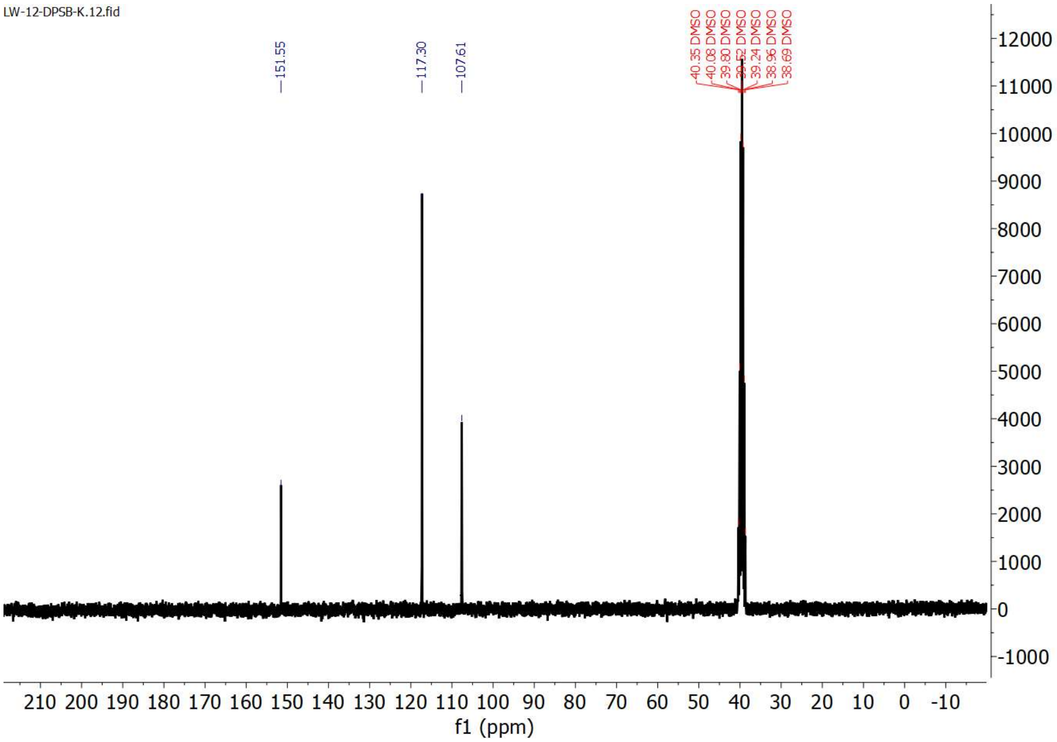

Figure 3.19. ^{13}C NMR of **2** in DMSO-d6.

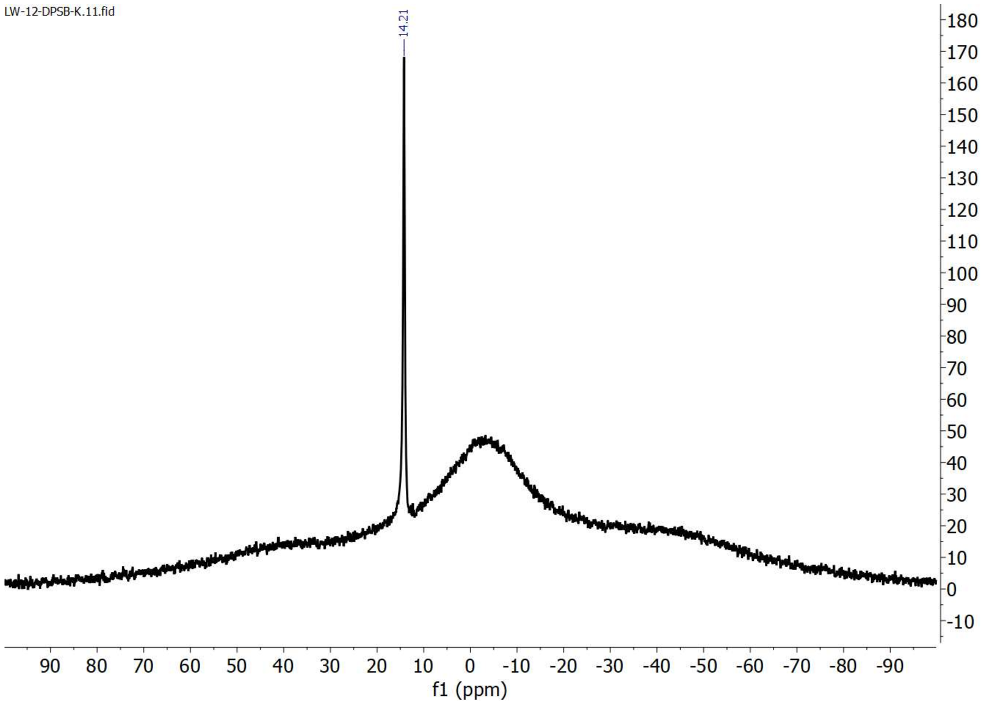

Figure 3.20. ^{11}B NMR of **2** in DMSO-d6.

3.6 References

(1) Yashima, E.; Maeda, K.; Iida, H.; Furusho, Y.; Nagai, K. Helical Polymers: Synthesis, Structures, and Functions. *Chem. Rev.* **2009,** *109* (11), 6102-6211. DOI: 10.1021/cr900162q.

(2) Nakano, T.; Okamoto, Y. Synthetic Helical Polymers: Conformation and Function. *Chem. Rev.* **2001**, *101* (12), 4013-4038. DOI: 10.1021/cr0000978.

(3) Hill, D. J.; Mio, M. J.; Prince, R. B.; Hughes, T. S.; Moore, J. S. A Field Guide to Foldamers. *Chem. Rev.* **2001**, *101* (12), 3893-4012. DOI: 10.1021/cr990120t.

(4) Zhang, D.-W.; Zhao, X.; Hou, J.-L.; Li, Z.-T. Aromatic Amide Foldamers: Structures, Properties, and Functions. *Chem. Rev.* **2012**, *112* (10), 5271-5316. DOI: 10.1021/cr300116k.

(5) Yashima, E.; Ousaka, N.; Taura, D.; Shimomura, K.; Ikai, T.; Maeda, K. Supramolecular Helical Systems: Helical Assemblies of Small Molecules, Foldamers, and Polymers with Chiral Amplification and Their Functions. *Chem. Rev.* **2016**, *116* (22), 13752-13990. DOI: 10.1021/acs.chemrev.6b00354.

(6) Kusanagi, H.; Chatani, Y.; Tadokoro, H. The crystal structure of isotactic poly(methyl methacrylate): packing-mode of double stranded helices. *Polymer* **1994**, *35* (10), 2028-2039. DOI: 10.1016/0032-3861(94)90224-0.

(7) Wang, Y.; He, Y.; Yu, Z.; Gao, J.; ten Brinck, S.; Slebodnick, C.; Fahs, G. B.; Zanelotti, C. J.; Hegde, M.; Moore, R. B.; Ensing, B.; Dingemans, T. J.; Qiao, R.; Madsen, L. A. Double helical conformation and extreme rigidity in a rodlike polyelectrolyte. *Nat. Commun.* **2019**, *10* (1), 801. DOI: 10.1038/s41467-019-08756-3.

(8) Hu, Y.; Teat, S. J.; Gong, W.; Zhou, Z.; Jin, Y.; Chen, H.; Wu, J.; Cui, Y.; Jiang, T.; Cheng, X.; Zhang, W. Single crystals of mechanically entwined helical covalent polymers. *Nat. Chem.* **2021**, *13* (7), 660-665. DOI: 10.1038/s41557-021-00686-2.

(9) Côté Adrien, P.; Benin Annabelle, I.; Ockwig Nathan, W.; O'Keeffe, M.; Matzger Adam, J.; Yaghi Omar, M. Porous, Crystalline, Covalent Organic Frameworks. *Science* **2005**, *310* (5751), 1166-1170. DOI: 10.1126/science.1120411 .

(10) O'Keeffe, M.; Peskov, M. A.; Ramsden, S. J.; Yaghi, O. M. The Reticular Chemistry Structure Resource (RCSR) Database of, and Symbols for, Crystal Nets. Acc. Chem. Res. 2008, 41 (12), 1782-1789. DOI: 10.1021/ar800124u.

(11) Jin, Y.; Wang, Q.; Taynton, P.; Zhang, W. Dynamic Covalent Chemistry Approaches Toward Macrocycles, Molecular Cages, and Polymers. Acc. Chem. Res. 2014, 47 (5), 1575-1586. DOI: 10.1021/ar500037v.

(12) Jin, Y.; Hu, Y.; Zhang, W. Tessellated multiporous two-dimensional covalent organic frameworks. *Nat. Rev. Chem.* **2017**, *1* (7), 0056. DOI: 10.1038/s41570-017-0056.

(13) Wayment, L. J.; Lei, Z.; Jin, Y.; Zhang, W. Recent Progress in Constructing Structurally Ordered Polymeric Architectures via Dynamic Covalent Chemistry. *CCS Chem.* **2023**, *5* (10), 2194-2206. DOI: 10.31635/ccschem.023.202303004.

(14) Kandambeth, S.; Dey, K.; Banerjee, R. Covalent Organic Frameworks: Chemistry beyond the Structure. *J. Am. Chem. Soc.* **2019**, *141* (5), 1807-1822. DOI: 10.1021/jacs.8b10334.

(15) Geng, K.; He, T.; Liu, R.; Dalapati, S.; Tan, K. T.; Li, Z.; Tao, S.; Gong, Y.; Jiang, Q.; Jiang, D. Covalent Organic Frameworks: Design, Synthesis, and Functions. *Chem. Rev.* **2020**, *120* (16), 8814-8933. DOI: 10.1021/acs.chemrev.9b00550.

(16) Evans, A. M.; Strauss, M. J.; Corcos, A. R.; Hirani, Z.; Ji, W.; Hamachi, L. S.; Aguilar-Enriquez, X.; Chavez, A. D.; Smith, B. J.; Dichtel, W. R. Two-Dimensional Polymers and Polymerizations. *Chem. Rev.* **2022**, *122* (1), 442-564. DOI: 10.1021/acs.chemrev.0c01184.

(17) Ma, T.; Li, J.; Niu, J.; Zhang, L.; Etman, A. S.; Lin, C.; Shi, D.; Chen, P.; Li, L.-H.; Du, X.; Sun, J.; Wang, W. Observation of Interpenetration Isomerism in Covalent Organic Frameworks. *J. Am. Chem. Soc.* **2018**, *140* (22), 6763-6766. DOI: 10.1021/jacs.8b03169.

(18) Gropp, C.; Ma, T.; Hanikel, N.; Yaghi, O. M. Design of higher valency in covalent organic frameworks. *Science* **2020**, *370* (6515), eabd6406. DOI: 10.1126/science.abd6406.

(19) Liu, Y.; Li, J.; Lv, J.; Wang, Z.; Suo, J.; Ren, J.; Liu, J.; Liu, D.; Wang, Y.; Valtchev, V.; Qiu, S.; Zhang, D.; Fang, Q. Topological Isomerism in Three-Dimensional Covalent Organic Frameworks. *J. Am. Chem. Soc.* **2023**, *145* (17), 9679-9685. DOI: 10.1021/jacs.3c01070.

(20) Wayment, L. J.; Wang, X.; Huang, S.; McCoy, M. S.; Chen, H.; Hu, Y.; Jin, Y.; Sharma, S.; Zhang, W. 3D Covalent Organic Framework as a Metastable Intermediate in the Formation of a Double-Stranded Helical Covalent Polymer. *J. Am. Chem. Soc.* **2023**, *145* (28), 15547-15552. DOI: 10.1021/jacs.3c04734.

(21) Gui, B.; Xin, J.; Cheng, Y.; Zhang, Y.; Lin, G.; Chen, P.; Ma, J.-X.; Zhou, X.; Sun, J.; Wang, C. Crystallization of Dimensional Isomers in Covalent Organic Frameworks. *J. Am. Chem. Soc.* **2023**, *145* (20), 11276-11281. DOI: 10.1021/jacs.3c01729.

(22) Wang, X.; Wada, Y.; Shimada, T.; Kosaka, A.; Adachi, K.; Hashizume, D.; Yazawa, K.; Uekusa, H.; Shoji, Y.; Fukushima, T.; Kawano, M.; Murakami, Y. Triple Isomerism in 3D Covalent Organic Frameworks. *J. Am. Chem. Soc.* **2024**, *146* (3),1832-1838. DOI: 10.1021/jacs.3c13863.

(23) Liu, Y.; Ma, Y.; Yang, J.; Diercks, C. S.; Tamura, N.; Jin, F.; Yaghi, O. M. Molecular Weaving of Covalent Organic Frameworks for Adaptive Guest Inclusion. *J. Am. Chem. Soc.* **2018**, *140* (47), 16015-16019. DOI: 10.1021/jacs.8b08949.

(24) Xie, Y.; Li, J.; Lin, C.; Gui, B.; Ji, C.; Yuan, D.; Sun, J.; Wang, C. Tuning the Topology of Three-Dimensional Covalent Organic Frameworks via Steric Control: From pts to Unprecedented ljh. *J. Am. Chem. Soc.* **2021**, *143* (19), 7279-7284. DOI: 10.1021/jacs.1c03042.

(25) Wu, X.; Han, X.; Liu, Y.; Liu, Y.; Cui, Y. Control Interlayer Stacking and Chemical Stability of Two-Dimensional Covalent Organic Frameworks via Steric Tuning. *J. Am. Chem. Soc.* **2018**, *140* (47), 16124-16133. DOI: 10.1021/jacs.8b08452.

(26) Wang, Y.; Liu, Y.; Li, H.; Guan, X.; Xue, M.; Yan, Y.; Valtchev, V.; Qiu, S.; Fang, Q. Three-Dimensional Mesoporous Covalent Organic Frameworks through Steric Hindrance Engineering. *J. Am. Chem. Soc*. **2020**, *142* (8), 3736-3741. DOI: 10.1021/jacs.0c00560.

(27) Xiao, Y.; Ling, Y.; Wang, K.; Ren, S.; Ma, Y.; Li, L. Constructing a 3D Covalent Organic Framework from 2D hcb Nets through Inclined Interpenetration. *J. Am. Chem. Soc*. **2023**, *145* (25), 13537-13541. DOI: 10.1021/jacs.3c03699.

(28) Ma, T.; Kapustin, E. A.; Yin, S. X.; Liang, L.; Zhou, Z.; Niu, J.; Li, L.-H.; Wang, Y.; Su, J.; Li, J.; Wang, X. Wang, W. D.; Wang, W.; Sun, J.; Yaghi, O.M. Single-crystal x-ray diffraction structures of covalent organic frameworks. *Science* **2018**, *361* (6397), 48-52. DOI: doi:10.1126/science.aat7679.

(29) Beaudoin, D.; Maris, T.; Wuest, J. D. Constructing monocrystalline covalent organic networks by polymerization. *Nat. Chem.* **2013**, *5* (10), 830-834. DOI: 10.1038/nchem.1730.

(30) Zhou, Z.; Zhang, L.; Yang, Y.; Vitorica-Yrezabal, I. J.; Wang, H.; Tan, F.; Gong, L.; Li, Y.; Chen, P.; Dong, X.; Liang, Z.; Yang, J.; Wang, C.; Hong, Y.; Qiu, Y.; Gölzhäuser, A.; Chen, X.; Qi, H.; Yang, S.; Liu, W.; Sun, J.; Zheng, Z. Growth of single-crystal imine-linked covalent organic frameworks using amphiphilic amino-acid derivatives in water. *Nat. Chem.* **2023**, *15* (6), 841-847. DOI: 10.1038/s41557-023-01181-6.

(31) Yu, B.; Lin, R.-B.; Xu, G.; Fu, Z.-H.; Wu, H.; Zhou, W.; Lu, S.; Li, Q.-W.; Jin, Y.; Li, J.-H.; Zhang, Z.; Wang, H.; Yan, Z.; Liu, X.; Wang, K.; Chen, B.; Jiang, J. Linkage conversions in single-crystalline covalent organic frameworks. *Nat. Chem.* **2024**, *16* (1), 114-121. DOI: 10.1038/s41557-023-01334-7.

(32) Yu, B.; Li, W.; Wang, X.; Li, J.-H.; Lin, R.-B.; Wang, H.; Ding, X.; Jin, Y.; Yang, X.; Wu, H.; Zhou, W.; Zhang, J.; Jiang, J. Observation of Interpenetrated Topology Isomerism for Covalent Organic Frameworks with Atom-Resolution Single Crystal Structures. *J. Am. Chem. Soc.* **2023**, *145* (46), 25332-25340. DOI: 10.1021/jacs.3c09001.

(33) Xu, H.-S.; Luo, Y.; Li, X.; See, P. Z.; Chen, Z.; Ma, T.; Liang, L.; Leng, K.; Abdelwahab, I.; Wang, L.; Li, R.; Shi, X.; Zhou, Y.; Lu, X. F; Zhao, X.; Liu, C.; Sun, J.; Loh, K. P. Single crystal of a one-dimensional metallo-covalent organic framework. *Nat. Commun.* **2020**, *11* (1), 1434. DOI: 10.1038/s41467-020-15281-1.

(34) Evans, A. M.; Parent, L. R.; Flanders, N. C.; Bisbey, R. P.; Vitaku, E.; Kirschner, M. S.; Schaller, R. D.; Chen, L. X.; Gianneschi, N. C.; Dichtel, W. R. Seeded growth of single-crystal two-dimensional covalent organic frameworks. *Science* **2018**, *361* (6397), 52-57. DOI: 10.1126/science.aar7883.

(35) Li, J.; Lin, C.; Ma, T.; Sun, J. Atomic-resolution structures from polycrystalline covalent organic frameworks with enhanced cryo-cRED. *Nat. Commun.* **2022**, *13* (1), 4016. DOI: 10.1038/s41467-022-31524-9.

(36) Sun, T.; Lei, W.; Ma, Y.; Zhang, Y.-B. Unravelling Crystal Structures of Covalent Organic Frameworks by Electron Diffraction Tomography. *Chinese J. Chem.* **2020**, *38* (10), 1153-1166. DOI: 10.1002/cjoc.202000120.

(37) Liu, Y.; Ma, Y.; Zhao, Y.; Sun, X.; Gándara, F.; Furukawa, H.; Liu, Z.; Zhu, H.; Zhu, C.; Suenaga, K.; Oleynikov, P.; Alshammari, A. S.; Zhang, X.; Terasaki, O.; Yaghi, O. M. Weaving of organic threads into a crystalline covalent organic framework. *Science* **2016**, *351* (6271), 365-369. DOI: 10.1126/science.aad4011.

(38) De Bolòs, E.; Martínez-Abadía, M.; Hernández-Culebras, F.; Haymaker, A.; Swain, K.; Strutyński, K.; Weare, B. L.; Castells-Gil, J.; Padial, N. M.; Martí-Gastaldo, C.; Khlobystov, A. N.; Saeki, A.; Melle-Franco, M.; Nannenga, B. L.; Mateo-Alonso, A. A Crystalline 1D Dynamic Covalent Polymer. *J. Am. Chem. Soc.* **2022**, *144* (34), 15443-15450. DOI: 10.1021/jacs.2c06446.

(39) Liu, B.-T.; Gong, S.-H.; Jiang, X.-T.; Zhang, Y.; Wang, R.; Chen, Z.; Zhang, S.; Kirlikovali, K. O.; Liu, T.-F.; Farha, O. K.; Cao, R. A solution processible single-crystal porous organic polymer. *Nat. Synth.* **2023**, *2* (9), 873-879. DOI: 10.1038/s44160-023-00316-4.

(40) Yang, Y.; Lin, E.; Wang, S.; Wang, T.; Wang, Z.; Zhang, Z. Single-Crystal One-Dimensional Porous Ladder Covalent Polymers. *J. Am. Chem. Soc.* **2024**, *146* (1), 782-790. DOI: 10.1021/jacs.3c10812.

(41) Ousaka, N.; Shimizu, K.; Suzuki, Y.; Iwata, T.; Itakura, M.; Taura, D.; Iida, H.; Furusho, Y.; Mori, T.; Yashima, E. Spiroborate-Based Double-Stranded Helicates: Meso-to-Racemo Isomerization and Ion-Triggered Springlike Motion of the Racemo-Helicate. *J. Am. Chem. Soc.* **2018**, *140* (49), 17027-17039. DOI: 10.1021/jacs.8b08268.

(42) Miwa, K.; Furusho, Y.; Yashima, E. Ion-triggered spring-like motion of a double helicate accompanied by anisotropic twisting. *Nat. Chem.* **2010**, *2* (6), 444-449. DOI: 10.1038/nchem.649.

(43) Chen, H.; Hu, Y.; Luo, C.; Lei, Z.; Huang, S.; Wu, J.; Jin, Y.; Yu, K.; Zhang, W. Spiroborate-Linked Ionic Covalent Adaptable Networks with Rapid Reprocessability and Closed-Loop Recyclability. *J. Am. Chem. Soc.* **2023**, *145* (16), 9112-9117. DOI: 10.1021/jacs.3c00774.

(44) Wang, X.; Bahri, M.; Fu, Z.; Little, M. A.; Liu, L.; Niu, H.; Browning, N. D.; Chong, S. Y.; Chen, L.; Ward, J. W.; Cooper, A. I. A Cubic 3D Covalent Organic Framework with nbo Topology. *J. Am. Chem. Soc.* **2021**, *143* (37), 15011-15016. DOI: 10.1021/jacs.1c08351.

(45) Hu, Y.; Dunlap, N.; Long, H.; Chen, H.; Wayment, L. J.; Ortiz, M.; Jin, Y.; Nijamudheen, A.; Mendoza-Cortes, J. L.; Lee, S.-H.; Zhang, W. Helical Covalent Polymers with Unidirectional Ion Channels as Single Lithium-Ion Conducting Electrolytes. *CCS Chem*. **2021**, *3* (12), 2762-2770. DOI: 10.31635/ccschem.021.202101257.

Chapter 4: Ionic Covalent Organic Frameworks Consisting of Tetraborate Nodes and Flexible Linkers

4.1 Abstract

Covalent organic frameworks (COFs) have emerged as versatile materials with many applications, such as carbon capture, molecular separation, catalysis, and energy storage. Traditionally, flexible building blocks have been avoided due to their potential to disrupt ordered structures. Recent studies have demonstrated intriguing properties and enhanced structural diversity achievable with flexible components by judicious selection of building blocks. This study presents a novel series of ionic COFs (ICOFs) consisting of tetraborate nodes and flexible linkers. These ICOFs use borohydrides to irreversibly deprotonate the alcohol monomers to achieve a high polymerization degree. Structural analysis confirms the *dia* topologies. Reticulation is explored using various monomers and metal counter-ions. Also, these frameworks exhibit excellent stability in alcohols and coordinating solvents. The materials are tested as single-ion conductive solid-state electrolytes. ICOF-203-Li displays one of the lowest activation energies reported for ion conduction. This tetraborate chemistry is anticipated to facilitate further structural diversity and functionality in crystalline polymers.

4.2 Introduction

Covalent organic frameworks (COFs) have emerged as an appealing platform for designing innovative materials with diverse applications such as carbon capture, molecular separation, heterogeneous catalysis, and energy storage.[1-6] The customizable structure of these crystalline polymers allows for tailoring them to specific applications by carefully selecting the monomers and linkages. Typically, COFs are designed using dynamic covalent chemistry (DCvC) and the principle of reticulation. The principle of reticulation dictates that molecular building blocks maintain a known geometry within the crystal lattice, while DCvC enables error correction during the polymerization to favor ordered networks.[7,8] With these principles, there has been tremendous success in designing highly crystalline polymetric architectures using rigid linkages and monomers.[9]

On the other hand, flexible monomers or linkages have traditionally been avoided in the design of crystalline materials due to their tendency to disrupt the thermodynamic drive toward ordered structures by introducing additional degrees of rotation.[10-13] Recent studies have shown that employing flexible monomers or linkages can lead to intriguing properties and enhance structural diversity. For instance, Fang et al. observed topological isomerization by using 4,4′,4″,4‴-([9,9′-bicarbazole]-3,3′,6,6′-tetrayl)tetrabenzaldehyde (BCTB-4CHO) as a monomer, which exhibits a low energy barrier for adopting a wide range of dihedral angles.[14] This flexibility allowed them to create *dia* net and *qzt* net structures with distinct properties. Another example is the spiroborate linkage, which has been used to form 1D and 3D polymers where the dihedral angle of the boron center can be varied from 66° to 90° due to the flexibility of the B-O bonds.[15, 16, 17, 18, 19] In all cases, the design requires a judicious selection of building blocks to achieve desired topologies.

Here, we present the synthesis and characterization of a novel series of ionic COFs (ICOFs), consisting of tetraborate nodes and flexible linkers. The design of these materials demonstrates how flexibility can be introduced into the node and linker while maintaining a predictable topology. Structural analysis confirms that the new series adopts *dia* topologies. The reticulation of this unique chemistry is explored with three different monomers and by varying the metal counter-ion. These frameworks exhibit excellent chemical stability in alcohols and coordinating solvents. We assess the materials as solid-state electrolytes to demonstrate their utility as single-ion conducting polymers. These ICOFs exhibit one of the lowest activation energies for ion conduction. We anticipate that this methodology can be broadly applied to other monomers. Many aldehyde monomers have been developed that could be easily transformed into alcohols. Thus, this chemistry will further the structural diversity of crystalline polymers and lead to the discovery of novel properties.

4.3 Results and Discussion

The conventional formation of charged borate species involves using boron sources like trimethyl borate or boric acid, along with a base. For spiroborate formation, the monomer design necessitates a catechol or diol monomer capable of chelating the boron center. The conversion rate was notably low when this approach was employed to synthesize ICOF-201-Li from 1,4-

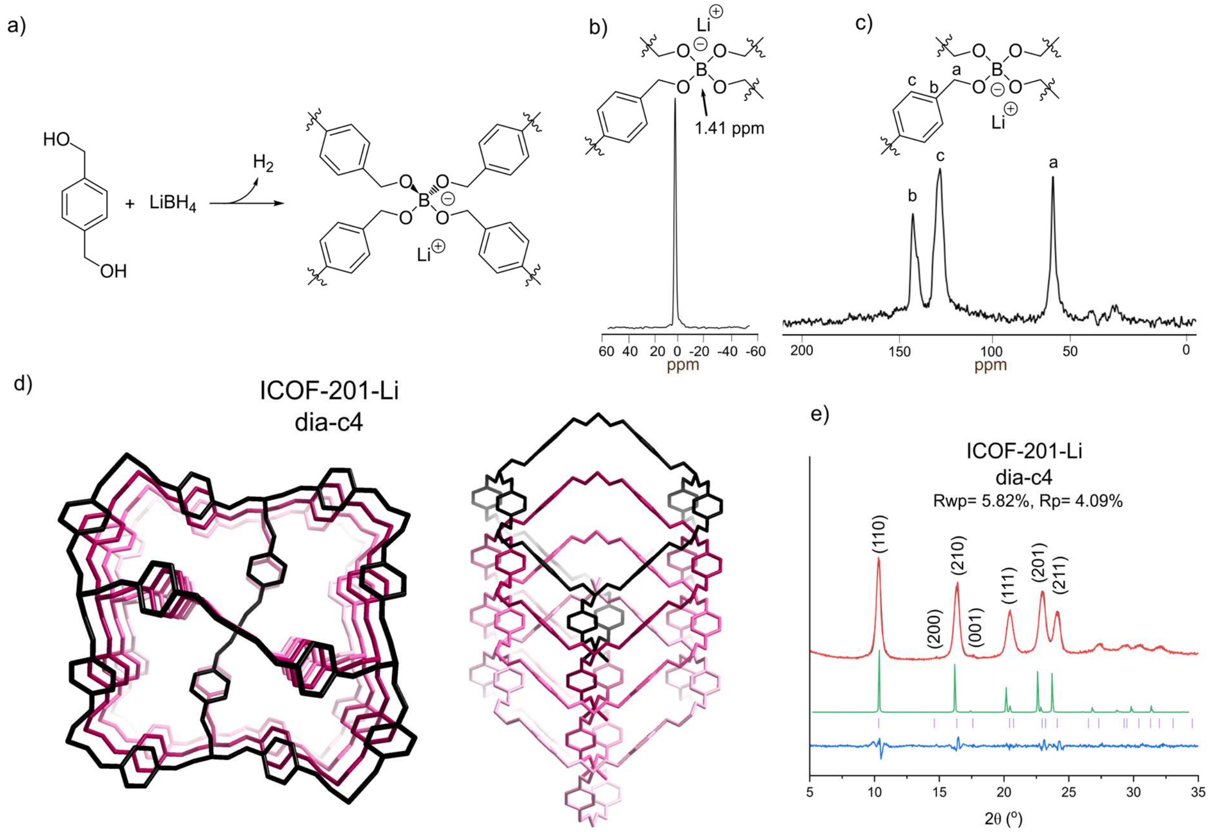

Figure 4.1. Synthesis and characterization of ICOF-201-Li. (a) The synthetic scheme of ICOF-201-Li which forms tetrahedral nodes at the boron center. Solid state 11B (b) and 13C (c) NMR of ICOF-201-Li. (d) ICOF-201-Li forms a four-fold interpenetrated dia topology. (e) Pawley refinement (black) of ICOF-201-Li. The experimental pattern (red) with the difference (light blue) and the Bragg reflections (purple). The simulation of the dia topology model with four-fold interpenetration is shown in green.

benzenedimethanol. This is likely due to the absence of a chelating interaction as a thermodynamic driving force to favor polymerization. So, in a closed system, there is limited driving force toward the polymerization. To overcome such limitation, the traditional boron reagents were replaced with lithium borohydride. Irreversibly deprotonating the alcohol monomers dramatically enhanced the kinetic driving force toward polymerization, while dynamic B-O bond exchange can still enable the error correction behavior.

ICOF-201-Li synthesis involved the reaction of lithium borohydride (LiBH4) with 1,4-benzenedimethanol in benzonitrile at 150°C for 7 days (Figure 4.1a). Fourier-transform infrared spectroscopy (FT-IR) evidenced the formation of a B-O bond at 1066 cm^{-1}, along with the complete reduction of the -OH stretch (Figure 4.5). Solid-state boron NMR revealed a single boron species at 1.41 ppm, which is similar to other alcohol based small molecules[20, 21] (Figure 4.1b). Solid-state carbon NMR displayed three carbon species, consistent with the expected structure (Figure 4.1c). SEM showed the morphology of the polycrystalline sample to be clusters of rods (Figure 4.6). We expected the topology of ICOF-201-Li to be a *dia* net. To determine if this was the appropriate topology, *dia* net models were created ranging from being non-interpenetrated to six-fold interpenetrated (Figure 4.7).[7] The experimental pattern matches well with the four-fold interpenetrated structure (Figure 4.1d and 4.1e). The dimensions after Pawley Refinement (Rwp= 5.82% and Rp= 4.09%) were found to be a=b= 12.1098 Å and c= 5.03920 Å with a space group of $P\overline{4}b2$.

Next, the reticulation and scope of this tetraborate chemistry were explored by varying the monomer structures. ICOF-202-Li (Figure 4.2a) and ICOF-203-Li (Figure 4.2c) were synthesized using 4,4’- bis(hydroxymethyl)biphenyl and 2,35,6,-tertrafluoro-1,4- benzenedimethanol, respectively. Subsequently, sodium borohydride ($NaBH_4$) replaced $LiBH_4$ to produce ICOF-203-

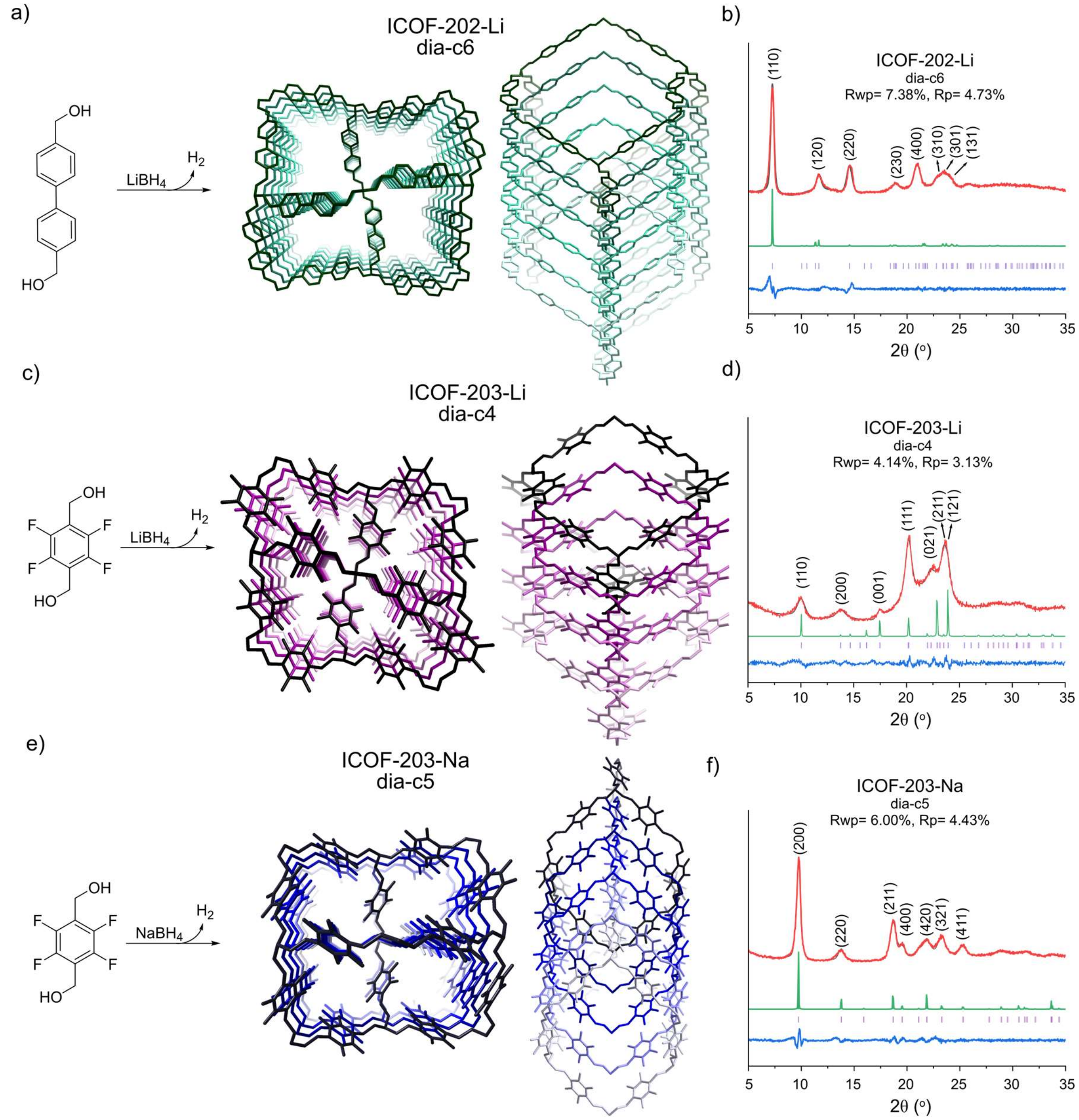

Figure 4.2. Synthesis and topology of ICOF-202-Li, ICOF-203-Li, and ICOF-203-Na. Synthetic scheme of ICOF-202-Li (a), ICOF-203-Li (c), and ICOF-203-Na (e). Pawley refinement (black) of ICOF-202-Li (b), ICOF-203-Li (d), and ICOF-203-Na (f) overlayed with the experimental patterns (red). The difference (light blue), the Bragg reflections (purple), and the simulation of the respective dia topology model (green) are also included.

Na (Figure 4.2e). Characterization and morphology analysis yielded results akin to those observed for ICOF-201-Li (Section 4.5.4). By extending the linker length in ICOF-202-Li, the interpenetration of the structure increased, resulting in a six-fold interpenetration compared to other models (Figure 4.11). The space group assigned to this model was Pnn2. The dimensions of the unit cell were determined by Pawley refinement, Rwp = 7.38% and Rp = 4.73%, to be a = 16.8265 Å, b = 17.6382 Å, and c = 4.87010 Å (Figure 4.2b).

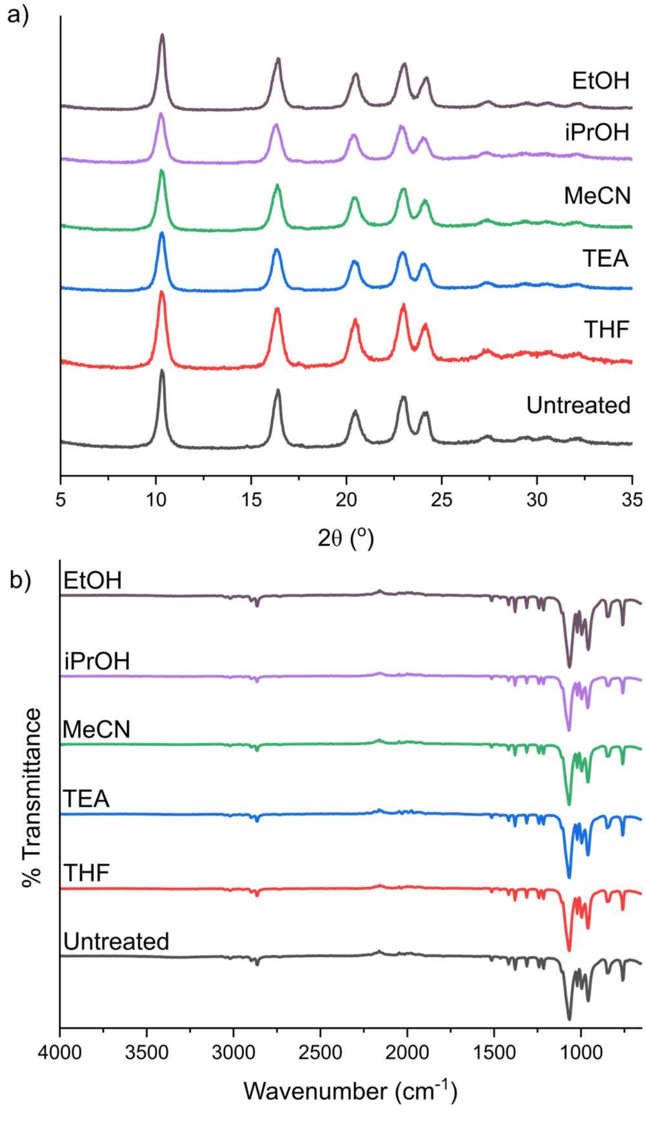

Figure 4.3. Comparison of ICOF-201-Li PXRD (a) and FT-IR (b) after various chemical treatments.

The design of ICOF-203-Li was chosen to evaluate the compatibility of this tetraborate chemistry with other functional groups. The fluorine on the monomers will reduce the nucleophilicity of the alcohols, but the framework is still formed with good yield. The experimental crystallinity was compared to various dia nets, ultimately aligning most closely with a four-fold interpenetrated dia net with a space group of Pba2 (Figure 4.15). Following Pawley refinement, the unit cell dimensions were determined as a = 12.8783 Å, b = 12.0796 Å, and c = 5.0743 Å (Figure 4.2d). Notably, the orientation of the linkers impacted the intensity of the peaks, as evidenced in the comparison between ICOF-203-Li and ICOF-203-Na (Figure 4.2d and 4.2f). The simulations revealed a closer match between the experimental pattern of ICOF-203-Li when the orientation of the aromatic ring is relatively flat. Conversely, in ICOF-203-Na, a better match in signal intensity was observed when the aromatic ring was oriented at a more angled position (Figure 4.2e). Additionally, ICOF-203-Na exhibited a five-fold interpenetrated structure (Figure 4.19). Following Pawley refinement, the dimensions of the unit cell were found to be a = b = 18.1731 Å and c = 5.854 Å, with Rwp = 6.00% and Rp = 4.43% (Figure 4.2f).

Next, the properties of the 3D tetraborate frameworks were tested in terms of stability and porosity. Originally, charged borate linkers were developed to improve the stability of the materials and introduce new functionality. ICOF-201-Li was tested against various solvents, such as alcohols and coordinating solvents, by soaking the ICOF in the solvents for 16 hours. Then, the solvent was removed, and the resulting solid was subjected to characterization. PXRD showed that crystallinity could remain against all solvents (Figure 4.3a), and IR showed no evidence of degradation (Figure 4.3b). The other ICOFs also remained largely unaffected by the chemical treatment (Section 4.5.5). Next, thermogravimetric analysis (TGA) tested the thermal stability. ICOF-201-Li showed a minor mass loss of less than 10 wt% until 435 °C (Figure 4.27). The stability of the other ICOFs was slightly lower because the mass loss of 10 wt% ranged from 300 to 420 °C (Figure 4.27). The porosity of the ICOFs was tested by measuring the nitrogen isotherm (Section 4.5.6). ICOF-201-Li, ICOF-202-Li, and ICOF-203-Li showed BET surface areas of 107 $m^2 g^{-1}$, 155 $m^2 g^{-1}$, and 219 $m^2 g^{-1}$, respectively. ICOF-203-Na showed a slightly higher BET surface area of 231 $m^2 g^{-1}$. These results demonstrate that fairly robust and porous frameworks can be constructed from simple building blocks via tetraborate chemistry.

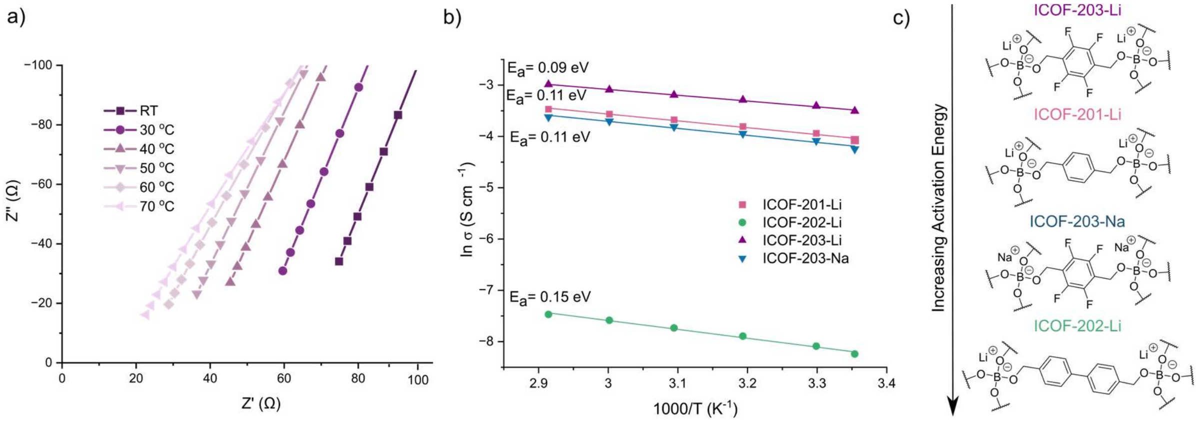

Figure 4.4. Structure-activity relationship of ICOF-201-Li to ICOF-203-Na (a) Nyquist plot of ICOF-203-Li at different temperatures. (b) Arrhenius plot of ICOF-201-Li to ICOF-203-Na with the calculated activation energy in eV per atom. (c) Repeating units of the ICOF-201-Li to ICOF-203-Na in order of activation energy.

Finally, we evaluated the ICOFs as solid-state electrolytes (SSE). An emerging strategy for improving the performance of solid polymer electrolytes involves generating ion hopping sites within ordered channels, similar to solid inorganic electrolytes.[22,23] These sites serve to uncouple cation conduction from the motion within the polymer chains, thereby enhancing conductivity. There has been much success in developing ICOFs SSE using this approach. [24-28] Additionally, there is growing research interest in sodium-ion batteries. The abundance of sodium, lower cost, and similar energy storage mechanism make it an attractive alternative to lithium-ion batteries.[29-32] The tetraborate platform in this work has great potential in advancing this research effort due to the ease of tunability of both the linkers and metal-ions.

The structure-activity relationship of the initial series of ICOF-200s were evaluated to understand how the structural features affect the ion conductivity. Prior to all measurements, the ICOFs were dried in a vacuum oven overnight at 120 °C. Then, a pellet of the respective ICOFs with 20 wt% of PYR13FSI, an environmentally friendly plasticizer, was created.[33]

Table 4.1. Summary of ion conductivity data of ICOF electrolytes at 30 °C and the respective activation energies.

ICOF	σ (S cm^{-1}) at 30 °C	E_a (eV/atom)
ICOF-201-Li	1.2 $x10^{-4}$	0.11
ICOF-202-Li	3.1 $x10^{-4}$	0.15
ICOF-203-Li	3.9 $x10^{-4}$	0.09
ICOF-203-Na	8.3 $x10^{-5}$	0.11

Electrochemical impedance spectroscopy was used to measure the ion conductivities across a temperature gradient of room temperature to 70 °C (Figure 4.4a and Figure 4.28).

Arrhenius plots were created to calculate the activation energy of ion conduction in each ICOF to understand the relationship between the structures and ion transportation (Figure 4.4b). ICOF-203-Li was found to have the lowest activation energy of 0.09 eV per atom and can reach the highest conductivity (Figure 4.4c and Table 4.1). The activation increases slightly to 0.11 eV when the fluorine substitutes are removed, as in ICOF-201-Li. Further increasing the linker length also increases (ICOF-202-Li) the activation energy to 0.15 eV (Figure 4.4b). The fluorine could contribute to the ion conductivity in two ways. First, the electronegativity of fluorine can weaken the electrostatic attraction between the tetraborate group and counter ion thus making the ions more mobile. Additionally, fluorine can act as a hopping site to facilitate ion conduction (Figure 4.4c). When the counterion is changed from lithium to sodium, then the activation energy of ion conduction increases to 0.11 eV. This is due to sodium-ions having a greater mass. Table 4.1 summarizes the ion conductivity at 30 °C and activation energy of the four ICOFs. It is anticipated that monomer designs can be tuned to improve the properties further.

4.4 Conclusions

In conclusion, this work has demonstrated a novel boron chemistry that creates ICOFs consisting of tetraborate nodes with flexible monomers. The synthesis requires borohydrides to irreversibly deprotonate the alcohol monomers to achieve a high polymerization degree, while the dynamic B-O bonds enable error correction to ensure the formation of crystalline polymers with long-range order. Variation in the monomers and metal ions utilized reveals how the interpenetration and monomer orientation will affect the experimental diffraction pattern. Notably, these frameworks exhibit good chemical and thermal stability. Finally, the impedance of the reported structure was tested to demonstrate the potential of this platform for developing solid-state electrolytes. ICOF-203-Li showed one of the lowest activation energies reported so far. Incorporating the tetraborate moieties opens avenues for further exploration and diversification of crystalline polymers, indicating a promising direction for future research.

4.5 Experimental section

4.5.1. Materials and Methods

The chemicals utilized in this study were procured from Aldrich Chemical Company, ComiBlock, TCL, or Oakwood Chemicals and were used without additional purification. Fourier-transform infrared (FT-IR) spectra were collected using an Agilent Technology Cary 630 FT-IR spectrometer. Scanning Electron Microscopy (SEM) images were captured at 30 kV using a JSM-640LV (LVSEM). Powder X-ray Diffraction (XRD) data were obtained on a Bruker D8 Advance A25 system with a monochromated Cu Kα radiation source, operated at 40 kV and 40 mA under ambient conditions. Solid-state Cross Polarization Magic Angle Spinning (CP/MAS) NMR spectra were acquired using an Inova 400 NMR spectrometer. ^{11}B MAS NMR was referenced to boron trifluoride etherate. Thermogravimetric analysis (TGA) was conducted using a thermogravimetric/differential thermal analyzer.

Electrochemical impedance spectroscopy (ESI) measurements were conducted using a Solartron 1280C and over a range of 1 MHz to 1 Hz with an oscillating voltage of 10 mV. The typical procedure used a pellet of the sample (60 mg) loaded into a cell. An ionic liquid (12 mg, 20 wt%) was added as a plasticizer. The pellets were between blocking titanium electrodes in 13 mm diameter polyetheretherketone (PEEK) lined titanium cell dies. The pellet's resistance was determined as the extrapolated high frequency intercept with the real x-axis of the Nyquist plot. Conductivity was calculated using equation (1), where L and A represent the pellet's thickness and cross-sectional area, respectively, while R is the measured resistance.

$$\sigma = L / R \times A$$

The material's activation energy was determined by taking EIS measurements over a range of temperatures. These tests were performed during the heating process within a small box furnace, allowing the temperature to equilibrate for one hour between scans. The activation energy could be directly determined by measuring the slope of the Arrhenius plot of the resulting conductivity values.

4.5.2. Experimental Procedure:

Synthesis procedure for ICOF-201-Li:

1,4-benzenedimethanol (41.4 mg, 0.3 mmol, 2 eq) and lithium borohydride (3.3 mg, 0.15 mmol, 1 eq) was added to an ampule. Then 1 mL of benzonitrile was added. The vial was frozen in liquid nitrogen and sealed under vacuum (100 mTor). The resulting mixture was heated at 150°C for 7 days. At the end of the reaction period, the polymer was isolated by rinsing the ampule with acetonitrile and centrifuging down the polymer. The polymer was washed with additional acetonitrile (2x 5 mL) and THF (2x 5 mL). The yield of the polymer was 34.8 mg (80%).

Synthesis of ICOF-202-Li:

4,4'-bis(hydroxymethyl)biphenyl (64.3 mg, 0.3 mmol, 2 eq) and lithium borohydride (3.3 mg, 0.15 mmol, 1 eq) was added to an ampule. Then 1 mL of benzonitrile was added. The vial was frozen in liquid nitrogen and sealed under vacuum (100 mTor). The resulting mixture was heated at 150°C for 7 days. At the end of the reaction period, the polymer was isolated by rinsing the ampule with acetonitrile and centrifuging down the polymer. The polymer was washed with additional acetonitrile (2x 5 mL) and THF (2x 5 mL). The yield of the polymer was 53.1 mg (87%).

Synthesis of ICOF-203-Li:

2,3,5,6-tetrafluoro-1,4-benzenedimethanol (63 mg, 0.3 mmol, 2 eq) and lithium borohydride (3.3 mg, 0.15 mmol, 1 eq) was added to an ampule. Then 1.5 mL of acetonitrile was added. The vial was frozen in liquid nitrogen and sealed under vacuum (100 mTor). The resulting mixture was heated at 150°C for 7 days. At the end of the reaction period, the polymer was isolated by rinsing the ampule with acetonitrile and centrifuging down the polymer. The polymer was washed with additional acetonitrile (2x 5 mL) and THF (2x 5 mL). The yield of the polymer was 50.8 mg (78%)

Synthesis of ICOF-203-Na:

2,3,5,6-tetrafluoro-1,4-benzenedimethanol (63 mg, 0.3 mmol, 2 eq) and sodium borohydride (5.7 mg, 0.15 mmol, 1 eq) was added to an ampule. Then 1 mL of acetonitrile was added. The vial was frozen in liquid nitrogen and sealed under vacuum (100 mTor). The resulting mixture was heated at 150°C for 7 days. At the end of the reaction period, the polymer was isolated by rinsing the ampule with acetonitrile and centrifuging down the polymer. The polymer was washed with additional acetonitrile (2x 5 mL) and THF (2x 5 mL). The yield of the polymer was 58.7 mg (87%).

4.5.3. ICOF-201-Li characterization.

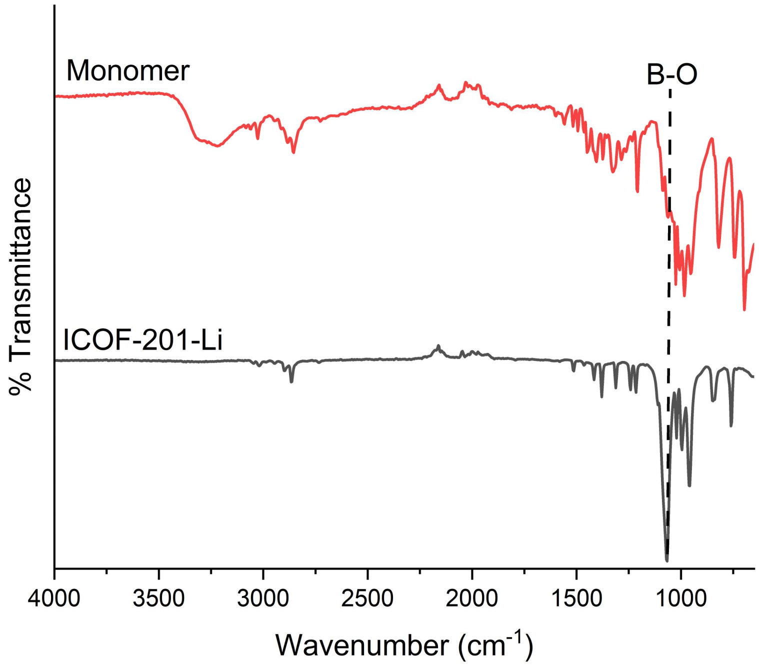

Figure 4.5. FT-IR of ICOF-201-Li and its monomer.

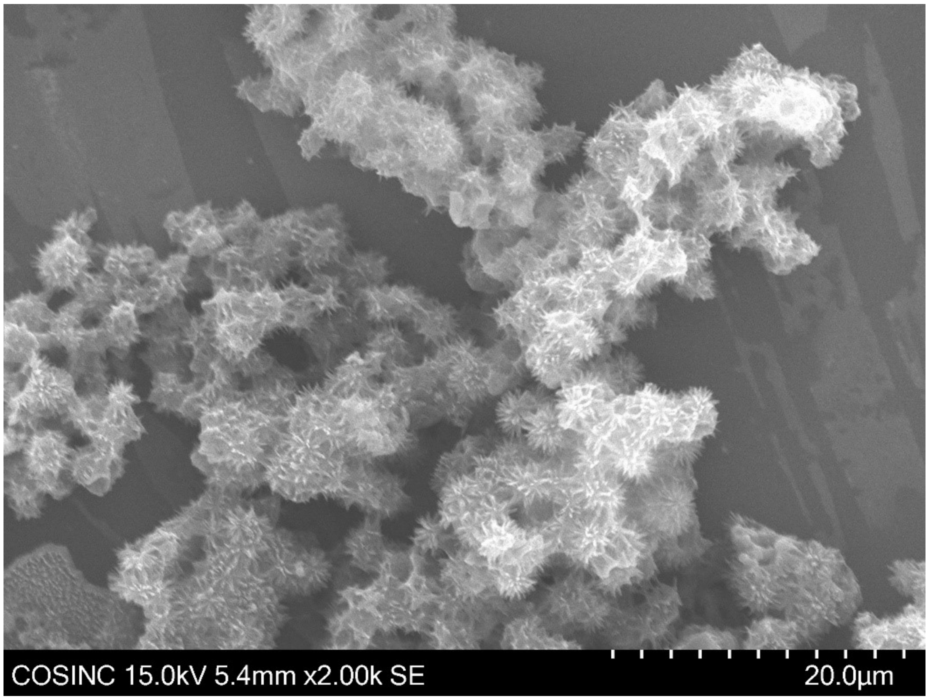

Figure 4.6. SEM image of ICOF-201-Li.

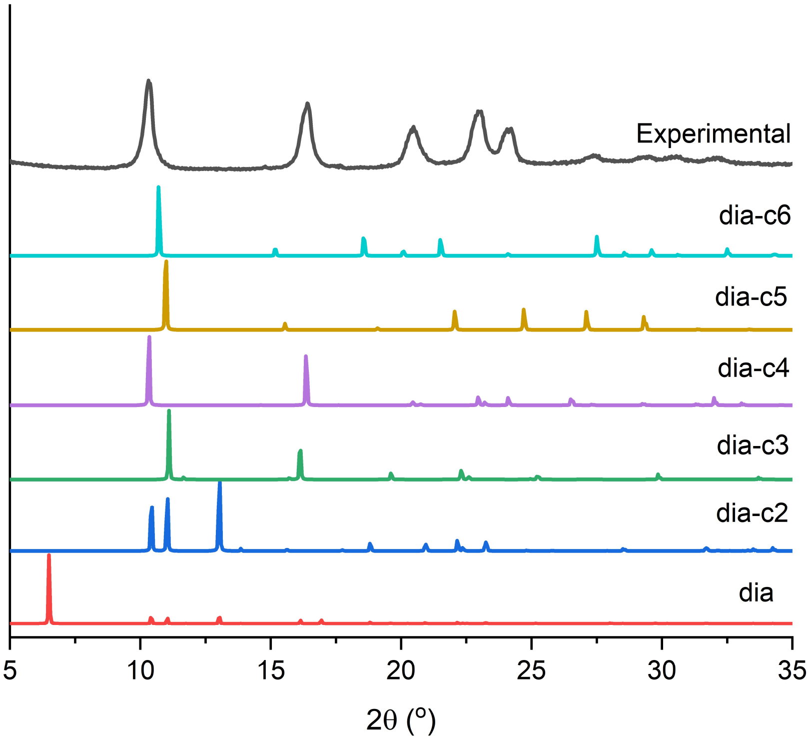

Figure 4.7. Simulated models for ICOF-201-Li from non-interpreted to six-fold interpenetrated.

4.5.4. Characterization of ICOF-202-Li, ICOF-203-Li and ICOF-203-Na

4.5.4.1. COF-202-Li

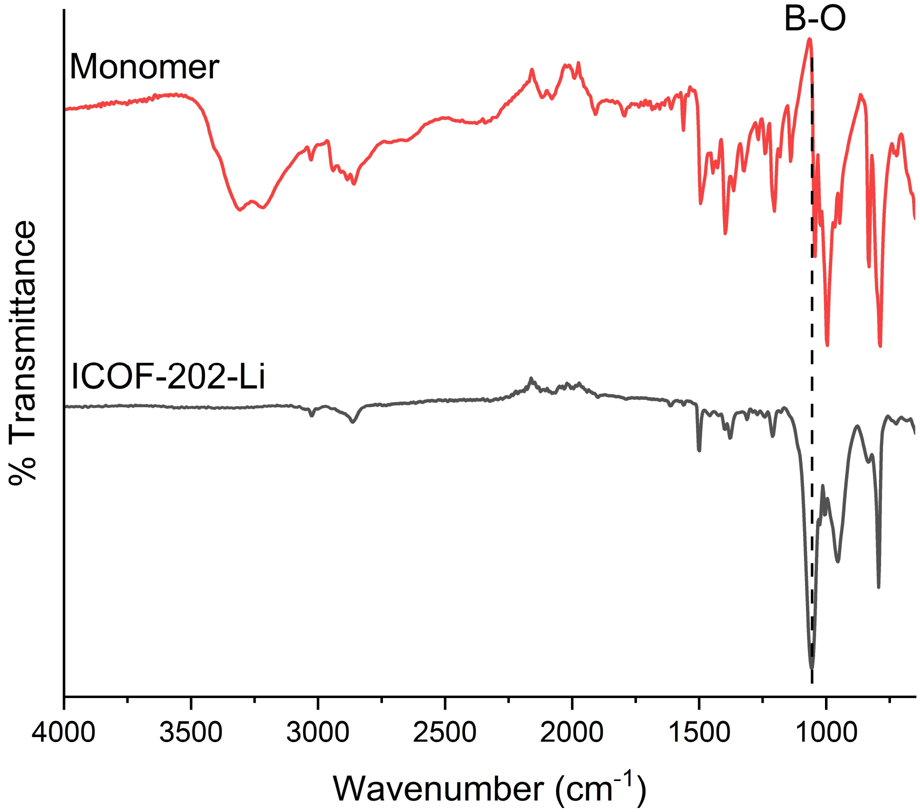

Figure 4.8. FT-IR of ICOF-202-Li and its monomer.

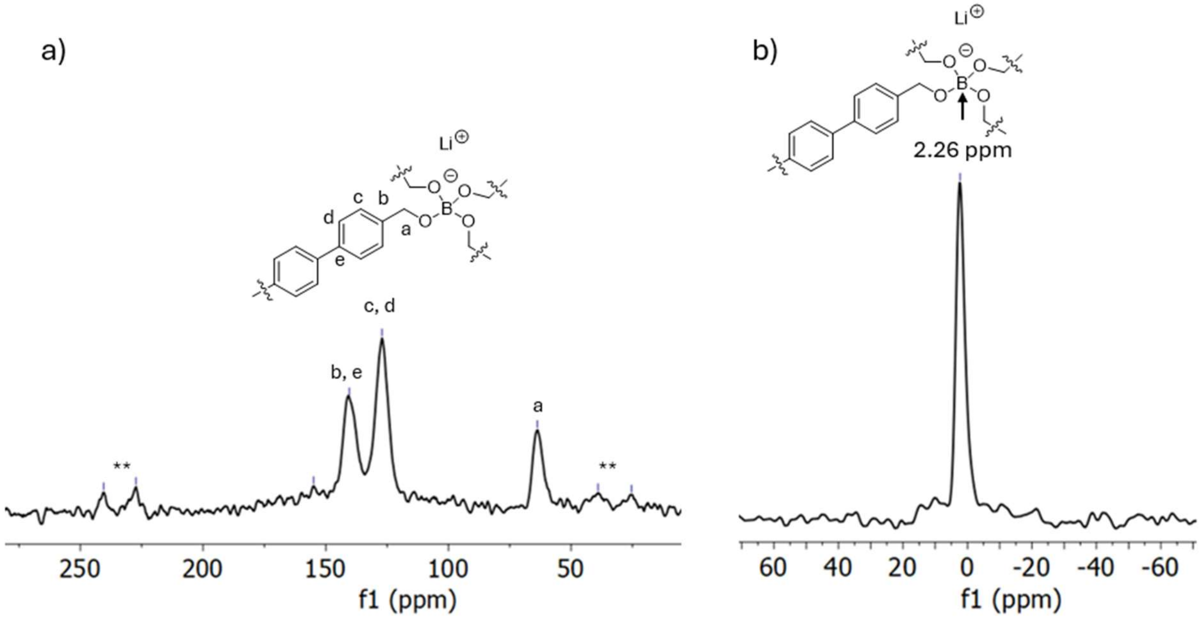

Figure 4.9. Solid state ^{13}C NMR (a) and ^{11}B NMR (b) of ICOF 202-Li.

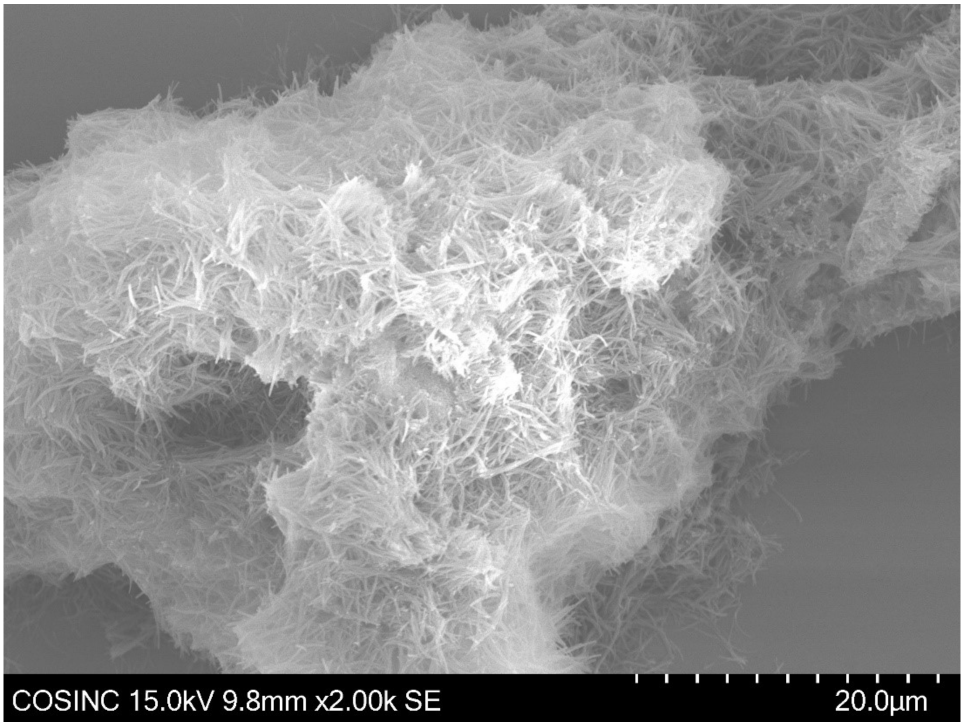

Figure 4.10. SEM of ICOF-202-Li.

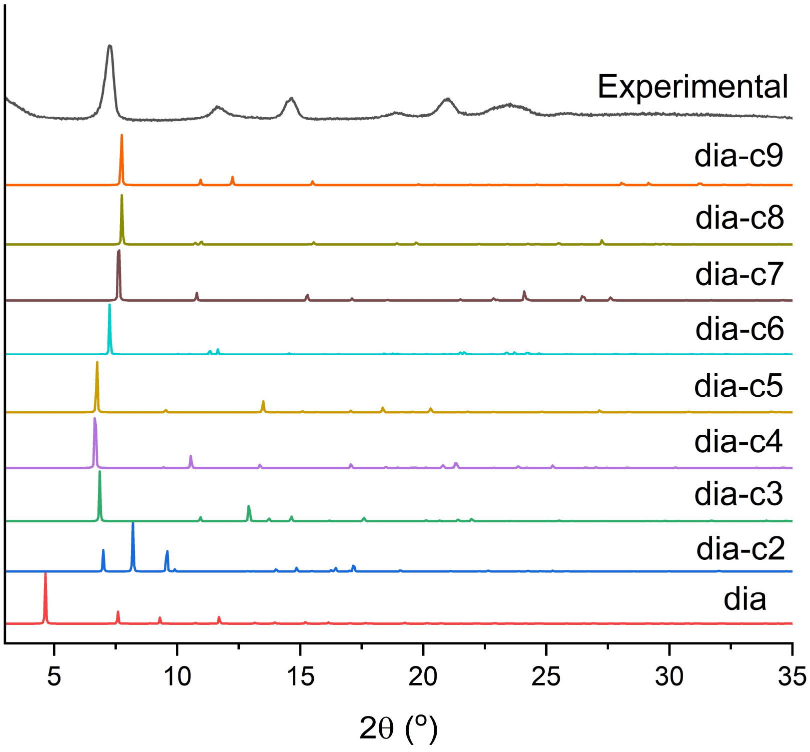

Figure 4.11. Simulated models for ICOF-202-Li from non-interpreted to nine-fold interpenetrated.

4.5.4.2 ICOF-203-Li

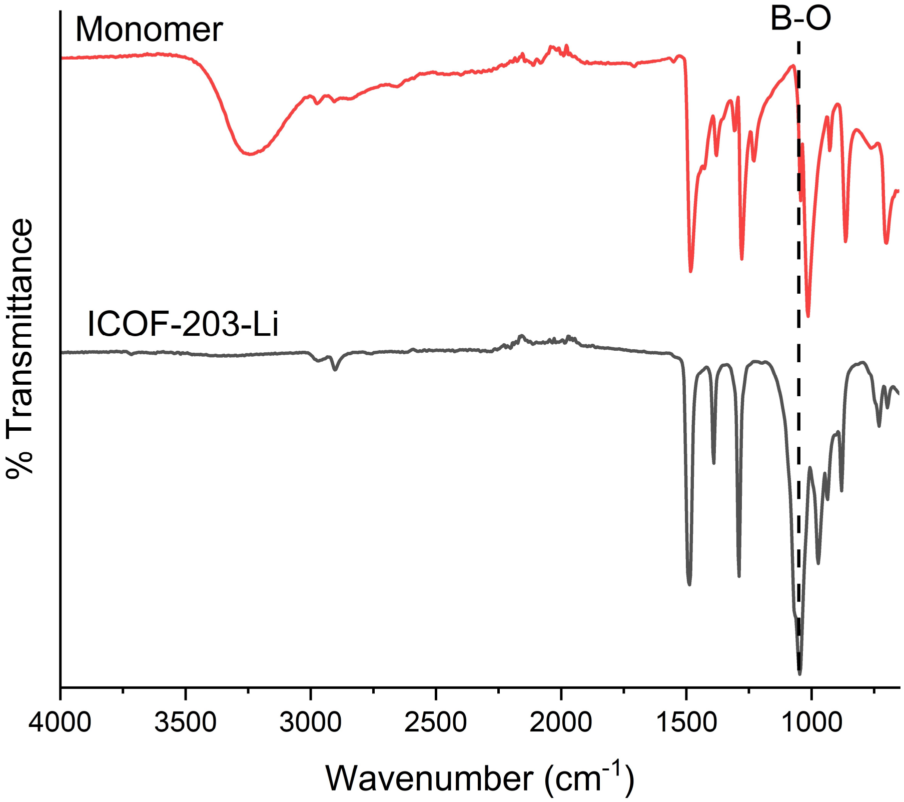

Figure 4.12. FTIR ICOF-203-Li and its monomer.

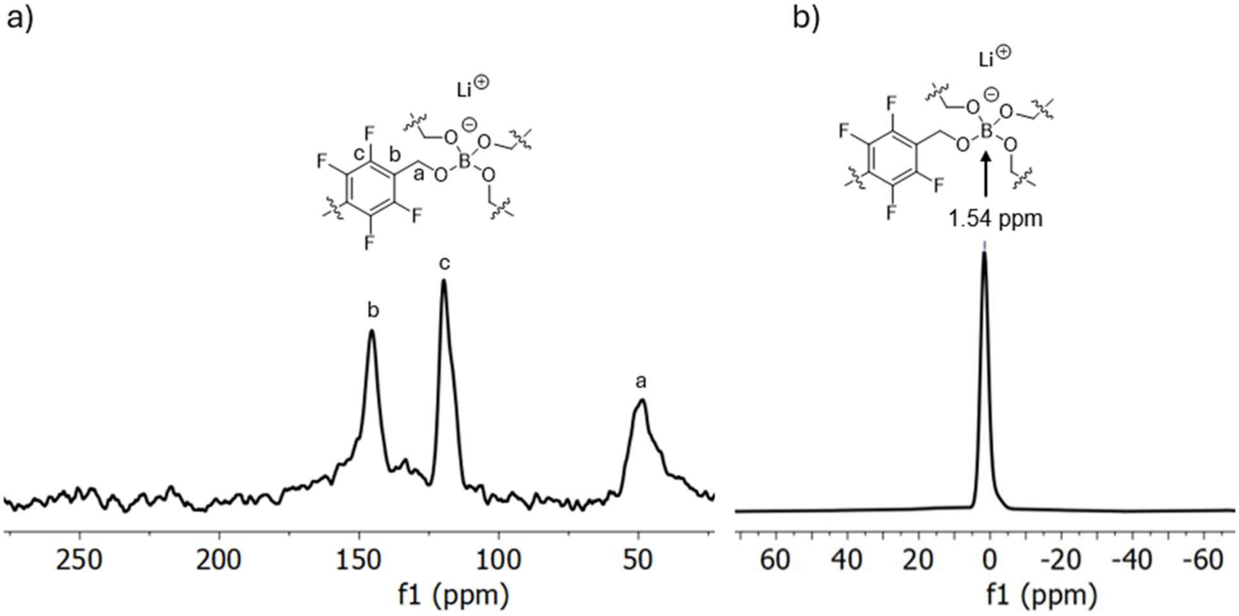

Figure 4.13. Solid state ^{13}C NMR (a) and ^{11}B NMR (b) of ICOF 203-Li.

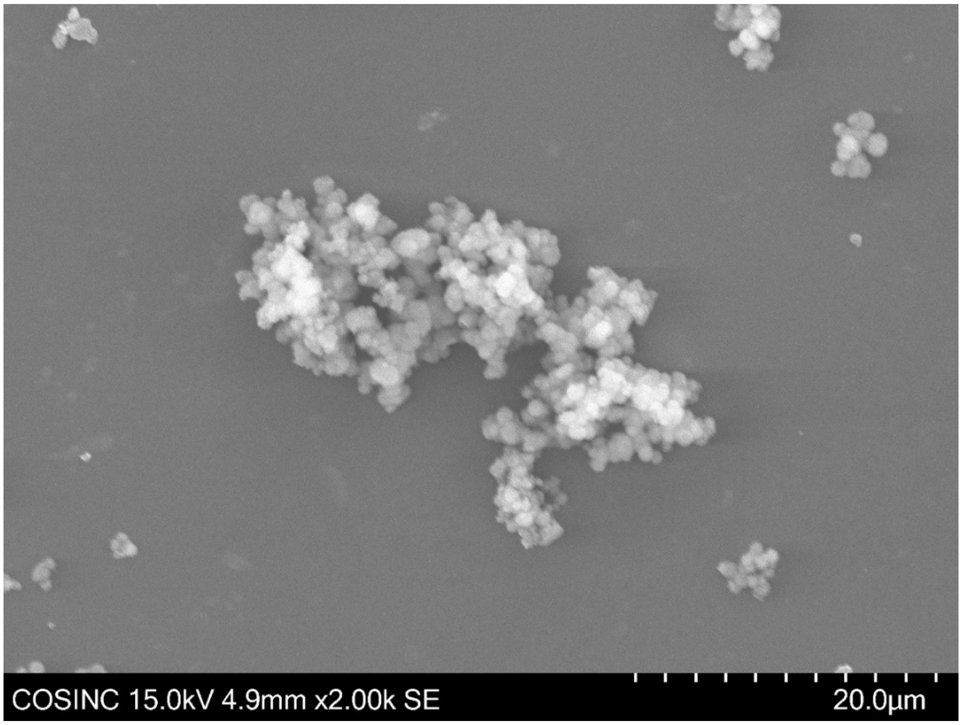

Figure 4.14. SEM of ICOF-203-Li.

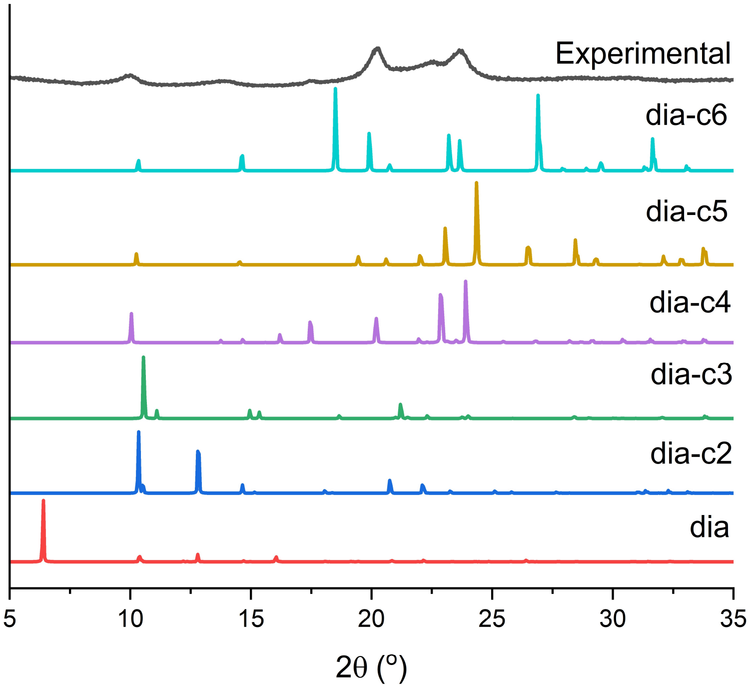

Figure 4.15. Simulated models for ICOF-203-Li from non-interpreted to six-fold interpenetrated.

4.5.4.3 ICOF-203-Na

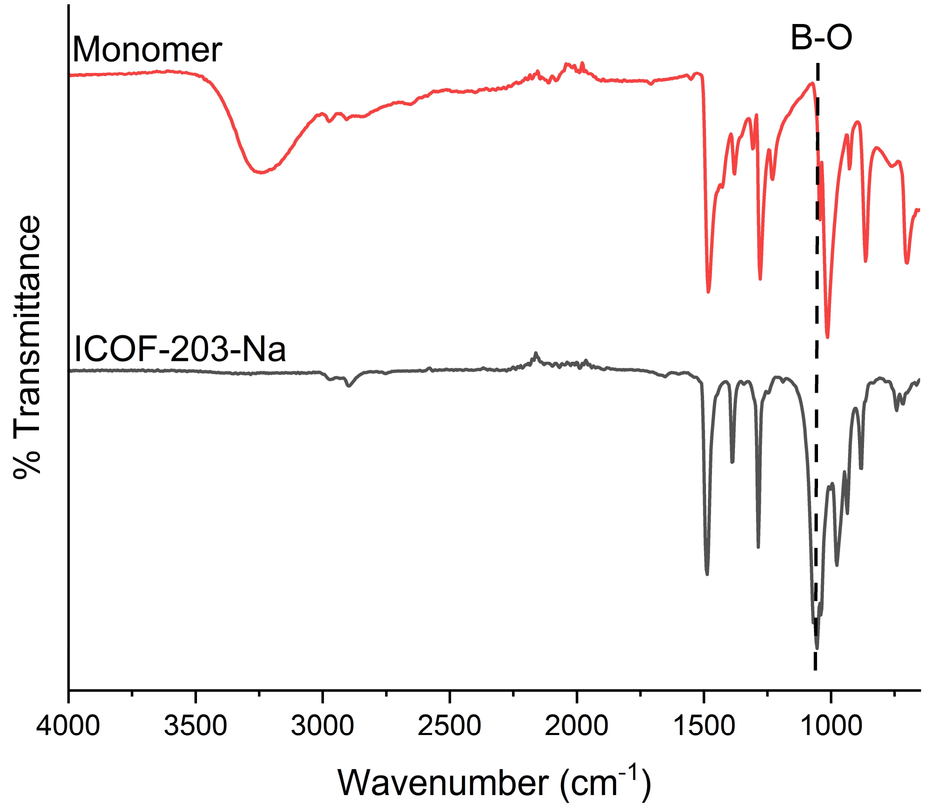

Figure 4.16. FTIR ICOF-203-Na and its monomer.

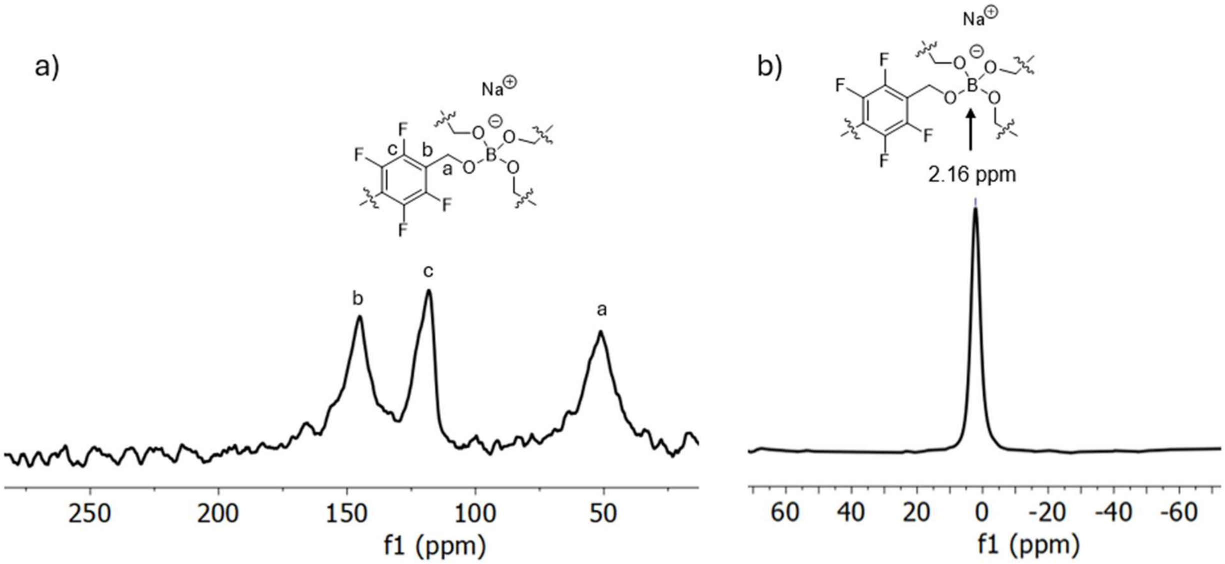

Figure 4.17. Solid state ^{13}C NMR (a) and ^{11}B NMR (b) of ICOF 203-Na.

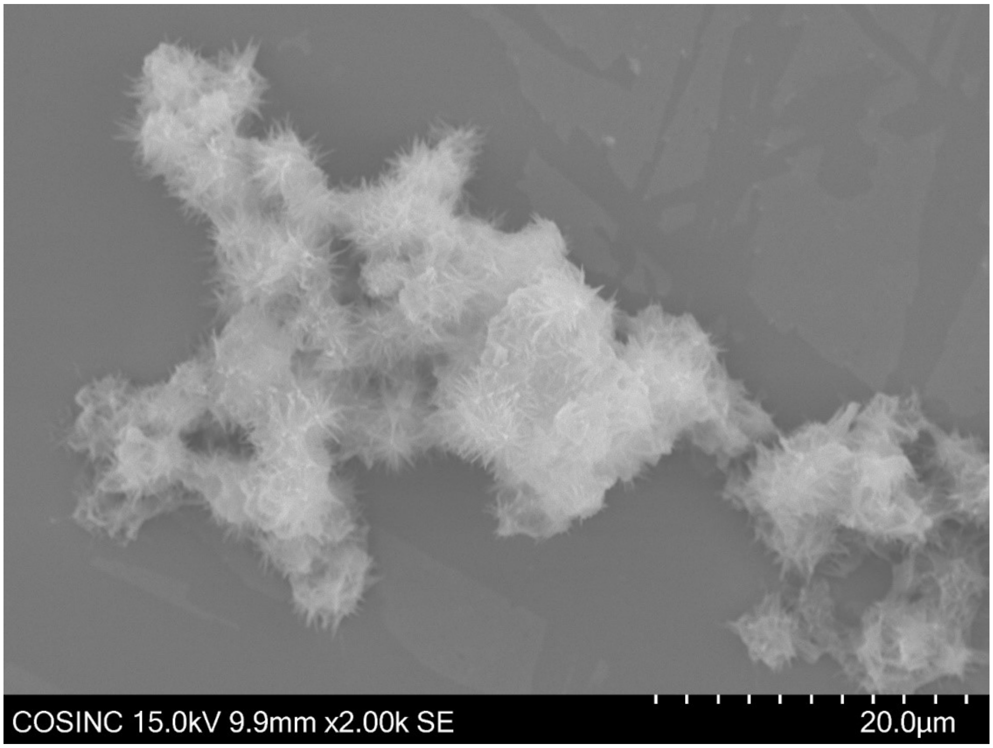

Figure 4.18. SEM of ICOF-203-Na.

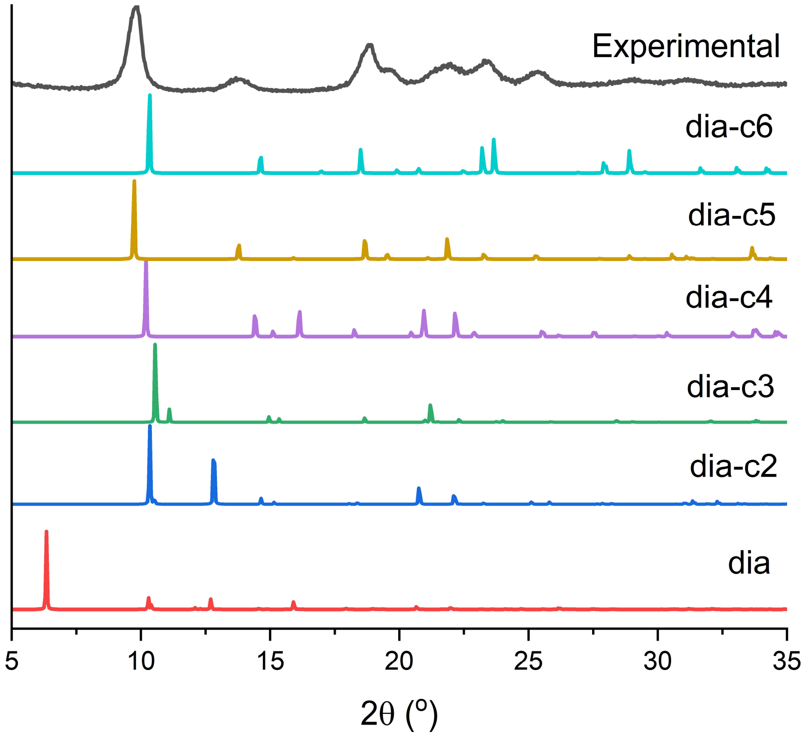

Figure 4.19. Simulated models for ICOF-203-Na from non-interpreted to six-fold interpenetrated.

4.5.5. Solvent Stability

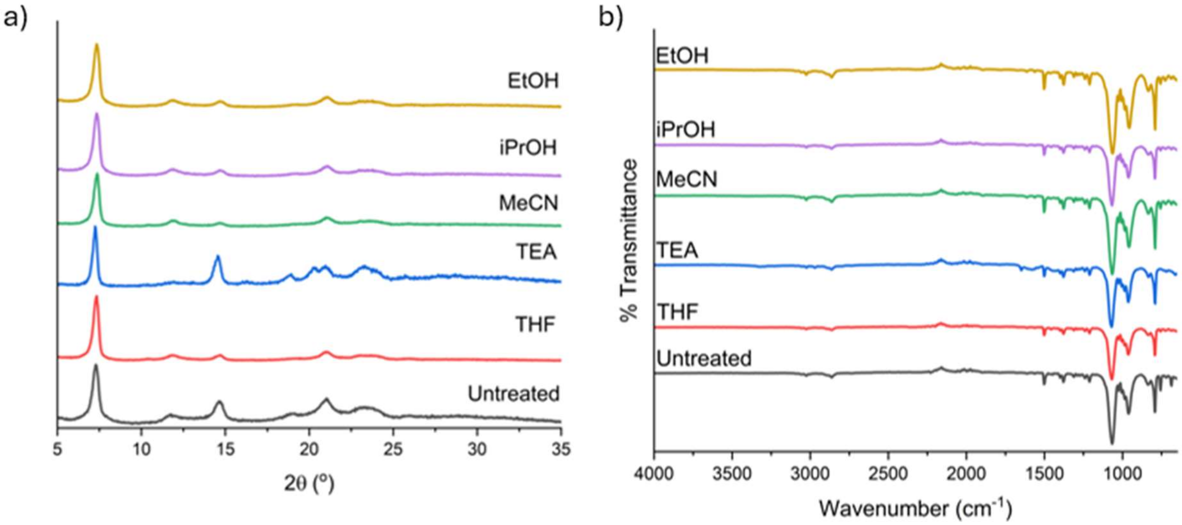

Figure 4.20. (a) PXRD and (b) FTIR of ICOF-202-Li after being soaked in different solvents.

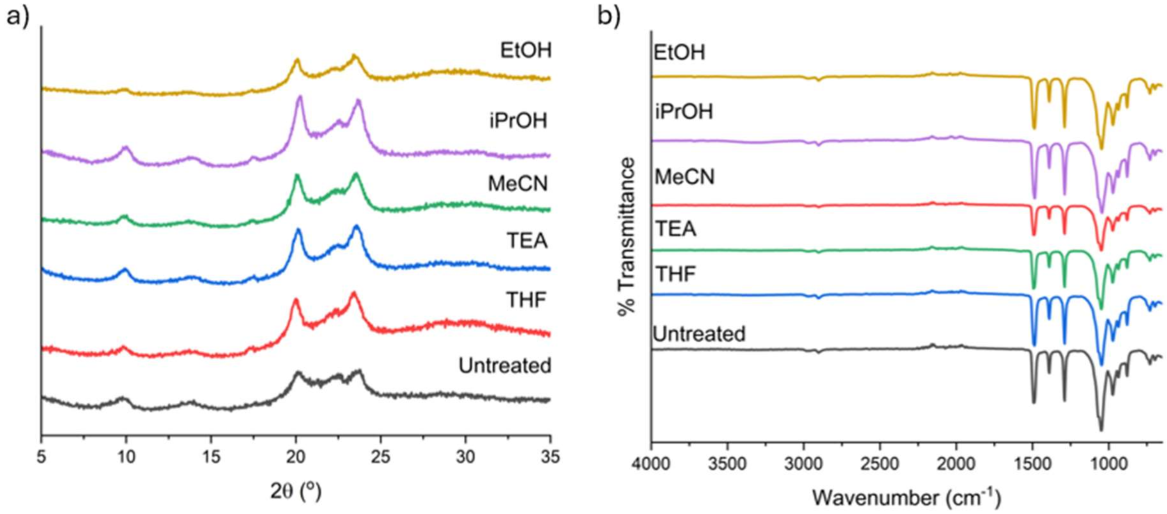

Figure 4.21. (a) PXRD and (b) FTIR of ICOF-203-Li after being soaked in different solvents.

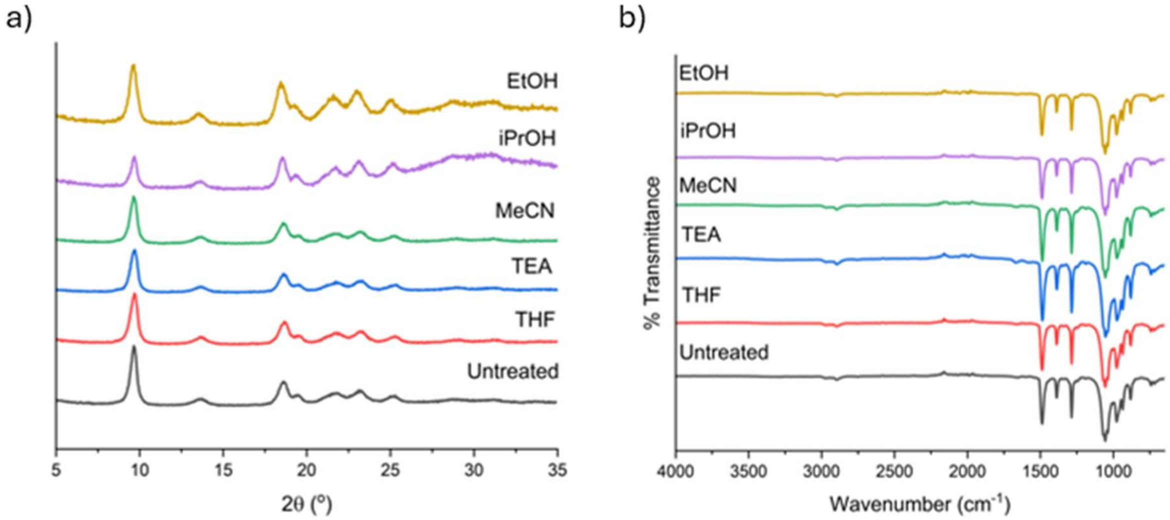

Figure 4.22. (a) PXRD and (b) FTIR of ICOF-203-Na after being soaked in different solvents.

4.5.6. Gas Adsorption

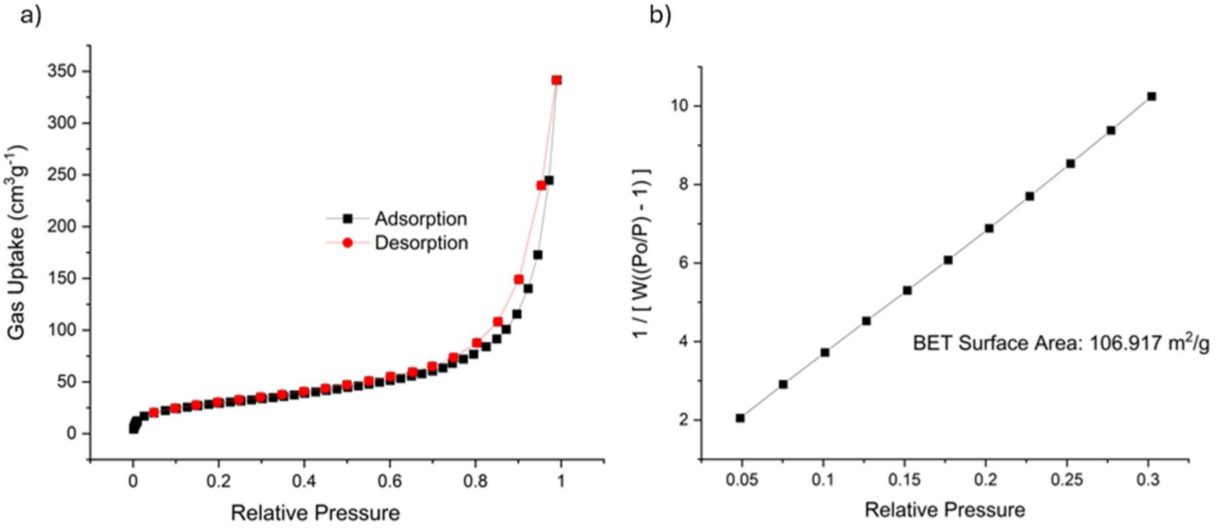

Figure 4.23. The nitrogen isotherm (a) and BET surface area (b) of ICOF-201-Li.

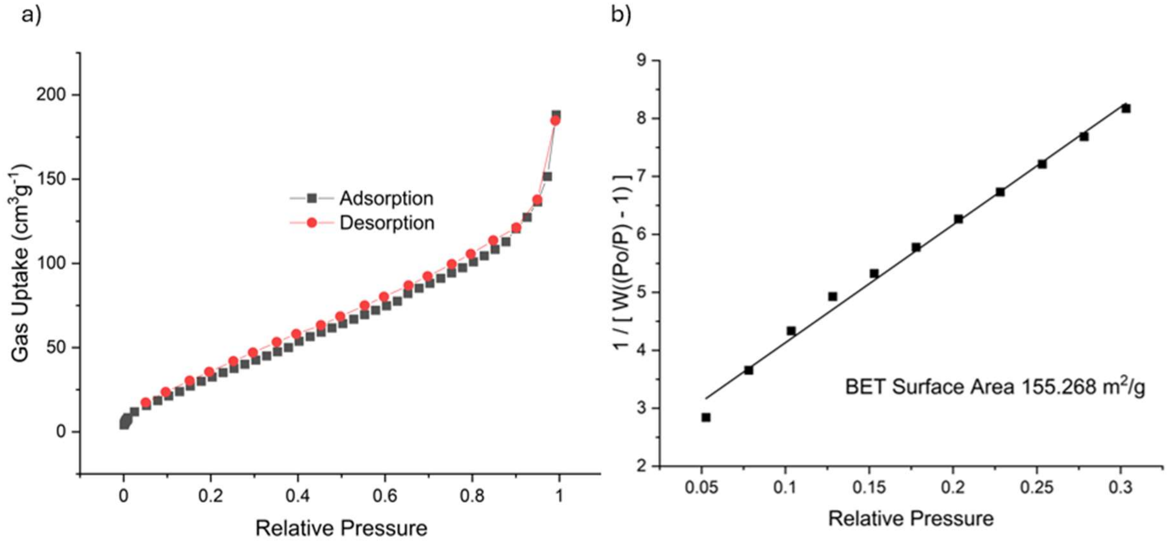

Figure 4.24. The nitrogen isotherm (a) and BET surface area (b) of ICOF-202-Li.

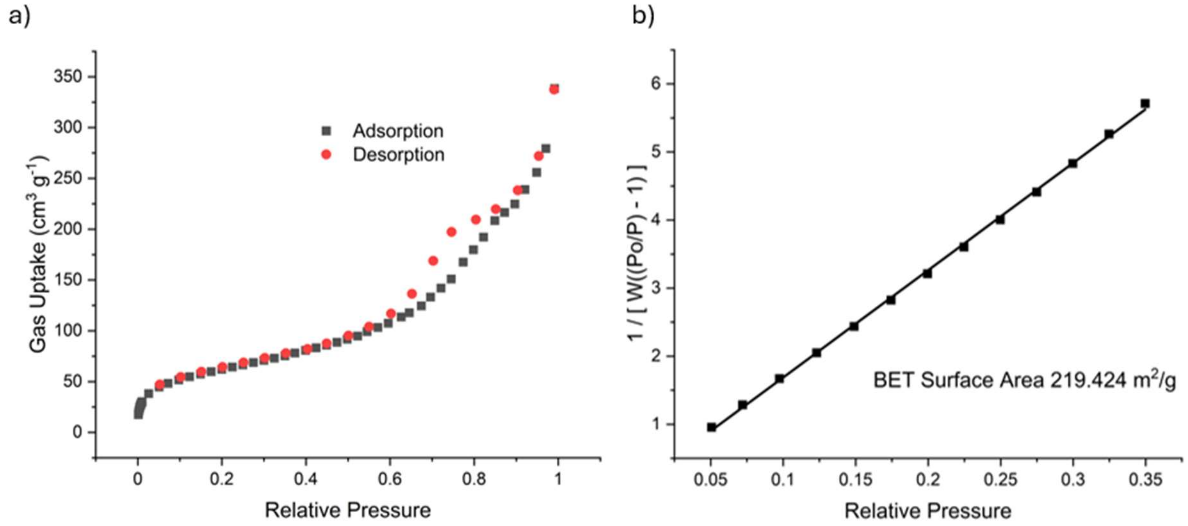

Figure 4.25. The nitrogen isotherm (a) and BET surface area (b) of ICOF-203-Li.

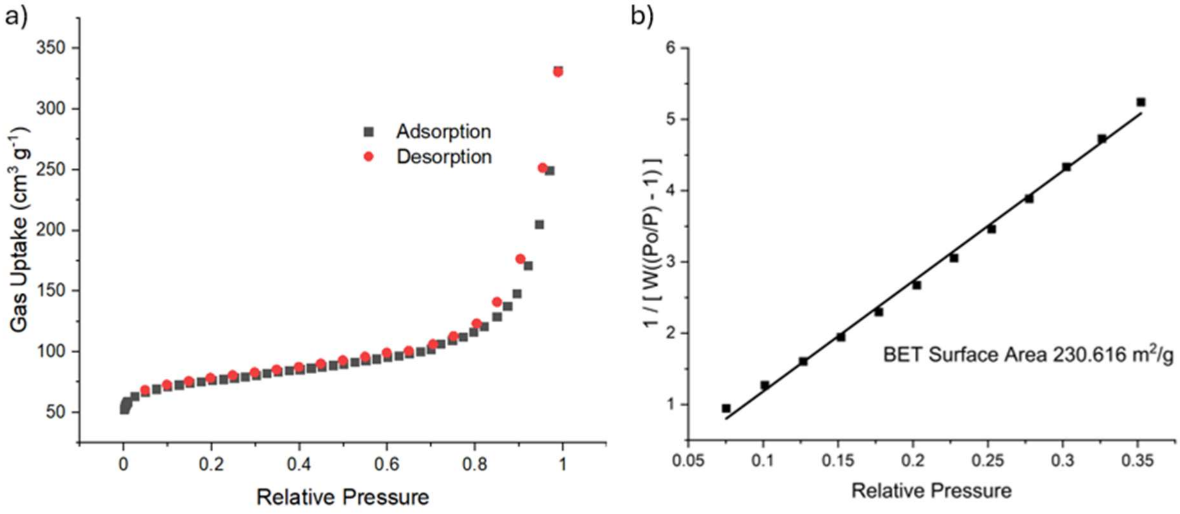

Figure 4.26. The nitrogen isotherm (a) and BET surface area (b) of ICOF-203-Na..

4.5.7 Thermogravimetric analysis

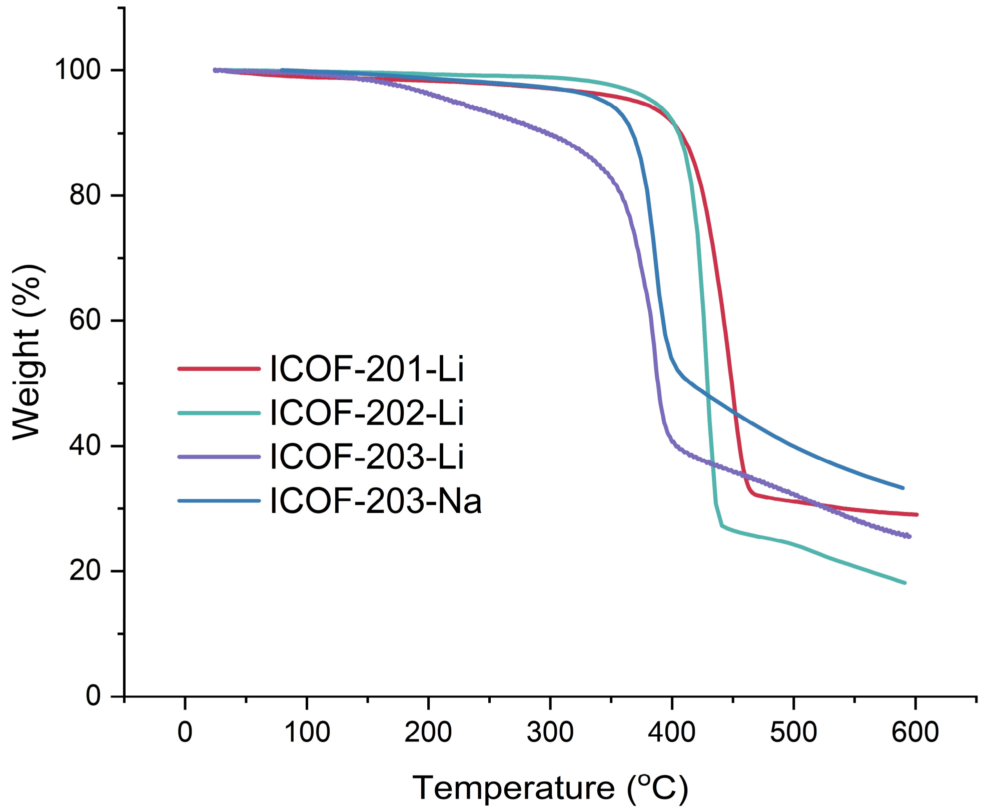

Figure 4.27. Thermogravimetric analysis of ICOFs.

4.5.8. Impendence measurements.

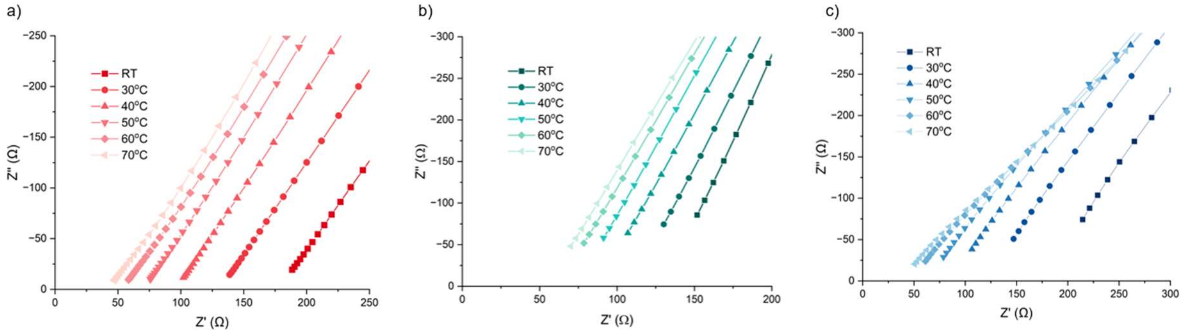

Figure 4.28. Variable temperature impendence measurements of ICOF-201-Li (a), ICOF-202-Li (b), and ICOF-203-Na (c).

4.5.9 . Atom Coordination Tables

4.5.9.1 Atom coordination tables of ICOF-201-Li models

Table 4.2. Atom coordination table of dia model of ICOF-201-Li.

<table>
<tr><td colspan="4">ICOF-201-Li Dia</td></tr>
<tr><td colspan="4">Space Group: I41/AMD
a= b= 17.0878
c= 23.1015
α= β= γ= 90</td></tr>
<tr><td>H</td><td>0.56088</td><td>-0.05447</td><td>0.36003</td></tr>
<tr><td>H</td><td>0.71795</td><td>0</td><td>0.27027</td></tr>
<tr><td>H</td><td>0.85467</td><td>0.5</td><td>0.94937</td></tr>
<tr><td>B</td><td>0.5</td><td>0</td><td>0.25</td></tr>
<tr><td>C</td><td>1.23089</td><td>-0.5</td><td>0.81613</td></tr>
<tr><td>C</td><td>1.17065</td><td>-0.5</td><td>0.85771</td></tr>
<tr><td>C</td><td>1.19072</td><td>-0.5</td><td>0.91662</td></tr>
<tr><td>O</td><td>1.07643</td><td>-0.5</td><td>0.78091</td></tr>
<tr><td>C</td><td>1.08505</td><td>-0.5</td><td>0.84135</td></tr>
<tr><td>Li</td><td>1</td><td>0</td><td>0</td></tr>
</table>

Table 4.3. Atom coordination table of dia-c2 model of ICOF-201-Li.

ICOF-201-Li dia-c2			
Space Group: P42/NNM a= b= 12.0947 Å c= 11.4769 Å α= β= γ= 90°			
H	0.5065	0.6153	0.72142
H	0.78277	0.78277	0.96051
H	0.646	0.646	0.90065
C	0.76952	0.76952	0.86831
C	0.82939	0.82939	0.78405
C	0.80892	0.80892	0.66567
C	0.91499	0.91499	0.81629
O	0.92371	0.92371	0.93787
B	0	0	0
Li	0.5	0.5	0

Table 4.4. Atom coordination table of dia-c3 model of ICOF-201-Li.

ICOF-201-Li dia-c3			
Space Group: I41/AMD a= b= 16.6099 Å c= 8.6567 Å α= β= γ= 90°			
H	0.43848	0.55624	0.79014
H	0.5	0.26459	1.41127
H	0.5	0.13101	1.29168
C	0.74067	0.5	0.71338
C	0.67219	0.5	0.80707
C	0.68279	0.5	0.96852
O	0.58019	0.5	0.58297
C	0.58678	0.5	0.74513
B	0	0	1
Li	0.5	0.5	1

Table 4.5. Atom coordination table of dia-c4 model of ICOF-201-Li.

ICOF-201-Li dia-c4			
Space Group: P-4B2 a= b= 12.1087 Å c= 5.0392 Å α= β= γ= 90°			
O	0.0702	0.93642	0.18466
C	0.0375	0.82791	0.19842
C	0.24698	0.1124	0.64603

C	0.24547	0.11073	0.367
C	0.31923	0.18481	0.77813
H	0.03029	0.79431	-0.0122
H	-0.04713	0.82275	0.29677
H	0.18738	0.05225	0.2577
H	0.32106	0.18703	1.00425
B	0	0	0
Li	0	0	0.5

Table 4.6. Atom coordination table of dia-c5 model of ICOF-201-Li.

ICOF-201-Li dia-c5			
Space Group: I41/A a= b= 16.1186 Å c= 4.8533 Å α= β= γ= 90°			
C	0.43534	0.72015	0.96099
C	0.51593	0.68969	0.92391
C	0.58056	0.72006	0.08731
O	0.47453	0.56633	0.68928
C	0.53482	0.62899	0.70071
H	0.38255	0.69617	0.82649
H	0.64636	0.69594	0.05573
H	0.59807	0.59977	0.74108
H	0.53625	0.66247	0.49385
Li	0	1	0.5
B	0	0.5	0.25

Table 4.7. Atom coordination table of dia-c6 model of ICOF-201-Li.

ICOF-201-Li dia-c6			
Space Group: P42/NNM a= b= 12.1096 Å c= 5.2208 Å α= β= γ= 90°			
C	0.35005	0.78983	0.66054
H	0.42335	0.82662	0.5857
H	0.38739	0.28468	0.79562
O	-0.0627	-0.0627	-0.18532
C	-0.18808	0.18808	-0.06913
C	-0.14489	0.14489	0.18224
B	0	0	0
Li	0	0	0.5

4.5.9.2 Atom coordination tables of ICOF-202-Li models

Table 4.8. Atom coordination table of dia model of ICOF-202-Li.

<table>
<tr><td colspan="4">ICOF-202-Li dia</td></tr>
<tr><td colspan="4">Space Group: I41/AMD
a= b= 23.2819 Å
c= 32.9738 Å
α= β= γ= 90°</td></tr>
<tr><td>H</td><td>0.38821</td><td>0.96126</td><td>-0.25875</td></tr>
<tr><td>H</td><td>0.34879</td><td>0</td><td>-0.10309</td></tr>
<tr><td>H</td><td>0.5</td><td>0.28089</td><td>0.50499</td></tr>
<tr><td>H</td><td>0.5</td><td>0.21067</td><td>-0.44265</td></tr>
<tr><td>H</td><td>0.08341</td><td>0.5</td><td>0.34349</td></tr>
<tr><td>C</td><td>0.20464</td><td>0.5</td><td>0.28622</td></tr>
<tr><td>C</td><td>0.14597</td><td>0.5</td><td>0.29489</td></tr>
<tr><td>C</td><td>0.12853</td><td>0.5</td><td>0.33554</td></tr>
<tr><td>O</td><td>0.04744</td><td>0.5</td><td>0.27401</td></tr>
<tr><td>C</td><td>0.10373</td><td>0.5</td><td>0.26017</td></tr>
<tr><td>C</td><td>0</td><td>0.66901</td><td>0.13317</td></tr>
<tr><td>C</td><td>0</td><td>0.72905</td><td>0.14111</td></tr>
<tr><td>C</td><td>0</td><td>0.74538</td><td>0.18267</td></tr>
<tr><td>B</td><td>0.5</td><td>0</td><td>-0.25</td></tr>
<tr><td>Li</td><td>0.5</td><td>0.5</td><td>0</td></tr>
</table>

Table 4.9. Atom coordination table of dia-c2 model of ICOF-202-Li.

<table>
<tr><td colspan="4">ICOF-202-Li dia-c2</td></tr>
<tr><td colspan="4">Space Group: P42/NNM
a= b= 17.8639 Å
c= 13.5266
α= β= γ= 90°</td></tr>
<tr><td>C</td><td>0.29032</td><td>0.61431</td><td>0.38754</td></tr>
<tr><td>C</td><td>0.24782</td><td>0.65653</td><td>0.32112</td></tr>
<tr><td>H</td><td>0.26931</td><td>0.56059</td><td>0.41233</td></tr>
<tr><td>H</td><td>0.19547</td><td>0.63213</td><td>0.29868</td></tr>
<tr><td>H</td><td>0.36659</td><td>0.56228</td><td>0.5403</td></tr>
<tr><td>C</td><td>0.27305</td><td>0.72695</td><td>0.28601</td></tr>
<tr><td>C</td><td>0.64078</td><td>0.35922</td><td>0.42164</td></tr>
<tr><td>C</td><td>-0.09485</td><td>-0.09485</td><td>-0.00806</td></tr>
<tr><td>O</td><td>-0.04737</td><td>-0.04737</td><td>-0.06381</td></tr>
<tr><td>B</td><td>0</td><td>0</td><td>0</td></tr>
<tr><td>Li</td><td>0</td><td>0</td><td>0.5</td></tr>
</table>

Table 4.10. Atom coordination table of dia-c3 model of ICOF-202-Li.

ICOF-202-Li dia-c3			
Space Group: I41/AMD a= b= 25.7943 Å c= 8.5161 Å α= β= γ= 90°			
C	0.14027	0.4533	0.94842
C	0.19318	0.45317	0.91333
H	0.21084	0.41558	0.90202
H	0.12024	0.41666	0.96223
H	0.45984	0.53587	0.79878
C	0.27873	0	0.3943
C	0.61334	0.5	0.78463
O	0.55075	0.5	0.58365
C	0.55636	0.5	0.74734
B	0	0	1
Li	0.5	0.5	1

Table 4.11. Atom coordination table of dia-c4 model of ICOF-202-Li.

ICOF-202-Li dia-c4			
Space Group: P-4B2 a= b= 18.7314 Å c= 4.7989 Å α= β= γ= 90°			
O	0.0412	0.95407	0.18967
C	0.0188	0.8819	0.19614
C	0.16422	0.07689	0.68562
C	0.22085	0.06002	0.50577
C	0.15715	0.14719	0.78406
C	0.20574	0.19975	0.70391
C	0.27061	0.1123	0.43148
C	0.26369	0.18216	0.53326
H	0.46878	0.62304	0.31978
H	0.51022	0.6404	-0.01587
H	0.09819	0.68504	0.70253
H	0.00588	0.77184	0.56819
H	0.38477	0.66112	0.92887
H	0.30045	0.75358	0.78231
B	0	0	0
Li	0	0	0.5

Table 4.12. Atom coordination table of dia-c5 model of ICOF-202-Li.

<table>
<tr><td colspan="4">ICOF-202-Li dia-c5</td></tr>
<tr><td colspan="4">Space Group: I41/AMD
a= b= 26.2477 Å
c= 6.4636 Å
α= β= γ= 90°</td></tr>
<tr><td>H</td><td>0.40134</td><td>0.4658</td><td>0.96658</td></tr>
<tr><td>H</td><td>0.33544</td><td>0.5</td><td>1.19238</td></tr>
<tr><td>H</td><td>0.25568</td><td>0.5</td><td>1.03955</td></tr>
<tr><td>C</td><td>0.72212</td><td>0.5</td><td>0.63893</td></tr>
<tr><td>C</td><td>0.32156</td><td>0.5</td><td>0.75686</td></tr>
<tr><td>H</td><td>0.58865</td><td>0</td><td>0.85158</td></tr>
<tr><td>C</td><td>0.72305</td><td>0</td><td>0.81911</td></tr>
<tr><td>C</td><td>0.67173</td><td>0</td><td>0.90264</td></tr>
<tr><td>C</td><td>0.62575</td><td>0</td><td>0.77862</td></tr>
<tr><td>O</td><td>0.53903</td><td>0</td><td>1.4266</td></tr>
<tr><td>C</td><td>0.59071</td><td>0</td><td>1.38004</td></tr>
<tr><td>C</td><td>0.6298</td><td>0</td><td>0.56235</td></tr>
<tr><td>H</td><td>0.31901</td><td>1</td><td>1.34056</td></tr>
<tr><td>B</td><td>0</td><td>0.5</td><td>0.75</td></tr>
<tr><td>Li</td><td>0</td><td>0</td><td>1</td></tr>
</table>

Table 4.13. Atom coordination table of dia-c6 model of ICOF-202-Li.

<table>
<tr><td colspan="4">ICOF-202-Li dia-c6</td></tr>
<tr><td colspan="4">Space Group: PNN2
a= 16.8265 Å
b= 17.6382 Å
c= 4.8701 Å
α= β= γ= 90°</td></tr>
<tr><td>C</td><td>0.54073</td><td>0.73412</td><td>0.99034</td></tr>
<tr><td>C</td><td>0.58935</td><td>0.7822</td><td>0.83628</td></tr>
<tr><td>H</td><td>0.47482</td><td>0.34994</td><td>0.52157</td></tr>
<tr><td>H</td><td>0.24515</td><td>0.48852</td><td>1.03469</td></tr>
<tr><td>H</td><td>0.16277</td><td>0.57538</td><td>0.30259</td></tr>
<tr><td>H</td><td>-0.04188</td><td>0.87194</td><td>-0.259</td></tr>
<tr><td>H</td><td>1.12093</td><td>0.17752</td><td>0.2187</td></tr>
<tr><td>H</td><td>0.2025</td><td>0.26494</td><td>0.48993</td></tr>
<tr><td>C</td><td>0.75767</td><td>0.95135</td><td>0.5264</td></tr>
<tr><td>C</td><td>0.70998</td><td>0.90152</td><td>0.67681</td></tr>
<tr><td>C</td><td>0.27638</td><td>0.17709</td><td>0.66736</td></tr>
<tr><td>C</td><td>0.57327</td><td>0.67236</td><td>0.13274</td></tr>
<tr><td>O</td><td>0.54652</td><td>0.54814</td><td>0.31761</td></tr>
<tr><td>C</td><td>0.86914</td><td>0.97752</td><td>0.19417</td></tr>
</table>

C	0.66693	0.34523	-0.1496
C	0.71378	0.29536	0.00437
H	0.34389	0.52582	0.48406
H	0.68266	0.61575	0.24353
H	0.76792	0.69827	0.96571
H	0.86298	1.03652	1.2721
H	-0.02234	-0.24578	0.50095
H	0.0623	0.67113	0.22613
C	0.8442	0.16089	0.62513
C	0.79557	0.20829	0.4674
C	0.17183	0.72994	0.3238
C	0.67954	0.4238	0.86552
O	0.55	0.45547	0.69444
C	0.97922	0.12461	0.8136
B	0	0	0.00581
Li	0	0	0.50637

Table 4.14. Atom coordination table of dia-c7 model of ICOF-202-Li.

<table>
<tr><td colspan="4">ICOF-202-Li dia-c7</td></tr>
<tr><td colspan="4">Space Group: I41/A
a= b= 23.1869 Å
c= 4.8884 Å
α= β= γ= 90 °</td></tr>
<tr><td>C</td><td>0.70261</td><td>1.03984</td><td>0.63787</td></tr>
<tr><td>O</td><td>0.54885</td><td>1.00871</td><td>0.06204</td></tr>
<tr><td>C</td><td>0.65941</td><td>1.0294</td><td>0.83095</td></tr>
<tr><td>C</td><td>0.63786</td><td>0.97379</td><td>0.8703</td></tr>
<tr><td>C</td><td>0.58911</td><td>0.96278</td><td>1.06647</td></tr>
<tr><td>C</td><td>0.72735</td><td>0.99436</td><td>0.48368</td></tr>
<tr><td>C</td><td>0.8353</td><td>1.07222</td><td>1.01358</td></tr>
<tr><td>C</td><td>0.43771</td><td>0.79139</td><td>0.95372</td></tr>
<tr><td>H</td><td>0.10863</td><td>0.45912</td><td>0.77239</td></tr>
<tr><td>H</td><td>0.0677</td><td>0.42137</td><td>0.51417</td></tr>
<tr><td>H</td><td>0.15155</td><td>0.38387</td><td>0.27803</td></tr>
<tr><td>H</td><td>0.22661</td><td>0.4</td><td>-0.04937</td></tr>
<tr><td>H</td><td>0.21594</td><td>0.58404</td><td>0.11638</td></tr>
<tr><td>H</td><td>0.14216</td><td>0.56506</td><td>0.44788</td></tr>
<tr><td>B</td><td>0.5</td><td>1</td><td>0.25</td></tr>
<tr><td>Li</td><td>0</td><td>0</td><td>0</td></tr>
</table>

Table 4.15. Atom coordination table of dia-c8 model of ICOF-202-Li.

ICOF-202-Li dia-c8			
Space Group: P4/NNC a= b= 16.1182 Å c= 9.5937 Å α= β= γ= 90°			
O	0.94251	1.45407	0.40095
C	0.80409	1.24298	0.04936
C	0.76932	1.30911	0.12661
C	0.81518	1.34844	0.23316
C	0.89927	1.33111	0.25491
C	0.93233	1.26364	0.18102
C	0.88708	1.22173	0.07939
C	0.9495	1.36719	0.37624
H	0.70463	1.32555	0.11457
H	0.78435	1.38968	0.30317
H	0.9914	1.23804	0.20869
H	0.91898	1.17288	0.02396
H	0.92612	1.33199	0.46557
H	1.01382	1.3539	0.35134
B	0.5	1	0.5
Li	0	0.5	0.25

Table 4.16. Atom coordination table of dia-c9 model of ICOF-202-Li.

ICOF-202-Li dia-c9			
Space Group: I-42D a= b= 22.8607 Å c= 4.4173 Å α= β= γ= 90°			
C	0.01986	0.20498	0.86364
O	0.01274	0.05175	0.20486
C	-0.03593	0.08969	0.26253
C	-0.03222	0.13919	0.50905
C	0.01951	0.16566	0.61457
C	-0.03261	0.22693	0.99513
C	0.66357	0.58474	1.87549
C	0.70504	0.58511	1.63561
H	0.06202	0.2208	0.93582
H	-0.07143	0.06218	0.33139
H	-0.05065	0.10828	0.05391
H	0.05996	0.15759	0.4978
H	0.65021	0.62627	1.96836
H	0.71981	0.62735	1.55909

B	0	0	0
Li	0	0	0.5

4.5.9.3 Atom coordination tables of ICOF-203-Li

Table 4.17. Atom coordination table of dia model of ICOF-203-Li.

ICOF-203-Li dia			
Space Group: I41/AMD a= b= 17.0469 Å c= 23.6756 Å α= β= γ= 90°			
H	0.56128	-0.05134	0.35624
F	0.72029	0	0.26046
F	0.86983	0.5	0.95307
B	0.5	0	0.25
C	1.23338	-0.5	0.817
C	1.17096	-0.5	0.85625
C	1.18883	-0.5	0.91424
O	1.07663	-0.5	0.78022
C	1.08519	-0.5	0.83916
Li	1	0	0

Table 4.18. Atom coordination table of dia-c2 model of ICOF-203-Li.

ICOF-203-Li dia-c2			
Space Group: P42/NNM a= b= 12.0936 Å c= 11.6916 Å α= β= γ= 90°			
H	0.50649	0.61524	0.71693
F	0.78122	0.78122	0.98146
F	0.63178	0.63178	0.91002
C	0.76741	0.76741	0.86714
C	0.82906	0.82906	0.78665
C	0.81038	0.81038	0.66956
C	0.91478	0.91478	0.81983
O	0.9237	0.9237	0.93903
B	0	0	0
Li	0.5	0.5	0

Table 4.19. Atom coordination table of dia-c3 model of ICOF-203-Li.

ICOF-203-Li dia-c3			
Space Group: I41/AMD a= b= 16.7519 Å c= 9.0594 Å α= β= γ= 90°			
H	0.43808	0.55532	0.77554
F	0.5	0.2587	1.42986
F	0.5	0.11737	1.29085
C	0.74358	0.5	0.71988
C	0.67328	0.5	0.80187
C	0.68206	0.5	0.95735
O	0.58056	0.5	0.57963
C	0.58813	0.5	0.73519
B	0	0	1
Li	0.5	0.5	1

Table 4.20. Atom coordination table of dia-c4 model of ICOF-203-Li.

ICOF-203-Li dia-c4			
Space Group: PBA2 a= 12.8783 Å b= 12.0796 Å c= 5.0743 Å α= β= γ= 90°			
O	0.06726	0.93735	0.18106
C	0.05762	0.82076	0.15357
C	0.23379	0.11851	0.6313
C	0.19507	0.2036	0.47025
C	0.34182	0.10248	0.64094
O	0.93965	0.92867	0.81233
C	0.83107	0.95105	0.82196
C	0.12988	0.76036	0.34607
C	0.09035	0.6747	0.50597
C	0.23785	0.77622	0.33989
F	0.90882	0.78407	0.43772
F	0.61894	0.98553	0.77187
F	0.48648	0.83769	0.53577
F	0.77838	0.6345	0.21535
H	0.92216	0.20467	0.94883
H	0.02406	0.20411	0.19358
H	0.81733	0.03858	0.76267
H	0.80066	0.93781	0.02508
B	0	0	0.99602

Li	0	0	0.49768

Table 4.21. Atom coordination table of dia-c5 model of ICOF-203-Li.

ICOF-203-Li dia-c5			
Space Group: I41/A a= b= 17.2423 Å c= 4.733 Å α= β= γ= 90 °			
C	0.43896	0.70906	0.98653
C	0.51497	0.69173	0.90933
C	0.57716	0.74055	0.03694
O	0.47954	0.56502	0.69333
C	0.53347	0.62801	0.69255
F	0.38039	0.67788	0.83598
F	0.64888	0.7415	-0.07951
H	0.59276	0.60666	0.73063
H	0.53285	0.65514	0.48243
Li	0	1	0.5
B	0	0.5	0.25

Table 4.22. Atom coordination table of dia-c6 model of ICOF-203-Li.

ICOF-203-Li dia-c6			
Space Group: P42/NNM a= b= 12.1096 Å c= 5.2208 Å α= β= γ= 90°			
C	0.35005	0.78983	0.66054
F	0.42335	0.82662	0.5857
H	0.38739	0.28468	0.79562
O	-0.0627	-0.0627	-0.18532
C	-0.18808	0.18808	-0.06913
C	-0.14489	0.14489	0.18224
B	0	0	0
Li	0	0	0.5

4.5.9.4 Atom coordination tables of ICOF-203-Na

Table 4.23. Atom coordination table of dia model of ICOF-203-Na.

ICOF-203-Na dia			
Space Group: I41/AMD a= b= 17.0469 Å c= 23.6756 Å α= β= γ= 90°			
H	0.56128	-0.05134	0.35624

F	0.72029	0	0.26046
F	0.86983	0.5	0.95307
B	0.5	0	0.25
C	1.23338	-0.5	0.817
C	1.17096	-0.5	0.85625
C	1.18883	-0.5	0.91424
O	1.07663	-0.5	0.78022
C	1.08519	-0.5	0.83916
Na	1	0	0

Table 4.24. Atom coordination table of dia-c2 model of ICOF-203-Na.

ICOF-203-Na dia-c2			
Space Group: P42/NNM a= b= 12.0936 Å c= 11.6916 Å α= β= γ= 90°			
H	0.50649	0.61524	0.71693
F	0.78122	0.78122	0.98146
F	0.63178	0.63178	0.91002
C	0.76741	0.76741	0.86714
C	0.82906	0.82906	0.78665
C	0.81038	0.81038	0.66956
C	0.91478	0.91478	0.81983
O	0.9237	0.9237	0.93903
B	0	0	0
Na	0.5	0.5	0

Table 4.25. Atom coordination table of dia-c3 model of ICOF-203-Na.

ICOF-203-Na dia-c3			
Space Group: I41/AMD a= b= 16.7519 Å c= 9.0594 Å α= β= γ= 90°			
H	0.43808	0.55532	0.77554
F	0.5	0.2587	1.42986
F	0.5	0.11737	1.29085
C	0.74358	0.5	0.71988
C	0.67328	0.5	0.80187
C	0.68206	0.5	0.95735
O	0.58056	0.5	0.57963
C	0.58813	0.5	0.73519
B	0	0	1
Na	0.5	0.5	1

Table 4.26. Atom coordination table of dia-c4 model of ICOF-203-Na.

ICOF-203-Na dia-c4			
Space Group: I41/AMD a= b= 12.2586 Å b= 12.2895 Å c= 5.86 Å α= β= γ= 90°			
O	0.0704	0.9355	0.16175
C	0.05069	0.82193	0.14881
C	0.24272	0.12484	0.65239
C	0.20569	0.22816	0.5781
C	0.34667	0.09101	0.57244
O	0.93555	0.92972	0.81399
C	0.82165	0.94818	0.83038
C	0.12417	0.75781	0.32626
C	0.09053	0.6539	0.40447
C	0.22736	0.79503	0.40228
F	0.88801	0.73031	0.6748
F	0.61375	0.9984	0.65741
F	0.49599	0.88781	0.31209
F	0.76873	0.61117	0.30701
H	0.93411	0.20745	-0.03784
H	1.03108	0.19396	0.19877
H	0.80373	1.0346	0.78129
H	0.79164	0.93051	1.02792
B	0	0	-0.01214
Na	0	0	0.48774

Table 4.27. Atom coordination table of dia-c5 model of ICOF-203-Na.

ICOF-203-Na dia-c5			
Space Group: I41/A a= b= 18.1731 Å c= 5.854 Å α= β= γ= 90°			
C	0.4555	0.75183	0.93102
C	0.50192	0.68799	0.94173
C	0.5471	0.69064	0.14336
O	0.47461	0.5617	0.67885
C	0.5179	0.6297	0.72529
F	0.41538	0.76299	0.7388
F	0.59596	0.63588	0.17334
H	0.57698	0.6141	0.72911
H	0.51102	0.66392	0.57238

B	0	0.5	0.25
Na	0	0	0.5

Table 4.28. Atom coordination table of dia-c6 model of ICOF-203-Na.

ICOF-203-Na dia-c6			
Space Group: P4/N a= b= 12.1088 Å c= 5.2205 Å α= β= γ= 90 °			
O	0.08355	-0.04637	0.82599
C	0.16176	0.07549	0.18528
C	0.20663	0.16557	0.34792
C	0.26942	0.13948	0.56409
C	0.3127	0.22386	0.71632
H	0.19734	0.08273	-0.01619
H	0.18588	-0.00771	0.27084
F	0.28527	0.04941	0.616
F	0.36381	0.20273	0.89304
B	0	0	0
Na	0	0	0.5

4.6 References

(1) Geng, K.; He, T.; Liu, R.; Dalapati, S.; Tan, K. T.; Li, Z.; Tao, S.; Gong, Y.; Jiang, Q.; Jiang, D. Covalent Organic Frameworks: Design, Synthesis, and Functions. *Chem. Rev.* **2020**, *120* (16), 8814-8933, DOI: 10.1021/acs.chemrev.9b00550.

(2) Feng, X.; Ding, X.; Jiang, D. Covalent organic frameworks. *Chem. Soc. Rev.* **2012**, *41* (18), 6010-6022, DOI: 10.1039/C2CS35157A.

(3) Ding, S.-Y.; Wang, W. Covalent organic frameworks (COFs): from design to applications. *Chem. Soc. Rev.* **2013**, *42* (2), 548-568, DOI: 10.1039/C2CS35072F.

(4) Diercks, C. S.; Yaghi, O. M. The atom, the molecule, and the covalent organic framework. *Science* **2017**, *355* (6328), eaal1585. DOI: doi:10.1126/science.aal1585.

(5) Jin, Y.; Hu, Y.; Zhang, W. Tessellated multiporous two-dimensional covalent organic frameworks. *Nat. Rev. Chem.* **2017**, *1* (7), 0056, DOI: 10.1038/s41570-017-0056.

(6) Guan, X.; Chen, F.; Fang, Q.; Qiu, S. Design and applications of three dimensional covalent organic frameworks. *Chem. Soc. Rev.* **2020**, *49* (5), 1357-1384, DOI: 10.1039/C9CS00911F.

(7) O'Keeffe, M.; Peskov, M. A.; Ramsden, S. J.; Yaghi, O. M. The Reticular Chemistry Structure Resource (RCSR) Database of, and Symbols for, Crystal Nets. *Acc. Chem. Res.* **2008**, *41* (12), 1782-1789. DOI: 10.1021/ar800124u.

(8) Jin, Y.; Yu, C.; Denman, R. J.; Zhang, W. Recent advances in dynamic covalent chemistry. *Chem. Soc. Rev.* **2013**, *42* (16), 6634-6654, DOI: 10.1039/C3CS60044K.

(9) Wayment, L. J.; Lei, Z.; Jin, Y.; Zhang, W. Recent Progress in Constructing Structurally Ordered Polymeric Architectures via Dynamic Covalent Chemistry. *CCS Chem.* **2023**, *5* (10), 2194-2206, DOI: 10.31635/ccschem.023.202303004.

(10) Xu, L.; Ding, S.-Y.; Liu, J.; Sun, J.; Wang, W.; Zheng, Q.-Y. Highly crystalline covalent organic frameworks from flexible building blocks. *Chem. Commun.* **2016**, *52* (25), 4706-4709, DOI: 10.1039/C6CC01171C.

(11) Zhao, C.; Diercks, C. S.; Zhu, C.; Hanikel, N.; Pei, X.; Yaghi, O. M. Urea-Linked Covalent Organic Frameworks. *J. Am. Chem. Soc.* **2018**, *140* (48), 16438-16441. DOI: 10.1021/jacs.8b10612.

(12) Han, X.; Xia, Q.; Huang, J.; Liu, Y.; Tan, C.; Cui, Y. Chiral Covalent Organic Frameworks with High Chemical Stability for Heterogeneous Asymmetric Catalysis. *J. Am. Chem. Soc.* **2017**, *139* (25), 8693-8697, DOI: 10.1021/jacs.7b04008.

(13) Lei, Z.; Wayment, L. J.; Cahn, J. R.; Chen, H.; Huang, S.; Wang, X.; Jin, Y.; Sharma, S.; Zhang, W. Cyanurate-Linked Covalent Organic Frameworks Enabled by Dynamic Nucleophilic Aromatic Substitution. *J. Am. Chem. Soc.* **2022**, *144* (39), 17737-17742, DOI: 10.1021/jacs.2c00778.

(14) Liu, Y.; Li, J.; Lv, J.; Wang, Z.; Suo, J.; Ren, J.; Liu, J.; Liu, D.; Wang, Y.; Valtchev, V.; Qiu, S.; Zhang, D.; Fang, Q. Topological Isomerism in Three-Dimensional Covalent Organic Frameworks. *J. Am. Chem. Soc.* **2023**, *145* (17), 9679-9685, DOI: 10.1021/jacs.3c01070.

(15) Du, Y.; Yang, H.; Whiteley, J. M.; Wan, S.; Jin, Y.; Lee, S.-H.; Zhang, W. Ionic Covalent Organic Frameworks with Spiroborate Linkage. *Angew. Chem. Int. Ed.* **2016**, *55* (5), 1737-1741, DOI:10.1002/anie.201509014.

(16) Hu, Y.; Teat, S. J.; Gong, W.; Zhou, Z.; Jin, Y.; Chen, H.; Wu, J.; Cui, Y.; Jiang, T.; Cheng, X.; Zhang, W. Single crystals of mechanically entwined helical covalent polymers. *Nat. Chem.* **2021**, *13* (7), 660-665. DOI: 10.1038/s41557-021-00686-2.

(17) Wang, X.; Bahri, M.; Fu, Z.; Little, M. A.; Liu, L.; Niu, H.; Browning, N. D.; Chong, S. Y.; Chen, L.; Ward, J. W.; Cooper, A. I. A Cubic 3D Covalent Organic Framework with nbo Topology. *J. Am. Chem. Soc.* **2021**, *143* (37), 15011-15016. DOI: 10.1021/jacs.1c08351.

(18) Wayment, L. J.; Wang, X.; Huang, S.; McCoy, M. S.; Chen, H.; Hu, Y.; Jin, Y.; Sharma, S.; Zhang, W. 3D Covalent Organic Framework as a Metastable Intermediate in the Formation of a Double-Stranded Helical Covalent Polymer. *J. Am. Chem. Soc.* **2023**, *145* (28), 15547-15552. DOI: 10.1021/jacs.3c04734.

(19) Wayment, L. J.; Teat, S. J.; Huang, S.; Chen, H.; Zhang, W. Dynamic Entwined Topology in Helical Covalent Polymers Dictated by Competing Supramolecular Interactions. *Angew. Chem. Int. Ed.* **2024**, e202403599. DOI: 10.1002/anie.202403599.

(20) Moriya, M.; Kato, D.; Sakamoto, W.; Yogo, T. Plastic crystalline lithium salt with solid-state ionic conductivity and high lithium transport number. *Chem. Commun.* **2011**, *47* (22), 6311-6313, DOI: 10.1039/C1CC00070E.

(21) Duncan, D. T.; Roy, B.; Piper, S. L.; Nguyen, C.; Howlett, P.; Forsyth, M.; MacFarlane, D. R.; Sun, J.; Kar, M. High-Ionicity Electrolytes Based on Bulky Fluoroborate Anions for Stable Na-Metal Cycling. *J. Phys. Chem. C* **2022**, *126* (44), 18918-18930. DOI: 10.1021/acs.jpcc.2c06187.

(22) Bocharova, V.; Sokolov, A. P. Perspectives for Polymer Electrolytes: A View from Fundamentals of Ionic Conductivity. *Macromolecules* **2020**, *53* (11), 4141-4157. DOI: 10.1021/acs.macromol.9b02742.

(23) Stolberg, M. A.; Paren, B. A.; Leon, P. A.; Brown, C. M.; Winter, G.; Gordiz, K.; Concellón, A.; Gómez-Bombarelli, R.; Shao-Horn, Y.; Johnson, J. A. Lamellar Ionenes with Highly Dissociative, Anionic Channels Provide Lower Barriers for Cation Transport. *J. Am. Chem. Soc.* **2023**, *145* (29), 16200-16209. DOI: 10.1021/jacs.3c05053.

(24) Hu, Y.; Wayment, L. J.; Haslam, C.; Yang, X.; Lee, S.-H.; Jin, Y.; Zhang, W. Covalent organic framework based lithium-ion battery: Fundamental, design and characterization. *EnergyChem* **2021**, *3* (1), 100048. DOI: 10.1016/j.enchem.2020.100048.

(25) Zhu, Y.; Bai, Q.; Ouyang, S.; Jin, Y.; Zhang, W. Covalent Organic Framework-based Solid-State Electrolytes, Electrode Materials, and Separators for Lithium-ion Batteries. *ChemSusChem* **2024**, *17* (1), e202301118. DOI: 10.1002/cssc.202301118.

(26) Zhu, D.; Xu, G.; Barnes, M.; Li, Y.; Tseng, C.-P.; Zhang, Z.; Zhang, J.-J.; Zhu, Y.; Khalil, S.; Rahman, M. M.; Verduzco, R.; Ajayan, P. M. Covalent Organic Frameworks for Batteries. *Adv. Funct. Mater.* **2021**, *31* (32), 2100505. DOI: 10.1002/adfm.202100505.

(27) Zhao, X.; Pachfule, P.; Thomas, A. Covalent organic frameworks (COFs) for electrochemical applications. *Chem. Soc. Rev.* **2021**, *50* (12), 6871-6913, DOI: 10.1039/D0CS01569E.

(28) Liang, X.; Tian, Y.; Yuan, Y.; Kim, Y. Ionic Covalent Organic Frameworks for Energy Devices. *Adv. Mater.* **2021**, *33* (52), 2105647. DOI: 10.1002/adma.202105647.

(29) Albertus, P.; Babinec, S.; Litzelman, S.; Newman, A. Status and challenges in enabling the lithium metal electrode for high-energy and low-cost rechargeable batteries. *Nat. Energy* **2018**, *3* (1), 16-21, DOI: 10.1038/s41560-017-0047-2

(30) Schneider, S. F.; Bauer, C.; Novák, P.; Berg, E. J. A modeling framework to assess specific energy, costs and environmental impacts of Li-ion and Na-ion batteries. *Sustain. Energy Fuels* **2019**, *3* (11), 3061-3070, DOI: 10.1039/c9se00427k

(31) Abraham, K. How comparable are sodium-ion batteries to lithium-ion counterparts? *ACS Energy Lett.* **2020**, *5* (11), 3544-3547, DOI: 10.1021/acsenergylett.0c02181

(32) Zhang, W.; Lu, J.; Guo, Z. Challenges and future perspectives on sodium and potassium ion batteries for grid-scale energy storage. *Mater. Today* **2021**, *50*, 400-417, DOI:10.1016/j.mattod.2021.03.015.

(33) Hu, Y.; Dunlap, N.; Long, H.; Chen, H.; Wayment, L. J.; Ortiz, M.; Jin, Y.; Nijamudheen, A.; Mendoza-Cortes, J. L.; Lee, S.-H.; Zhang, W. Helical Covalent Polymers with Unidirectional Ion Channels as Single Lithium-Ion Conducting Electrolytes. *CCS Chem.* **2021**, *3* (12), 2762-2770, DOI: 10.31635/ccschem.021.202101257.

Chapter 5: Summary and Future Work.

5.1 Summary

This doctoral research has advanced the structural evolution of crystalline polymers by uncovering mechanistic insights into polymer formation. It has also shown the significant role of supramolecular interactions in shaping crystalline 1D polymers and introduced innovative boron-based linkages. A substantial portion of this investigation involved the synthesis of monomers, polymer creation, and structural simulations to elucidate how varying parameters influence equilibrium.

The initial two chapters concentrate on utilizing spiroborate linkages to generate diverse polymers, including srs-COF, HCP-Li, HCP-Na, and HCP-K. The research observed that irrespective of the counter-ion used, polymerization initially proceeds through a srs framework before transitioning to an HCP structure. The persistence of the srs framework is contingent upon reaction conditions, with shorter reaction times and lower temperatures favoring the srs topology, while longer reaction times and higher temperatures promote HCP formation. Additionally, altering the counter-ion affects equilibrium due to slight changes in solvent solution caused by differences in solubility between lithium hydroxide, sodium hydroxide, and potassium hydroxide.

The third chapter focuses on investigating how supramolecular interactions vary with different counter-ions. It was found that HCP-Li is assembled through hydrogen bonding, whereas larger counter-ions predominantly facilitate metal coordination, thereby hindering strong hydrogen bonding interactions. This metal coordination alters the orientation of 1D polymer strands, preventing them from adopting the correct geometry for hydrogen bonding. We also demonstrate that HCP-Li can be transformed to HCP-Na or K though ion exchange. Which suggests that entwinement mode can be dynamic and we could use ion exchange as a method to form new HCPs.

The fourth chapter delves into the development of a novel boron linkage. Given the flexibility of B-O bonds, the study explores the utilization of flexible alcohol monomers to design borate frameworks. Boron serves as a tetrahedral center, connecting four linkers, offering a promising approach to polymer design that addresses limitations associated with monomers requiring diols, such as catechol, which have seen limited development compared to aldehyde monomers. The final chapter details progress made in synthesizing shape persistent structures that could be useful themselves or as part of a framework.

5.2 Future work

Further exploration of this research holds promise for developing novel materials with diverse applications. The utilization of the HCP platform as a solid-state electrolyte for lithium batteries represents just one avenue[1], with potential extensions to sodium and potassium-based HCPs, particularly as interest in alternative battery materials grows due to the scarcity of lithium. Exploring alternative monomers could yield HCP variants with enhanced properties such as porosity, additional ion transport channels, or doping capabilities. Additionally, investigating the impact of changing the counter-ion to a chiral organic base could offer insights into tuning chirality and exploring hydrogen-bonded entwinement.

The unexplored potential of the srs-COF topology presents another avenue for research. The stability and chirality of the srs phase warrant investigation, especially considering its persistence observed during the formation of HCP-Na. The unique combination of anionic backbone, flexible B-O bonds, and potential porosity make srs-based materials intriguing candidates for applications in metal ion batteries or molecular separation. Integration of new monomer could further enhance the properties of srs phases.

Preliminary data suggests that the tetra borate chemistry introduced in Chapter 4 holds promise due to its charged nature and limited porosity. Leveraging the extensive range of aldehyde monomers developed for imine-lined COFs could facilitate the design of diverse structures using this chemistry platform, potentially unlocking a wide array of applications. Moreover, this methodology will enable materials structures to be finely tuned to gain a greater understanding in the functions of the materials.

5.3 References

(1) Hu, Y.; Dunlap, N.; Long, H.; Chen, H.; Wayment Lacey, J.; Ortiz, M.; Jin, Y.; Nijamudheen, A.; Mendoza-Cortes Jose, L.; Lee, S.-h.; et al. Helical Covalent Polymers with Unidirectional Ion Channels as Single Lithium-Ion Conducting Electrolytes. *CCS Chemistry* **2021**, *3* (12), 2762-2770. DOI: 10.31635/ccschem.021.202101257.

Bibliography

Chapter 1

(1) Shoulders, M. D.; Raines, R. T. Collagen Structure and Stability. *Annu. Rev. Biochem.* **2009**, *78* (1), 929-958. DOI: 10.1146/annurev.biochem.77.032207.120833.

(2) Coudrillier, B.; Pijanka, J.; Jefferys, J.; Sorensen, T.; Quigley, H. A.; Boote, C.; Nguyen, T. D. Collagen structure and mechanical properties of the human sclera: analysis for the effects of age. *J. Biomech. Eng.* **2015**, *137* (4), 041006.

(3) Lehn, J.-M. From supramolecular chemistry towards constitutional dynamic chemistry and adaptive chemistry. *Chem. Soc. Rev.* **2007**, *36* (2), 151-160, DOI: 10.1039/B616752G.

(4) Moulin, E.; Cormos, G.; Giuseppone, N. Dynamic combinatorial chemistry as a tool for the design of functional materials and devices. *Chem. Soc. Rev.* **2012**, *41* (3), 1031-1049, DOI: 10.1039/C1CS15185A.

(5) Rowan, S. J.; Cantrill, S. J.; Cousins, G. R. L.; Sanders, J. K. M.; Stoddart, J. F. Dynamic Covalent Chemistry. *Angew. Chem. Int. Ed.* **2002**, *41* (6), 898-952 DOI: 10.1002/1521-3773(20020315)41:6.

(6) Jin, Y.; Yu, C.; Denman, R. J.; Zhang, W. Recent advances in dynamic covalent chemistry. *Chem. Soc. Rev.* **2013**, *42* (16), 6634-6654, DOI: 10.1039/C3CS60044K.

(7) Wayment, L. J.; Lei, Z.; Jin, Y.; Zhang, W. Recent Progress in Constructing Structurally Ordered Polymeric Architectures via Dynamic Covalent Chemistry. *CCS Chem.* **2023**, *5* (10), 2194-2206. DOI: doi:10.31635/ccschem.023.202303004.

(8) Natraj, A.; Ji, W.; Xin, J.; Castano, I.; Burke, D. W.; Evans, A. M.; Strauss, M. J.; Ateia, M.; Hamachi, L. S.; Gianneschi, N. C.; ALOthman, Z. A.; Sun, J.; Yusuf, K.; Dichtel, W. R. Single-Crystalline Imine-Linked Two-Dimensional Covalent Organic Frameworks Separate Benzene and Cyclohexane Efficiently. *J. Am. Chem. Soc.* **2022**, *144* (43), 19813-19824. DOI: 10.1021/jacs.2c07166.

(9) Day, R. W.; Bediako, D. K.; Rezaee, M.; Parent, L. R.; Skorupskii, G.; Arguilla, M. Q.; Hendon, C. H.; Stassen, I.; Gianneschi, N. C.; Kim, P.; Dincă, M. Single Crystals of Electrically Conductive Two-Dimensional Metal–Organic Frameworks: Structural and Electrical Transport Properties. *ACS Cent. Sci.* **2019**, *5* (12), 1959-1964. DOI: 10.1021/acscentsci.9b01006.

(10) Zhang, J.; Zhou, G.; Un, H.-I.; Zheng, F.; Jastrzembski, K.; Wang, M.; Guo, Q.; Mücke, D.; Qi, H.; Lu, Y.; Wang, Z.; Liang, Y.; Löffler, Kaiser, U.; Franeheim, T.; Mateo-Alonso, A.; Huang, Z.; Sirringhaus, H.; Feng, X.; Dong, R. Wavy Two-Dimensional Conjugated Metal–Organic Framework with Metallic Charge Transport. *J. Am. Chem. Soc.* **2023**, *145* (43), 23630-23638. DOI: 10.1021/jacs.3c07682.

(11) a. Jin, Y.; Wang, Q.; Taynton, P.; Zhang, W. Dynamic Covalent Chemistry Approaches Toward Macrocycles, Molecular Cages, and Polymers. *Acc. Chem. Res.* **2014**, *47* (5), 1575-1586. DOI: 10.1021/ar500037v. b. Zhang, W.; Moore, J. S. "Shape-Persistent Macrocycles: Structures and Synthetic Approaches from Arylene and Ethynylene Building Blocks" (review) *Angew. Chem. Int. Ed.* **2006**, 45, 4416-4439.

(12) Huang, S.; Lei, Z.; Jin, Y.; Zhang, W. By-design molecular architectures via alkyne metathesis. *Chem. Sci.* **2021**, *12* (28), 9591-9606, DOI: 10.1039/D1SC01881G.

(13) Lee, S.; Yang, A.; Moneypenny, T. P., II; Moore, J. S. Kinetically Trapped Tetrahedral Cages via Alkyne Metathesis. *J. Am. Chem. Soc.* **2016**, *138* (7), 2182-2185. DOI: 10.1021/jacs.6b00468.

(14) Evans, A. M.; Strauss, M. J.; Corcos, A. R.; Hirani, Z.; Ji, W.; Hamachi, L. S.; Aguilar-Enriquez, X.; Chavez, A. D.; Smith, B. J.; Dichtel, W. R. Two-Dimensional Polymers and Polymerizations. *Chem. Rev.* **2022**, *122* (1), 442-564. DOI: 10.1021/acs.chemrev.0c01184.

(15) Han, J.; Feng, J.; Kang, J.; Chen, J.-M.; Du, X.-Y.; Ding, S.-Y.; Liang, L.; Wang, W. Fast growth of single-crystal covalent organic frameworks for laboratory x-ray diffraction. *Science* **2024**, *383* (6686), 1014-1019. DOI: 10.1126/science.adk8680 .

(16) Wang, X.; Wada, Y.; Shimada, T.; Kosaka, A.; Adachi, K.; Hashizume, D.; Yazawa, K.; Uekusa, H.; Shoji, Y.; Fukushima, T.; et al. Triple Isomerism in 3D Covalent Organic Frameworks. *J. Am. Chem. Soc.* **2024**. DOI: 10.1021/jacs.3c13863.

(17) Côté Adrien, P.; Benin Annabelle, I.; Ockwig Nathan, W.; O'Keeffe, M.; Matzger Adam, J.; Yaghi Omar, M. Porous, Crystalline, Covalent Organic Frameworks. *Science* **2005**, *310* (5751), 1166-1170. DOI: 10.1126/science.1120411.

(18) El-Kaderi, H. M.; Hunt, J. R.; Mendoza-Cortés, J. L.; Côté, A. P.; Taylor, R. E.; O'Keeffe, M.; Yaghi, O. M. Designed Synthesis of 3D Covalent Organic Frameworks. *Science* **2007**, *316* (5822), 268-272. DOI: doi:10.1126/science.1139915.

(19) Martínez-Abadía, M.; Stoppiello, C. T.; Strutynski, K.; Lerma-Berlanga, B.; Martí-Gastaldo, C.; Saeki, A.; Melle-Franco, M.; Khlobystov, A. N.; Mateo-Alonso, A. A Wavy Two-Dimensional Covalent Organic Framework from Core-Twisted Polycyclic Aromatic Hydrocarbons. *J. Am. Chem. Soc.* **2019**, *141* (36), 14403-14410. DOI: 10.1021/jacs.9b07383.

(20) Evans, A. M.; Parent, L. R.; Flanders, N. C.; Bisbey, R. P.; Vitaku, E.; Kirschner, M. S.; Schaller, R. D.; Chen, L. X.; Gianneschi, N. C.; Dichtel, W. R. Seeded growth of single-crystal two-dimensional covalent organic frameworks. *Science* **2018**, *361* (6397), 52-57. DOI: 10.1126/science.aar7883.

(21) Du, Y.; Yang, H.; Whiteley, J. M.; Wan, S.; Jin, Y.; Lee, S.-H.; Zhang, W. Ionic Covalent Organic Frameworks with Spiroborate Linkage. *Angew. Chem. Int. Ed.* **2016**, *55* (5), 1737-1741, DOI: 10.1002/anie.201509014.

(22) Hu, Y.; Teat, S. J.; Gong, W.; Zhou, Z.; Jin, Y.; Chen, H.; Wu, J.; Cui, Y.; Jiang, T.; Cheng, X.; Zhang, W. Single crystals of mechanically entwined helical covalent polymers. *Nat. Chem.* **2021**, *13* (7), 660-665. DOI: 10.1038/s41557-021-00686-2.

(23) Wang, X.; Bahri, M.; Fu, Z.; Little, M. A.; Liu, L.; Niu, H.; Browning, N. D.; Chong, S. Y.; Chen, L.; Ward, J. W.; Cooper, A. I. A Cubic 3D Covalent Organic Framework with nbo Topology. *J. Am. Chem. Soc.* **2021**, *143* (37), 15011-15016, DOI: 10.1021/jacs.1c08351.

(24) Xu, Q.; Wang, X.; Huang, S.; Hu, Y.; Teat, S. J.; Settineri, N. S.; Chen, H.; Wayment, L. J.; Jin, Y.; Sharma, S.; Zhang, W. Dynamic Covalent Self-sorting in Molecular and Polymeric Architectures Enabled by Spiroborate Bond Exchange. *Angew. Chem. Int. Ed.* **2023**, *62* (27), e202304279. DOI: 10.1002/anie.202304279.

(25) Wayment, L. J.; Wang, X.; Huang, S.; McCoy, M. S.; Chen, H.; Hu, Y.; Jin, Y.; Sharma, S.; Zhang, W. 3D Covalent Organic Framework as a Metastable Intermediate in the Formation of a Double-Stranded Helical Covalent Polymer. *J. Am. Chem. Soc.* **2023**, *145* (28), 15547-15552. DOI: 10.1021/jacs.3c04734.

(26) Wayment, L. J.; Teat, S. J.; Huang, S.; Chen, H.; Zhang, W. Dynamic Entwined Topology in Helical Covalent Polymers Dictated by Competing Supramolecular Interactions. *Angew. Chem. Int. Ed.*, e202403599. DOI: 10.1002/anie.202403599.

(27) Hunt, J. R.; Doonan, C. J.; LeVangie, J. D.; Côté, A. P.; Yaghi, O. M. Reticular Synthesis of Covalent Organic Borosilicate Frameworks. *J. Am. Chem. Soc.* **2008**, *130* (36), 11872-11873. DOI: 10.1021/ja805064f.

(28) Gropp, C.; Ma, T.; Hanikel, N.; Yaghi Omar, M. Design of higher valency in covalent organic frameworks. *Science* **2020**, *370* (6515), eabd6406. DOI: 10.1126/science.abd6406.

(29) Liu, B.-T.; Gong, S.-H.; Jiang, X.-T.; Zhang, Y.; Wang, R.; Chen, Z.; Zhang, S.; Kirlikovali, K. O.; Liu, T.-F.; Farha, O. K.; Cao, R. A solution processible single-crystal porous organic polymer. *Nat. Synth.* **2023**, *2* (9), 873-879. DOI: 10.1038/s44160-023-00316-4.

(30) Uribe-Romo, F. J.; Hunt, J. R.; Furukawa, H.; Klöck, C.; O'Keeffe, M.; Yaghi, O. M. A Crystalline Imine-Linked 3-D Porous Covalent Organic Framework. *J. Am. Chem. Soc.* **2009**, *131* (13), 4570-4571. DOI: 10.1021/ja8096256.

(31) Beaudoin, D.; Maris, T.; Wuest, J. D. Constructing monocrystalline covalent organic networks by polymerization. *Nat. Chem.* **2013**, *5* (10), 830-834. DOI: 10.1038/nchem.1730.

(32) Alahakoon, S. B.; Tan, K.; Pandey, H.; Diwakara, S. D.; McCandless, G. T.; Grinffiel, D. I.; Durand-Silva, A.; Thonhauser, T.; Smaldone, R. A. 2D-Covalent Organic Frameworks with Interlayer Hydrogen Bonding Oriented through Designed Nonplanarity. *J. Am. Chem. Soc.* **2020**, *142* (30), 12987-12994. DOI: 10.1021/jacs.0c03409.

(33) Kandambeth, S.; Shinde, D. B.; Panda, M. K.; Lukose, B.; Heine, T.; Banerjee, R. Enhancement of Chemical Stability and Crystallinity in Porphyrin-Containing Covalent Organic Frameworks by Intramolecular Hydrogen Bonds. *Angew. Chem. Int. Ed.* **2013**, *52* (49), 13052-13056. DOI: 10.1002/anie.201306775.

(34) Xu, H.; Gao, J.; Jiang, D. Stable, crystalline, porous, covalent organic frameworks as a platform for chiral organocatalysts. *Nat. Chem.* **2015**, *7* (11), 905-912. DOI: 10.1038/nchem.2352.

(35) Uribe-Romo, F. J.; Doonan, C. J.; Furukawa, H.; Oisaki, K.; Yaghi, O. M. Crystalline Covalent Organic Frameworks with Hydrazone Linkages. *J. Am. Chem. Soc.* **2011**, *133* (30), 11478-11481. DOI: 10.1021/ja204728y.

(36) Dalapati, S.; Jin, S.; Gao, J.; Xu, Y.; Nagai, A.; Jiang, D. An Azine-Linked Covalent Organic Framework. *J. Am. Chem. Soc.* **2013**, *135* (46), 17310-17313. DOI: 10.1021/ja4103293.

(37) Guo, J.; Xu, Y.; Jin, S.; Chen, L.; Kaji, T.; Honsho, Y.; Addicoat, M. A.; Kim, J.; Saeki, A.; Ihee, H.; Seki, S.; Irle, S.; Hiramoto, M.; Gao, J.; Jiang, D. Conjugated organic framework with three-dimensionally ordered stable structure and delocalized π clouds. *Nat. Commun.* **2013**, *4* (1), 2736. DOI: 10.1038/ncomms3736.

(38) Mahmood, J.; Lee, E. K.; Jung, M.; Shin, D.; Jeon, I.-Y.; Jung, S.-M.; Choi, H.-J.; Seo, J.-M.; Bae, S.-Y.; Sohn, S.-D.; et al. Nitrogenated holey two-dimensional structures. *Nat. Commun.* **2015**, *6* (1), 6486. DOI: 10.1038/ncomms7486.

(39) Meng, Z.; Aykanat, A.; Mirica, K. A. Proton Conduction in 2D Aza-Fused Covalent Organic Frameworks. *Chem. Mater.* **2019**, *31* (3), 819-825. DOI: 10.1021/acs.chemmater.8b03897.

(40) Wang, M.; Ballabio, M.; Wang, M.; Lin, H.-H.; Biswal, B. P.; Han, X.; Paasch, S.; Brunner, E.; Liu, P.; Chen, M.; et al. Unveiling Electronic Properties in Metal–Phthalocyanine-Based Pyrazine-Linked Conjugated Two-Dimensional Covalent Organic Frameworks. *J. Am. Chem. Soc.* **2019**, *141* (42), 16810-16816. DOI: 10.1021/jacs.9b07644.

(41) Meng, Z.; Stolz, R. M.; Mirica, K. A. Two-Dimensional Chemiresistive Covalent Organic Framework with High Intrinsic Conductivity. *J. Am. Chem. Soc.* **2019**, *141* (30), 11929-11937. DOI: 10.1021/jacs.9b03441.

(42) Li, X.; Wang, H.; Chen, H.; Zheng, Q.; Zhang, Q.; Mao, H.; Liu, Y.; Cai, S.; Sun, B.; Dun, C.; Gordan, M. P.; Zheng, H.; Reimer, J. A.; Urban, J. J.; Ciston, J.; Tan, T.; Chan, E. M.; Zhang, J.; Liu, Y. Dynamic Covalent Synthesis of Crystalline Porous Graphitic Frameworks. *Chem* **2020**, *6* (4), 933-944. DOI: 10.1016/j.chempr.2020.01.011.

(43) Kandambeth, S.; Mallick, A.; Lukose, B.; Mane, M. V.; Heine, T.; Banerjee, R. Construction of Crystalline 2D Covalent Organic Frameworks with Remarkable Chemical (Acid/Base) Stability via a Combined Reversible and Irreversible Route. *J. Am. Chem. Soc.* **2012**, *134* (48), 19524-19527. DOI: 10.1021/ja308278w.

(44) Banerjee, S.; Tripathy, R.; Cozzens, D.; Nagy, T.; Keki, S.; Zsuga, M.; Faust, R. Photoinduced Smart, Self-Healing Polymer Sealant for Photovoltaics. *ACS Appl. Mater. Interfaces* **2015**, *7* (3), 2064-2072. DOI: 10.1021/am508096c.

(45) Haase, F.; Troschke, E.; Savasci, G.; Banerjee, T.; Duppel, V.; Dörfler, S.; Grundei, M. M. J.; Burow, A. M.; Ochsenfeld, C.; Kaskel, S.; et al. Topochemical conversion of an imine- into a thiazole-linked covalent organic framework enabling real structure analysis. *Nat. Commun.* **2018**, *9* (1), 2600. DOI: 10.1038/s41467-018-04979-y.

(46) Waller, P. J.; AlFaraj, Y. S.; Diercks, C. S.; Jarenwattananon, N. N.; Yaghi, O. M. Conversion of Imine to Oxazole and Thiazole Linkages in Covalent Organic Frameworks. *J. Am. Chem. Soc.* **2018**, *140* (29), 9099-9103. DOI: 10.1021/jacs.8b05830.

(47) Wang, K.; Jia, Z.; Bai, Y.; Wang, X.; Hodgkiss, S. E.; Chen, L.; Chong, S. Y.; Wang, X.; Yang, H.; Xu, Y.; Feng, F., Ward, J. W.; Cooper, A. I. Synthesis of Stable Thiazole-Linked Covalent Organic Frameworks via a Multicomponent Reaction. *J. Am. Chem. Soc.* **2020**, *142* (25), 11131-11138. DOI: 10.1021/jacs.0c03418.

(48) Grunenberg, L.; Savasci, G.; Terban, M. W.; Duppel, V.; Moudrakovski, I.; Etter, M.; Dinnebier, R. E.; Ochsenfeld, C.; Lotsch, B. V. Amine-Linked Covalent Organic Frameworks as a Platform for Postsynthetic Structure Interconversion and Pore-Wall Modification. *J. Am. Chem. Soc.* **2021**, *143* (9), 3430-3438. DOI: 10.1021/jacs.0c12249.

(49) Wei, P.-F.; Qi, M.-Z.; Wang, Z.-P.; Ding, S.-Y.; Yu, W.; Liu, Q.; Wang, L.-K.; Wang, H.-Z.; An, W.-K.; Wang, W. Benzoxazole-Linked Ultrastable Covalent Organic Frameworks for Photocatalysis. *J. Am. Chem. Soc.* **2018**, *140* (13), 4623-4631. DOI: 10.1021/jacs.8b00571.

(50) Hu, Z.; Hu, F.; Deng, L.; Yang, Y.; Xie, Q.; Gao, Z.; Pan, C.; Jin, Y.; Tang, J.; Yu, G.; Zhang, W. Reprocessible Triketoenamine-Based Vitrimers with Closed-Loop Recyclability. *Angew. Chem. Int. Ed.* **2023**, *62* (34), e202306039. DOI: 10.1002/anie.202306039.

(51) Sick, T.; Rotter, J. M.; Reuter, S.; Kandambeth, S.; Bach, N. N.; Döblinger, M.; Merz, J.; Clark, T.; Marder, T. B.; Bein, T.; Medina, D. D. Switching on and off Interlayer Correlations and Porosity in 2D Covalent Organic Frameworks. *J. Am. Chem. Soc.* **2019**, *141* (32), 12570-12581. DOI: 10.1021/jacs.9b02800.

(52) Kang, C.; Yang, K.; Zhang, Z.; Usadi, A. K.; Calabro, D. C.; Baugh, L. S.; Wang, Y.; Jiang, J.; Zou, X.; Huang, Z.; Zhao, D. Growing single crystals of two-dimensional covalent organic frameworks enabled by intermediate tracing study. *Nat. Commun.* **2022**, *13* (1), 1370. DOI: 10.1038/s41467-022-29086-x.

(53) Xu, S.; Liao, Z.; Dianat, A.; Park, S.-W.; Addicoat, M. A.; Fu, Y.; Pastoetter, D. L.; Fabozzi, F. G.; Liu, Y.; Cuniberti, G.; Richter, M.; Hecht, S.; Feng, X. Combination of Knoevenagel Polycondensation and Water-Assisted Dynamic Michael-Addition-Elimination for the Synthesis of Vinylene-Linked 2D Covalent Organic Frameworks. *Angew. Chem. Int. Ed.* **2022**, *61* (21), e202202492. DOI: 10.1002/anie.202202492.

(54) Ma, T.; Kapustin, E. A.; Yin, S. X.; Liang, L.; Zhou, Z.; Niu, J.; Li, L.-H.; Wang, Y.; Su, J.; Li, J.; Wang, X.; Wang, W. D.; Wang, W.; Sun, J.; Yaghi, O. M. Single-crystal x-ray diffraction structures of covalent organic frameworks. *Science* **2018**, *361* (6397), 48-52. DOI: 10.1126/science.aat7679.

(55) Hu, Y.; Wu, C.; Pan, Q.; Jin, Y.; Lyu, R.; Martinez, V.; Huang, S.; Wu, J.; Wayment, L. J.; Clark, N. A.; Raschke, M. B.; Zhao, Y.; Zhang, W. Synthesis of γ-graphyne using dynamic covalent chemistry. *Nat. Synth.* **2022**, *1* (6), 449-454. DOI: 10.1038/s44160-022-00068-7.

(56) Calik, M.; Sick, T.; Dogru, M.; Döblinger, M.; Datz, S.; Budde, H.; Hartschuh, A.; Auras, F.; Bein, T. From Highly Crystalline to Outer Surface-Functionalized Covalent Organic Frameworks—A Modulation Approach. *J. Am. Chem. Soc.* **2016**, *138* (4), 1234-1239. DOI: 10.1021/jacs.5b10708.

(57) Castano, I.; Evans, A. M.; Li, H.; Vitaku, E.; Strauss, M. J.; Brédas, J.-L.; Gianneschi, N. C.; Dichtel, W. R. Chemical Control over Nucleation and Anisotropic Growth of Two-Dimensional Covalent Organic Frameworks. *ACS Cent. Sci.* **2019**, *5* (11), 1892-1899. DOI: 10.1021/acscentsci.9b00944.

(58) Jin, Y.; Hu, Y.; Zhang, W. Tessellated multiporous two-dimensional covalent organic frameworks. *Nat. Rev. Chem.* **2017**, *1* (7), 0056. DOI: 10.1038/s41570-017-0056.

(59) Côté, A. P.; Benin, A. I.; Ockwig, N. W.; O'Keeffe, M.; Matzger, A. J.; Yaghi, O. M. Porous, Crystalline, Covalent Organic Frameworks. *Science* **2005**, *310* (5751), 1166-1170. DOI: 10.1126/science.1120411.

(60) Zhu, Y.; Wan, S.; Jin, Y.; Zhang, W. Desymmetrized Vertex Design for the Synthesis of Covalent Organic Frameworks with Periodically Heterogeneous Pore Structures. *J. Am. Chem. Soc.* **2015**, *137* (43), 13772-13775. DOI: 10.1021/jacs.5b09487.

(61) Pang, Z.-F.; Xu, S.-Q.; Zhou, T.-Y.; Liang, R.-R.; Zhan, T.-G.; Zhao, X. Construction of Covalent Organic Frameworks Bearing Three Different Kinds of Pores through the Heterostructural Mixed Linker Strategy. *J. Am. Chem. Soc.* **2016**, *138* (14), 4710-4713. DOI: 10.1021/jacs.6b01244.

(62) Zhou, T.-Y.; Xu, S.-Q.; Wen, Q.; Pang, Z.-F.; Zhao, X. One-Step Construction of Two Different Kinds of Pores in a 2D Covalent Organic Framework. *J. Am. Chem. Soc.* **2014**, *136* (45), 15885-15888. DOI: 10.1021/ja5092936.

(63) Dalapati, S.; Jin, E.; Addicoat, M.; Heine, T.; Jiang, D. Highly Emissive Covalent Organic Frameworks. *J. Am. Chem. Soc.* **2016**, *138* (18), 5797-5800. DOI: 10.1021/jacs.6b02700.

(64) Qian, C.; Qi, Q.-Y.; Jiang, G.-F.; Cui, F.-Z.; Tian, Y.; Zhao, X. Toward Covalent Organic Frameworks Bearing Three Different Kinds of Pores: The Strategy for Construction and COF-to-COF Transformation via Heterogeneous Linker Exchange. *J. Am. Chem. Soc.* **2017**, *139* (19), 6736-6743. DOI: 10.1021/jacs.7b02303.

(65) Feng, X.; Dong, Y.; Jiang, D. Star-shaped two-dimensional covalent organic frameworks. *CrystEngComm* **2013**, *15* (8), 1508-1511, DOI: 10.1039/C2CE26371H.

(66) Yang, H.; Du, Y.; Wan, S.; Trahan, G. D.; Jin, Y.; Zhang, W. Mesoporous 2D covalent organic frameworks based on shape-persistent arylene-ethynylene macrocycles. *Chem. Sci.* **2015**, *6* (7), 4049-4053, DOI: 10.1039/C5SC00894H.

(67) Haug, W. K.; Wolfson, E. R.; Morman, B. T.; Thomas, C. M.; McGrier, P. L. A Nickel-Doped Dehydrobenzoannulene-Based Two-Dimensional Covalent Organic Framework for the Reductive Cleavage of Inert Aryl C–S Bonds. *J. Am. Chem. Soc.* **2020**, *142* (12), 5521-5525. DOI: 10.1021/jacs.0c01026.

(68) Baldwin, L. A.; Crowe, J. W.; Pyles, D. A.; McGrier, P. L. Metalation of a Mesoporous Three-Dimensional Covalent Organic Framework. *J. Am. Chem. Soc.* **2016**, *138* (46), 15134-15137. DOI: 10.1021/jacs.6b10316.

(69) Huang, S.; Choi, J. Y.; Xu, Q.; Jin, Y.; Park, J.; Zhang, W. Carbazolylene-Ethynylene Macrocycle based Conductive Covalent Organic Frameworks. *Angew. Chem. Int. Ed.* **2023**, *62* (22), e202303538. DOI: 10.1002/anie.202303538.

(70) Zhu, Q.; Wang, X.; Clowes, R.; Cui, P.; Chen, L.; Little, M. A.; Cooper, A. I. 3D Cage COFs: A Dynamic Three-Dimensional Covalent Organic Framework with High-Connectivity Organic Cage Nodes. *J. Am. Chem. Soc.* **2020**, *142* (39), 16842-16848. DOI: 10.1021/jacs.0c07732.

(71) Guan, X.; Chen, F.; Fang, Q.; Qiu, S. Design and applications of three dimensional covalent organic frameworks. *Chem. Soc. Rev.* **2020**, *49* (5), 1357-1384. DOI: 10.1039/C9CS00911F.

(72) Liu, Y.; Li, J.; Lv, J.; Wang, Z.; Suo, J.; Ren, J.; Liu, J.; Liu, D.; Wang, Y.; Valtchev, V.; Qiu, S.; Zhang, D.; Fang, Q. Topological Isomerism in Three-Dimensional Covalent Organic Frameworks. *J. Am. Chem. Soc.* **2023**, *145* (17), 9679-9685. DOI: 10.1021/jacs.3c01070.

(73) Gui, B.; Xin, J.; Cheng, Y.; Zhang, Y.; Lin, G.; Chen, P.; Ma, J.-X.; Zhou, X.; Sun, J.; Wang, C. Crystallization of Dimensional Isomers in Covalent Organic Frameworks. *J. Am. Chem. Soc.* **2023**, *145* (20), 11276-11281. DOI: 10.1021/jacs.3c01729.

(74) Xu, H.-S.; Luo, Y.; Li, X.; See, P. Z.; Chen, Z.; Ma, T.; Liang, L.; Leng, K.; Abdelwahab, I.; Wang, L.; Li, R.; Shi, X.; Zhou, Y.; Lu, X. F.; Zhao, X.; Liu, C.; Sun, J.; Loh, K. P. Single crystal of a one-dimensional metallo-covalent organic framework. *Nat. Commun.* **2020**, *11* (1), 1434. DOI: 10.1038/s41467-020-15281-1.

(75) De Bolòs, E.; Martínez-Abadía, M.; Hernández-Culebras, F.; Haymaker, A.; Swain, K.; Strutyński, K.; Weare, B. L.; Castells-Gil, J.; Padial, N. M.; Martí-Gastaldo, C.; Khlobstov, A. N.; Saeki, A.; Melle-Franco, M.; Nannenga, B. L.; Mateo-Alonso, A. A Crystalline 1D Dynamic Covalent Polymer. *J. Am. Chem. Soc.* **2022**, *144* (34), 15443-15450. DOI: 10.1021/jacs.2c06446.

(76) Yang, Y.; Lin, E.; Wang, S.; Wang, T.; Wang, Z.; Zhang, Z. Single-Crystal One-Dimensional Porous Ladder Covalent Polymers. *J. Am. Chem. Soc.* **2024**, *146* (1), 782-790. DOI: 10.1021/jacs.3c10812.

(77) Liu, Y.; Ma, Y.; Zhao, Y.; Sun, X.; Gándara, F.; Furukawa, H.; Liu, Z.; Zhu, H.; Zhu, C.; Suenaga, K.; Oleynikov, P.; Alshammari, A. S.; Zhang, X.; Terasaki, O.; Yaghi, O. M. Weaving of organic threads into a crystalline covalent organic framework. *Science* **2016**, *351* (6271), 365-369. DOI: 10.1126/science.aad4011.

Chapter 2

(1) Watson, J. D.; Crick, F. H. C. Molecular Structure of Nucleic Acids: A Structure for Deoxyribose Nucleic Acid. *Nature* **1953**, *171* (4356), 737-738. DOI: 10.1038/171737a0.

(2) Hill, D. J.; Mio, M. J.; Prince, R. B.; Hughes, T. S.; Moore, J. S. A Field Guide to Foldamers. *Chem. Rev.* **2001**, *101* (12), 3893-4012. DOI: 10.1021/cr990120t.

(3) Zhang, D.-W.; Zhao, X.; Hou, J.-L.; Li, Z.-T. Aromatic Amide Foldamers: Structures, Properties, and Functions. *Chem. Rev.* **2012**, *112* (10), 5271-5316. DOI: 10.1021/cr300116k.

(4) Yashima, E.; Ousaka, N.; Taura, D.; Shimomura, K.; Ikai, T.; Maeda, K. Supramolecular Helical Systems: Helical Assemblies of Small Molecules, Foldamers, and Polymers with Chiral Amplification and Their Functions. *Chem. Rev.* **2016**, *116* (22), 13752-13990. DOI: 10.1021/acs.chemrev.6b00354.

(5) Nakano, T.; Okamoto, Y. Synthetic Helical Polymers: Conformation and Function. *Chem. Rev.* **2001**, *101* (12), 4013-4038. DOI: 10.1021/cr0000978.

(6) Yashima, E.; Maeda, K.; Iida, H.; Furusho, Y.; Nagai, K. Helical Polymers: Synthesis, Structures, and Functions. *Chem. Rev.* **2009**, *109* (11), 6102-6211. DOI: 10.1021/cr900162q.

(7) Hu, Y.; Teat, S. J.; Gong, W.; Zhou, Z.; Jin, Y.; Chen, H.; Wu, J.; Cui, Y.; Jiang, T.; Cheng, X.; Zhang, W. Single crystals of mechanically entwined helical covalent polymers. *Nat. Chem.* **2021**, *13* (7), 660-665. DOI: 10.1038/s41557-021-00686-2.

(8) Hu, Y.; Dunlap, N.; Long, H.; Chen, H.; Wayment, L. J.; Ortiz, M.; Jin, Y.; Nijamudheen, A.; Mendoza-Cortes, J. L.; Lee, S.-h.; Zhang, W. Helical Covalent Polymers with Unidirectional Ion Channels as Single Lithium-Ion Conducting Electrolytes. *CCS Chem.* **2021**, *3* (12), 2762-2770. DOI: 10.31635/ccschem.021.202101257.

(9) Ji, Q.; Lirag, R. C.; Miljanić, O. Š. Kinetically controlled phenomena in dynamic combinatorial libraries. *Chem. Soc. Rev.* **2014**, *43* (6), 1873-1884. DOI: 10.1039/C3CS60356C.

(10) Safont-Sempere, M. M.; Fernández, G.; Würthner, F. Self-Sorting Phenomena in Complex Supramolecular Systems. *Chem. Rev.* **2011**, *111* (9), 5784-5814. DOI: 10.1021/cr100357h.

(11) Liu, M.; Zhang, L.; Wang, T. Supramolecular Chirality in Self-Assembled Systems. *Chem. Rev.* **2015**, *115* (15), 7304-7397. DOI: 10.1021/cr500671p.

(12) Hsu, C.-W.; Miljanić, O. Š. Self-sorting through Dynamic Covalent Chemistry. In *Dynamic Covalent Chemistry*, 2017; pp 253-286.

(13) Wang, X.; Bahri, M.; Fu, Z.; Little, M. A.; Liu, L.; Niu, H.; Browning, N. D.; Chong, S. Y.; Chen, L.; Ward, J. W.; Cooper, A. I. A Cubic 3D Covalent Organic Framework with nbo Topology. *J. Am. Chem. Soc.* **2021**, *143* (37), 15011-15016. DOI: 10.1021/jacs.1c08351.

(14) Du, Y.; Yang, H.; Whiteley, J. M.; Wan, S.; Jin, Y.; Lee, S.-H.; Zhang, W. Ionic Covalent Organic Frameworks with Spiroborate Linkage. *Angew. Chem. Int. Ed.* **2016**, *55* (5), 1737-1741. DOI: 10.1002/anie.201509014.

(15) Downard, A.; Nieuwenhuyzen, M.; Seddon, K. R.; van den Berg, J.-A.; Schmidt, M. A.; Vaughan, J. F. S.; Welz-Biermann, U. Structural Features of Lithium Organoborates. *Cryst. Growth Des.* **2002**, *2* (2), 111-119. DOI: 10.1021/cg010035q.

(16) O'Keeffe, M.; Peskov, M. A.; Ramsden, S. J.; Yaghi, O. M. The Reticular Chemistry Structure Resource (RCSR) Database of, and Symbols for, Crystal Nets. *Acc. Chem. Res.* **2008**, *41* (12), 1782-1789. DOI: 10.1021/ar800124u.

(17) Yaghi, O. M.; O'Keeffe, M.; Ockwig, N. W.; Chae, H. K.; Eddaoudi, M.; Kim, J. Reticular synthesis and the design of new materials. *Nature* **2003**, *423* (6941), 705-714. DOI: 10.1038/nature01650.

(18) Kalmutzki, M. J.; Hanikel, N.; Yaghi, O. M. Secondary building units as the turning point in the development of the reticular chemistry of MOFs. *Sci. Adv. 4* (10), eaat9180. DOI: 10.1126/sciadv.aat9180.

(19) Park, J.; Hinckley, A. C.; Huang, Z.; Chen, G.; Yakovenko, A. A.; Zou, X.; Bao, Z. High Thermopower in a Zn-Based 3D Semiconductive Metal–Organic Framework. *J. Am. Chem. Soc.* **2020**, *142* (49), 20531-20535. DOI: 10.1021/jacs.0c09573.

(20) Liu, Y.; Ma, Y.; Zhao, Y.; Sun, X.; Gándara, F.; Furukawa, H.; Liu, Z.; Zhu, H.; Zhu, C.; Suenaga, K.; Oleynikov, P.; Alshammari, A. S.; Zhang, X.; Terasaki, O.; Yaghi, O. M. Weaving of organic threads into a crystalline covalent organic framework. *Science* **2016**, *351* (6271), 365-369. DOI: 10.1126/science.aad4011.

(21) Yahiaoui, O.; Fitch, A. N.; Hoffmann, F.; Fröba, M.; Thomas, A.; Roeser, J. 3D Anionic Silicate Covalent Organic Framework with srs Topology. *J. Am. Chem. Soc.* **2018**, *140* (16), 5330-5333. DOI: 10.1021/jacs.8b01774.

(22) Han, X.; Yuan, C.; Hou, B.; Liu, L.; Li, H.; Liu, Y.; Cui, Y. Chiral covalent organic frameworks: design, synthesis and property. *Chem. Soc. Rev.* **2020**, *49* (17), 6248-6272. DOI: 10.1039/D0CS00009D.

(23) Krebs, F. C.; Schiødt, N. C.; Batsberg, W.; Bechgaard, K. Purification of 2, 3, 6, 7, 10, 11-Hexamtheoxytriphenylene and Preparation of Hexakiscarbonylmethyl and Hexakiscyanomethyl Derivatives of 2, 3, 6, 7, 10, 11-Hexahydroxytriphenylene. *Synthesis* **1997**, 1285-1290.

(24) O'Keeffe, M.; Peskov, M. A.; Ramsden, S. J.; Yaghi, O. M. The Reticular Chemistry Structure Resource (RCSR) Database of, and Symbols for, Crystal Nets. *Acc. Chem. Res.* **2008**, *41* (12), 1782-1789. DOI: 10.1021/ar800124u.

(25) Park, J.; Hinckley, A. C.; Huang, Z.; Chen, G.; Yakovenko, A. A.; Zou, X.; Bao, Z. High Thermopower in a Zn-Based 3D Semiconductive Metal–Organic Framework. *J. Am. Chem. Soc.* **2020**, *142* (49), 20531-20535. DOI: 10.1021/jacs.0c09573.

(26) Hu, Y.; Teat, S. J.; Gong, W.; Zhou, Z.; Jin, Y.; Chen, H.; Wu, J.; Cui, Y.; Jiang, T.; Cheng, X.; Zhang, W. Single crystals of mechanically entwined helical covalent polymers. *Nat. Chem.* **2021**, *13* (7), 660-665. DOI: 10.1038/s41557-021-00686-2.

Chapter 3

(1) Yashima, E.; Maeda, K.; Iida, H.; Furusho, Y.; Nagai, K. Helical Polymers: Synthesis, Structures, and Functions. *Chem. Rev*. **2009,** *109* (11), 6102-6211. DOI: 10.1021/cr900162q.

(2) Nakano, T.; Okamoto, Y. Synthetic Helical Polymers: Conformation and Function. *Chem. Rev.* **2001**, *101* (12), 4013-4038. DOI: 10.1021/cr0000978.

(3) Hill, D. J.; Mio, M. J.; Prince, R. B.; Hughes, T. S.; Moore, J. S. A Field Guide to Foldamers. *Chem. Rev.* **2001**, *101* (12), 3893-4012. DOI: 10.1021/cr990120t.

(4) Zhang, D.-W.; Zhao, X.; Hou, J.-L.; Li, Z.-T. Aromatic Amide Foldamers: Structures, Properties, and Functions. *Chem. Rev*. **2012**, *112* (10), 5271-5316. DOI: 10.1021/cr300116k.

(5) Yashima, E.; Ousaka, N.; Taura, D.; Shimomura, K.; Ikai, T.; Maeda, K. Supramolecular Helical Systems: Helical Assemblies of Small Molecules, Foldamers, and Polymers with Chiral Amplification and Their Functions. *Chem. Rev.* **2016**, *116* (22), 13752-13990. DOI: 10.1021/acs.chemrev.6b00354.

(6) Kusanagi, H.; Chatani, Y.; Tadokoro, H. The crystal structure of isotactic poly(methyl methacrylate): packing-mode of double stranded helices. *Polymer* **1994**, *35* (10), 2028-2039. DOI: 10.1016/0032-3861(94)90224-0.

(7) Wang, Y.; He, Y.; Yu, Z.; Gao, J.; ten Brinck, S.; Slebodnick, C.; Fahs, G. B.; Zanelotti, C. J.; Hegde, M.; Moore, R. B.; Ensing, B.; Dingemans, T. J.; Qiao, R.; Madsen, L. A. Double helical conformation and extreme rigidity in a rodlike polyelectrolyte. *Nat. Commun.* **2019**, *10* (1), 801. DOI: 10.1038/s41467-019-08756-3.

(8) Hu, Y.; Teat, S. J.; Gong, W.; Zhou, Z.; Jin, Y.; Chen, H.; Wu, J.; Cui, Y.; Jiang, T.; Cheng, X.; Zhang, W. Single crystals of mechanically entwined helical covalent polymers. *Nat. Chem.* **2021**, *13* (7), 660-665. DOI: 10.1038/s41557-021-00686-2.

(9) Côté Adrien, P.; Benin Annabelle, I.; Ockwig Nathan, W.; O'Keeffe, M.; Matzger Adam, J.; Yaghi Omar, M. Porous, Crystalline, Covalent Organic Frameworks. *Science* **2005**, *310* (5751), 1166-1170. DOI: 10.1126/science.1120411 .

(10) O'Keeffe, M.; Peskov, M. A.; Ramsden, S. J.; Yaghi, O. M. The Reticular Chemistry Structure Resource (RCSR) Database of, and Symbols for, Crystal Nets. Acc. Chem. Res. 2008, 41 (12), 1782-1789. DOI: 10.1021/ar800124u.

(11) Jin, Y.; Wang, Q.; Taynton, P.; Zhang, W. Dynamic Covalent Chemistry Approaches Toward Macrocycles, Molecular Cages, and Polymers. Acc. Chem. Res. 2014, 47 (5), 1575-1586. DOI: 10.1021/ar500037v.

(12) Jin, Y.; Hu, Y.; Zhang, W. Tessellated multiporous two-dimensional covalent organic frameworks. *Nat. Rev. Chem.* **2017**, *1* (7), 0056. DOI: 10.1038/s41570-017-0056.

(13) Wayment, L. J.; Lei, Z.; Jin, Y.; Zhang, W. Recent Progress in Constructing Structurally Ordered Polymeric Architectures via Dynamic Covalent Chemistry. *CCS Chem.* **2023**, *5* (10), 2194-2206. DOI: 10.31635/ccschem.023.202303004.

(14) Kandambeth, S.; Dey, K.; Banerjee, R. Covalent Organic Frameworks: Chemistry beyond the Structure. *J. Am. Chem. Soc.* **2019**, *141* (5), 1807-1822. DOI: 10.1021/jacs.8b10334.

(15) Geng, K.; He, T.; Liu, R.; Dalapati, S.; Tan, K. T.; Li, Z.; Tao, S.; Gong, Y.; Jiang, Q.; Jiang, D. Covalent Organic Frameworks: Design, Synthesis, and Functions. *Chem. Rev.* **2020**, *120* (16), 8814-8933. DOI: 10.1021/acs.chemrev.9b00550.

(16) Evans, A. M.; Strauss, M. J.; Corcos, A. R.; Hirani, Z.; Ji, W.; Hamachi, L. S.; Aguilar-Enriquez, X.; Chavez, A. D.; Smith, B. J.; Dichtel, W. R. Two-Dimensional Polymers and Polymerizations. *Chem. Rev.* **2022**, *122* (1), 442-564. DOI: 10.1021/acs.chemrev.0c01184.

(17) Ma, T.; Li, J.; Niu, J.; Zhang, L.; Etman, A. S.; Lin, C.; Shi, D.; Chen, P.; Li, L.-H.; Du, X.; Sun, J.; Wang, W. Observation of Interpenetration Isomerism in Covalent Organic Frameworks. *J. Am. Chem. Soc.* **2018**, *140* (22), 6763-6766. DOI: 10.1021/jacs.8b03169.

(18) Gropp, C.; Ma, T.; Hanikel, N.; Yaghi, O. M. Design of higher valency in covalent organic frameworks. *Science* **2020**, *370* (6515), eabd6406. DOI: 10.1126/science.abd6406.

(19) Liu, Y.; Li, J.; Lv, J.; Wang, Z.; Suo, J.; Ren, J.; Liu, J.; Liu, D.; Wang, Y.; Valtchev, V.; Qiu, S.; Zhang, D.; Fang, Q. Topological Isomerism in Three-Dimensional Covalent Organic Frameworks. *J. Am. Chem. Soc.* **2023**, *145* (17), 9679-9685. DOI: 10.1021/jacs.3c01070.

(20) Wayment, L. J.; Wang, X.; Huang, S.; McCoy, M. S.; Chen, H.; Hu, Y.; Jin, Y.; Sharma, S.; Zhang, W. 3D Covalent Organic Framework as a Metastable Intermediate in the Formation of a Double-Stranded Helical Covalent Polymer. *J. Am. Chem. Soc.* **2023**, *145* (28), 15547-15552. DOI: 10.1021/jacs.3c04734.

(21) Gui, B.; Xin, J.; Cheng, Y.; Zhang, Y.; Lin, G.; Chen, P.; Ma, J.-X.; Zhou, X.; Sun, J.; Wang, C. Crystallization of Dimensional Isomers in Covalent Organic Frameworks. *J. Am. Chem. Soc.* **2023**, *145* (20), 11276-11281. DOI: 10.1021/jacs.3c01729.

(22) Wang, X.; Wada, Y.; Shimada, T.; Kosaka, A.; Adachi, K.; Hashizume, D.; Yazawa, K.; Uekusa, H.; Shoji, Y.; Fukushima, T.; Kawano, M.; Murakami, Y. Triple Isomerism in 3D Covalent Organic Frameworks. *J. Am. Chem. Soc.* **2024**, *146* (3),1832-1838. DOI: 10.1021/jacs.3c13863.

(23) Liu, Y.; Ma, Y.; Yang, J.; Diercks, C. S.; Tamura, N.; Jin, F.; Yaghi, O. M. Molecular Weaving of Covalent Organic Frameworks for Adaptive Guest Inclusion. *J. Am. Chem. Soc.* **2018**, *140* (47), 16015-16019. DOI: 10.1021/jacs.8b08949.

(24) Xie, Y.; Li, J.; Lin, C.; Gui, B.; Ji, C.; Yuan, D.; Sun, J.; Wang, C. Tuning the Topology of Three-Dimensional Covalent Organic Frameworks via Steric Control: From pts to Unprecedented ljh. *J. Am. Chem. Soc.* **2021**, *143* (19), 7279-7284. DOI: 10.1021/jacs.1c03042.

(25) Wu, X.; Han, X.; Liu, Y.; Liu, Y.; Cui, Y. Control Interlayer Stacking and Chemical Stability of Two-Dimensional Covalent Organic Frameworks via Steric Tuning. *J. Am. Chem. Soc.* **2018**, *140* (47), 16124-16133. DOI: 10.1021/jacs.8b08452.

(26) Wang, Y.; Liu, Y.; Li, H.; Guan, X.; Xue, M.; Yan, Y.; Valtchev, V.; Qiu, S.; Fang, Q. Three-Dimensional Mesoporous Covalent Organic Frameworks through Steric Hindrance Engineering. *J. Am. Chem. Soc.* **2020**, *142* (8), 3736-3741. DOI: 10.1021/jacs.0c00560.

(27) Xiao, Y.; Ling, Y.; Wang, K.; Ren, S.; Ma, Y.; Li, L. Constructing a 3D Covalent Organic Framework from 2D hcb Nets through Inclined Interpenetration. *J. Am. Chem. Soc.* **2023**, *145* (25), 13537-13541. DOI: 10.1021/jacs.3c03699.

(28) Ma, T.; Kapustin, E. A.; Yin, S. X.; Liang, L.; Zhou, Z.; Niu, J.; Li, L.-H.; Wang, Y.; Su, J.; Li, J.; Wang, X. Wang, W. D.; Wang, W.; Sun, J.; Yaghi, O.M. Single-crystal x-ray diffraction structures of covalent organic frameworks. *Science* **2018**, *361* (6397), 48-52. DOI: doi:10.1126/science.aat7679.

(29) Beaudoin, D.; Maris, T.; Wuest, J. D. Constructing monocrystalline covalent organic networks by polymerization. *Nat. Chem.* **2013**, *5* (10), 830-834. DOI: 10.1038/nchem.1730.

(30) Zhou, Z.; Zhang, L.; Yang, Y.; Vitorica-Yrezabal, I. J.; Wang, H.; Tan, F.; Gong, L.; Li, Y.; Chen, P.; Dong, X.; Liang, Z.; Yang, J.; Wang, C.; Hong, Y.; Qiu, Y.; Gölzhäuser, A.; Chen, X.; Qi, H.; Yang, S.; Liu, W.; Sun, J.; Zheng, Z. Growth of single-crystal imine-linked covalent organic frameworks using amphiphilic amino-acid derivatives in water. *Nat. Chem.* **2023**, *15* (6), 841-847. DOI: 10.1038/s41557-023-01181-6.

(31) Yu, B.; Lin, R.-B.; Xu, G.; Fu, Z.-H.; Wu, H.; Zhou, W.; Lu, S.; Li, Q.-W.; Jin, Y.; Li, J.-H.; Zhang, Z.; Wang, H.; Yan, Z.; Liu, X.; Wang, K.; Chen, B.; Jiang, J. Linkage conversions in single-crystalline covalent organic frameworks. *Nat. Chem.* **2024**, *16* (1), 114-121. DOI: 10.1038/s41557-023-01334-7.

(32) Yu, B.; Li, W.; Wang, X.; Li, J.-H.; Lin, R.-B.; Wang, H.; Ding, X.; Jin, Y.; Yang, X.; Wu, H.; Zhou, W.; Zhang, J.; Jiang, J. Observation of Interpenetrated Topology Isomerism for Covalent Organic Frameworks with Atom-Resolution Single Crystal Structures. *J. Am. Chem. Soc.* **2023**, *145* (46), 25332-25340. DOI: 10.1021/jacs.3c09001.

(33) Xu, H.-S.; Luo, Y.; Li, X.; See, P. Z.; Chen, Z.; Ma, T.; Liang, L.; Leng, K.; Abdelwahab, I.; Wang, L.; Li, R.; Shi, X.; Zhou, Y.; Lu, X. F; Zhao, X.; Liu, C.; Sun, J.; Loh, K. P. Single crystal of a one-dimensional metallo-covalent organic framework. *Nat. Commun.* **2020**, *11* (1), 1434. DOI: 10.1038/s41467-020-15281-1.

(34) Evans, A. M.; Parent, L. R.; Flanders, N. C.; Bisbey, R. P.; Vitaku, E.; Kirschner, M. S.; Schaller, R. D.; Chen, L. X.; Gianneschi, N. C.; Dichtel, W. R. Seeded growth of single-crystal two-dimensional covalent organic frameworks. *Science* **2018**, *361* (6397), 52-57. DOI: 10.1126/science.aar7883.

(35) Li, J.; Lin, C.; Ma, T.; Sun, J. Atomic-resolution structures from polycrystalline covalent organic frameworks with enhanced cryo-cRED. *Nat. Commun.* **2022**, *13* (1), 4016. DOI: 10.1038/s41467-022-31524-9.

(36) Sun, T.; Lei, W.; Ma, Y.; Zhang, Y.-B. Unravelling Crystal Structures of Covalent Organic Frameworks by Electron Diffraction Tomography. *Chinese J. Chem.* **2020**, *38* (10), 1153-1166. DOI: 10.1002/cjoc.202000120.

(37) Liu, Y.; Ma, Y.; Zhao, Y.; Sun, X.; Gándara, F.; Furukawa, H.; Liu, Z.; Zhu, H.; Zhu, C.; Suenaga, K.; Oleynikov, P.; Alshammari, A. S.; Zhang, X.; Terasaki, O.; Yaghi, O. M. Weaving of organic threads into a crystalline covalent organic framework. *Science* **2016**, *351* (6271), 365-369. DOI: 10.1126/science.aad4011.

(38) De Bolòs, E.; Martínez-Abadía, M.; Hernández-Culebras, F.; Haymaker, A.; Swain, K.; Strutyński, K.; Weare, B. L.; Castells-Gil, J.; Padial, N. M.; Martí-Gastaldo, C.; Khlobystov, A. N.; Saeki, A.; Melle-Franco, M.; Nannenga, B. L.; Mateo-Alonso, A. A Crystalline 1D Dynamic Covalent Polymer. *J. Am. Chem. Soc.* **2022**, *144* (34), 15443-15450. DOI: 10.1021/jacs.2c06446.
(39) Liu, B.-T.; Gong, S.-H.; Jiang, X.-T.; Zhang, Y.; Wang, R.; Chen, Z.; Zhang, S.; Kirlikovali, K. O.; Liu, T.-F.; Farha, O. K.; Cao, R. A solution processible single-crystal porous organic polymer. *Nat. Synth.* **2023**, *2* (9), 873-879. DOI: 10.1038/s44160-023-00316-4.
(40) Yang, Y.; Lin, E.; Wang, S.; Wang, T.; Wang, Z.; Zhang, Z. Single-Crystal One-Dimensional Porous Ladder Covalent Polymers. *J. Am. Chem. Soc.* **2024**, *146* (1), 782-790. DOI: 10.1021/jacs.3c10812.
(41) Ousaka, N.; Shimizu, K.; Suzuki, Y.; Iwata, T.; Itakura, M.; Taura, D.; Iida, H.; Furusho, Y.; Mori, T.; Yashima, E. Spiroborate-Based Double-Stranded Helicates: Meso-to-Racemo Isomerization and Ion-Triggered Springlike Motion of the Racemo-Helicate. *J. Am. Chem. Soc.* **2018**, *140* (49), 17027-17039. DOI: 10.1021/jacs.8b08268.
(42) Miwa, K.; Furusho, Y.; Yashima, E. Ion-triggered spring-like motion of a double helicate accompanied by anisotropic twisting. *Nat. Chem.* **2010**, *2* (6), 444-449. DOI: 10.1038/nchem.649.
(43) Chen, H.; Hu, Y.; Luo, C.; Lei, Z.; Huang, S.; Wu, J.; Jin, Y.; Yu, K.; Zhang, W. Spiroborate-Linked Ionic Covalent Adaptable Networks with Rapid Reprocessability and Closed-Loop Recyclability. *J. Am. Chem. Soc.* **2023**, *145* (16), 9112-9117. DOI: 10.1021/jacs.3c00774.
(44) Wang, X.; Bahri, M.; Fu, Z.; Little, M. A.; Liu, L.; Niu, H.; Browning, N. D.; Chong, S. Y.; Chen, L.; Ward, J. W.; Cooper, A. I. A Cubic 3D Covalent Organic Framework with nbo Topology. *J. Am. Chem. Soc.* **2021**, *143* (37), 15011-15016. DOI: 10.1021/jacs.1c08351.
(45) Hu, Y.; Dunlap, N.; Long, H.; Chen, H.; Wayment, L. J.; Ortiz, M.; Jin, Y.; Nijamudheen, A.; Mendoza-Cortes, J. L.; Lee, S.-H.; Zhang, W. Helical Covalent Polymers with Unidirectional Ion Channels as Single Lithium-Ion Conducting Electrolytes. *CCS Chem.* **2021**, *3* (12), 2762-2770. DOI: 10.31635/ccschem.021.202101257.

Chapter 4

(1) Geng, K.; He, T.; Liu, R.; Dalapati, S.; Tan, K. T.; Li, Z.; Tao, S.; Gong, Y.; Jiang, Q.; Jiang, D. Covalent Organic Frameworks: Design, Synthesis, and Functions. *Chem. Rev.* **2020**, *120* (16), 8814-8933, DOI: 10.1021/acs.chemrev.9b00550.
(2) Feng, X.; Ding, X.; Jiang, D. Covalent organic frameworks. *Chem. Soc. Rev.* **2012**, *41* (18), 6010-6022, DOI: 10.1039/C2CS35157A.
(3) Ding, S.-Y.; Wang, W. Covalent organic frameworks (COFs): from design to applications. *Chem. Soc. Rev.* **2013**, *42* (2), 548-568, DOI: 10.1039/C2CS35072F.
(4) Diercks, C. S.; Yaghi, O. M. The atom, the molecule, and the covalent organic framework. *Science* **2017**, *355* (6328), eaal1585. DOI: doi:10.1126/science.aal1585.
(5) Jin, Y.; Hu, Y.; Zhang, W. Tessellated multiporous two-dimensional covalent organic frameworks. *Nat. Rev. Chem.* **2017**, *1* (7), 0056, DOI: 10.1038/s41570-017-0056.
(6) Guan, X.; Chen, F.; Fang, Q.; Qiu, S. Design and applications of three dimensional covalent organic frameworks. *Chem. Soc. Rev.* **2020**, *49* (5), 1357-1384, DOI: 10.1039/C9CS00911F.
(7) O'Keeffe, M.; Peskov, M. A.; Ramsden, S. J.; Yaghi, O. M. The Reticular Chemistry Structure Resource (RCSR) Database of, and Symbols for, Crystal Nets. *Acc. Chem. Res.* **2008**, *41* (12), 1782-1789. DOI: 10.1021/ar800124u.

(8) Jin, Y.; Yu, C.; Denman, R. J.; Zhang, W. Recent advances in dynamic covalent chemistry. *Chem. Soc. Rev.* **2013**, *42* (16), 6634-6654, DOI: 10.1039/C3CS60044K.

(9) Wayment, L. J.; Lei, Z.; Jin, Y.; Zhang, W. Recent Progress in Constructing Structurally Ordered Polymeric Architectures via Dynamic Covalent Chemistry. *CCS Chem*. **2023**, *5* (10), 2194-2206, DOI: 10.31635/ccschem.023.202303004.

(10) Xu, L.; Ding, S.-Y.; Liu, J.; Sun, J.; Wang, W.; Zheng, Q.-Y. Highly crystalline covalent organic frameworks from flexible building blocks. *Chem. Commun.* **2016**, *52* (25), 4706-4709, DOI: 10.1039/C6CC01171C.

(11) Zhao, C.; Diercks, C. S.; Zhu, C.; Hanikel, N.; Pei, X.; Yaghi, O. M. Urea-Linked Covalent Organic Frameworks. *J. Am. Chem. Soc.* **2018**, *140* (48), 16438-16441. DOI: 10.1021/jacs.8b10612.

(12) Han, X.; Xia, Q.; Huang, J.; Liu, Y.; Tan, C.; Cui, Y. Chiral Covalent Organic Frameworks with High Chemical Stability for Heterogeneous Asymmetric Catalysis. *J. Am. Chem. Soc.* **2017**, *139* (25), 8693-8697, DOI: 10.1021/jacs.7b04008.

(13) Lei, Z.; Wayment, L. J.; Cahn, J. R.; Chen, H.; Huang, S.; Wang, X.; Jin, Y.; Sharma, S.; Zhang, W. Cyanurate-Linked Covalent Organic Frameworks Enabled by Dynamic Nucleophilic Aromatic Substitution. *J. Am. Chem. Soc.* **2022**, *144* (39), 17737-17742, DOI: 10.1021/jacs.2c00778.

(14) Liu, Y.; Li, J.; Lv, J.; Wang, Z.; Suo, J.; Ren, J.; Liu, J.; Liu, D.; Wang, Y.; Valtchev, V.; Qiu, S.; Zhang, D.; Fang, Q. Topological Isomerism in Three-Dimensional Covalent Organic Frameworks. *J. Am. Chem. Soc.* **2023**, *145* (17), 9679-9685, DOI: 10.1021/jacs.3c01070.

(15) Du, Y.; Yang, H.; Whiteley, J. M.; Wan, S.; Jin, Y.; Lee, S.-H.; Zhang, W. Ionic Covalent Organic Frameworks with Spiroborate Linkage. *Angew. Chem. Int. Ed.* **2016**, *55* (5), 1737-1741, DOI:10.1002/anie.201509014.

(16) Hu, Y.; Teat, S. J.; Gong, W.; Zhou, Z.; Jin, Y.; Chen, H.; Wu, J.; Cui, Y.; Jiang, T.; Cheng, X.; Zhang, W. Single crystals of mechanically entwined helical covalent polymers. *Nat. Chem.* **2021**, *13* (7), 660-665. DOI: 10.1038/s41557-021-00686-2.

(17) Wang, X.; Bahri, M.; Fu, Z.; Little, M. A.; Liu, L.; Niu, H.; Browning, N. D.; Chong, S. Y.; Chen, L.; Ward, J. W.; Cooper, A. I. A Cubic 3D Covalent Organic Framework with nbo Topology. *J. Am. Chem. Soc.* **2021**, *143* (37), 15011-15016. DOI: 10.1021/jacs.1c08351.

(18) Wayment, L. J.; Wang, X.; Huang, S.; McCoy, M. S.; Chen, H.; Hu, Y.; Jin, Y.; Sharma, S.; Zhang, W. 3D Covalent Organic Framework as a Metastable Intermediate in the Formation of a Double-Stranded Helical Covalent Polymer. *J. Am. Chem. Soc.* **2023**, *145* (28), 15547-15552. DOI: 10.1021/jacs.3c04734.

(19) Wayment, L. J.; Teat, S. J.; Huang, S.; Chen, H.; Zhang, W. Dynamic Entwined Topology in Helical Covalent Polymers Dictated by Competing Supramolecular Interactions. *Angew. Chem. Int. Ed.* **2024**, e202403599. DOI: 10.1002/anie.202403599.

(20) Moriya, M.; Kato, D.; Sakamoto, W.; Yogo, T. Plastic crystalline lithium salt with solid-state ionic conductivity and high lithium transport number. *Chem. Commun.* **2011**, *47* (22), 6311-6313, DOI: 10.1039/C1CC00070E.

(21) Duncan, D. T.; Roy, B.; Piper, S. L.; Nguyen, C.; Howlett, P.; Forsyth, M.; MacFarlane, D. R.; Sun, J.; Kar, M. High-Ionicity Electrolytes Based on Bulky Fluoroborate Anions for Stable Na-Metal Cycling. *J. Phys. Chem. C* **2022**, *126* (44), 18918-18930. DOI: 10.1021/acs.jpcc.2c06187.

(22) Bocharova, V.; Sokolov, A. P. Perspectives for Polymer Electrolytes: A View from Fundamentals of Ionic Conductivity. *Macromolecules* **2020**, *53* (11), 4141-4157. DOI: 10.1021/acs.macromol.9b02742.

(23) Stolberg, M. A.; Paren, B. A.; Leon, P. A.; Brown, C. M.; Winter, G.; Gordiz, K.; Concellón, A.; Gómez-Bombarelli, R.; Shao-Horn, Y.; Johnson, J. A. Lamellar Ionenes with Highly Dissociative, Anionic Channels Provide Lower Barriers for Cation Transport. *J. Am. Chem. Soc.* **2023**, *145* (29), 16200-16209. DOI: 10.1021/jacs.3c05053.

(24) Hu, Y.; Wayment, L. J.; Haslam, C.; Yang, X.; Lee, S.-H.; Jin, Y.; Zhang, W. Covalent organic framework based lithium-ion battery: Fundamental, design and characterization. *EnergyChem* **2021**, *3* (1), 100048. DOI: 10.1016/j.enchem.2020.100048.

(25) Zhu, Y.; Bai, Q.; Ouyang, S.; Jin, Y.; Zhang, W. Covalent Organic Framework-based Solid-State Electrolytes, Electrode Materials, and Separators for Lithium-ion Batteries. *ChemSusChem* **2024**, *17* (1), e202301118. DOI: 10.1002/cssc.202301118.

(26) Zhu, D.; Xu, G.; Barnes, M.; Li, Y.; Tseng, C.-P.; Zhang, Z.; Zhang, J.-J.; Zhu, Y.; Khalil, S.; Rahman, M. M.; Verduzco, R.; Ajayan, P. M. Covalent Organic Frameworks for Batteries. *Adv. Funct. Mater.* **2021**, *31* (32), 2100505. DOI: 10.1002/adfm.202100505.

(27) Zhao, X.; Pachfule, P.; Thomas, A. Covalent organic frameworks (COFs) for electrochemical applications. *Chem. Soc. Rev.* **2021**, *50* (12), 6871-6913, DOI: 10.1039/D0CS01569E.

(28) Liang, X.; Tian, Y.; Yuan, Y.; Kim, Y. Ionic Covalent Organic Frameworks for Energy Devices. *Adv. Mater.* **2021**, *33* (52), 2105647. DOI: 10.1002/adma.202105647.

(29) Albertus, P.; Babinec, S.; Litzelman, S.; Newman, A. Status and challenges in enabling the lithium metal electrode for high-energy and low-cost rechargeable batteries. *Nat. Energy* **2018**, *3* (1), 16-21, DOI: 10.1038/s41560-017-0047-2

(30) Schneider, S. F.; Bauer, C.; Novák, P.; Berg, E. J. A modeling framework to assess specific energy, costs and environmental impacts of Li-ion and Na-ion batteries. *Sustain. Energy Fuels* **2019**, *3* (11), 3061-3070, DOI: 10.1039/c9se00427k

(31) Abraham, K. How comparable are sodium-ion batteries to lithium-ion counterparts? *ACS Energy Lett.* **2020**, *5* (11), 3544-3547, DOI: 10.1021/acsenergylett.0c02181

(32) Zhang, W.; Lu, J.; Guo, Z. Challenges and future perspectives on sodium and potassium ion batteries for grid-scale energy storage. *Mater. Today* **2021**, *50*, 400-417, DOI:10.1016/j.mattod.2021.03.015.

(33) Hu, Y.; Dunlap, N.; Long, H.; Chen, H.; Wayment, L. J.; Ortiz, M.; Jin, Y.; Nijamudheen, A.; Mendoza-Cortes, J. L.; Lee, S.-H.; Zhang, W. Helical Covalent Polymers with Unidirectional Ion Channels as Single Lithium-Ion Conducting Electrolytes. *CCS Chem.* **2021**, *3* (12), 2762-2770, DOI: 10.31635/ccschem.021.202101257.

Chapter 5

(1) Hu, Y.; Dunlap, N.; Long, H.; Chen, H.; Wayment, L. J.; Ortiz, M.; Jin, Y.; Nijamudheen, A.; Mendoza-Cortes, J. L.; Lee, S.-H.; Zhang, W. Helical Covalent Polymers with Unidirectional Ion Channels as Single Lithium-Ion Conducting Electrolytes. *CCS Chem.* **2021**, *3* (12), 2762-2770, DOI: 10.31635/ccschem.021.202101257.